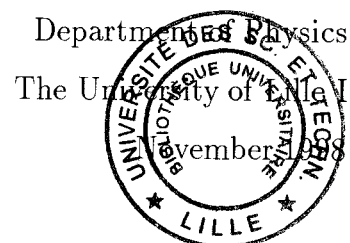


Quantification of MQMAS Spectra and Application to the Study of Microporous Materials

by

LAURENT DELEVOYE

A thesis submitted to the Faculty of Science
of the University of Lille I
for the degree of
Doctor of Philosophy



To my Mother

Acknowledgements

I would like to thank the following people: the staff of the “Laboratoire de Dynamique et Structure des Matériaux Moléculaires”, and its two successive directors, Profs. J. Lefebvre and M. Descamps; Profs. J-P. Amoureux for initiating me to the theoretical background of solid-state NMR and his constructive corrections of the manuscript; Prof. C. Fernandez for having introduced me to MQMAS and for sharing his computing and programming skills with me; all those colleagues who showed interest in my various research projects: Dr. M. Welch, Prof. D. Freude, Dr. M. Pruski, Prof. J. B’Nagy; D.R. D. Massiot and D.R. F. Taulelle who accepted to review this work.

I want to express my special thanks to: Dr. J. Klinowski for accepting me within his research group, for advising and encouraging me to pursue more applied work in NMR; Dr. S. Ganapathy for his friendship and for taking the time to share with me his extensive knowledge and expertise in the field; my friends, Alain, Anthony, François-Xavier, Jérôme, Pierre, Yves, Maria Dolores, Shuangxi, Heyong, Alejandro, José Ramon, who helped in many different ways but all contributed in making these three years memorable.

I am especially indebted to my family which have given me unconditional support all through these years and finally Yvonne for her commitment to me, and for her constant support both on the academic and the personal

front.

Contents

Acknowledgements	v
Introduction	xvii
1 Spin interactions in solids	1
1.1 Basics in NMR	1
1.1.1 Spin Angular Momentum	1
1.1.2 Zeeman Interaction	2
1.1.3 Pulsed NMR	3
1.1.4 Multiple-Quantum Transitions	6
1.2 Spin Hamiltonians in Solids	8
1.2.1 Origin of Interactions	9
1.2.2 Mathematical Tools	10
1.2.3 Hamiltonians of Spin Interactions	15
1.3 Motional Narrowing	20
1.3.1 General	21
1.3.2 Averaging First-order interactions	22
1.3.3 Second-order Averaging	30
1.4 Conclusion	41
1.5 La Résonance Magnétique dans les Solides (résumé)	43

1.5.1	Généralités sur les Interactions dans les Solides	43
1.5.2	Moyennage Spatial de l'Interaction Quadrupolaire	49
2	Averaging with MQMAS	59
2.1	Basics of Two Dimensional MQMAS	59
2.1.1	Theoretical Consideration of Spin Terms	59
2.1.2	Theory of MQMAS	65
2.1.3	Acquisition and Processing	71
2.2	Optimization of 2D MQMAS	79
2.2.1	Improvements of MQMAS	79
2.2.2	Determination of Experimental Parameters	92
2.3	Further on with MQMAS	102
2.3.1	Scaling spectra	103
2.3.2	Determination of Quadrupolar Parameters	106
2.3.3	Combination With Other Spin Manipulations	110
2.4	Conclusion	118
2.5	L'expérience MQMAS (résumé)	120
2.5.1	Bases Théoriques du MQMAS	120
2.5.2	Optimisation de la Séquence z -filtering MQMAS	125
2.5.3	Avantages du MQMAS	128
3	Quantification of MQMAS spectra	137
3.1	Problem of Quantitative NMR	137
3.1.1	Quantification of MAS spectra	137
3.1.2	Using MQMAS and MAS Spectra	141
3.1.3	Using Isotropic MQMAS projection	144
3.1.4	Distribution of Nucleus Surroundings	146
3.2	Basics of Regularization Method	151

3.2.1	General	151
3.2.2	Numerical Approach	153
3.2.3	Linear Regularization Method	158
3.3	Quantification using Regularisation Method	161
3.3.1	Description of REGULAR	161
3.3.2	Application to the Quantification of ^{27}Al and ^{17}O MQ- MAS spectra	170
3.4	Conclusion	176
3.5	Quantification des spectres MQMAS (résumé)	178
3.5.1	Quantification en RMN	178
3.5.2	Méthode de Régularisation	182
3.5.3	Régularisation appliquée aux spectres MQMAS	185
4	Quelques Applications du MQMAS	193
4.1	Etude structurale d'amphiboles	193
4.2	Caractérisation des sites ^{27}Al dans une levyne	200
4.3	Caractérisation des cations dans l'ETS-10	207
	Conclusion	223
	Appendix	227

List of Figures

1.1	Vectorial representation of a pulse effect	5
1.2	Zeeman energy levels	7
1.3	Coherence-order pathways	7
1.4	Magic angle spinning experiment	26
1.5	Static and MAS spectra	29
1.6	Second- and fourth-Legendre polynomials	38
1.7	Double rotor system	38
1.8	Pulse sequence for dynamic-angle spinning experiment	40
2.1	Effects of first- and second-order quadrupolar interactions	64
2.2	Basic two-dimensional NMR experiment	66
2.3	Echo pathway for $I = 3/2$	70
2.4	Echo pathway for $I = 5/2$	70
2.5	2D 3QMAS dataset in time domain for spins $3/2$ and $5/2$	74
2.6	Echo and antiecho pathways for a spin $I = 3/2$	74
2.7	Echo and antiecho 2D datasets	76
2.8	Different steps of the data processing	80
2.9	Frydman's three-pulse MQMAS sequence	82
2.10	Two-pulse MQMAS sequence	83
2.11	Efficiency of the two-pulse sequence as a function of τ_2	84
2.12	z -filter sequence	85

2.13	Three-pulse shifted-echo sequence	87
2.14	Split- t_1 3QMAS sequence	89
2.15	Selected pathways in a z -filter sequence as a function of the number N_2 of phases applied to the third pulse	94
2.16	3QMAS spectra of $\text{AlPO}_4 - 14$ acquired with $N_2=4$ and $N_2 = 1$	95
2.17	Experimental optimization of the pulse lengths τ_1 and τ_2 using the z -filter sequence	100
2.18	3QMAS and CP 3QMAS spectra of $\text{AlPO}_4 - 11$	108
2.19	CP 3QMAS pulse sequence	112
2.20	Comparison of 3QMAS and CP-3QMAS isotropic projections .	114
2.21	Comparison of 3QMAS and 3Q-REDOR isotropic projections	115
2.22	3Q-REDOR pulse sequence	117
3.1	Amplitude of the central transition as a function of the pulse length τ_1 (<i>for a single crystallite</i>)	139
3.2	Amplitude of the central transition as a function of the pulse length τ_1 (<i>for a powder</i>)	140
3.3	Efficiency of the 3QMAS z -filter experiment versus the quadrupo- lar constant C_Q	143
3.4	Individual 1D MAS lineshapes for the 5 sites in $\text{AlPO}_4 - 11$.	145
3.5	Effects of a gaussian distribution of isotropic chemical shift δ_{CS}	149
3.6	Effects of a gaussian distribution of quadrupolar constant C_Q .	150
3.7	Density matrix for a spin $I = 5/2$	164
3.8	Representation of the "leap-frog" method	165
3.9	Single-quantum elements in the density matrix	166
3.10	set of 1D spectra generated by PULSAR	169
3.11	quantification of the ^{27}Al sites in $\text{AlPO}_4 - 11$ using REGULAR	171
3.12	MAS and simulated 1D spectra of the ZSM - 5	173

3.13	^{17}O 3QMAS spectrum of the ZSM – 5	173
3.14	Quantification of ^{17}O sites in the ZSM – 5	174
4.1	Schematic representation of the structure of ETS-10	208
4.2	Other schematic representation of the structure of ETS-10	209
4.3	Main steps in REGULAR	228

List of Tables

1.1	Magnitude of interactions in solids	9
1.2	Reduced Wigner rotation matrix	12
1.3	Constants C^λ	13
1.4	δ_D , δ_σ and η_σ parameters of dipolar and chemical shift interactions	19
1.5	irreducible spherical dipolar and chemical shift tensors	19
1.6	irreducible spin tensors for dipolar and chemical shift interactions	19
1.7	New spherical tensor components	35
2.1	$C_4^I(p)$ and $R(I, p)$ values	68
2.2	Phase cycle for excitation of triple-quantum coherences (real part in t_1)	76
2.3	Phase cycle for excitation of triple-quantum coherences (imaginary part in t_1)	76
2.4	Phase cycle for the z -filter sequence	96
2.5	Optimum flip-angles for the z -filter experiment	97
2.6	K values as a function of the spin number I	110
3.1	various parameters obtained by fitting the slices of the 3QMAS spectrum of $\text{AlPO}_4 - 11$	144

3.2	Most relevant experimental parameters introduced in the PUL- SAR calculation	170
3.3	Quantitative results obtained with QUASAR and REGULAR	175

Introduction

High-resolution NMR

Despite its short existence, Nuclear Magnetic Resonance (NMR) has become a powerful technique of investigation used for research in a wide range of domains: biology, physics, chemistry, etc. Indeed, unlike other spectroscopic methods, NMR has the special feature of being able to select separately each nucleus. Therefore, it is possible to probe the local environment of a specific nucleus through the characterisation of its interactions. Thanks to the Brownian motion of molecules, interactions in liquids are restricted to an isotropic component such that the NMR spectrum is composed of extremely narrow bands. Thus, the distinction between the different groups of atoms within the structure of a molecule is possible. The development of two-dimensional NMR experiments in 1971 is an event to underline, as it gave new insights to the technique. From then on, a huge number of new experiments emerged, mainly dedicated to liquids. Today, two- and even three-dimensional NMR experiments are essential to determine the structure of biological molecules, which can sometimes involve thousands of atoms!

Solid-state NMR has still not reached this stage of high resolution. The problem comes from the rigidity of the crystal lattice, which renders the different interactions anisotropic. Moreover, researchers often study powder samples in NMR since it is difficult to obtain single-crystals of sufficient

dimensions ($> 1\text{mm}^3$). Consequently, the anisotropic features of the interactions, in addition to the presence of crystallites of various orientations, generate homogeneous and inhomogeneous broadenings of the resonances. For spin $I = 1/2$, these anisotropic broadenings can be averaged out either by rotating the sample at a certain angle (magic angle) or by manipulating the spins using appropriate pulse sequences.

Other spins ($I > 1/2$) undergo an additional *quadrupolar* interaction which contributes to the broadening of the NMR spectrum. Unfortunately, the magic angle rotation does not cancel out the whole quadrupolar broadening. Since quadrupolar nuclei constitute almost 3/4 of the existing elements, it has always been of high interest for researchers in material science to find new methods of averaging these anisotropies.

Solid-state NMR of quadrupolar nuclei

For quadrupolar nuclei, the development of new methods of high resolution has been slower compared to other fields in NMR. Indeed, the theoretical foundations used up to then in solid-state NMR needed time to mature. Moreover, certain technological challenges, such as the rotation of the sample at high speeds, have hindered the application of the theory. In 1988, two new experiments based on the double rotation of the sample were proposed to enable scientists to obtain isotropic spectra of quadrupolar nuclei. These techniques (DOUBLE ROTATION and DYNAMIC ANGLE SPINNING) rely on the manipulation of the spatial part of the quadrupolar Hamiltonian. With these methods, researchers had to face the problem of spinning simultaneously or sequentially a given sample at two specific angles. However, such technological challenges have still not been fully overcome, which explains why double rotation experiments have failed to become routine experiments in chemistry.

While many were trying to solve the problem of spinning a sample at two different angles, a few researchers started to focus their attention on the spin part of the Hamiltonian. They highlighted the fact that the Hamiltonian is dependent of the multiple- and single-quantum transition that is excited. Unfortunately single-quantum transitions are the only observable transitions in NMR. It was in 1995 that Frydman showed that the averaging of the quadrupolar broadenings is experimentally possible. In fact he replaced the second rotation of the sample by a correlation of single- and multiple-quantum transitions in a *two-dimensional* experiment. This *Multiple-Quantum Magic Angle Spinning* experiment efficiently combines the manipulation of both spatial and spin parts of the Hamiltonian. Therefore, it technologically requires the equipment used for simple magic angle spinning experiments.

Organization of the Ph.D.

I started my Ph.D. within the group of Prof. Amoureux in December 1995, that is about 8 months after Frydman presented his first experimental results on MQMAS. Thus, my work was naturally oriented towards the development of this method and especially the problem of the quantification of 2D spectra.

At the same time, I had the strong desire to work with Dr. Klinowski whose interest was to use the MQMAS experiment to solve structural problems in microporous materials. Through a collaboration developed between the two laboratories, I was able to share my time between the laboratory in Lille (France) and the one in Cambridge (UK). In Cambridge, the laboratory is equipped with Chemagnetics facilities. Thus, I had to first adapt the MQMAS experiment to the available hardware. Then, Dr. Klinowski put me in contact with Dr. Welch from the Natural History Museum of Lon-

don, in order to apply the MQMAS experiments to the study of minerals (amphiboles).

In Lille, Prof. Amoureux's group has had over ten years of experience in the development of numerical calculations applied to NMR experiments. The softwares (QUASAR, PULSAR) written by Profs. Amoureux and Fernandez have been of great help for the improvement of the MQMAS experiment. At the time I commenced my Ph.D., MQMAS spectrum provided poor quantitative information. Thus, as a student in their group, I was asked to contribute to the development of a numerical method, which would correct the intensities.

On several occasions, I have had the possibility to meet professors, lecturers and students from other laboratories who came to Lille to get a better understanding of the MQMAS experiment. These encounters have been challenging as it often gave me the chance to apply both the MQMAS technique and the method of quantification, which I was developing, to samples with structural uncertainties. The materials were microporous materials (zeolites) containing quadrupolar nuclei (^{27}Al , ^{17}O , ^{23}Na).

Organization of the manuscript

I deliberately chose to write my thesis in english despite the extra work that I knew it would require. After working in Cambridge and with researchers coming from the US, India and Germany, it was important for me to complete my three years of research with a manuscript that they could understand and thus, fairly evaluate. However, I have included a summary in french at the end of each chapter in order to fulfill the conditions of submission for a french university.

The first chapter of this manuscript concerns the theoretical basics of

NMR. After a general section to introduce the phenomena involved in NMR, I give the different interactions, which occur in solids. The development of the Hamiltonian has been limited to the quadrupolar interaction only. Then, I focus on the spatial part of the quadrupolar Hamiltonian until I obtain an expression for the first-order interaction. The basics of magic angle spinning experiments are explained at that point. A development of the Hamiltonian to the second-order is also achieved in order to get an equation, which will be the starting point for the second chapter on MQMAS.

Whereas spin parts of the quadrupolar Hamiltonian were left out in the first chapter, they are introduced in the second chapter explicitly written in order to explain how it is possible to remove quadrupolar broadenings by correlating the single- and multiple-quantum coherences in a two-dimensional MAS experiment. In a further section, I go through with detail the main steps involved in the acquisition and the processing of a 2D MQMAS spectrum and I present as well the optimal experimental conditions that should be used. Finally, a selected example demonstrates the flexibility of the technique by showing combination of other spin manipulations (CP and REDOR) that are possible with the MQMAS experiment.

The third chapter starts by showing the problem that occurs when one wants to obtain quantitative results in solid-state NMR of quadrupolar nuclei. It is stated and explained why such information is difficult to obtain when materials are *badly crystallised* or *amorphous*. Thus, the theoretical foundations of the method of quantification are given. Such a calculation requires a program, namely PULSAR, which can take into account experimental parameters to simulate the NMR lineshape. At this point, I give two examples of quantification by inversion of the MQMAS spectrum in order to demonstrate the validity of the method.

Finally, the fourth chapter is the grouping of three articles published or in the process of being published that present new and interesting results.

Chapter 1

Spin interactions in solids

1.1 Basics in NMR

1.1.1 Spin Angular Momentum

Nuclear Magnetic Resonance phenomenon results from the interaction of magnetic fields (static and oscillating) with physical properties of the nuclei, specifically linked to the spin of the considered particle. The theoretical study of NMR could be lead by simply considering the nucleus as a small magnet. Its physical properties would then come from classical mechanics. However, quantum mechanics is convenient, even necessary, as it introduces new properties for the nucleus. Indeed, NMR is only possible when the system under consideration possesses a magnetic moment $\boldsymbol{\mu}$ as well as an angular momentum \mathbf{J} so that $\boldsymbol{\mu}=\gamma\mathbf{J}$. γ is the gyromagnetic ratio that differentiates nuclei from each other. As \mathbf{J} is proportional to the spin kinetic momentum \mathbf{I} , the magnetic moment of a spin will be written

$$\boldsymbol{\mu} = \gamma\hbar\mathbf{I} \tag{1.1}$$

where $\hbar = h/2\pi$ denotes the reduced Planck's constant.

Of course, in the quantum theory, $\boldsymbol{\mu}$, \mathbf{J} and \mathbf{I} are treated as operators. Then, \mathbf{I}^2 has eigenvalues $I(I+1)$ which are either integer or half-integer. We must also consider eigenvalues m of the projection I_z of \mathbf{I} onto the Oz axis, taken parallel to the static magnetic field \mathbf{B}_0 . I and m are denoted the spin quantum number and the magnetic quantum number respectively, the latter taking any of the $2I+1$ values, $I, I-1, \dots, -I$.

Consequently, nuclei A_ZX with a spin quantum number equal to zero (for A and Z even) are not sensitive to NMR excitation. Other nuclei can be observed by NMR, their spin number I being integer or half-integer. We will further distinguish nuclei with spin quantum number I equal to $1/2$ from quadrupolar nuclei for which the spin number I can take any integer or half-integer values superior to $1/2$. The present work is mainly dedicated to the latter category as quadrupolar nuclei represent 75% of the periodic table and reveal an important source of structural information.

1.1.2 Zeeman Interaction

The application of an external static magnetic field \mathbf{B}_0 to the spin system produces a coupling with the magnetic moment $\boldsymbol{\mu}$. The interaction between \mathbf{B}_0 and $\boldsymbol{\mu}$ is commonly named the Zeeman interaction and involves an energy of amount $-\boldsymbol{\mu} \cdot \mathbf{B}_0$. Taking the field \mathbf{B}_0 along the z -direction, we find

$$\mathcal{H}_z = -\gamma\hbar B_0 I_z \quad (1.2)$$

The eigenvalues of the Zeeman Hamiltonian are multiples of the eigenvalues m of I_z so that the allowed energies are

$$E_m = m\gamma\hbar B_0 \quad (1.3)$$

with $m = I, I - 1, \dots, -I$.

These eigenvalues are illustrated in Fig. 1.2 for the case $I = 3/2$, corresponding to nuclei such as ^{23}Na and ^{11}B . It must be noted that the levels are equally spaced, the distance between successive levels being $\Delta E = \gamma\hbar B_0$.

The energy distribution of individual nuclear momenta under \mathbf{B}_0 is ruled by the Boltzmann theory which says that there is a population difference to the benefit of the lowest energies. Consequently, this Boltzmann distribution of energy levels creates a macroscopic magnetization $\mathbf{M}_0 = \sum_{i=1}^N \boldsymbol{\mu}_i$ which is directly linked to the paramagnetism detectable in NMR. \mathbf{M}_0 and \mathbf{B}_0 are related by the paramagnetism susceptibility, denoted χ . The coefficient χ is written

$$\chi = \frac{N\hbar^2\gamma^2 I(I+1)}{3kT} \quad (1.4)$$

Eq. 1.4 points out that the efficiency of an NMR excitation strongly depends on the gyromagnetic ratio γ of the nucleus and that the intensity of the NMR signal is proportional to the number N of particles in the sample.

1.1.3 Pulsed NMR

The acquisition of an NMR signal is liable to the detection of the paramagnetism. However, this is generally rendered difficult due to the fact that at room temperature, χ ($\approx 10^{-5}$) is small and the corresponding paramagnetism is hidden by the electronic diamagnetism. Therefore, modern NMR has found in the resonance phenomenon a way to increase the paramagnetic effect.

The most common way of producing magnetic resonances is to apply an alternating magnetic field \mathbf{B}_1 perpendicularly to the static magnetic field \mathbf{B}_0 . This alternating field will induce transitions between the Zeeman energy levels provided that the resonance condition is fulfilled. Since the Zeeman levels are separated by a quantity $\Delta E = \gamma\hbar B_0$, we can deduce the Larmor frequency $\omega_0 = \gamma B_0$.^{1, 2} Considering the actual values for B_0 (up to 21 Tesla), the Larmor frequency is in the radio-frequency domain.

It may be helpful now to examine the behavior of the magnetization after the application of a radio-frequency pulse, at the Larmor frequency, perpendicular to \mathbf{B}_0 . This is illustrated in Fig. 1.1. At equilibrium (Fig. 1.1-a), the magnetization \mathbf{M}_0 is parallel to \mathbf{B}_0 . Then, a rf pulse creates a precession of the magnetization through the torque $\mathbf{M} \wedge \mathbf{B}_1$ (Fig. 1.1-b) which is equivalent to inducing transitions between Zeeman levels. At resonance, the magnetization can thus be transferred into the plan $x'Oy'$ perpendicular to \mathbf{B}_0 if the pulse length is correctly adapted ($\pi/2$ pulse). Finally, when the rf field \mathbf{B}_1 is removed, the magnetization \mathbf{M} is described by the differential Eq. 1.5, if we only consider the effect of \mathbf{B}_0 . Therefore, it appears that this equation describes a perpetual motion of the magnetization \mathbf{M} around \mathbf{B}_0 .

$$\frac{d\mathbf{M}}{dt} = \gamma\mathbf{M} \wedge \mathbf{B}_0 \quad (1.5)$$

Bloch³ introduced a longitudinal relaxation time T_1 and a transverse relaxation time T_2 in order to illustrate the last stage of a pulsed experiment: the relaxation times result from the interactions of the nucleus with its environment. Thus, Bloch equations (Eqs. 1.6 after a $\pi/2$ pulse) contain exponential terms in T_1 and T_2 that impose the magnetization to return to its

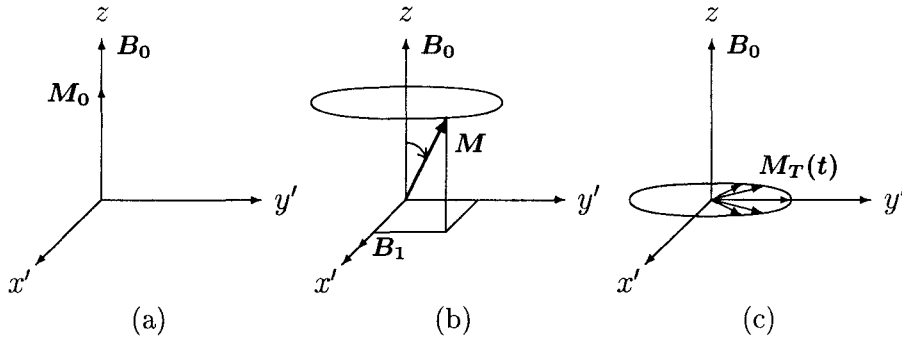


Figure 1.1: Vectorial representation of the influence of a pulse excitation on the magnetization

equilibrium position.

$$\begin{cases} M_T(t) = M_0 e^{-t/T_2} e^{i\Delta\omega t} \\ M_z(t) = M_0 (1 - e^{-t/T_1}) \end{cases} \quad (1.6)$$

$M_T(t)$ denotes the complex relaxation in the transverse plan $x'Oy'$ and it is commonly named the Free Induction Decay (FID) (Fig. 1.1-c). $\Delta\omega = \omega - \omega_0$ corresponds to the offset, i.e., the difference between the frequency of the spin system and the Larmor frequency.

The acquisition of an NMR signal consists of recording real and imaginary parts of the FID. This is carried out by a synchronous detection dephased by 90° . A Fourier transform of these two signals yields absorption and dispersive spectra.

The advantage of pulsed NMR, in comparison with previous continuous-wave techniques, rests with the ability to obtain a spectrum over a wide frequency range, in a limited time and with a signal-noise ratio (S/N) increased by successive repetitions of the pulse sequence. Today, we realize

that this technique has also lead NMR to even more complexe multiple-pulse experiments.

1.1.4 Multiple-Quantum Transitions

We have previously shown that an rf field \mathbf{B}_1 at Larmor frequency induces transition between the $2I + 1$ energy levels of a spin I . The most common experiment is composed of a single weak pulse that will induce transitions between adjacent energy levels. Such transitions are denoted single-quantum transitions as they involve only one energy $\gamma\hbar B_0$. Additionally, non-adjacent transitions can be excited by applying a stronger rf field.⁴ The latter will be referred to as p -quantum transitions when involving an energy equal to $p\gamma\hbar B_0$. This definition naturally suggests another possible representation of the energy levels of a spin I , in terms of multiple-quantum transitions (Fig. 1.3). This diagram is usually preferred in multiple-pulse NMR studies, especially for two-dimensional NMR experiments. The deliberate separation of transitions of opposite sign ($p/2 \longrightarrow -p/2$ and $-p/2 \longrightarrow p/2$) will be further justified when two-dimensional experiments will be introduced.

Multiple-pulse experiments allow the excitation of various different single- and multiple-quantum transitions. However, the selection rule of Eq. 1.7 clearly states that only single-quantum transitions are observable in NMR, i.e. whatever the number of pulses and whatever the multiple-quantum transitions involved in the sequence, the pulse preceding the acquisition must be optimized in order to populate mainly single-quantum levels. It must be pointed out that the convention is to take $p = -1$ for the acquisition.

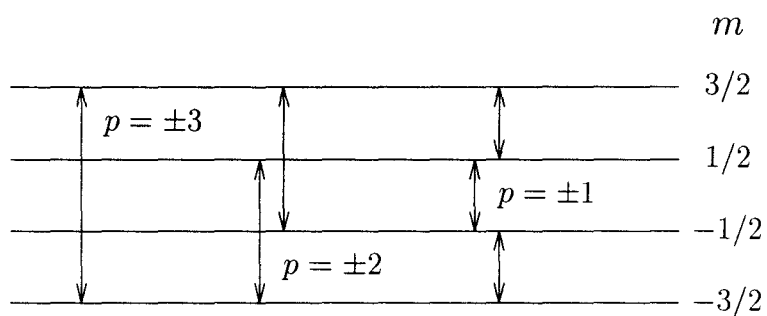


Figure 1.2: Zeeman energy levels for a nucleus with $I = 3/2$

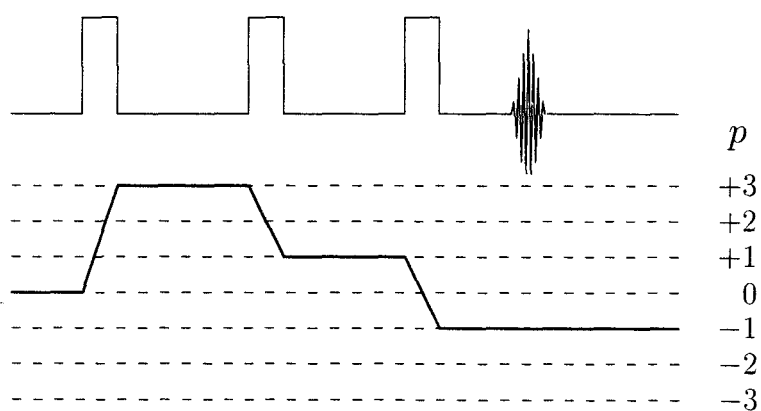


Figure 1.3: representation in terms of coherence-order pathways p , deduced from Fig. 1.2. Coherence-order pathways of opposite signs are considered separately.

$$\sum_i \Delta m_i = \pm 1 \quad (1.7)$$

Even though quantum mechanics is not necessary to understand the basics in NMR, it becomes essential when elaborate interpretations of NMR spectra have to be made. Bloch equations are basically limited to liquid NMR where most internal interactions that affect the relaxation are averaged out by Brownian motion of molecules. In solids, different interactions generally alter the relaxation of the spins. Thus, solid-state NMR spectra are rendered even more complicated by various broadenings. On the other hand, solid-state NMR may bring valuable structural information provided that these broadenings are correctly interpreted. Special quantum mechanical developments are required to explain NMR spectra of solids. Therefore, the next section will overview the tools as well as the main principles that one may encounter in solid-state NMR. We will mostly consider the quadrupolar interaction as it remains the central topic of the present work.

1.2 Spin Hamiltonians in Solids

A nucleus has different ways to communicate with its surroundings.⁵ We previously considered the effects of long distance interactions with external magnetic fields such as \mathbf{B}_0 and \mathbf{B}_1 . However, even though these two interactions are essential in NMR, they do not provide any relevant information on the structure of the materials. Therefore, in addition to the Zeeman interactions, local magnetizations have to be taken into account to explain the relaxation of the spins and to understand the shape of the spectra.⁶ These internal interactions have different origins and they strongly depend on the local symmetry around the nucleus. We will limit the present work to the

study of the three most important ones in solid-state NMR, i.e. the dipole-dipole, chemical shift and quadrupolar interactions. They can be classified in terms of magnitude with respect to the dominant Zeeman interaction (Table 1.1).

<i>Zeeman</i>	<i>Quadrupolar</i>	<i>Dipolar</i>	<i>Chemical Shift</i>
10^8	10^6	$10^3 - 10^4$	$10^3 - 10^4$

Table 1.1: Order of magnitude of the interactions in solids (given for ^{27}Al at 104.10^6 Hz, $B_0 = 9.39$ Teslas).

1.2.1 Origin of Interactions

Dipole-Dipole Coupling

Classically, nuclei can be considered as magnetic dipoles. Thus, in liquids and solids, there exists a dipolar interaction resulting from the coupling between two magnetic dipoles. Experimentally, such couplings lead to a broadening of the NMR spectrum. Therefore, the study of dipolar interactions, which are dependent on the interatomic distances, provides important information on the structural features of the materials. However, when considering the magnitude of this interaction compared to the others present in solids, we notice that it is largely dominated by the quadrupolar interaction. Moreover, many nuclei are generally coupled with each other and the extraction of structural information from the resulting broadening is consequently made much more complicated.

Chemical Shift Interaction

Generally speaking, interactions result from the mutual influence of two coupling partners.^{7, 8} Indeed, the action of the applied static magnetic field \mathbf{B}_0 is opposed to a local magnetic field created by the electron cloud around the nucleus. This magnetization generates an induced magnetic field, proportional to \mathbf{B}_0 so that the real field that a nucleus undergoes is given by

$$B_{real} = (1 - \sigma)B_0 \quad (1.8)$$

where σ is a proportional constant.

Quadrupolar Interaction

When the spin number I is greater than $1/2$, the nucleus possesses an electric quadrupole momentum due to the non spherical distribution of the protons. The interaction of the local electric field gradients, EFGs, with this quadrupole momentum leads to the corresponding quadrupolar interaction. This interaction is generally considered to be the most important in magnitude and consequently provides a unique mean of determining the local environment of the nucleus. Indeed, quadrupole effects are strongly linked to the local symmetry of the nucleus. In a cubic symmetry, the quadrupolar interaction vanishes whereas quadrupole effects are amplified when the environment becomes more asymmetrical.

1.2.2 Mathematical Tools

Irreducible Spherical Tensors

In solids, spin interactions can be represented in the laboratory frame (LAB) by a nine component cartesian tensor. Nevertheless, it is more convenient to

express them in terms of irreducible spherical tensors when rotations are involved. The nine components of the irreducible spherical tensor are deduced from the cartesian components using Eqs. 1.9.

$$\left\{ \begin{array}{l} A_{00} = -(1/\sqrt{3})[A_{xx} + A_{yy} + A_{zz}] \\ A_{10} = -(i/\sqrt{2})[A_{xy} + A_{yx}] \\ A_{1\pm 1} = -(1/2)[A_{zx} - A_{xz} \pm i(A_{zy} - A_{yz})] \\ A_{20} = (1/\sqrt{6})[3A_{zz} - (A_{xx} + A_{yy} + A_{zz})] \\ A_{2\pm 1} = \mp(1/2)[A_{xz} + A_{zx} \pm i(A_{yz} - A_{zy})] \\ A_{2\pm 2} = (1/2)[A_{xx} - A_{yy} \pm i(A_{xy} - A_{yx})] \end{array} \right. \quad (1.9)$$

Laboratory Frame and Principal Axis System

In monocrystalline samples and for each species, there exists a Principal Axis System (PAS) for each interaction depending on the symmetry of the surroundings (the axes of the PAS are defined with capital letters XYZ). In this PAS of eigenvectors, the interaction will be represented by a diagonal tensor. In polycrystalline or disordered samples, each crystal is associated with its own PAS. But, in NMR final calculations should be completed in the laboratory frame (LAB=Oxyz) where the relaxation will be measured. Moreover, the static magnetic field \mathbf{B}_0 is also linked to this frame, taken parallel to the z -axis. Therefore, we must finally define the Euler angles α, β, γ by which the laboratory frame can be brought in coincidence with the PAS for a crystal, for a particular species and a given interaction.

Parameters characterizing one interaction are known into its PAS so that a rotation has to be applied in order to deduce the components of this tensor into the laboratory frame (Eq. 1.10). The tensor components will be referred to as the capital letter A_{lm} in the laboratory frame and as the lower case a_{lm}

in the PAS.

$$A_{lm} = \sum_{m'=-l}^{+l} \mathcal{D}_{m'm}^{(l)}(\alpha, \beta, \gamma) a_{lm'} \quad (1.10)$$

where the $D_{m'm}^{(l)}$ are Wigner matrix elements^{6, 9}

$$\mathcal{D}_{m'm}^{(l)}(\alpha, \beta, \gamma) = e^{-im'\alpha} d_{m'm}^{(l)}(\beta) e^{-im\gamma} \quad (1.11)$$

The second-order ($l = 2$) reduced matrix elements $d_{m'm}^{(2)}(\beta)$ are found in Table 1.2.

m'	2	1	m 0	-1	-2
2	$\left(\frac{1+\cos\beta}{2}\right)^2$	$-\frac{1+\cos\beta}{2} \sin\beta$	$\sqrt{\frac{3}{8}} \sin^2\beta$	$-\frac{1-\cos\beta}{2} \sin\beta$	$\left(\frac{1-\cos\beta}{2}\right)^2$
1	$\frac{1+\cos\beta}{2} \sin\beta$	$\cos^2\beta - \frac{1-\cos\beta}{2}$	$-\sqrt{\frac{3}{8}} \sin 2\beta$	$\frac{1+\cos\beta}{2} - \cos^2\beta$	$-\frac{1-\cos\beta}{2} \sin\beta$
0	$\sqrt{\frac{3}{8}} \sin^2\beta$	$\sqrt{\frac{3}{8}} \sin 2\beta$	$\frac{3\cos^2\beta-1}{2}$	$-\sqrt{\frac{3}{8}} \sin 2\beta$	$\sqrt{\frac{3}{8}} \sin^2\beta$
-1	$\frac{1-\cos\beta}{2} \sin\beta$	$\frac{1+\cos\beta}{2} - \cos^2\beta$	$\sqrt{\frac{3}{8}} \sin 2\beta$	$\cos^2\beta - \frac{1-\cos\beta}{2}$	$-\frac{1+\cos\beta}{2} \sin\beta$
-2	$\left(\frac{1-\cos\beta}{2}\right)^2$	$\frac{1-\cos\beta}{2} \sin\beta$	$\sqrt{\frac{3}{8}} \sin^2\beta$	$\frac{1+\cos\beta}{2} \sin\beta$	$\left(\frac{1+\cos\beta}{2}\right)^2$

Table 1.2: Reduced Wigner rotation matrix elements $d_{m',m}^{(2)}(\beta)$ in terms of the Eulerian angle β

Spin Hamiltonian in Spherical Representation

The spin Hamiltonian can be expressed for each interaction λ (λ taking the values Q, D or σ for respectively the quadrupolar, dipolar and chemical shift interactions) as

$$\mathcal{H}_\lambda = C^\lambda \sum_{i,j=1}^3 R_{i,j}^\lambda T_{j,i}^\lambda \quad (1.12)$$

in the cartesian reference system.⁹ The C^λ are constants which are given for each interaction in Table 1.3.

<i>Quadrupolar</i>	<i>Dipolar</i>	<i>Chemical Shift</i>
$C^Q = \frac{eQ}{2I(2I-1)}$	$C^D = -2\gamma_I\gamma_S$	$C^\sigma = \gamma_I$

Table 1.3: Constants C^λ encountered in Spin Hamiltonians for the three interactions.

In both cartesian and spherical representations, the spin Hamiltonian is the scalar product of a spatial tensor R^λ and a spin tensor T^λ .

Spatial components are generally better known in the PAS where the tensor describing the interaction is diagonal.

$$R_{(PAS)}^\lambda = \begin{pmatrix} R_{XX} & 0 & 0 \\ 0 & R_{YY} & 0 \\ 0 & 0 & R_{ZZ} \end{pmatrix}$$

However, instead of these three eigenvalues R_{XX}, R_{YY}, R_{ZZ} , it is often convenient to introduce three parameters that better characterize the strength of the interaction. One of them is the trace $\text{Tr}(R^\lambda)$ of the tensor from which the two others will be deduced and denoted δ_λ and η_λ . Eq. 1.13 shows that δ_λ relates to the strength of the anisotropy, whereas η_λ (Eq. 1.14) symbolizes the asymmetry of the interaction ($\eta_\lambda = 0$ in a cubic environment).

$$\delta_\lambda = R_{ZZ} - \text{Tr}(R^\lambda) \quad (1.13)$$

$$\eta_\lambda = \frac{R_{YY} - R_{XX}}{\delta_\lambda} \quad (1.14)$$

As far as spin tensor components $T_{j,i}^\lambda$ are concerned, they stem from the product of two vector components X_j and Y_i (Eq. 1.15). The vector \mathbf{X} is always a nuclear spin vector \mathbf{I} whereas the second vector \mathbf{Y} can be the same nuclear spin vector \mathbf{I} (for $\lambda=Q$), another nuclear spin vector \mathbf{S} ($\lambda=D$) or the external magnetic field \mathbf{B}_0 ($\lambda = \sigma$).

$$T_{j,i}^\lambda = X_j Y_i \quad (1.15)$$

with $(i, j = x, y, z)$

As previously mentioned, a representation in terms of irreducible spherical tensors^{6, 9} is preferable for a theoretical study of polycrystalline and amorphous samples due to the multiple rotations that are to be performed (from PAS to LAB frame and later when the sample will be spun). The spin Hamiltonian is therefore written in a general form

$$\mathcal{H}_\lambda = C^\lambda \sum_l \sum_{m=-l}^{+l} (-1)^m R_{l,-m}^\lambda T_{l,m}^\lambda \quad (1.16)$$

where the spherical tensor components $R_{l,-m}$ and $T_{l,m}$ are derived from the Cartesian tensor components $R_{i,j}$ and $T_{j,i}$ using Eqs. 1.9.

It is now interesting to study each interaction in detail, taking into account its origin and using the previous presented definitions of tensors. We

will further discover that Eq. 1.16 can be significantly simplified by considering the particular symmetries of each interaction. The next section will focus on the quadrupolar case whereas results for chemical shift and dipolar interactions will be discussed briefly.

1.2.3 Hamiltonians of Spin Interactions

Quadrupole Hamiltonian

The quadrupolar interaction comes from the coupling of the electric quadrupole moment of a spin I with an electric field gradient depending on the spatial coordinates of the electric charges. In a cartesian basis, the quadrupolar Hamiltonian can be expressed as

$$\mathcal{H}_Q = \frac{eQ}{2I(2I-1)} \mathbf{I} \cdot \mathbf{Q} \cdot \mathbf{I} \quad (1.17)$$

where the spatial tensor operator \mathbf{Q} is commonly named the *electric field gradient* (EFG). In its PAS, the EFG tensor has three eigenvalues V_{XX} , V_{YY} and V_{ZZ} .

Nevertheless, convenient parameters $\text{Tr}(\mathbf{Q})$, δ_Q and η_Q are introduced to characterize the EFG. As \mathbf{Q}_{PAS} must satisfy the Laplace's equation $\nabla \cdot \mathbf{Q}_{PAS} = 0$, we find that the spatial tensor is traceless ($\text{Tr}(\mathbf{Q}) = 0$). Consequently, the quadrupolar interaction can be fully described by the δ_Q and η_Q parameters that are respectively labelled the *field gradient* and the *asymmetry parameter* of the quadrupolar interaction.

V_{ZZ} being taken equal to eq , quadrupolar parameters are directly deduced from Eqs. 1.13 and 1.14,

$$\delta_Q = V_{ZZ} = eq \quad (1.18)$$

$$\eta_Q = \frac{V_{YY} - V_{XX}}{V_{ZZ}} \quad (1.19)$$

and the EFG tensor will be written in the PAS,

$$Q_{(PAS)} = eq \cdot \begin{pmatrix} \frac{\eta_Q - 1}{2} & 0 & 0 \\ 0 & \frac{-\eta_Q - 1}{2} & 0 \\ 0 & 0 & 1 \end{pmatrix}$$

A standard measure of the strength of the quadrupole coupling is also found in the quadrupolar coupling constant

$$C_Q = \frac{e^2 q Q}{h} \quad (1.20)$$

which has more pleasant units of frequency. This parameter will be later preferred to δ_Q to describe the strength of the quadrupolar interaction whereas η_Q will be kept to describe the deviation of the field gradient from axial symmetry.

Then, spatial spherical components of the EFG are deduced from cartesian components (matrix $Q_{(PAS)}$) using the set of Eqs. 1.9.

$$\begin{cases} r_{00}^{(Q)} = r_{10}^{(Q)} = r_{1\pm 1}^{(Q)} = r_{2\pm 1}^{(Q)} = 0 \\ r_{20}^{(Q)} = \sqrt{\frac{3}{2}} eq \\ r_{2\pm 2}^{(Q)} = eq \eta_Q / 2 \end{cases} \quad (1.21)$$

We notice that rank-0 and rank-1 tensor components are null and rank-2 tensor is composed of only three nonzero components. In terms of irreducible spherical tensor operators, the Hamiltonian of Eq. 1.16 can therefore be grandly simplified in the case of the quadrupolar interaction if we only consider nonzero $R_{l,m}^Q$ components that derive from the $r_{l,m}^Q$ of Eqs. 1.21. Only $l = 2$ and $m = 0, \pm 2$ terms must be retained in the Hamiltonian, leading to the quadrupolar Hamiltonian \mathcal{H}_Q

$$\mathcal{H}_Q = \frac{eQ}{2I(2I-1)} \sum_{m=-2}^{+2} (-1)^m R_{2,-m}^Q T_{2,m}^Q \quad (1.22)$$

As far as spin part of the interaction is concerned, the components of the tensor $T_{i,j}^Q = I_i I_j$ can be reduced in spherical components using the same Eqs. 1.9. This transformation leads to the five components of Eqs. 1.23 if we neglect spin terms with $l \neq 2$ that do not appear in the quadrupolar Hamiltonian.

$$\begin{cases} T_{20}^{(Q)} = \frac{1}{\sqrt{6}}(3I_z^2 - I(I-1)) \\ T_{2\pm 1}^{(Q)} = \mp \frac{1}{2}(I_{\pm} I_z + I_z I_{\pm}) \\ T_{2\pm 2}^{(Q)} = \frac{1}{2} I_{\pm}^2 \end{cases} \quad (1.23)$$

with $I_{\pm} = I_x \pm iI_y$

Dipolar and Chemical Shift Interactions

A dipolar interaction concerns the coupling of two spins, I and S , and its strength is logically proportional to the inverse cube of the distance r between the two coupling partners. For the same reason as previously stated, the dipolar tensor is traceless. On the contrary, the chemical shift tensor

has a trace in the PAS. Results concerning both of these interactions are summarized in Table 1.4.

$$\mathbf{D}_{(PAS)} = \frac{1}{r^3} \cdot \begin{pmatrix} -\frac{1}{2} & 0 & 0 \\ 0 & -\frac{1}{2} & 0 \\ 0 & 0 & 1 \end{pmatrix}$$

$$\boldsymbol{\sigma}_{(PAS)} = \begin{pmatrix} \sigma_{11} & 0 & 0 \\ 0 & \sigma_{22} & 0 \\ 0 & 0 & \sigma_{33} \end{pmatrix}$$

Spatial components of the irreducible spherical tensors in the PAS are deduced from the cartesian tensors $\mathbf{D}_{(PAS)}$ and $\boldsymbol{\sigma}_{(PAS)}$, for dipolar and chemical shift interactions, respectively and results are given in Table 1.5.

Spin components of the irreducible spherical tensors are then calculated regarding that $T_{i,j}^D = I_i S_j$ and $T_{i,j}^\sigma = I_i B_{0j}$ (Table 1.6).

According to these simplifications, dipolar and chemical shift Hamiltonians \mathcal{H}_D and \mathcal{H}_σ are written

$$\mathcal{H}_D = -\gamma_I \gamma_S \sum_{m=-2}^{+2} (-1)^m R_{2,-m}^D T_{2,m}^D \quad (1.24)$$

and

$$\mathcal{H}_\sigma = \gamma_I \sum_{l=0,2} \sum_{m=-l}^{+l} (-1)^m R_{l,-m}^\sigma T_{l,m}^\sigma \quad (1.25)$$

It must be pointed out that the development of the chemical shift Hamiltonian \mathcal{H}_σ will give one additional term with respect to other Hamiltonians \mathcal{H}_D and \mathcal{H}_Q , for $l = 0$.

Interaction	Trace	δ_λ	η_λ
Dipolar	$\text{Tr} \mathbf{D} = 0$	$\frac{1}{r^3}$	0
Chemical shift	$\text{Tr} \boldsymbol{\sigma} = \sigma_{iso}$	$\frac{2}{3} \Delta\sigma$	$\frac{3}{2} \frac{\sigma_{22} - \sigma_{11}}{\Delta\sigma}$

Table 1.4: δ_D , δ_σ and η_σ parameters of dipolar and chemical shift interactions as a function of r , $\sigma_{iso} = (\sigma_{11} + \sigma_{22} + \sigma_{33})/3$ and $\Delta\sigma = 3(\sigma_{33} - \sigma_{iso})/2$, respectively.

Interaction	r_{00}^λ	r_{20}^λ	$r_{2\pm 2}^\lambda$
Dipolar	0	$\sqrt{\frac{3}{2}} \frac{1}{r^3}$	0
Chemical shift	$-\sqrt{3} \sigma_{iso}$	$\sqrt{\frac{2}{3}} \Delta\sigma$	$-\frac{\Delta\sigma}{3} \eta_\sigma$

Table 1.5: Components of the irreducible spherical dipolar and chemical shift tensors.

Interaction	T_{00}	T_{20}	$T_{2\pm 1}$	$T_{2\pm 2}$
Dipolar	not used	$\frac{1}{\sqrt{6}}(3I_z S_z - \mathbf{I} \cdot \mathbf{S})$	$\mp \frac{1}{2}(I_\pm S_z + I_z S_\pm)$	$\frac{1}{2} I_\pm S_\pm$
Chemical shift	$-\frac{1}{\sqrt{3}}(I_z B_0)$	$\sqrt{\frac{2}{3}} I_z B_0$	$\mp \frac{1}{2} I_\pm B_0$	0

Table 1.6: Second-rank irreducible spin tensors for dipolar and chemical shift interactions ($I_\pm = I_x \pm iI_y$ and $S_\pm = S_x \pm iS_y$)

So far, we have summarized the most relevant results of quantum mechanics concerning interactions in solids, focusing on the quadrupolar one. This led to the general form of the quadrupolar Hamiltonian (Eq. 1.22) and the definition of the various terms that compose its expression. In order to see the effect that each interaction has on the spin-relaxation as well as on appearance of the final NMR spectra, we now have to develop the different Hamiltonians taking into account the experimental characteristics. Basically, interactions in solids result in a broadening of the spectrum and for the last 40 years, rotations of the sample have been considered as the best way to fake the brownian movements in liquids. We will now develop quantum mechanical calculations to explain how rotations about one or more axes can affect spectra in NMR.

1.3 Motional Narrowing

In 1959, Andrew and co-workers¹⁰ proved that anisotropic dipolar broadening could be removed by spinning the sample about an axis inclined at a specific “magic angle” with respect to the static magnetic field. By using a perturbation theory, we will show that, to first order, magic angle rotation cancels all interactions. However, quadrupolar interactions are worth considering in detail: indeed, Magic-Angle Spinning (MAS) experiments do not completely average out the quadrupolar broadening. Therefore, second-order correction must be considered in the quadrupole case, which justified the use of double rotation experiments.

1.3.1 General

Let us consider the total Hamiltonian of a spin as a sum of two terms: a dominant Zeeman interaction in high-field NMR and a weaker interaction such as the chemical shift anisotropy or the quadrupolar coupling. As calculations are logically made in the Zeeman basis, the perturbed Hamiltonian becomes explicitly time-dependent in this representation so that the total hamiltonian is written

$$\mathcal{H} = \mathcal{H}_z + \mathcal{H}_\lambda(t) \quad (1.26)$$

However, such time-dependency can be overcome by using an Average Hamiltonian Theory (AHT)¹¹ which consists of a sum of time-independent Hamiltonians (also called the Magnus expansion)¹²

$$\mathcal{H}_\lambda(t) = \mathcal{H}_\lambda^{(1)} + \mathcal{H}_\lambda^{(2)} + \mathcal{H}_\lambda^{(3)} + \dots \quad (1.27)$$

which approximates the time-dependent Hamiltonian of Eq. 1.26.

The first term of Eq. 1.27 is the first-order correction to the Zeeman interaction. We will see that the first-order correction is equivalent to keeping the terms in the Hamiltonian which commute with the Zeeman interaction. The next term in the Magnus expansion is referred to as the second-order correction which is required if the first-order correction vanishes for certain transitions. Actually, we will demonstrate that the second-order correction is necessary for the quadrupolar interaction. The other terms are higher-order corrections that are rarely taken into consideration in NMR.

1.3.2 Averaging First-order interactions

Static Hamiltonian

During the relaxation process, spins subject to an external magnetic field as well as to an internal interaction λ may be described by the Hamiltonian

$$\mathcal{H} = \mathcal{H}_z + \mathcal{H}_\lambda = -\omega_0 I_z + C^\lambda \sum_{l=0,2} \sum_{m=-l}^{+l} (-1)^m R_{l,-m}^\lambda T_{l,m}^\lambda, \quad (1.28)$$

in terms of irreducible spherical tensors. Note that we consider the perturbed hamiltonian of the chemical shift interaction ($l = 0, 2$) bearing in mind that the term for which $l = 0$ should be removed in dipolar and quadrupolar cases.

The dominant Zeeman Hamiltonian constitutes the zeroth-order term and the first-order correction is found by keeping the secular terms of the Hamiltonian \mathcal{H}_λ , i.e., terms of \mathcal{H}_λ that commute with the Zeeman interaction. Then making use of the commutation rule

$$[I_z, T_{2,m}] = m T_{2,m}, \quad (1.29)$$

we find that terms for which $m \neq 0$ vanish so that the total Hamiltonian is simplified to the first-order and given by

$$\mathcal{H} = -\omega_0 I_z + C^\lambda R_{0,0}^\lambda T_{0,0}^\lambda + C^\lambda R_{2,0}^\lambda T_{2,0}^\lambda. \quad (1.30)$$

The second term of Eq. 1.30 does not exist in dipolar and quadrupolar Hamiltonians and should simply be removed. However, for chemical shift interaction, the total Hamiltonian may be written, after appropriate substitutions using components of spin and spatial tensors in Tables 1.5 and 1.6

$$\mathcal{H}_\sigma^{\text{tot}} = -\omega_0 I_z + \omega_0 I_z \sigma_{\text{iso}} + \omega_0 \sqrt{\frac{2}{3}} I_z R_{2,0}^\sigma. \quad (1.31)$$

The second term of Eq. 1.31 contains the isotropic chemical shift σ_{iso} which is usually included within the Zeeman interaction so that the effective Larmor frequency is now $\omega'_0 = (1 - \sigma_{\text{iso}})\omega_0$. Consequently, the spectrum will be shifted compared to the 'pure' Zeeman spectrum but Zeeman levels will still be separated by the same energy.

The anisotropic broadening arises from the last term of Eq. 1.30. $R_{2,0}^\lambda$ can be developed for each interaction using Eqs. 1.10 and 1.11 to show that the spatial tensor $R_{2,0}^\lambda$ depends on the orientation of the PAS relative to the Zeeman interaction's reference frame (LAB frame) given by the three Euler angles. Eq. 1.32 stems from the expansion of the spatial $R_{2,0}^Q$ term in the quadrupolar case. Such developments for dipolar and chemical shift interactions yield similar results.

$$\mathcal{H}_Q^{(1)} = \frac{e^2 q Q}{8I(2I-1)} [3 \cos^2 \beta - 1 + \eta_Q \sin^2 \beta \cos 2\alpha] (3I_z^2 - I^2) \quad (1.32)$$

For a single crystal, where only one orientation of the PAS is present, the anisotropy will be the same for all equivalent nuclei and the spectrum will consist of one line. However, in polycrystalline or disordered samples, each crystallite has its own set of euler angles and will contribute to the final spectrum with different intensities and frequencies. The consequence is a broadening of the spectrum that we usually denote the anisotropic powder pattern.

It is worth looking at the frequency shift resulting from the first-order correction to the quadrupolar perturbation. The quadrupolar frequency per-

turbation between Zeeman levels m and $m + 1$ derives from Eq. 1.32 and is written

$$\begin{aligned}\omega_{m+1,m}^{(1)} &= \frac{1}{\hbar} \left[\langle m+1 | \mathcal{H}_Q^{(1)} | m+1 \rangle - \langle m | \mathcal{H}_Q^{(1)} | m \rangle \right] \\ &= \left(m + \frac{1}{2} \right) \frac{3e^2qQ}{4I(2I-1)\hbar} \left[3 \cos^2 \beta - 1 + \eta_Q \sin^2 \beta \cos 2\alpha \right] \quad (1.33) \\ &= \left(m + \frac{1}{2} \right) \frac{\omega_Q}{2} \left[3 \cos^2 \beta - 1 + \eta_Q \sin^2 \beta \cos 2\alpha \right]\end{aligned}$$

where

$$\omega_Q = \frac{3e^2qQ}{2I(2I-1)\hbar} \quad (1.34)$$

is commonly named the quadrupolar frequency.¹³

Note that $\bar{\omega}_Q$ is also called the angular dependent frequency and written as

$$\bar{\omega}_Q = \frac{\omega_Q}{2} \left[3 \cos^2 \beta - 1 + \eta_Q \sin^2 \beta \cos 2\alpha \right] \quad (1.35)$$

The most relevant information that follows from this equation is that for the central ($1/2 \leftrightarrow -1/2$) transition, the frequency is unchanged from the Zeeman frequency. Therefore, a second-order correction is essential to compute the actual quadrupolar frequency for this central transition.

The anisotropic part of Eq. 1.30 suggests that an averaging of the anisotropic part goes through the manipulation of either the spin term by multiple-pulse experiment or the spatial term using sample reorientation. Waugh et al.¹⁴ have invented a series of pulse sequences, among them the well-known WAHUA sequence, in order to average out first-order interactions by manipulating the spin part of the Hamiltonian. In particular, they proved that

homonuclear dipolar broadening could be removed. However, such pulse sequences are not applicable to the averaging of the second-order quadrupolar interactions since the amplitude of this interaction is generally much greater than the amplitude of the available rf fields ($\mathcal{H}_Q \gg \mathcal{H}_{\text{rf}}$). Therefore, methods using sample reorientation have revealed to be more efficient to get rid of broadenings arising from first-order dipolar, chemical shift as well as quadrupolar interaction. These techniques will be discussed in the following section.

Magic Angle Spinning

Let us consider that the sample is now rotating at a frequency ω_r about an axis inclined at θ with respect to the static field. In that case, the relation between PAS and LAB frames is clearly time-dependent. However, this problem can be overcome by using two transformations (see Fig. 1.4). The first one concerns the PAS in a sample-fixed frame (rotor) and is time-independent whereas the second transformation is time-dependent since it describes the rotor frame into the LAB frame. The latter transformation is expressed through the euler angles $(\omega_r t, \theta, \zeta)$.

The spatial tensor components are deduced from their values in the PAS, using these two successive transformations

$$R_{2,m}^\lambda = \sum_{m'=-2}^{+2} \mathcal{D}_{m',m}^{(2)}(\omega_r t, \theta, \zeta) \sum_{m''=-2}^{+2} \mathcal{D}_{m'',m'}^{(2)}(\alpha, \beta, \gamma) r_{2,m''}^\lambda. \quad (1.36)$$

If we apply this relation to the term $R_{2,0}^\lambda$, with $m = 0$, we find

$$R_{2,0}^\lambda = \sum_{m'=-2}^{+2} \mathcal{D}_{m',0}^{(2)}(\omega_r t, \theta, 0) \sum_{m''=-2}^{+2} \mathcal{D}_{m'',m'}^{(2)}(\alpha, \beta, \gamma) r_{2,m''}^\lambda, \quad (1.37)$$

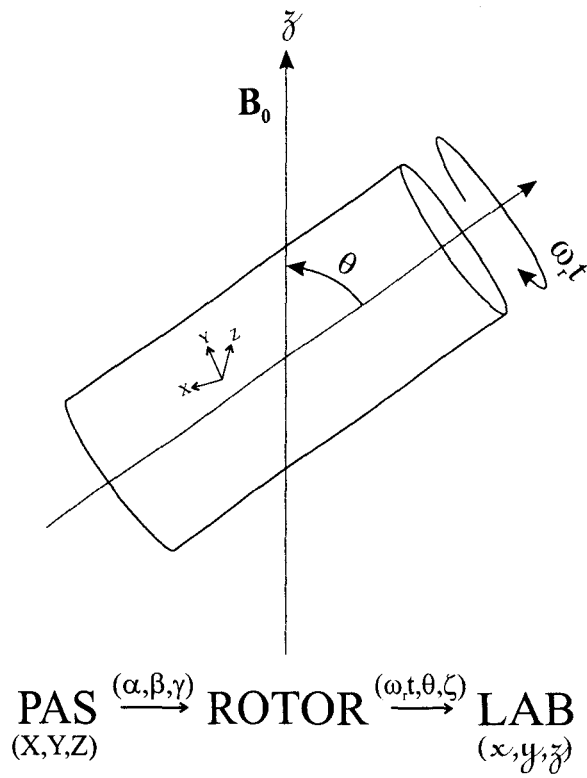


Figure 1.4: Representation of the magic angle spinning experiment, showing the different transformations

with $m'' = 0, \pm 2$ due to nonzero $r_{2,m''}^\lambda$ values.

The reduction of the second-order Wigner rotation matrices using Eq. 1.11 leads to

$$R_{2,0}^\lambda = \sum_{m'=-2}^{+2} e^{-im'\omega_r t} d_{m',0}^{(2)}(\theta) \sum_{m''=-2}^{+2} \mathcal{D}_{m'',m'}^{(2)}(\alpha, \beta, \gamma) r_{2,m''}^\lambda. \quad (1.38)$$

The second sum in Eq. 1.38, with $m' = 0$, coincides with the previous static case (term into square brackets in Eq. 1.32). The first sum gives rise to a time-independent component (for $m' = 0$) proportional to $d_{0,0}^{(2)}(\theta)$ and time-dependent terms for $m' = \pm 1, \pm 2$. However, in the fast-spinning limit, spinning sidebands arising from the time-dependent terms, which we group in the function $F(\pm\omega_r t + \gamma, 2(\pm\omega_r t + \gamma))$, disappear. For the sake of simplicity, we will consider that the spinning speed is much higher than the strength of the interaction as to ignore these oscillating terms. However, some authors^{15, 16} have given these expressions and readers should refer to their papers. Therefore, Eq. 1.38 can be rewritten as

$$R_{2,0}^\lambda = d_{0,0}^{(2)}(\theta) \sum_{m''=-2}^{+2} \mathcal{D}_{m'',0}^{(2)}(\alpha, \beta, 0) r_{2,m''}^\lambda + F(\pm\omega_r t + \gamma, 2(\pm\omega_r t + \gamma)). \quad (1.39)$$

Eq. 1.39 shows that whatever the perturbed interaction, the first-order correction is proportional to the reduced Wigner matrix $d_{0,0}^{(2)}(\theta)$ which simply varies as second Legendre polynomials

$$P_2(\cos \theta) = \frac{3 \cos^2 \theta - 1}{2}. \quad (1.40)$$

Since this polynomial can be zeroed, it is possible to completely average first-order anisotropies by selecting a rotation axis of $\theta = \arctan(1/\sqrt{3}) =$

54.74° which corresponds to the well-known “magic angle”. The effect of the magic angle rotation is illustrated in Fig. 1.5. The width of the sodium resonance is reduced by a factor of at least 3 compared to the spectrum taken under static condition.

As an example, the frequency of a crystallite is given in Eq. 1.41 in first-order correction theory for the quadrupolar interaction as a perturbation of the Zeeman one.

$$\omega_{m,m+1} \approx -\omega_0 + \left(m + \frac{1}{2}\right) \frac{\omega_Q}{4} (3 \cos^2 \theta - 1) [3 \cos^2 \beta - 1 + \eta_Q \sin^2 \beta \cos 2\alpha] \quad (1.41)$$

We have seen that first-order interactions could be removed provided that the sample is spun at sufficient high-speed, at a magic-angle of 54.74° with respect to the static field. Heteronuclear dipolar broadenings are generally easily averaged out by standard MAS experiments but chemical shift anisotropies are sometimes so broad (a few MHz for ^{51}V) that spinning sidebands are present even at high-spinning speed (up to 35 kHz). In such a case, the spinning sidebands of one site may overlap with other non-equivalent sites. A simulation of the powdered pattern, including spinning sidebands, can be performed in order to extract parameters (η_σ) that illustrate the local symmetry of the nucleus.¹⁷ In such a case, time-dependent terms $F(\pm\omega_r t + \gamma, 2(\pm\omega_r t + \gamma))$ have to be taken into account to approximate the experimental results with accuracy. Moreover, the anisotropic part of the chemical shift Hamiltonian $\mathcal{H}_\sigma^{\text{tot}}$ given in Eq. 1.31 is proportional to the static magnetic field \mathbf{B}_0 ($\omega_0 = \gamma B_0$) so that the anisotropic broadening increases with the static field. Consequently, several experiments at high and low static fields may be necessary to distinguish the effects of the different interactions that a nucleus undergoes.

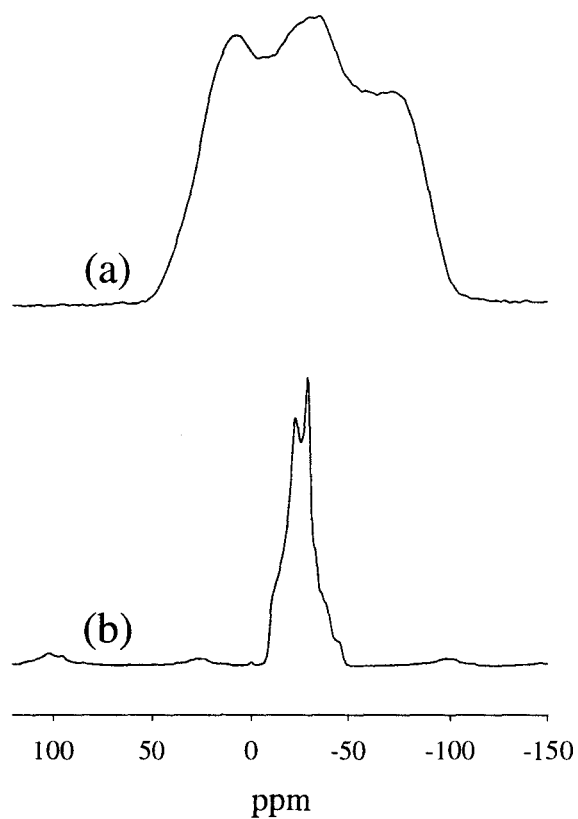


Figure 1.5: ^{23}Na spectra of Na_2SO_4 under static (a) and magic angle spinning (b) conditions. In the static case, the linewidth is due to the contributions of the quadrupolar, dipolar and CSA interactions. In MAS, only the second-order quadrupolar contribution remains.

As far as the quadrupolar interaction is concerned, we have seen that the frequency of the central transition remains unchanged by a first-order correction. Consequently, second-order effects must be considered to determine whether they are large enough to cause observable perturbations to the energy levels. Furthermore, we will demonstrate that other sample reorientations, more complex than MAS, can completely average out the quadrupolar broadening due to the first- and second-order Hamiltonian terms.

1.3.3 Second-order Averaging

Theory

The theoretical approach will be slightly different than the one used in first-order corrections as the expression of second-order frequencies will not be given literally. We will rather focus on the spatial terms that arise from a second-order energy correction, deliberately omitting the spin terms that will be given in Chapter two. Since second-order theory is relevant to quadrupolar interaction only, superscript Q, that previously denoted quadrupolar parameters in contrast with dipolar and chemical shift ones, will simply be removed.

Let us now consider the second-order energy correction to the Zeeman energy calculated using a Static Perturbation Theory:^{18, 19}

$$E_n^{(2)} = \sum_{n' \neq n} \frac{\langle n | \mathcal{H}_Q | n' \rangle \langle n' | \mathcal{H}_Q | n \rangle}{E_n^{(0)} - E_{n'}^{(0)}} \quad (1.42)$$

where $E_n^{(0)} |n\rangle = -n\omega_0 |n\rangle$.

By substituting Eq. 1.22 and after separating spatial and spin elements, we find

$$E_n^{(2)} = \frac{C^2}{\omega_0} \sum_{m,m'} (-1)^{m+m'} R_{2,-m} R_{2,-m'} \sum_{n' \neq n} \frac{\langle n|T_{2,m}|n'\rangle \langle n'|T_{2,m'}|n\rangle}{n' - n}. \quad (1.43)$$

The selection rule in Eq. 1.44 imposes that $n = m + n'$ and $n' = m' + n$ be true simultaneously.

$$\langle n|T_{2,m}|n'\rangle \propto \delta_{n,m+n'} \quad (1.44)$$

This leads to considering $m = -m'$ and replacing n' by $n - m$ so that Eq. 1.43 becomes

$$E_n^{(2)} = \frac{C^2}{\omega_0} \sum_{m \neq 0} R_{2,-m} R_{2,m} \frac{\langle n|T_{2,m}|n-m\rangle \langle n-m|T_{2,-m}|n\rangle}{-m}. \quad (1.45)$$

After a last straightforward substitution, the second-order energies of Eq. 1.46 can be converted into the operator $\mathcal{H}_Q^{(2)}$ of Eq. 1.47.

$$E_n^{(2)} = -\frac{C^2}{\omega_0} \sum_{m \neq 0} R_{2,-m} R_{2,m} \frac{\langle n|T_{2,m}T_{2,-m}|n\rangle}{m} \quad (1.46)$$

$$\mathcal{H}_Q^{(2)} = \frac{C^2}{\omega_0} \sum_{m > 0} R_{2,-m} R_{2,m} \frac{[T_{2,-m}, T_{2,m}]}{m} \quad (1.47)$$

Once again, the perturbed Hamiltonian is composed of products from both spin and spatial components that can be studied separately. This suggests that we still have two approaches available to remove the broadening introduced by this additional second-order term. The spin part of this Hamiltonian will be of high interest when multiple-quantum experiments will be

introduced in Chapter two. Here, we will be concerned about the spatial components that we will now develop.

First, only $m = 1$ and $m = 2$ values in Eq. 1.47 contribute to providing secular terms in the Hamiltonian. Since it has been shown before that non-secular terms in a spin Hamiltonian have a very small effect on lineshapes,²⁰ the expansion of the second-order quadrupolar term leads to

$$\mathcal{H}_Q^{(2)} = \frac{C^2}{\omega_0} \left(R_{2,-1} R_{2,1} [T_{2,-1}, T_{2,1}] + \frac{1}{2} R_{2,-2} R_{2,2} [T_{2,-2}, T_{2,2}] \right). \quad (1.48)$$

Such product of spatial tensors $R_{2,-m} R_{2,m}$ can be written explicitly for $m = 1$ and $m = 2$ in terms of the spherical components of the EFG in the PAS and the second order reduced matrix elements, using Eqs. 1.10 and 1.11.

$$\begin{aligned} R_{2,-m} R_{2,m} &= \sum_{m'=-2}^{+2} \mathcal{D}_{m',-m}^{(2)}(\alpha, \beta, \gamma) r_{2,m'} \sum_{m''=-2}^{+2} \mathcal{D}_{m'',m}^{(2)}(\alpha, \beta, \gamma) r_{2,m''} \\ &= \sum_{m'=-2}^{+2} \sum_{m''=-2}^{+2} e^{-i(m'+m'')\alpha} d_{m',-m}^{(2)}(\beta) d_{m'',m}^{(2)}(\beta) r_{2,m'} r_{2,m''} \end{aligned} \quad (1.49)$$

It is of interest to note that the second-order quadrupolar frequencies do not depend on the euler angle γ as it has disappeared from Eq. 1.49. Only nonzero spherical components $r_{2,m'}$ need to be included in this formula. Nevertheless, such an expansion is time-demanding. Thus, a computational approach is generally preferred (for more details, see Mueller²¹).

Certain rules on spherical tensors can advantageously be used in order to simplify such an equation. Indeed, quantum mechanics states that a product of spherical tensors $R_{l_1,m_1} R_{l_2,m_2}$ can be reduced into new irreducible spherical tensors of the spin operators $R_{L,M}$. These new tensors are expressible in terms of Clebsch-Gordan coefficients. In a general way, the transformation of the product of two spherical tensors $R_{l_1,m_1} R_{l_2,m_2}$ is written

$$R_{l_1, m_1} R_{l_2, m_2} = \sum_{L, M} \langle l_1, l_2, m_1, m_2 | l_1, l_2, L, M \rangle R_{L, M}, \quad (1.50)$$

where $\langle l_1, l_2, m_1, m_2 | l_1, l_2, L, M \rangle$ are the Clebsch-Gordan coefficients. We should specify that the only nonzero Clebsch-Gordan coefficients are those which simultaneously fulfill the two conditions expressed in Eqs. 1.51.

$$\left\{ \begin{array}{l} |l_1 - l_2| \leq L \leq |l_1 + l_2| \\ M = m_1 + m_2 \end{array} \right. \quad (1.51)$$

If we apply the first rule to our specific case, with $l_1 = l_2 = 2$, we find that the product transforms as rank-0 to rank-4 tensors ($0 \leq L \leq 4$). Moreover, products of Wigner rotation matrices $\mathcal{D}_{m', -m}^{(2)}(\alpha, \beta, \gamma) \mathcal{D}_{m'', m}^{(2)}(\alpha, \beta, \gamma)$ that appear in Eq. 1.49 can be reduced as well, by manipulating Eq 1.52.

$$\begin{aligned} \mathcal{D}_{m', -m}^{(2)}(\alpha, \beta, \gamma) \mathcal{D}_{m'', m}^{(2)}(\alpha, \beta, \gamma) &= \sum_{L=0}^4 \sum_{N, M=-L}^L \langle 2, 2, m', m'' | 2, 2, L, N \rangle \times \\ &\quad \langle 2, 2, -m, m | 2, 2, L, M \rangle \mathcal{D}_{N, M}^{(L)}(\alpha, \beta, \gamma) \end{aligned} \quad (1.52)$$

Rule 1.53 gives the sign of the first Clebsch-Gordan coefficient in Eq. 1.52 with respect to interchange m' and m'' . Therefore, we find that the coefficients have opposite sign when L is odd. As we sum over m' and m'' , these terms ($L = 1, 3$) vanish so that the only contributions come from terms for which $L = 0, 2, 4$. The second Clebsch-Gordan coefficient in Eq. 1.52 imposes that $N = 0$ (see Eq.C69 in Messiah²²).

$$\langle l_1, l_2, m_2, m_1 | l_1, l_2, L, N \rangle = (-1)^{l_1 + l_2 - L} \langle l_1, l_2, m_1, m_2 | l_1, l_2, L, N \rangle \quad (1.53)$$

These simplifications lead to a reduction of the product $R_{2,-m}R_{2,m}$ into a sum of rank-0, rank-2 and rank-4 tensors. The Hamiltonian of Eq. 1.48 can be rewritten

$$\mathcal{H}_Q^{(2)} = \frac{C^2}{\omega_0} [\xi_0 \tilde{R}_{0,0} + \xi_2 \tilde{R}_{2,0} + \xi_4 \tilde{R}_{4,0}], \quad (1.54)$$

where the $\tilde{R}_{L,0}$ are the new irreducible spherical tensors of the spatial operators and the ξ_L include all other terms of Eq. 1.48 that have not been explicitly given. ξ_L s mostly enclose spin operators as they result from the expansion of commutators $[T_{2,-m}T_{2,m}]$ (see Chapter two).

The rotation of the sample about a fixed axis at an angle θ with respect to \mathbf{B}_0 yields the same kind of calculations than for the first-order correction except for the fact that an additional $\tilde{R}_{4,0}$ spatial term emerges. Thus, we find that $\tilde{R}_{L,0}$ are modulated by the rotation as expressed in Eq. 1.55 where use has been made of Eqs. 1.10 and 1.11.

$$\tilde{R}_{L,0}(t) = \sum_{m'=-L}^L \sum_{m''=-L}^L e^{-m'\omega_r t} d_{m',0}^{(L)}(\theta) \mathcal{D}_{m'',m'}^{(L)}(\alpha, \beta, \gamma) \tilde{r}_{L,m''} \quad (1.55)$$

It is worth pointing out the similitude with Eq. 1.38 resulting from the first-order correction of a spinning sample. The $\tilde{r}_{L,m''}$ (Table 1.7) are the new spherical tensor components²³ which are deduced from the products $r_{2,m'}T_{2,m''}$ making use of the formalism of Clebsch-Gordan coefficients (Eq. 1.50).

If fast spinning speed is applied in order to remove time-dependent terms ($m' \neq 0$ in Eq. 1.55), the second-order quadrupole Hamiltonian can be written

$$\begin{aligned}
\tilde{r}_{0,0} &= -\frac{1}{5}(3 + \eta^2)(eq)^2 \\
\tilde{r}_{2,0} &= \frac{1}{14}(\eta^2 - 3)(eq)^2 & \tilde{r}_{2,\pm 2} &= \frac{1}{7}\sqrt{\frac{3}{2}}\eta(eq)^2 \\
\tilde{r}_{4,0} &= \frac{1}{140}(18 + \eta^2)(eq)^2 & \tilde{r}_{4,\pm 2} &= \frac{3}{70}\sqrt{\frac{5}{2}}\eta(eq)^2 & \tilde{r}_{4,\pm 4} &= \frac{1}{4\sqrt{70}}\eta^2(eq)^2
\end{aligned}$$

Table 1.7: New spherical tensor components

$$\begin{aligned}
\mathcal{H}_Q^{(2)} = \frac{C^2}{\omega_0} \left\{ \overbrace{d_{0,0}^{(0)}(\theta)}^1 \left(\xi_0 \overbrace{\mathcal{D}_{0,0}^{(0)}(\alpha, \beta, 0)}^1 \tilde{r}_{0,0} \right) + d_{0,0}^{(2)}(\theta) \left(\xi_2 \sum_{m''=-2}^2 \mathcal{D}_{m'',0}^{(2)}(\alpha, \beta, 0) \tilde{r}_{2,m''} \right) + \right. \\
\left. d_{0,0}^{(4)}(\theta) \left(\xi_4 \sum_{m''=-4}^4 \mathcal{D}_{m'',0}^{(4)}(\alpha, \beta, 0) \tilde{r}_{4,m''} \right) \right\}.
\end{aligned} \tag{1.56}$$

Lets us now detail the last equation with special care for the θ -dependent reduced matrix elements $d_{0,0}^{(L)}(\theta)$. The first term does not depend on angles as rank-0 matrix element $d_{0,0}^{(0)}(\theta)$ is equal to 1. Therefore, this part generates a frequency shift. This Quadrupolar Induced Shift (QIS) is proportional to C^2/ω_0 so that we can expect it to decrease at high magnetic fields. Second- and third parts are angular dependent and lead to an anisotropic second-order broadening when samples are composed of many crystallites. However, these two parts are scaled by the second- and fourth-order components $d_{0,0}^{(2)}(\theta)$ and $d_{0,0}^{(4)}(\theta)$ which vary as second- and fourth-Legendre polynomials $P_2(\cos \theta)$ and $P_4(\cos \theta)$, respectively. $P_2(\cos \theta)$ appeared previously in the first-order correction (see page 27) and can be found in Table 1.2. Therefore, a rotation at $\theta_m = 54.7^\circ$ not only averages away anisotropic terms arising from the correction to the first-order Hamiltonians (dipolar, chemical shift and quadrupolar) but it also cancels the second term of Eq. 1.56.

The new term that occurred in the second-order Hamiltonian $\mathcal{H}_Q^{(2)}$ is given

by the fourth-Legendre polynomial $P_4(\cos \theta)$:

$$d_{0,0}^{(4)}(\theta) = P_4(\cos \theta) = \frac{1}{8}(35 \cos^4 \theta - 30 \cos^2 \theta + 3). \quad (1.57)$$

Both $P_2(\cos \theta)$ and $P_4(\cos \theta)$ are plotted in Fig.1.6 as functions of the angle θ . These curves show that Legendre polynomials do not have a common root and also proves that a rotation about a single axis does not completely remove the second-order anisotropies. However, a partial narrowing is still possible provided that the rotation angle is correctly selected. The magic angle experiment leaves the last part of Eq. 1.56, scaled by a factor of ~ 0.5 . Moreover, since anisotropic parts are functions of the asymmetry parameter η , other angles can give a better line narrowing by decreasing simultaneously the contributions of $P_2(\cos \theta)$ and $P_4(\cos \theta)$. Such experiments where the angle θ is different from the magic-angle are denoted Variable Angle Sample Spinning (VASS).^{16, 24} Finally, the complete removal of anisotropic broadenings requires a rotation at two angles. The next section shows how such double rotation techniques can be implemented.

Experimental Features

In 1988, double rotation experiments were proposed by Llor et al.²⁵ in Saclay and the Pines group in Berkeley,²⁶ independently. They announced that it was possible to suppress the whole second-order quadrupolar anisotropies by spinning the sample at two angles. Two techniques emerged depending on whether the sample was spun simultaneously (DOuble Rotation DOR)^{27, 28} or sequentially (Dynamic Angle Spinning DAS)²⁹ at two angles.

For DOR, the angles are easily chosen to simultaneously annul the rank-2 and rank-4 Legendre polynomials. A schematic figure of the double rotor

is shown in Fig. 1.7. DOR probes are basically composed of an outer rotor, spinning at the magic angle and in which a smaller rotor (inner) that encloses the sample, is inserted. The orientation of the inner rotor with respect to the outer rotor must be one of the two roots of $P_4(\cos \theta)$ (see Fig. 1.6). Experimentally, the best NMR sensitivity is obtained for an inner angle $\theta = 30.5^\circ$ mainly due to a better filling factor of the rotor. A single pulse excitation is sufficient to get a DOR spectrum.

Several articles and contributions have dealt with the theoretical principles of DOR. As far as we are concerned, we will accept that anisotropic terms that are associated to the Legendre polynomials $P_2(\cos \theta)$ and $P_4(\cos \theta)$ vanish if the sample is simultaneously spun at these two angles, provided that the spinning speed is sufficient. The implementation of such experiment is very tricky and up to now, only few research groups have been able to develop DOR probes. The main problem lies in spinning these two rotors at high spinning speeds to avoid the increase in the number of spinning sidebands. At present, the dimensions of the inner and outer rotors in addition to the technological challenge of simultaneous double rotation limit the spinning speeds to 8 kHz and 1.8 kHz for inner and outer rotors, respectively. Thus, DOR spectra are often obscured by the numerous rotational sidebands. The method of synchronizing the acquisition with the outer rotor has been proposed to reduce by a factor of 2 the presence of sidebands in the final spectrum.³⁰

The most important developments of DOR are without any doubt due to the Berkeley's group which built the first probe, in association with Samoson in Tallin, as well as published the experimental evidence of the removal of second-order quadrupolar interactions. Later, spectrometer manufacturers (Bruker, Doty, Chemagnetics) also invested time and money in the produc-

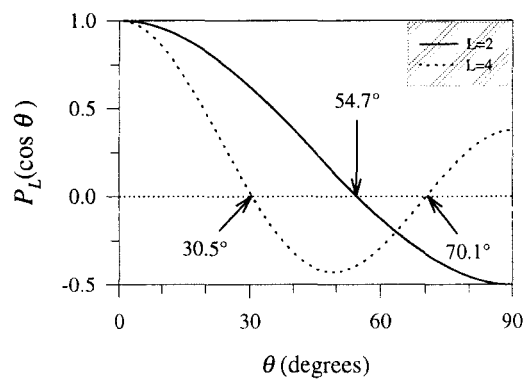


Figure 1.6: Plot of second- ($L=2$) and fourth- ($L=4$) Legendre polynomials.

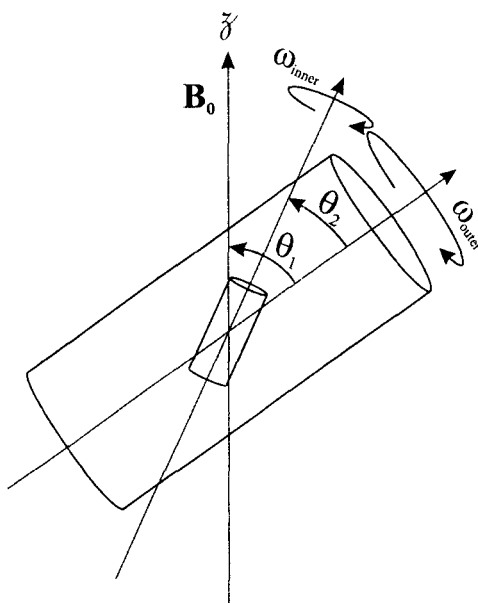


Figure 1.7: Double rotor system

tion of DOR probes that would be used as a routine. However, the weak reliability of DOR probes that is due to the technological complexity, has refrained the impact of this technique.

At the same time, Dynamic Angle Spinning (DAS) experiment was suggested as a possible substitute for DOR. This technique is based on a two dimensional recording of single-quantum evolutions at two different angles. The basic DAS sequence (Fig. 1.8) is made of several pulses that transfer the magnetization while the rotor is switched between two angles that are chosen to fulfill the following equations:

$$\begin{cases} P_2(\cos \theta_1)t_1 + P_2(\cos \theta_2)t_2 = 0 \\ P_4(\cos \theta_1)t_1 + P_4(\cos \theta_2)t_2 = 0 \end{cases} \quad (1.58)$$

This series of equations has an infinite set of solutions that are commonly called DAS complementary angles. However, instrumental constraints as well as theoretical considerations ($t_1 = t_2$) encourage the use of the two angles $\theta_1 = 37.38^\circ$ and $\theta_2 = 79.19^\circ$. We should point out that DAS complementary angles have nothing to do with the roots of Legendre polynomials.

Since two-dimensional experiments will be fully explained in Chapter two, we will not enter into the details of two-dimensional DAS experiments but we rather refer the reader to the numerous articles. Briefly, the combination of these two angles creates an echo signal in time domain t_2 . Furthermore, it can be demonstrated that the anisotropic part totally refocuses at the top of this echo.

Experimentally, we record a 2D spectrum of which the projections onto the two axes are similar to the 1D spectra at the two DAS angles. A shearing

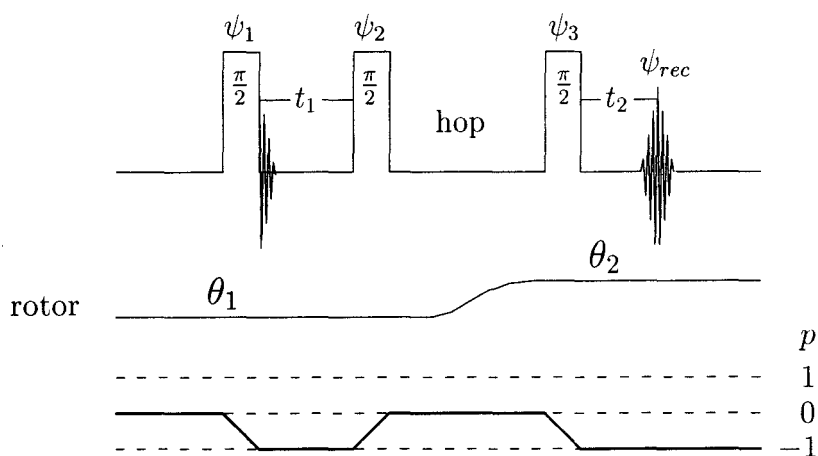


Figure 1.8: Pulse sequence for dynamic-angle spinning experiment

transformation yields an isotropic projection where crystallographically non equivalent sites should be clearly separated. A commercial MAS probe is obviously not adequate for performing DAS experiments. The direction of the rotor axis must be quickly reoriented while maintaining stable bearing and drive pressures. However, the idea of changing the orientation of the rotor during the experiment was not a new one since a few techniques such as magic angle hopping, had been previously invented to correlate isotropic and anisotropic spectra in a two-dimensional experiment. At the same time as they investigated the potential of DOR, the Berkeley's group built a DAS probe and they later published some results that evidenced the capability of the method to remove quadrupolar broadenings.^{31, 32}

However, DAS experiment suffers from a major limitation: while the rotor is switched from $\theta_1 = 37.38^\circ$ to $\theta_2 = 79.19^\circ$, the magnetization must be stored along the z axis (second $\pi/2$ pulse in Fig. 1.8). Since the hopping time cannot mechanically be inferior to about 30 msec, nuclei for which the relaxation is faster than 100 msec are not good candidates. Thus, an

important nucleus such as aluminium cannot always be studied through DAS technique. Moreover, a broadening occurs during the hopping period due to the dipolar “flip-flop” terms. Finally, the mechanical constraints make it so that the filling factor of a DAS probe is poor. Due to the small interest of manufacturers in this experiment, researchers that would be interested in running DAS experiments must either build their own probe or collaborate with the few groups, mainly originating from Berkeley, that technologically master this experiment. Of course, such handicap completely stopped the development of DAS .

1.4 Conclusion

In this first chapter, we have given the expression of the first- and second-order Hamiltonians under MAS conditions. We got to the point that the single-pulse MAS technique could only remove first-order dipolar, chemical shift anisotropy and quadrupolar contributions. More complex sample reorientations (DOR and DAS) are needed for a complete removal of the quadrupolar broadening. However, insolvable technical problems have shown the limits of NMR sequences based on sample reorientations.

In terms of quantum mechanics, we observe that researchers have taken full advantage of the spatial part of the Hamiltonian to develop MAS (first-order averaging) and DOR/DAS (second-order averaging) techniques. But, it can be noticed that spin terms have been kept in their general form. Indeed, we only mention the possibility to cancel first-order homonuclear dipolar interactions, using multiple-pulse sequences (WAHUHA). The second chapter will show that a careful consideration of the spin terms for the second-order quadrupolar interactions yields a new NMR technique which combines

sample orientation (MAS) and multiple-pulse manipulations to provide an isotropic spectrum of quadrupolar nuclei, free of any first- and second-order broadening.

1.5 La Résonance Magnétique dans les Solides (résumé)

1.5.1 Généralités sur les Interactions dans les Solides

Principes de Base de la RMN

Le phénomène de Résonance Magnétique Nucléaire est lié à l'existence pour une particule donnée, d'un moment magnétique $\boldsymbol{\mu} = \gamma \hbar \mathbf{I}$, où γ est le rapport gyromagnétique du noyau, $\hbar = h/2\pi$ la constante de Planck réduite, et \mathbf{I} , le moment cinétique de spin. Sous l'effet d'un champ magnétique statique \mathbf{B}_0 , les moments magnétiques individuels se répartissent statistiquement suivant une distribution de Boltzmann, sur les $2I + 1$ niveaux d'énergie Zeeman $E_m = m\gamma\hbar B_0$, avec $m = I, I - 1, \dots, -I$ pour créer un paramagnétisme nucléaire qui donne lieu à un signal détectable.

Les différents noyaux A_ZX de la table périodique des éléments peuvent ainsi être classés selon la valeur de leur spin I : les noyaux de spin nul qui ne sont pas observables en RMN, et les noyaux de spin entier et semi-entier. En ce qui concerne l'étude que nous présentons ici, il conviendra de séparer les noyaux de spin $1/2$ (${}^1\text{H}$, ${}^{13}\text{C}$, ${}^{29}\text{Si}$, ${}^{31}\text{P}$, ...) et les noyaux quadrupolaires, de spin $I > 1/2$ (${}^{17}\text{O}$, ${}^{27}\text{Al}$, ${}^{23}\text{Na}$, ${}^{11}\text{B}$, ...). Cette dernière famille nous intéressera tout particulièrement puisque les noyaux quadrupolaires représentent à la fois 75% des éléments de la table périodique et une source importante d'information sur la structure du composé étudié.

Aujourd'hui, la RMN moderne fait appel au phénomène de résonance pour "doper" l'effet paramagnétique par rapport au diamagnétisme électronique. Experimentalement, un champ magnétique oscillant \mathbf{B}_1 (champ radio-fréquence) est appliqué, perpendiculairement à \mathbf{B}_0 pour induire des transi-

tions entre les différents niveaux d'énergies E_m . Les conditions de résonance correspondent à une fréquence de Larmor $\omega_0 = \gamma B_0$. Après l'impulsion radiofréquence ω , le retour à l'équilibre du système de spins, sous l'action du champ statique, est enregistré dans le plan perpendiculaire à \mathbf{B}_0 pour donner le signal d'induction libre (FID).

Le principal avantage de la RMN en mode pulsé est qu'elle permet d'acquérir un spectre sur une large gamme de fréquence, en un temps limité. De plus, même si la règle de sélection $\sum_i \Delta m_i = \pm 1$ stipule clairement que seules les transitions entre niveaux d'énergies consécutifs sont observables, il est possible d'imaginer des séquences impulsionnelles complexes qui induiront des transitions entre niveaux d'énergies non adjacents. La technique MQMAS (Multiple-Quantum Magic Angle Spinning), présentée au Chapitre 2, utilise d'ailleurs les propriétés de ces transitions à multi-quantas. Les figures 1.2 et 1.3 montrent la correspondance entre niveaux d'énergies m et ordres de cohérence p .

Les équations de Bloch (cf. section 1.1.3) permettent de comprendre les phénomènes liés au retour à l'équilibre du système. Cependant, cette description se limite à l'étude par RMN des liquides, pour lesquels la plupart des interactions internes sont moyennées par le mouvement brownien des molécules. Par contre, plusieurs interactions, de natures différentes, influencent la relaxation des spins dans les solides. Par conséquent, les spectres sont plus difficiles à interpréter à cause des élargissements résultants (échantillons de poudre). Cependant, une correcte interprétation de ces élargissements peut fournir des informations importantes quant à la structure du matériau.

Les trois interactions les plus importantes sont introduites dans la section suivante. Nous ne donnerons que l'origine des interactions dipolaire et de déplacement chimique (cf. Section 1.2 pour plus de détails) afin de centrer la

discussion sur l'interaction quadrupolaire et ses caractéristiques.

Importance des Interactions dans les Solides

Un noyau possède différentes façons de “communiquer” avec son environnement à courte ou longue distance. Ainsi, nous avons précédemment vu l'influence des champs magnétiques externes \mathbf{B}_0 et \mathbf{B}_1 . Pourtant, ces interactions Zeeman n'apportent aucune information structural sur le matériau. Il faut donc prendre en compte les effets des champs magnétiques locaux qui influencent la relaxation des spins.

L'interaction dipolaire est liée au couplage de deux noyaux I et S , considérés comme des dipôles magnétiques. Expérimentalement, un tel couplage se traduit en RMN des solides par un élargissement des raies de résonance. L'interaction dipolaire est inversement proportionnel au cube de la distance interatomique $r_{I,S}$, ce qui rend son étude intéressante. Malheureusement, les effets de cette interaction sont souvent masqués par d'autres interactions, notamment quadrupolaires, dont l'amplitude est 100 à 1000 fois plus importante.

L'interaction de déplacement chimique (CSA) résulte du couplage indirect du champ statique \mathbf{B}_0 avec le nuage électronique entourant le noyau. En effet, sous l'action de \mathbf{B}_0 , les nuages électroniques se polarisent et créent un champ magnétique local qui s'oppose à \mathbf{B}_0 . Ainsi, le champ statique réel que subissent le noyau devient $B_{\text{reel}} = (1 - \sigma)B_0$ où σ est le tenseur d'écrantage chimique.

L'interaction quadrupolaire provient du couplage des gradients de champs électriques avec le moment quadrupolaire électrique que possède tout noyau de spin $I > 1/2$. L'effet quadrupolaire est étroitement lié à la

symétrie locale du noyau et constitue un outil irremplaçable pour sonder son environnement.

Même si chaque interaction peut être décrite dans le repère du laboratoire (LAB), par un tenseur cartésien à 9 composantes, il est préférable de l'exprimer en termes de tenseur sphérique irréductible lorsque des rotations diverses interviennent. Ainsi, pour chaque cristallite, un système d'axes propres (PAS) dans lequel une interaction donnée est représentée par un tenseur diagonal, est défini. Dans un échantillon de poudre, chaque cristallite est associée à son propre PAS. Les équations permettant de passer du repère d'axes propres (PAS) au repère du laboratoire (LAB) sont données au paragraphe 1.2.2 (Eqs. 1.10 et 1.11).

L'Hamiltonien quadrupolaire s'écrit comme le produit d'une partie spatiale $R_{2,-m}^Q$ et d'une partie opérateur de spin $T_{2,m}^Q$, dans un repère sphérique (Eq. 1.59).

$$\mathcal{H}_Q = \frac{eQ}{2I(2I-1)} \sum_{m=-2}^{+2} (-1)^m R_{2,-m}^Q T_{2,m}^Q \quad (1.59)$$

Les composantes du tensor $T_{i,j}^Q = I_i I_j$ peuvent être réduites à partir des composantes cartésiennes, en composantes sphériques avec les équations 1.9. Quant aux composantes sphériques de la partie spatiale, elles sont calculées à partir des composantes sphériques du gradient de champ électrique $r_{l,m}^Q$, elles mêmes déduites des composantes cartésiennes de ce tenseur. Lors de ces opérations, 2 paramètres δ_Q et η_Q , sont introduits pour caractériser au mieux le gradient de champ électrique. La détermination du paramètre d'asymétrie η_Q est d'autant plus importante qu'il est directement lié à l'environnement local du noyau. Les expressions des différents tenseurs peuvent être consultés à la section 1.2.3.

Afin de comprendre l'effet de l'interaction quadrupolaire sur le spectre d'un échantillon de poudre, il est maintenant nécessaire de développer l'Hamiltonien (Eq. 1.59) en tenant compte des définitions précédentes. Que l'échantillon soit statique ou en rotation autour d'un axe (cf. 1.5.2), nous appliquerons la théorie de l'Hamiltonien moyen (AHT). En effet, nous considérons l'Hamiltonien quadrupolaire comme une perturbation à l'interaction Zeeman dominante. L'Hamiltonien total \mathcal{H} est donc défini par

$$\mathcal{H} = \mathcal{H}_z + \mathcal{H}_Q^{(1)} + \mathcal{H}_Q^{(2)} + \dots, \quad (1.60)$$

où $\mathcal{H}_Q^{(i)}$ sont les corrections de l'Hamiltonien quadrupolaire à l'ordre i . A noter que seuls les termes de 1er et de 2nd ordres ont une influence significative sur l'allure du spectre RMN.

Le calcul de la réponse d'un système de spins passent par le développement de l'Hamiltonien quadrupolaire (Eq. 1.59) en considérant la somme sur m . Cependant, il ne faut tenir compte que des valeurs de m pour lesquelles les composantes sphériques $r_{l,m}^Q$ ne sont pas nulles ($r_{l,m}^Q = 0$ pour $l \neq 2$ et $m \neq 0, \pm 2$). Puisqu'il ne faut garder que la partie de l'Hamiltonien qui commute avec l'interaction Zeeman, nous ne gardons finalement que la composante sphérique $r_{20}^Q = \sqrt{3/2}eq$. Enfin, par l'intermédiaire des matrices de Wigner, nous obtenons une expression de l'Hamiltonien quadrupolaire au 1er ordre dépendante des angles d'Euler α et β (les angles d'Euler α, β, γ définissent l'orientation du PAS d'un cristallite pour une espèce donnée par rapport au référentiel du laboratoire). La règle de sélection limitant l'observation du signal aux seules transitions Zeeman adjacentes ($m, m + 1$), la fréquence quadrupolaire calculée au 1er ordre s'écrit

$$\omega_{m+1,m}^{(1)} = \left(m + \frac{1}{2}\right) \frac{\omega_Q}{2} \left[3 \cos^2 \beta - 1 + \eta_Q \sin^2 \beta \cos 2\alpha\right], \quad (1.61)$$

où

$$\omega_Q = \frac{3e^2qQ}{2I(2I-1)\hbar} \quad (1.62)$$

est communément appelée la fréquence quadrupolaire.

L'équation 1.61 nous apporte des indications supplémentaires sur l'interaction quadrupolaire et ses effets en RMN. D'abord, la fréquence d'un cristallite dépend de son orientation α, β par rapport au champ statique. Dans un échantillon polycristallin (poudre) ou désordonné, chaque cristallite a une orientation différente et par conséquent une intensité et une fréquence différentes. La somme des contributions de tous les cristallites donnent un spectre large et discontinu. La deuxième observation que l'on peut faire sur cette équation est pour la transition centrale ($1/2 \leftrightarrow -1/2$) : sa fréquence s'annule prouvant que le calcul au premier ordre n'est pas suffisant. C'est pour cela qu'il nous faudra pousser le calcul de l'Hamiltonien quadrupolaire jusqu'au second ordre pour la transition centrale.

L'équation 1.59 suggère que l'annulation des élargissements du à l'interaction quadrupolaire passe par la manipulation des termes de spins $T_{2,m}^Q$ en utilisant des séquences à plusieurs pulses (séquences WAHAFU) ou des termes spatiaux $R_{2,-m}^Q$ en orientant l'échantillon de façon judicieuse (MAS, DOR et DAS). La deuxième catégorie d'expériences est de loin la plus efficace puisqu'elle ne se limite pas à la seule interaction dipolaire mais permet aussi d'éliminer l'élargissement dû aux interactions plus fortes telles que le CSA et le quadrupolaire. La partie suivante montrera par un calcul au 1er ordre puis au 2nd ordre, comment une rotation de l'échantillon autour d'un

ou de plusieurs axes peut considérablement réduire la largeur du spectre en solide, jusqu'à le rendre isotrope.

1.5.2 Moyennage Spatial de l'Interaction Quadrupolaire

Au 1er Ordre

Si nous mettons maintenant l'échantillon en rotation à la fréquence ω_r , autour d'un axe faisant un angle θ avec le champ statique, la relation entre les référentiels PAS et LAB est dépendante du temps. Cependant, ce problème peut être surmonté en divisant le mouvement en deux parties, l'une indépendante du temps (du PAS au ROTOR), et l'autre dépendante du temps (du ROTOR au LAB). Ces transformations et les angles d'Euler qui y sont associées sont représentés sur la figure 1.4.

La composante spatiale $R_{2,0}^Q$ qui apparaît dans le calcul de l'Hamiltonien quadrupolaire, se déduit des composantes $r_{2,m''}^Q$ dans le PAS, grâce à deux transformations successives et s'écrit

$$R_{2,0}^\lambda = \sum_{m'=-2}^{+2} e^{-im'\omega_r t} d_{m',0}^{(2)}(\theta) \sum_{m''=-2}^{+2} \mathcal{D}_{m'',m'}^{(2)}(\alpha, \beta, \gamma) r_{2,m''}^\lambda. \quad (1.63)$$

La seconde somme dans l'équation 1.63 coïncide avec le calcul au premier ordre dans le cas d'un échantillon statique, si $m' = 0$ (cf. Section 1.5.1). Par contre, la fréquence dépendante des angles d'Euler α, β sera maintenant modulé par les termes provenant du développement de la première somme. Brièvement, la première somme est égale à $d_{m',0}^{(2)}(\theta)$ (cf. Table 1.2) auquel il faut ajouter des termes dépendants du temps ($m' = \pm 1, \pm 2$). Toutefois, nous ne tiendrons pas compte des termes dépendants du temps puisque leur contribution est quasiment nulle à haute vitesse de rotation de l'échantillon. Quant à l'élément $d_{m',0}^{(2)}(\theta)$, il est tout simplement le polynôme de Legendre

d'ordre 2, $P_2(\cos \theta) = (3 \cos^2 \theta - 1)/2$. Enfin, la fréquence d'un cristallite, calculée au premier ordre de la théorie de l'Hamiltonien moyen, prend une forme très similaire au cas statique mis à part la dépendance en θ .

$$\omega_{m,m+1} \approx -\omega_0 + \left(m + \frac{1}{2}\right) \frac{\omega_Q}{4} (3 \cos^2 \theta - 1) [3 \cos^2 \beta - 1 + \eta_Q \sin^2 \beta \cos 2\alpha] \quad (1.64)$$

Il apparaît que la partie dépendante de l'orientation du cristallite, et donc à l'origine de l'élargissement des spectres de poudre peut être éliminé en annulant le polynôme de Legendre $P_2(\cos \theta)$ par une rotation de l'échantillon autour d'un axe faisant un angle $\theta_M = 54.74^\circ$ avec le champ statique. La principale caractéristique qui fait de θ_M un angle magique est qu'il permet d'annuler toutes les interactions du premier ordre (dipolaire, CSA et quadrupolaire). Néanmoins, pour l'interaction quadrupolaire, nous avons vu qu'un calcul au second ordre s'impose dans certains cas (transition centrale). En effet, la figure 1.5 montre que la rotation à l'angle magique réduit considérablement la largeur de la raie sans pour autant éliminer toutes les discontinuités. L'élargissement résultant est en fait la contribution de l'interaction quadrupolaire au second ordre. La section suivante résume donc le calcul au second ordre pour l'interaction quadrupolaire afin d'introduire les expériences de rotation à 2 angles (DOR et DAS).

Au 2nd Ordre

Le calcul au second ordre est pour plusieurs raisons, plus complexe et nous encourageons le lecteur à se reporter à la partie en anglais traitant de ce sujet (cf. 1.3.3). L'Hamiltonien quadrupolaire au second ordre s'écrit encore comme le produit de termes de spins et de termes spatiaux.

$$\mathcal{H}_Q^{(2)} = \frac{C^2}{\omega_0} \sum_{m>0} R_{2,-m} R_{2,m} \frac{[T_{2,-m}, T_{2,m}]}{m} \quad (1.65)$$

Le commutateur $[T_{2,-m}, T_{2,m}]$ sera d'une grande importance dans le deuxième chapitre lorsque nous étudierons l'expérience MQMAS. Ici, le développement du produit $R_{2,-m} R_{2,m}$ doit nous permettre de simplifier l'expression de l'Hamiltonien. En mécanique quantique, un tel produit de tenseurs sphériques peut être réduit en une somme de tenseurs sphériques irréductibles $R_{L,M}$ dans laquelle interviennent les coefficients de Clebsch-Gordan. Les conditions d'annulation de ces coefficients permettent ensuite de réduire l'Hamiltonien à une somme de 3 tenseurs d'ordre 0, 2 et 4. L'Hamiltonien quadrupolaire au second-ordre se simplifie alors pour donner l'expression Eq. 1.66.

$$\mathcal{H}_Q^{(2)} = \frac{C^2}{\omega_0} [\xi_0 \tilde{R}_{0,0} + \xi_2 \tilde{R}_{2,0} + \xi_4 \tilde{R}_{4,0}] \quad (1.66)$$

$\tilde{R}_{L,0}$ sont les nouveaux tenseurs sphériques irréductibles de la partie spatiale alors que tous les autres termes, notamment la partie opérateur de spin $[T_{2,-m}, T_{2,m}]$, sont regroupés dans les valeurs ξ_L qui seront développées au chapitre 2.

Comme pour le calcul au premier ordre de l'interaction quadrupolaire, nous trouvons que les termes $\tilde{R}_{L,0}$ sont modulés par la rotation à un angle θ par rapport au champ statique. Ainsi, en utilisant les équations 1.10 et 1.11, les 3 tenseurs $\tilde{R}_{L,0}$, avec $L = 0, 2, 4$, s'écrivent

$$\tilde{R}_{L,0}(t) = \sum_{m'=-L}^L \sum_{m''=-L}^L e^{-m'\omega_r t} d_{m',0}^{(L)}(\theta) \mathcal{D}_{m'',m'}^{(L)}(\alpha, \beta, \gamma) \tilde{r}_{L,m''}, \quad (1.67)$$

où les termes $\tilde{r}_{L,m''}$ (Table 1.7) sont les nouvelles composantes du tenseur sphérique, calculées grâce au formalisme des coefficients de Clebsch-Gordan.

Finalement, en ne considérant que les termes indépendants du temps ($m' = 0$ dans l'équation 1.67), l'Hamiltonien (Eq. 1.68) s'écrit comme la somme de 3 termes, modulés par les éléments de matrices $d_{0,0}^{(L)}$.

$$\mathcal{H}_Q^{(2)} = \frac{C^2}{\omega_0} \left\{ \overbrace{d_{0,0}^{(0)}(\theta)}^1 \left(\xi_0 \overbrace{\mathcal{D}_{0,0}^{(0)}(\alpha, \beta, 0)}^1 \tilde{r}_{0,0} \right) + d_{0,0}^{(2)}(\theta) \left(\xi_2 \sum_{m''=-2}^2 \mathcal{D}_{m'',0}^{(2)}(\alpha, \beta, 0) \tilde{r}_{2,m''} \right) + d_{0,0}^{(4)}(\theta) \left(\xi_4 \sum_{m''=-4}^4 \mathcal{D}_{m'',0}^{(4)}(\alpha, \beta, 0) \tilde{r}_{4,m''} \right) \right\} \quad (1.68)$$

La partie correspondant à $L = 0$ est indépendante des angles d'Euler et donne lieu à un simple déplacement quadrupolaire induit. Puis, nous retrouvons le polynôme de Legendre d'ordre 2, $d_{0,0}^{(2)}(\theta) = P_2(\cos \theta)$, qui permet d'éliminer la deuxième partie de l'équation 1.68 par une rotation à l'angle magique. Enfin, la troisième partie est proportionnelle au polynôme de Legendre d'ordre 4,

$$d_{0,0}^{(4)}(\theta) = P_4(\cos \theta) = \frac{1}{8}(35 \cos^4 \theta - 30 \cos^2 \theta + 3), \quad (1.69)$$

qui ne s'annule pas pour $\theta_M = 54.7^\circ$. Par conséquent, ce dernier terme, dépendant des angles d'Euler α, β , conduit à un élargissement du spectre de la transition centrale pour un échantillon de poudre.

Comme les polynômes de Legendre d'ordres 2 et 4 n'ont pas de racine commune, il faut faire appel à des expériences plus complexes dans lesquelles l'échantillon est en rotation, simultanément ou séquentiellement, à deux angles judicieusement choisis. Ainsi, en 1988, Llor et Virlet à Saclay, ont proposé en même temps que le groupe d'A. Pines à Berkeley, deux expériences, DOR (DOuble Rotation) et DAS (Dynamic Angle Spinning), qui permet-

tent d'éliminer tous les élargissements dus à l'interaction quadrupolaire au second-ordre.

Pour ces deux expériences, il est nécessaire de posséder des sondes spéciales car la double rotation n'est pas facile techniquement. En effet, pour le DOR, il faut mettre en rotation un rotor (interne) dans lequel nous mettons l'échantillon, à l'intérieur d'un second rotor (externe) lui même tournant avec une autre orientation par rapport à \mathbf{B}_0 . Les vitesses de rotation sont limitées à 8 kHz pour le rotor interne et 1.8 kHz pour le rotor externe, de sorte que de nombreuses bandes de rotation viennent encombrer le spectre. Les angles d'inclinaison des rotors internes et externes sont ceux annulant les polynômes de Legendre d'ordre 2 et 4. Quant au DAS, la rotation se fait séquentiellement aux angles θ_1 et θ_2 qui constituent une paire remplissant les conditions de l'équation 1.58. La séquence de pulses d'une expérience DAS est représentée à la figure 1.8. Elle correspond à une expérience à 2 dimensions pendant laquelle les spins évoluent pendant t_1 à l'angle θ_1 puis pendant t_2 à l'angle θ_2 . Par corrélation des évolutions pendant t_1 et t_2 , nous acquérons un signal d'écho au sommet duquel l'anisotropie quadrupolaire est annulée. Cependant, l'aimantation doit être stockée le long du champ statique lors du changement d'orientation du rotor. Une telle manoeuvre requiert plusieurs dizaines de millisecondes, de sorte que les noyaux relaxant très vite (< 100 msec) ne peuvent pas être étudiés avec le DAS.

Finalement, nous constatons que les méthodes de double rotation (DOR et DAS), même si elles permettent théoriquement de se débarrasser des termes anisotropes de l'interaction quadrupolaire, n'ont pas eu un impact très important sur les nombreux chercheurs utilisant la RMN comme moyen d'investigation. En effet, le challenge technologique qu'il fallait surmonter a probablement rendu ces deux expériences impossible à utiliser en routine. Le

chapitre suivant va nous montrer que l'interaction quadrupolaire au second ordre peut quand même être éliminé à condition de ne pas se limiter à un moyennage spatial de l'Hamiltonien.

Bibliography

1. RABI I., KELLOG J. AND ZACHARIAS J. *Phys. Rev.* 53 (1938), p. 318.
2. ERNST R. *Adv. Magn. Reson.* 2 (1966), p. 1.
3. BLOCH F. *Phys. Rev.* 70 (1960), p. 460.
4. VEGA S. *Phys. Rev.* 23 (1981), p. 3152.
5. ABRAGAM A. *The Principles of Nuclear Magnetism*. Clarendon Press Oxford, 1961.
6. MEHRING M. *High Resolution NMR Spectroscopy in Solids*. Springer-Verlag, 1976.
7. LAMB W. *Phys. Rev.* 60 (1941), p. 817.
8. RAMSEY N. *Phys. Rev.* 78 (1950), p. 699.
9. HAEBERLEN U. *High Resolution NMR in Solids: Selective Averaging*. Academic Press, 1976.
10. ANDREW E., BRADBURY A. AND EADES R. *Nature* 82 (1958), p. 1659.
11. HAEBERLEN U. AND WAUGH J. *Phys. Rev.* 175 (1968), p. 453.
12. MAGNUS W. *Commun. Pure and Appl. Math.* 7 (1954), p. 649.

13. FREUDE D. AND HAASE J. *Quadrupole Effects in Solid-State Nuclear Magnetic Resonance*. Springer-Verlag, 1993.
14. WAUGH J., HUBER L. AND HAEBERLEN U. *Phys. Rev. Lett.* 7 (1954), p. 649.
15. A.SAMOSON. *Chem. Phys. Lett.* 119, 1 (1985), pp. 29–32.
16. LEFEBVRE F., AMOUREUX J.-P., FERNANDEZ C. AND DEROUANE E. *J. Chem. Phys.* 86, 11 (1987), pp. 6070–6076.
17. MARICQ M. AND WAUGH J. *J. Chem. Phys.* 70, 7 (1979), pp. 3300–3316.
18. GOLDMAN M., GRANDINETTI P., LLOR A., OLEJNICZAK Z., SACHLEBEN J. AND ZWANZIGER J. *J. Chem. Phys.* 97, 12 (1992), pp. 8947–8960.
19. CHMELKA B. AND ZWANZIGER J. *Solid-State NMR line Narrowing Methods for Quadrupolar Nuclei: Double Rotation and Dynamic-Angle Spinning*. Springer-Verlag, 1994.
20. LEVITT M., RALEIGH D., CREUZET F. AND GRIFFIN R. *J. Chem. Phys.* 92 (1990), p. 6347.
21. MUELLER K. *Dynamic-Angle Spinning and Double Rotation of Quadrupolar Nuclei*. PhD thesis, Lawrence Berkeley Laboratory, University of California, 1991.
22. MESSIAH A. *Quantum Mechanics, Volume II*. North-Holland Publishing Company, Amsterdam.
23. AMOUREUX J.-P. *Solid-State NMR 2* (1993), pp. 83–88.

24. GANAPATHY S., SCHRAMM S. AND OLDFIELD E. *J. Chem. Phys.* 77 (1982), pp. 4360–4365.
25. LLOR A. AND VIRLET J. Bad Aussee, Austria. In *Ninth Experimental NMR Conference*, May 1998.
26. PINES A. Bad Aussee, Austria. In *Ninth Experimental NMR Conference*, May 1998.
27. LLOR A. AND VIRLET J. *Chem. Phys. Lett.* 152 (1988), pp. 248–253.
28. SAMOSON A., LIPPMAA E. AND PINES A. *Mol. Phys.* 65 (1988), pp. 1013–1018.
29. MUELLER K., SUN B., CHINGAS G., ZWANZIGER J., TERAO T. AND PINES A. *Mol. Phys.* 86 (1990), pp. 470–487.
30. SAMOSON A. AND LIPPMA E. *J. of Magn. Reson.* 84 (1989), pp. 410–416.
31. MUELLER K., CHINGAS G. AND PINES A. *Rev. Sci. Instrum.* 62 (1991), pp. 1445–1452.
32. EASTMAN M., GRANDINETTI P., LEE Y. AND PINES A. *J. of Magn. Reson.* 98 (1992), pp. 333–341.



Chapter 2

Averaging with MQMAS

2.1 Basics of Two Dimensional MQMAS

2.1.1 Theoretical Consideration of Spin Terms

Quadrupolar Hamiltonian

In Chapter one, we deliberately left the spin terms out of our consideration to focus on the theoretical explanation of reorientation methods in solid-state NMR. So far, commutators $[T_{2,-m}, T_{2,m}]$ have not been developed and we rather introduced the terms ξ_L in which we included all the expressions that were not of concern at that time, especially the spin parts of the quadrupolar Hamiltonian. However, the spin commutators can no longer be ignored and they must be given explicitly in order to explain the theory of MQMAS.

Actually, the mathematical tools required to express the spin commutators have been given in Chapter one. Indeed, $[T_{2,-m}, T_{2,m}]$ terms, for $m = 1, 2$ are nothing else but products of spherical tensors that can be reduced using the formalism of Eq. 1.50, replacing spatial components by spin components. Therefore, we similarly find that the spin products trans-

form as rank-0 to rank-4 tensors. Then, the symmetry of Clebsch-Gordan coefficients (Eq. 1.53) are considered to simplify the expression. The development of the commutator $T_{2,-m}T_{2,m} - T_{2,m}T_{2,-m}$ into irreducible spherical tensors $T_{L,0}$ (with $0 \leq L \leq 4$) clearly shows that some components will vanish depending on the sign of their Clebsch-Gordan coefficients. We finally observe that only $L = 1, 3$ terms subsist.

We previously expressed the second-order quadrupolar Hamiltonian into the following sum

$$\mathcal{H}_Q^{(2)} = \frac{C^2}{\omega_0} \sum_{L=0,2,4} \xi_L \tilde{R}_{L,0}. \quad (2.1)$$

According to Duer,¹ ξ_L values are given in Eqs. 2.2 as functions of rank-1 and rank-3 irreducible spherical tensors $\tilde{T}_{1,0}$ and $\tilde{T}_{3,0}$.

$$\begin{cases} \xi_0 = \frac{1}{10} [-3\sqrt{10}\tilde{T}_{3,0} + \tilde{T}_{1,0}(3 - 4I(I + 1))] \\ \xi_2 = \frac{1}{10} [-12\sqrt{10}\tilde{T}_{3,0} - \tilde{T}_{1,0}(3 - 4I(I + 1))] \\ \xi_4 = \frac{1}{10} [-34\sqrt{10}\tilde{T}_{3,0} + 3\tilde{T}_{1,0}(3 - 4I(I + 1))] \end{cases} \quad (2.2)$$

where

$$\begin{aligned} \tilde{T}_{1,0} &= I_z \\ \tilde{T}_{3,0} &= \sqrt{\frac{1}{10}} I_z [5I_z^2 - 3I(I + 1) + 1]. \end{aligned} \quad (2.3)$$

Quadrupolar Frequency $\omega_Q^{(2)}(m)$

Let us consider the second-order quadrupolar frequency $\omega_Q^{(2)}(m)$ for an energy level m :

$$\omega_Q^{(2)}(m) = \frac{C^2}{\omega_0} \sum_{L=0,2,4} \langle m | \xi_L | m \rangle \tilde{R}_{L,0}. \quad (2.4)$$

The $\langle m|\xi_L|m\rangle$ terms are found proportional to the $C_L^I(m)$ coefficients that are given in Eqs. 2.6. We have chosen the notation used by Frydman et al.²

$$\langle m|\xi_L|m\rangle = \frac{C_L^I(m)}{4}, \quad (2.5)$$

where

$$\begin{aligned} C_0^I(m) &= 2m[I(I+1) - 3m^2] \\ C_2^I(m) &= 2m[8I(I+1) - 12m^2 - 3] \\ C_4^I(m) &= 2m[18I(I+1) - 34m^2 - 5]. \end{aligned} \quad (2.6)$$

With the help of Wigner matrices, the new spherical tensor components $\tilde{r}_{L,0}$ in the PAS (Table 1.7) come out in the expression of the second-order quadrupolar frequency $\omega_Q^{(2)}(m)$. However, it is usual to replace $\tilde{r}_{L,0}$ components by $\tilde{\rho}_{L,0} = \tilde{r}_{L,0}/(eq)^2$ so that the quadrupolar frequency ω_Q of Eq. 1.34 is apparent in the expression of $\omega_Q^{(2)}(m)$. The angle-dependent terms have been grouped into the $A_L(\alpha, \beta)$ that are given in Eqs. 2.9.

$$\omega_Q^{(2)}(m) = \frac{\omega_Q^2}{36\omega_0} \sum_{L=0,2,4} C_L^I(m) A_L(\alpha, \beta) \quad (2.7)$$

where

$$A_L(\alpha, \beta) = \sum_{m'=-L}^L \mathcal{D}_{m',0}^{(L)}(\alpha, \beta, 0) \tilde{\rho}_{L,m'} \quad (2.8)$$

Making use of the reduced Wigner matrices, the Euler angle-dependent terms take the following form:

$$\begin{aligned}
A_0(\alpha, \beta) &= \tilde{\rho}_{0,0} \\
A_2(\alpha, \beta) &= \tilde{\rho}_{2,0} d_{0,0}^{(2)}(\beta) + 2 \tilde{\rho}_{2,2} d_{2,0}^{(2)}(\beta) \cos 2\alpha \\
A_4(\alpha, \beta) &= \tilde{\rho}_{4,0} d_{0,0}^{(4)}(\beta) + 2 \tilde{\rho}_{4,2} d_{2,0}^{(4)}(\beta) \cos 2\alpha + 2 \tilde{\rho}_{4,4} d_{4,0}^{(4)}(\beta) \cos 4\alpha
\end{aligned} \tag{2.9}$$

When a rotation about a single axis is applied to the sample, the equation slightly differs: the procedure is identical to the one we used in the first chapter and it leads to the emergence of the Legendre polynomials $P_L(\theta)$. Therefore, for the case where the time-dependent terms are removed by a high spinning speed, the second-order quadrupolar frequency is simply written

$$\omega_Q^{(2)}(m) = \frac{\omega_Q^2}{36\omega_0} \left[A_0 C_0^I(m) + A_2(\alpha, \beta) C_2^I(m) P_2(\cos \theta) + A_4(\alpha, \beta) C_4^I(m) P_4(\cos \theta) \right]. \tag{2.10}$$

Quadrupolar Induced Shifts

Once more, we find the three parts that compose the second-order quadrupolar frequency. The first term which is α -, β -independent, causes a quadrupolar induced shift (ω_{QIS}) to be added to the actual chemical shift of the nucleus. On the other hand, second and third terms yield the anisotropic broadening and they will be of great interest for explaining the concept of MQMAS. The quadrupolar induced shifts $\omega_{m,-m}^{QIS}$ can be calculated for the central transition ($1/2, -1/2$) as well as for the general case of a symmetric transition ($m, -m$) using Eq. 2.11.

$$\omega_{m,-m}^{QIS} = \tilde{\rho}_{0,0} \frac{\omega_Q^2}{36\omega_0} \left[\langle m | C_0^I(m) | m \rangle - \langle -m | C_0^I(-m) | -m \rangle \right] \tag{2.11}$$

Thus, we find that the additional shift due to the second-order quadrupolar interaction can be written

$$\omega_{m,-m}^{QIS} = \frac{2m \omega_Q^2}{30 \omega_0} \left(1 + \frac{\eta^2}{3}\right) [I(I+1) - 3m^2]. \quad (2.12)$$

In the MQMAS experiment, we will excite symmetric triple-quantum ($m = 3/2$) or higher-order transitions and therefore the calculation of $\omega_{m,-m}^{QIS}$ is justified. However, the selection rule that we mentioned in Chapter one, clearly stated that only adjacent transitions ($m, m - 1$) could be directly observed. Moreover, most standard NMR experiments are concerned with the observation of the central transition ($-1/2, 1/2$) for which the quadrupolar induced shift is

$$\omega_{-1/2,1/2}^{QIS} = -\frac{\omega_Q^2}{30 \omega_0} \left(1 + \frac{\eta^2}{3}\right) \left[I(I+1) - \frac{3}{4}\right]. \quad (2.13)$$

A few experiments take advantage of the properties of the quadrupolar induced shift which is more important for satellite transitions than for the central transition. This is the case of the SATRAS experiment that enables the separation of non-equivalent sites by optimizing the acquisition of the satellite transitions on a one dimensional MAS spectrum.^{3, 4} But, the excitation of satellite transitions remains restricted to sites with moderate ω_Q values and single-quantum excitation of the central transition has been so far the first choice in solid-state NMR.

The effect of the quadrupolar induced shift on the NMR spectrum is summarized in Fig. 2.1. The central transition is not affected by a first-order correction whereas the second-order quadrupolar correction causes the central and satellite bands to be shifted.

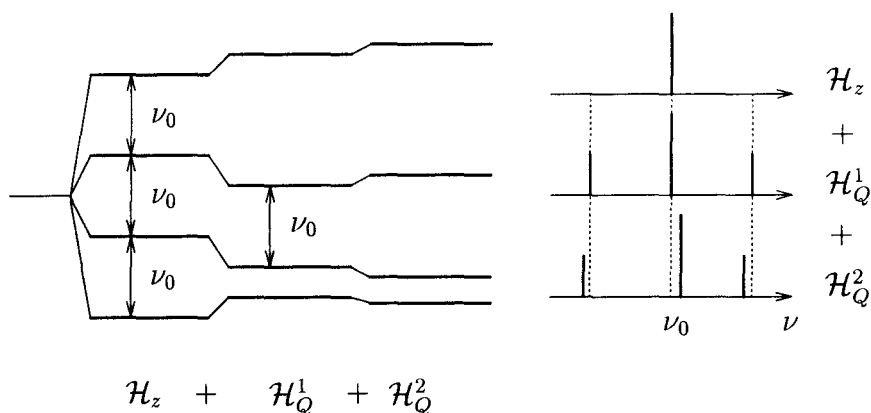


Figure 2.1: Effects of first- and second-order quadrupolar interactions on energy levels (left) and resonances (right). Centerband is not affected by first-order quadrupolar interactions whereas second-order shifts it by a quantity $\omega_{-1/2,+1/2}^{QIS}$. This figure corresponds to a single-crystal description.

Amongst anisotropic terms in Eq. 2.10, only rank-4 remains when the sample is spun at the magic angle at sufficient high speed, since rank-2 term vanishes and rank-0 term yields an extra frequency shift (QIS) only. Therefore, Duer et al.,⁵ and later Frydman² took advantage of the properties of the $C_4^I(m)$ coefficients to propose the ingenious MQMAS experiment contrary to their predecessors who focused on spatial degrees of freedom to get rid of anisotropic broadening. These coefficients are explicitly related to the spin number I of the nucleus and m (or $p = 2m$) the excited transition. It is worth noticing the main advantage of the MQMAS experiment which is to require a sample rotation about a single axis: high spinning speeds can be reached (15 kHz for 4 mm rotors) with standard reliable probes, allowing experiments to be performed under extreme conditions (high and low temperatures) for a wide selection of nuclei.

2.1.2 Theory of MQMAS

Two dimensional experiments

The fact that we are unable to directly observe coherence orders but only single quantum transitions, constitutes the main drawback in NMR. Nevertheless, several authors had investigated multiple quantum transitions and later came to the conclusion that the resolution would be enhanced only in particular cases.^{6, 7} However, these investigations were mainly based on theoretical calculations and these authors concluded that there was not much of an experimental future. In the three years preceding the publication of Frydman's first MQMAS spectrum, it can be fairly said that researchers underestimated the impact that these "invisible" transitions would have on the development of solid-state NMR of quadrupolar nuclei. Unlike them, Frydman made a good use of the potentiality of two dimensional NMR to observe these "forbidden" coherences.

Today, multi-dimensional (2D and 3D) experiments are commonplace in liquid state NMR whereas until now only a few techniques (DAS, Nutation, Hetcor) in solid state NMR use two-dimensional recordings. Moreover, the technical complexity of these techniques and sometimes their lack of resolution have refrained their development.

Two-dimensional NMR emerged in 1971 when Jeener proposed the addition of a second time domain. Three years later, Ernst verified the experimental feasibility of this great discovery. The simplest two dimensional experiment requires at least two pulses as presented in Fig. 2.2. The last pulse must be optimized in order to transfer the magnetization in $p = -1$, the only observable transitions. On the contrary, the first pulse can excite

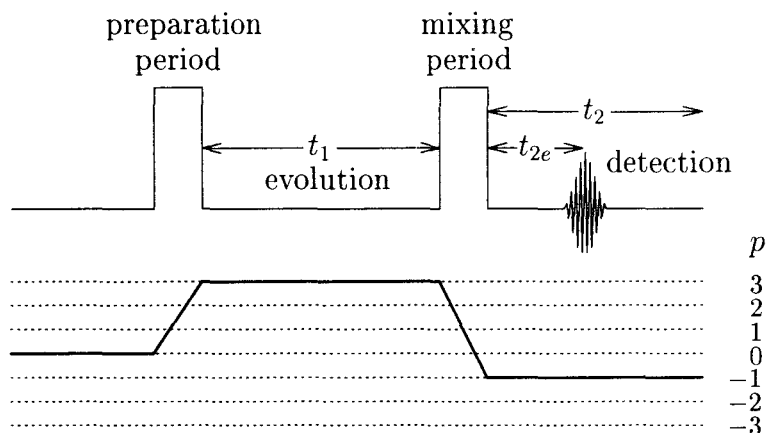


Figure 2.2: Basic two-dimensional NMR experiment.

other coherence orders. Whereas the evolution of single quantum transitions is recorded in the time domain t_2 , the evolution of coherences between the two pulses is monitored indirectly by a systematic increment of time t_1 . This sequence being similar to the Hahn echo sequence,⁸ we observe an echo signal that slightly moves at t_{2e} in the time domain t_2 as t_1 increases. Figs. 2.5 represents two examples of an acquired 2D dataset in time domain for spins $3/2$ and $5/2$. We can already notice that for short values of t_1 the echo is truncated on its left side. The dataset in time domain, must be Fourier transformed in both dimensions to obtain a two dimensional spectrum in frequency, for which the projection onto the ω_1 -axis allows the observation of the coherences that evolved during t_1 . Thus, the basic MQMAS experiment proposed by Frydman and later improved by several authors⁹⁻¹¹ consisted in exciting triple quantum $p = 3$ or higher order $p = 5, 7, 9$ transitions to follow their evolution during t_1 before converting the magnetization into single quantum coherence $p = -1$.

Removing Quadrupolar Anisotropies

In order to understand how anisotropic rank-4 terms disappear from Eq. 2.10, we should look at the signal that is recorded in the t_2 domain. The detected signal is of the form

$$s(t_1, t_2) = \exp -i(\omega_p t_1 + \omega_{-1} t_2). \quad (2.14)$$

where the efficiency of the different pulse transfers ($0Q \rightarrow pQ$ and $pQ \rightarrow -1Q$) are not taken into account.

It is worth noticing that we will be now concerned about symmetric transitions only. We also remind the readers that a coherence order p corresponds to the symmetric transition between energy levels ($m \rightarrow -m$), with its opposite coherence order $-p$ being equivalent to the transition ($-m \rightarrow m$). Consequently, coherence orders $p = 2m$ will now replace m in equations and functions that have been previously defined.

Frequencies $\omega_p = \omega_{m,-m}$ are calculated the same way as the quadrupolar induced shift in Eq 2.11, this time including both rank-0 and rank-4 terms of Eq. 2.10, whereas rank-2 term is left out due to the rotation at the magic angle θ_M . For the sake of clarity, angular-dependent terms are grouped together into the expressions of B_0 and $B_4(\alpha, \beta, \cos \theta_M)$. We obtain the following expressions for ω_{-1} and ω_p :

$$\begin{aligned} \omega_{-1} &= B_0 C_0^I(-1) + B_4(\alpha, \beta, \cos \theta_M) C_4^I(-1) \\ \omega_p &= B_0 C_0^I(p) + B_4(\alpha, \beta, \cos \theta_M) C_4^I(p) \end{aligned} \quad (2.15)$$

where

$$\begin{aligned}
B_0 &= \frac{\omega_Q^2}{18\omega_0} A_0 \\
B_4(\alpha, \beta, \cos \theta_M) &= \frac{\omega_Q^2}{18\omega_0} A_4(\alpha, \beta) P_4(\cos \theta_M).
\end{aligned}
\tag{2.16}$$

After inserting expressions of ω_{-1} and ω_p into Eq. 2.14, we find that the only angular dependent term B_4 disappears when the echo t_{2e} is linked to t_1 by the relation

$$t_{2e} = -\frac{C_4^I(p)}{C_4^I(-1)} t_1 = R(I, p) t_1. \tag{2.17}$$

The coefficients $R(I, p)$ are deduced from Eqs. 2.6 and given in Table 2.1 for each spin number I and permitted coherence order p . Nevertheless, most nuclei we investigated in this work have spin numbers 3/2 and 5/2 and we limited the excitation to the triple-quantum excitation $p = 3$.

Spin I	Coherence p	$C_4^I(p)$	$R(I, p)$
3/2	1	54	1
3/2	3	-42	-7/9
5/2	1	144	1
5/2	3	228	19/12
5/2	5	-300	-25/12

Table 2.1: $C_4^I(p)$ and $R(I, p)$ values as functions of the spin number I and the coherence order p .

The next step is to excite the correct multiple-quantum transition so that the signal refocuses in the positive time domain t_2 . Of course, this is related to the sign of the coefficient $R(I, p)$. We can observe in Table 2.1 that this coefficient is positive for every case, except when $p = 2I$ for which

it is negative. Therefore, the latter experimental condition (triple-quantum excitation on spin $3/2$, quintuple-quantum on spin $5/2$, etc.) will see the signal refocusing for negative time t_{2e} if the pathway is chosen to be identical to the one in Fig. 2.2 ($0 \rightarrow +p \rightarrow -1$). Yet, as the sign of $R(I, p)$ changes with the sign of p , the symmetrical pathway ($0 \rightarrow -p \rightarrow -1$) will yield the desired echo signal in positive time t_2 .

Frydman's experiment

In 1995, Frydman et al.,² published the first experimental results on MQMAS and thus, proved that second-order quadrupolar broadening could be removed from spectra leading to a substantial improvement of the line narrowing. They monitored the behavior of $I = 3/2$ and $5/2$ spins, under MAS conditions, subjected to triple-quantum and single-quantum correlation. The selected coherence transfer pathways were ($0 \rightarrow -3 \rightarrow -1$) and ($0 \rightarrow +3 \rightarrow -1$) for spins $I = 3/2$ and $5/2$, respectively. These pathways yield a refocusing of the anisotropies. Isotropic echos (with no quadrupolar anisotropy) were detected at times $t_{2e} = R(I, p)t_1$. This is illustrated in Figs. 2.3 and 2.4.

It can be noted that, in this first application of MQMAS, the 2D dataset in time domain was not Fourier transformed in both dimensions to get a 2D plot of the different sites in frequencies. An isotropic MAS spectrum can be obtained by Fourier transformation of the free induction decay along an axis with the slope of $|R(I, p)|^{-1}$. This corresponds to taking the summun

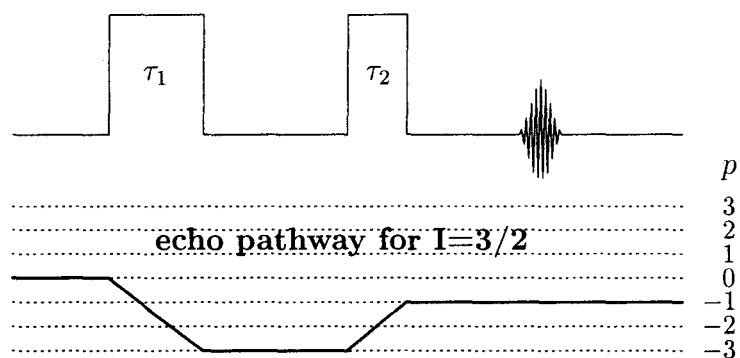


Figure 2.3: Coherence order pathway leading to an echo signal in the acquisition time domain for $I = 3/2$

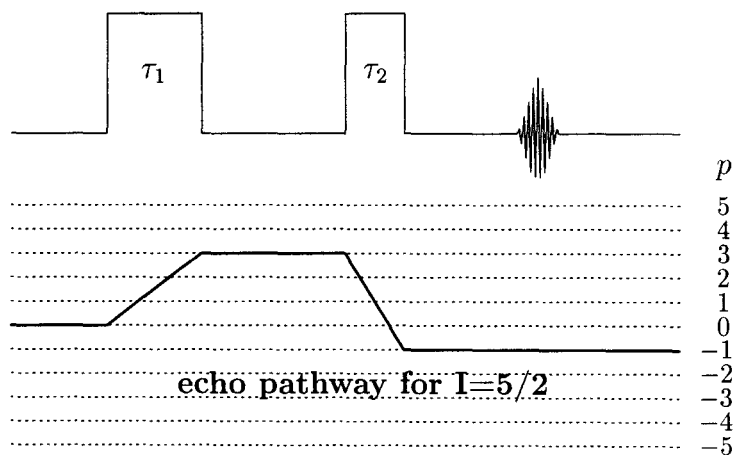


Figure 2.4: Coherence order pathway leading to an echo signal in the acquisition time domain for $I = 5/2$

of the echo signal for which the rank-4 part of the quadrupolar Hamiltonian vanishes.

Figs. 2.5 stem from a triple quantum excitation on $I = 3/2$ and $5/2$ spins respectively. We clearly see that the echo moves along the axis of slope $R(I, p)^{-1}$.

The main purpose of the MQMAS experiment was for sure the acquisition of a spectrum free of quadrupolar broadening. This has been achieved by Frydman and co-authors when they showed these isotropic MAS spectra. Since the acquisition follows a 2D mode, one step further was achieved by processing the data in a 2D mode, to extract the maximum information from the dataset in the time domain. Two-dimensional processing is all the more important that 2D spectra will constitute the basis of our method of quantification of MQMAS spectra.

2.1.3 Acquisition and Processing

Many books and articles cover the acquisition and processing of two dimensional spectra in NMR. Yet, the most complete work is probably the book written by Ernst et al.¹² They extensively explain the different modes of acquisition and the processing that follows. As far as the following section is concerned, we will describe the States and Hypercomplex methods that we used in our experiments, with the view of providing general rules that are applicable to other acquisition modes.

Acquisition

The datasets that are displayed in the previous section (Figs. 2.5) are unlikely to produce acceptable spectra after 2D Fourier transformation because they lack parts that are essential to remove dispersive components of the

final spectrum. Thus, a “good” acquisition procedure is vital to get pure-absorption spectra.

Two- and one-dimensional acquisitions are similar as far as the requirements are concerned to obtain pure absorption spectra. First, both real and imaginary parts of the signal must be recorded in both t_2 and t_1 dimensions. Indeed, in general the spectrum is out of phase after Fourier transformation and additional phase is needed. This does not occur when the excitation is exactly on resonance. In two-dimensional techniques, like in one-dimensional experiments, a linear combination of the real and imaginary signals yield a perfect phasing of the spectrum. In single-pulse experiments, the acquisition of real and imaginary parts is carried out by a synchronous detection of 2 signal dephased by 90° . In the dimension t_1 the evolution of the signal can not be directly monitored. Thus, the only available way is to influence the evolution time by applying a phase-shift to the pulses. This corresponds to the method of States¹³ which stipulates that the imaginary part of a 2D signal is obtained by adding a phase

$$\psi^{prep} = \frac{\pi}{2|p|} \quad (2.18)$$

to the phase of the first pulse (preparation pulse). In the case of an excitation of coherence orders $p = 3$, we need to run a second experiment with a phase shift of 30° to the first pulse.

Furthermore, we can observe on the same datasets (Figs.2.5) that for short t_1 increments, the echo signal is truncated on its left side. Like for 1D experiments for which the electronic dead time sometimes hides an important part of the FID, the truncation of the echo in 2D acquisition also yields distorted spectra. Yet, the missing part of the echo can be retrieved if, in addition to the echo signal, we record the evolution in t_2 of the anti-echo.

The anti-echo is quite simply expressed as the “mirror image” pathway as shown in Fig. 2.6. Fig. 2.7 exhibits the evolution of the echo and antiecho signals in time domain as t_1 is increased.

The selection of the echo and anti-echo pathways is governed by different rules that are suitable to all 2D acquisition methods involving as many pulses as desired. The theoretical foundation can be found in pages 294-301 of Ernst et al.¹²

1. Before the first pulse is applied, the system is at equilibrium ($p = 0$) while the coherence order is $p = -1$ for acquisition, after the last pulse. Thus, for a pulse sequence composed of n pulses, we find that $\sum_{i=1}^n \Delta p_i = -1$ (in which $\Delta p_i = p_{i+1} - p_i$) and the phase of one of the pulses can be fixed (often kept equal to zero).
2. The phase of the receiver ψ^{rec} must also be shifted in order to select the desired pathway. If ψ_i is the phase of the i^{th} pulse, a convenient approach is to choose a shift $\psi^{rec} = -\sum_{i=1}^n \Delta p_i \psi_i$.
3. The choice of the number N_i of phases that we will apply to a pulse, in order to select a desired pathway, combined with the two previous statements, does not ensure that all other possible pathways will be rejected. In fact, other pathways might be selected depending on N_i and calculated using Eq. 2.19.

$$\Delta p_i^{(selected)} = \Delta p_i^{(desired)} \pm nN_i, \quad (2.19)$$

where $n = 0, 1, 2, \dots$

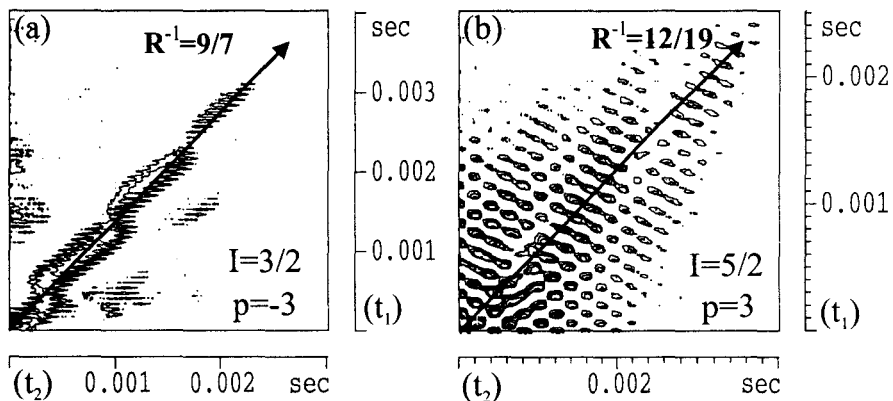


Figure 2.5: 2D 3QMAS dataset in time domain for spins $3/2$ and $5/2$ showing the echo moving along an axis of slope $R(I, p)^{-1}$. ^{23}Na and ^{27}Al 3QMAS datasets were obtained with sodium sulfate Na_2SO_4 (a) and aluminophosphate $\text{AlPO}_4 - 14$ (b), respectively.

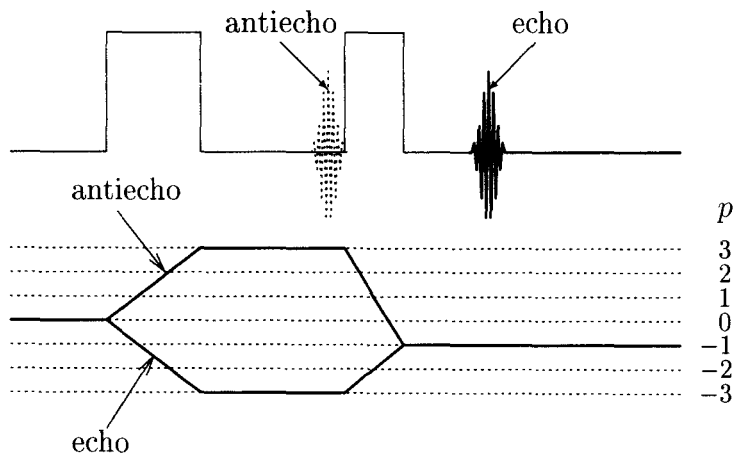


Figure 2.6: Echo and antiecho pathways for a spin $I = 3/2$

4. The selection of one or several pathways is achieved by systematically incrementing the phase of each pulse by

$$\psi_i = \frac{k_i 2\pi}{N_i}, \quad (2.20)$$

with $k_i = 0, 1, \dots, N_i - 1$.

5. Since the pulses must be cycled separately, the total number of phases in the sequence is $N = N_1 \cdot N_2 \cdot \dots \cdot N_n$. Because of the first rule mentioned, one of the values N_i can always be taken equal to 1.

Let us consider the phase cycle of the two-pulse sequence. The phase of the first pulse can be kept null (rule 1) and it is necessary to cycle the second pulse in order to select both the echo and anti-echo pathways. The echo and anti-echo signals can be recorded in two separated experiments by choosing N_2 big enough to select a single pathway. This is the alternative echo/anti-echo method. Still, we can make a good use of the third rule mentioned before since it appears that the selection of both echo and anti-echo pathways occurs for $N_2 = 2p$ ($N_2 = 6, 10, \dots$ for triple-, quintuple-, ... quantum experiments). The phase of the receiver is deduced from the second rule. In the triple-quantum excitation, this receiver phase follows the equation $\psi^{rec} = -\Delta p_2 \psi_2 = +4\psi_2$ ($\psi_1 = 0$) for $I = 5/2, 7/2, 9/2$. The phase cycle of a 3QMAS experiment is given in Table 2.2.

A second experiment should be performed with the following phase cycle (Table 2.3) in order to record the imaginary part in t_1 . A shift of 30° ($\pi/2p = 30^\circ$ for triple-quantum excitation) is applied to the phase of the first pulse.

The rest of the acquisition procedure must be adapted to the spectrometer itself (software, hardware). For example, some spectrometers only accept receiver phases of $0^\circ, 90^\circ, 180^\circ, 270^\circ$ forcing the cycles to be adequately

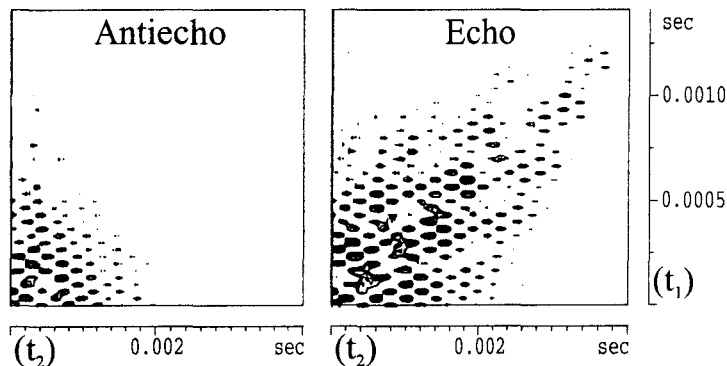


Figure 2.7: ^{27}Al echo and antiecho 2D datasets obtained on a $\text{AlPO}_4 - 14$.

ψ_1	0	...				
ψ_2	0	60	120	180	240	300
ψ^{rec}	0	240	120	0	240	120

Table 2.2: Phase cycle for excitation of triple-quantum coherences (echo and anti-echo pathways) in a two-pulse sequence.

ψ_1	30	...				
ψ_2	0	60	120	180	240	300
ψ^{rec}	0	240	120	0	240	120

Table 2.3: Imaginary part in t_1 for a triple-quantum excitation.

shifted (rule 2). As far as our experiments are concerned, they have been obtained on two different spectrometers: ASX400 (Bruker) and CMX400 (Chemagnetics). Even though these spectrometers differ by their environment, the experiments are performed with similar pulse programs. However, the specific parts (real/imaginary) that we must record, are stored differently. Thus, the processing programs had to be adapted to the software available on each machine (XwinNMR for Bruker and Spinsight for Chemagnetics). The next section will be constrained to giving a general procedure to the two-dimensional processing of MQMAS datasets.

Processing

We have previously observed the important role of the anti-echo pathway. In fact, the processing of the 2D dataset consists in the summation of the relative contributions of the echo and anti-echo signals, S_E and S_A . If the pulse sequence is chosen in order to acquire the two signals $S_E(t_1, t_2)$ and $S_A(t_1, t_2)$ independently, a Fourier transformation in both dimensions leads to two dispersive spectra $S_E(\omega_1, \omega_2)$ and $S_A(\omega_1, \omega_2)$ which must be judiciously summed to get a pure absorption 2D spectrum. However, we rather opted for a method of acquisition that mixes echo and anti-echo contributions (hyper-complex method). Thus, for each increment t_1 , the signal $S_X(t_1, t_2)$ observed is a linear combination of the two mirror-coherence pathways. The phase cycle in Table 2.3 generates the imaginary signal in t_1 and constitutes a second linear combination $S_Y(t_1, t_2)$ of the two pathways.

Consequently, both echo and anti-echo signals can be retrieved according to Eqs. 2.21.

$$\begin{aligned}
S_E(t_1, t_2) &= S_X(t_1, t_2) - iS_Y(t_1, t_2) \\
S_A(t_1, t_2) &= S_X(t_1, t_2) + iS_Y(t_1, t_2)
\end{aligned}
\tag{2.21}$$

Due to the interdependence of t_1 and t_2 , the different sites which appear after Fourier transformation, are aligned along an axis of slope $R(I, p)^{-1}$. Thus, a shearing transformation (pages 336-339 in Ernst et al.¹²) may be applied in order to bring this axis parallel to the horizontal ω_2 -axis. The shearing can be completed either in the frequency domain (ω_1, ω_2) or in the mixed domain (t_1, ω_2) . The latter method which consists in applying a t_1 -dependent first-order correction has been chosen. Mathematically, we multiply the echo and anti-echo signals, after Fourier transformation in t_2 , by an exponential dependent on $\phi(t_1, \omega_2) = R(I, p) \omega_2 t_1$.

$$\begin{aligned}
S'_E(t_{iso}, \omega_2) &= e^{i\phi(t_1, \omega_2)} S_E(t_1, \omega_2) \\
S'_A(t_{iso}, \omega_2) &= e^{-i\phi(t_1, \omega_2)} S_A(t_1, \omega_2)
\end{aligned}
\tag{2.22}$$

Finally, a pure absorption 2D spectrum is obtained by Fourier transforming $S'_E(t_{iso}, \omega_2)$ and $S'_A(t_{iso}, \omega_2)$ with respect to t_{iso} and after a last summation:

$$S(\omega_{iso}, \omega_2) = S'_E(\omega_{iso}, \omega_2) + S'_A(-\omega_{iso}, \omega_2)
\tag{2.23}$$

2D representations are shown in Fig. 2.8 for the different stages of the processing for the echo and anti-echo signals. They illustrate the effect of shearing and Fourier transformations. The phasing of the 2D spectrum may be achieved after the second Fourier transformation. However, it may be helpful to phase the ω_2 -dimension in the mixed domain (t_1, ω_2) by independently phasing the first row ($t_1 = 0$) and applying the phase to the rest of

the rows. Likewise, all kinds of mathematical treatments (apodization, zero filling, etc.) are recommended on condition that one integrates the correct shear factor $R(I, p)$ to the echo and $-R(I, p)$ to the anti-echo.

So far, we have given the essential conditions necessary to acquire a pure absorption spectrum: the anti-echo pathway should be recorded to restore the truncated part of the echo and the method of States yields real and imaginary signals for the second dimension. We also presented some elements of the processing in case the acquisition follows a hypercomplex method. The shearing transformation was also tackled taking into account the special feature of MQMAS experiment, i.e. the shear factor $R(I, p)$. Hence, this section was roughly common to any two-dimensional experiment in liquid- and solid-state NMR.

However, these requirements alone do not ensure that the final 2D spectrum will be perfect. Many parameters that exclusively depend on the MQMAS experiment should be optimized in order to increase the S/N ratio as well as to improve the quality of the spectrum. The latter point is all the more crucial that the method of quantification that we propose in the next chapter is based on the 2D spectrum. Consequently, the next section will be concerned with the many improvements that MQMAS experiment has gone through as well as the optimization of experimental parameters such as pulse lengths, radio frequency power, delays between pulses, etc..

2.2 Optimization of 2D MQMAS

2.2.1 Improvements of MQMAS

The excitation of multiple-quantum transitions had been extensively investigated prior to the discovery of MQMAS. In order to select double-quantum

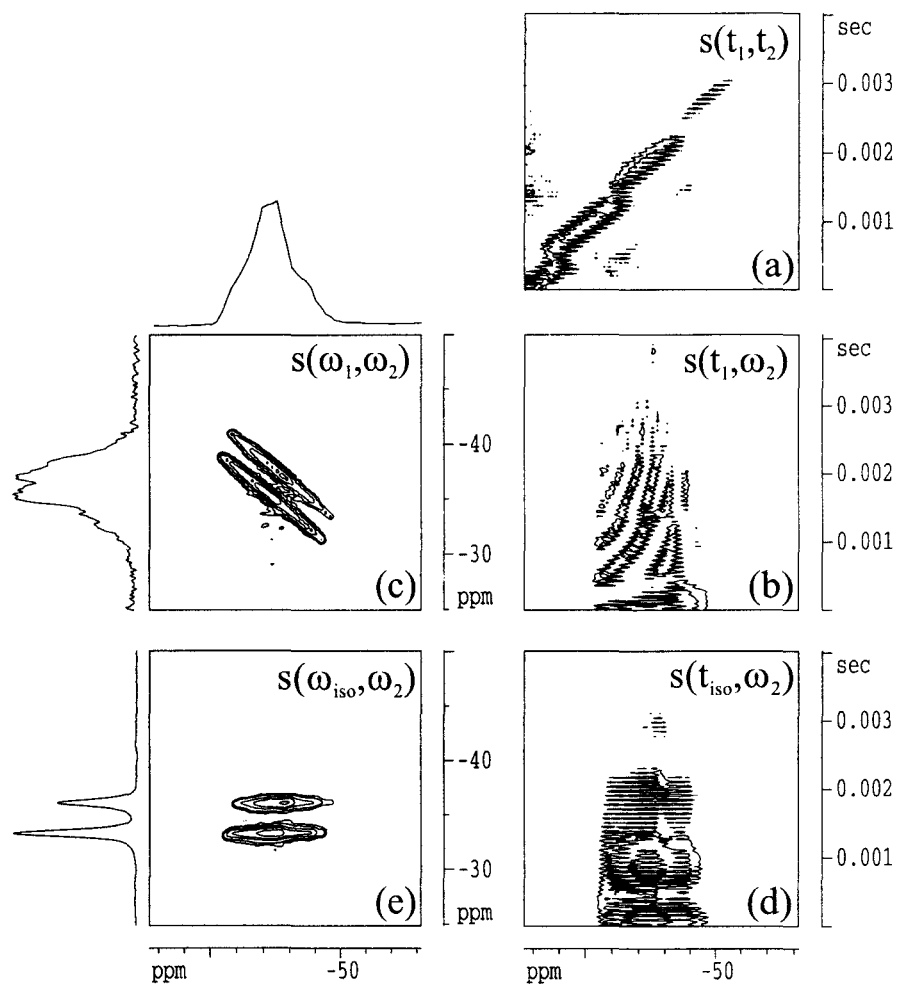


Figure 2.8: Representation of the different steps of the processing of a 2D dataset. (a) 2D dataset in time domain; datasets in mixed domain before (b) and after (d) shearing calculation; final 2D spectra in frequency domain before (c) and after (e) shearing. ^{23}Na 3QMAS dataset obtained with a mixture of sodium sulfate Na_2SO_4 and sodium oxalate $\text{Na}_2\text{C}_2\text{O}_4$.

coherence pathways for spin $I = 1$, Bodenhausen¹⁴ used a three-pulse excitation sequence in which the preparation part was composed of two pulses (Fig. 2.9). Frydman et al. used the same pulse sequence to excite triple quantum transitions in their preliminary work.² Yet, as the MQMAS technique immediately proved to be technically simple, most researchers dealing with the “state of the art” NMR applied themselves to improving the original Frydman’s experiments. It has therefore been exemplified that a single preparation pulse can create a larger amount of multiple-quantum coherences, thus reducing the sequence to two pulses.⁹⁻¹¹ Frydman compared the two sequences to reach the conclusion that the latter was even more efficient. This improvement was followed by many others that we will now describe. However, the variety of MQMAS sequences that have emerged in the last three years makes it difficult to offer a complete review. Some contributions will just be cited and we encourage the reader to refer to the corresponding articles.

Drawbacks of the two-pulse sequence

Let us consider the two-pulse sequence shown in Fig. 2.10 as the basic MQMAS experiment. The processing of 2D datasets requires that both the echo and anti-echo be simultaneously or separately recorded. This does not prevent dispersive parts from being present after Fourier transformation if the two mirror pathways do not contribute with the same efficiency. Therefore, care must be taken to set pulse lengths that identically excite echo and anti-echo coherence pathways. The preparation pulse is supposed to transfer the

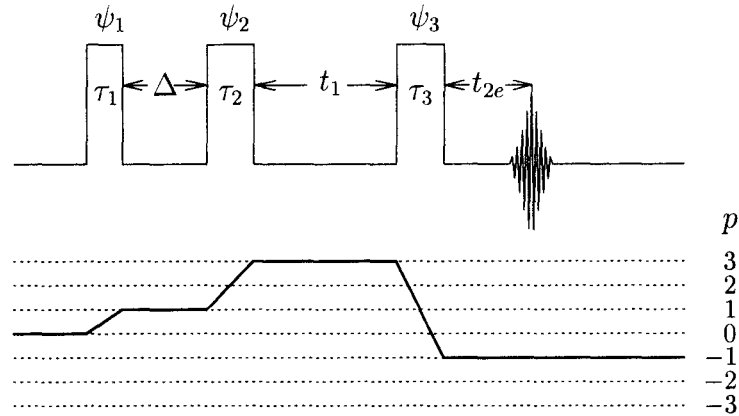


Figure 2.9: Three-pulse sequence originally used by Frydman (echo signal for spin $I > 3/2$). The preparation part is composed of two pulses for the excitation of the triple-quantum coherences. Δ was chosen to be close to the inverse of the quadrupolar frequency $\Delta \simeq 1/\nu_Q$.

magnetization from equilibrium (along \mathbf{B}_0) to the triple-quantum coherences $p = \pm 3$. The jumps associated with this transfer are identical in absolute terms and equal to $|\Delta p| = 3$. Therefore, the first pulse should be optimized to create a maximum of triple-quantum coherences, regardless of the relative proportion of echo and anti-echo coherences. On the other hand, the mixing pulse must be set so that the transfer from the triple-quantum coherences to the observable coherence level $p = -1$ does not favour one pathway to the detriment of the symmetrical one. Therein lies the difficulty of the method that involves two different jumps $\Delta p = +2$ and $\Delta p = -4$ between the coherence levels. To illustrate this, we have compared the total echo and antiecho signal intensities for a spin $3/2$ as a function of the length of the second pulse p_2 for two rf fields (Fig. 2.11-a,b)). The ^{23}Na 3QMAS data were collected at 105.8 MHz on a Na_2SO_4 sample using phase cycles that selected the echo and the antiecho pathways. The length of the first pulse

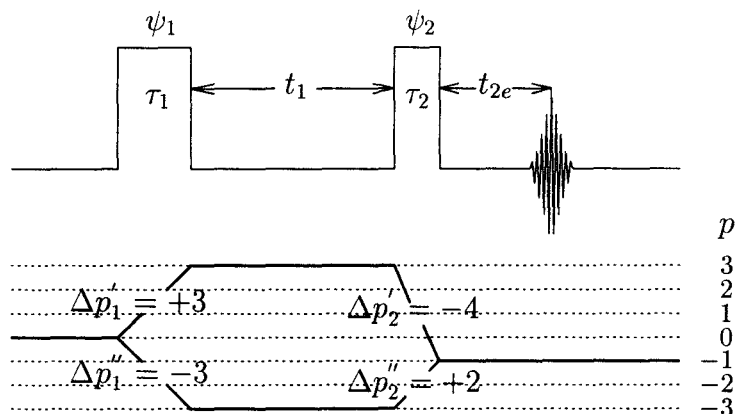


Figure 2.10: Two-pulse triple-quantum MAS sequence. A single pulse is revealed sufficient for the triple-quantum excitation.

was previously optimized to excite a maximum amount of triple-quantum coherences. The curves clearly show the dependency of triple- to single-quantum coherence transfer processes on both τ_2 and the rf field. Moreover, the maximum of efficiency measured on a powder for the echo does not coincide with the maximum for the antiecho. Therefore, the pulse length τ_2 that corresponds to the crossing point, should be preferred to the maximum of the echo in order to decrease the dispersion even if the loss of efficiency in the 3Q conversion process might be significant. It has also been proved that the position of the crossing point was dependent of the quadrupolar strength of the site, especially for spins larger than 3/2, thus making the optimization of this pulse impossible when the samples enclose different sites within a wide range of C_Q . We have observed the same kind of behavior for the triple-quantum excitation of spin 5/2 (Fig. 2.11-c,d). Several authors have shown that the equalization of efficiencies becomes increasingly difficult for higher-order multiple-quantum experiments.¹⁵

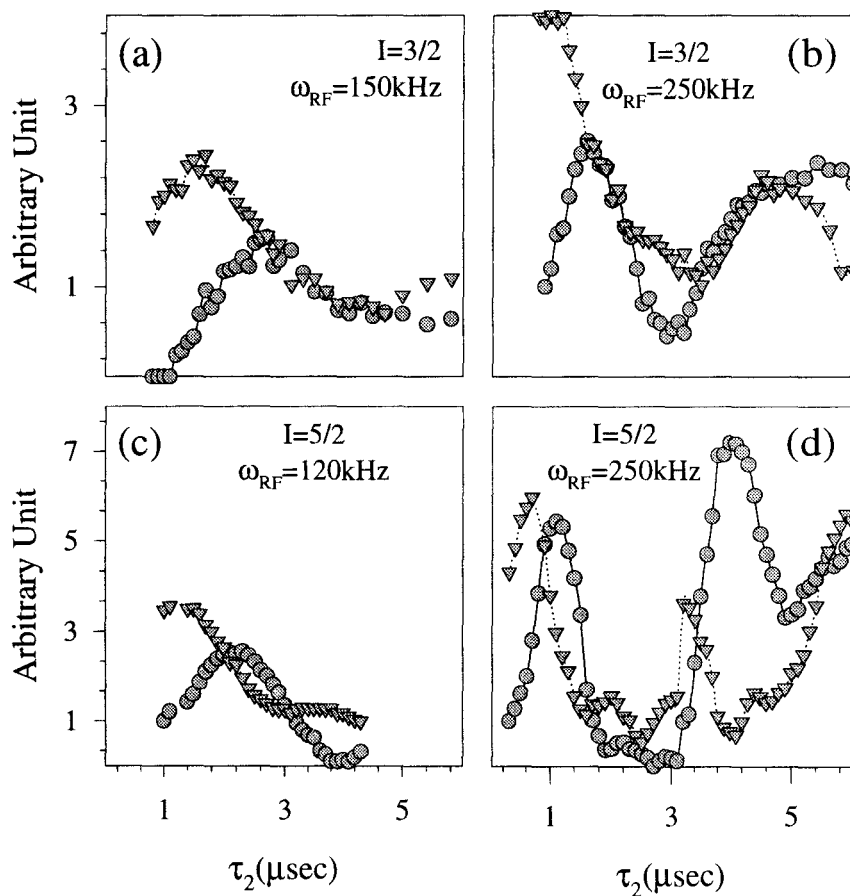


Figure 2.11: Variation of the efficiency of triple-quantum conversion as a function of the pulse length τ_2 using the two-pulse sequence for spin 3/2 (^{23}Na in Na_2SO_4) and spin 5/2 (^{27}Al in zeolite Y sample) at two rf fields. Echo and antiecho coherence pathways were recording separately using adequate phase cycles.

Z-Filtering in MQMAS

The major problem of the 2D MQMAS experiment remains that the second pulse should transfer the magnetization for both mirror-coherence pathways ($\pm p$) with equal efficiency for each crystallite. For some multiple site samples with similar C_Q s, the two pulse sequence yields fairly good 2D spectra, especially with spins $3/2$. But most of the time, dispersive parts arise for species with extreme C_Q s.

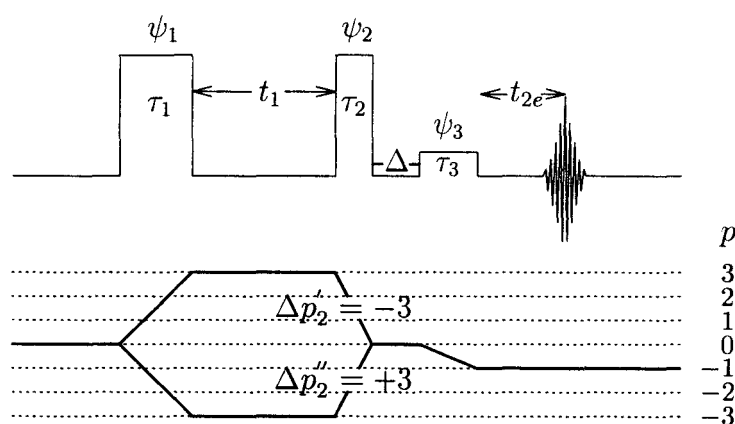


Figure 2.12: Three-pulse experiment including a z -filter to render mirror coherence pathways symmetrical

An alternative scheme for the two-pulse sequence can be found using an additional z -filter.¹⁶ This method was employed in DAS to store the magnetization along B_0 while the orientation of the rotor was switched to the magic angle for a first-order averaging during acquisition.¹⁷ Brown et al.¹⁸ have described a complex MQMAS pulse sequence that includes the z -filter principle. Later, Amoureux et al.¹⁹ adapted the z -filter to the original two-pulse experiment as shown in Fig. 2.12. The aim of this modification was to

make the two mirror-pathways symmetrical after the triple-quantum evolution. Thus, the second pulse transfers the signal from coherence levels $\pm p$ to the level $p = 0$ so that the jump is unique and equal to $|\Delta p| = 3$. We will see in section 2.2.2 that when using the z -filter approach, the experimental optimization of τ_2 is grandly simplified. Another advantage is that the equal contribution of the echo and antiecho pathways $(0, \pm p, 0, -1)$ is achieved regardless of the spin number and the order of the selected coherences, whatever the pulse length τ_2 . Hence, the choice of τ_2 is not as critical as in the two-pulse sequence since a bad setting will just result in a slightly reduced S/N ratio. The main drawback is probably that the efficiency of the three-pulse method is slightly lower than in the two-pulse one because of the extra z -filter pulse. Nevertheless, we considered that the quality of the MQMAS spectra was of higher importance than the small increase in time of the data collection. The spectra that we present here have been exclusively recorded with this z -filter sequence and readers should refer to section 2.2.2 which concentrates on its optimization.

Alternative Pulse Sequences

Taking advantage of the evolution (1990's) of the 2D DAS technique,²⁰ alternative pulse sequences have been proposed for MQMAS.^{10, 18, 21} Yet, among these several variations, we have decided to focus on a few of them that we think may have a greater impact on the NMR community.

It has previously been shown that the truncation of the echo signal for short t_1 leads to dispersive parts on the 2D spectrum, in the frequency domain. At that time, we got around the problem by acquiring an amplitude-modulated signal where the mirror-coherence pathway (antiecho) provided the missing part of the echo. However, the acquisition of the whole echo

even for short t_1 would keep us from selecting both pathways. The sequence shown in Fig. 2.13 includes an additional delay τ , followed by a selective π -pulse, that shifts the echo signal in the positive time domain t_2 . Consequently, even when the delay t_1 is minimum, the echo is not truncated on its left side provided that τ is of sufficient length (typically half the width of the echo). Afterwards, the echo moves forward in t_2 as t_1 increases. Massiot et al.¹⁰ gave the possible phase cycles for the shifted-echo sequence and for spins $3/2$ and $5/2$. Real and imaginary parts in t_1 can be accessed using the method of States. In this class of experiments where only one pathway is selected at a time, the signal is said to be phase-modulated. It must be pointed out that provided an adequate phase cycle, the whole antiecho may be separately recorded in the time domain t_2 . However, this shifted antiecho experiment requires a longer delay τ since the antiecho moves backward in t_2 . A shifted-echo experiment will therefore generally be preferred to gain a better S/N ratio.

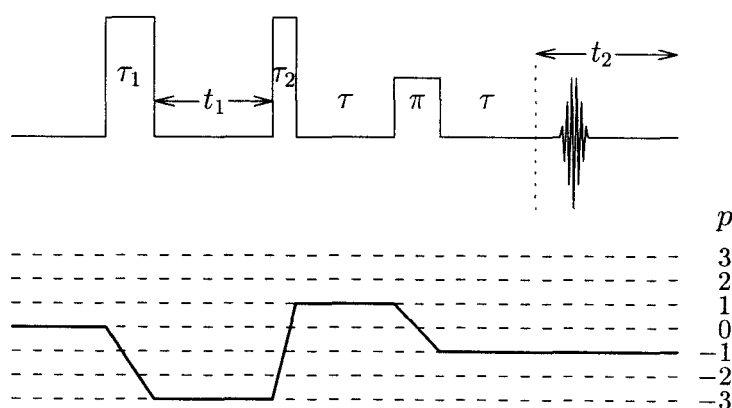


Figure 2.13: Three-pulse shifted-echo sequence for $I = 3/2$

Using the equations that allow for the hypercomplex acquisition mode,

both echo and antiecho pathways can still be selected simultaneously to obtain an amplitude-modulated whole-echo signal. In such a case, the evolution in t_2 stems from a linear combination of the two pathways that can be retrieved during the processing as explained in section 2.1.3. The acquisition of the antiecho may appear useless since the whole-echo is present in the acquisition domain. However, the main purpose is here to increase the S/N ratio. Grandinetti et al.²⁰ measured the S/N ratio of 2D DAS NMR spectra obtained with various DAS pulse sequences. They noticed that the hypercomplex shifted-echo approach could provide up to a factor of $\sqrt{2}$ enhancement in sensitivity over the phase-modulated shifted-echo method. Thus, Massiot et al. adapted this acquisition mode to the triple-quantum excitation in their paper,¹⁰ in which pulse sequences are given. Of course, relaxation phenomena may be significant during the delays τ since they must be set long enough to allow for the acquisition of the whole antiecho.

Up to now, no comparison of these different acquisition procedures has been made for MQMAS. Thus, it is difficult to recommend one over the others. Some of the methods grandly improve the quality of the spectra but generally require one or more additional pulses that reduce the S/N ratio through relaxation. As far as we are concerned, we think that the z -filter approach is essential for the reasons that were listed earlier. Furthermore, we also opted for an amplitude-modulated (hypercomplex) acquisition.

Split- t_1 Experiments

With previous methods, the observation of an isotropic dimension is easily obtained when a mathematical calculation (shearing) is performed during the processing of a spectrum. Yet, Brown et al.²² suggested that this transformation could lead to distorted lineshapes. Thus, they designed an ingenious

MQMAS sequence that took into account the shearing ratio $R(I, p)$ during the acquisition rendering the mathematical shearing process useless. Fig. 2.14 shows this pulse sequence as well as the coherence transfer pathway diagram for the acquisition of a split- t_1 experiment (spin $3/2$). The t_1 -period is split into triple- and single-quantum evolution periods in the ratio of $R(I, p)$. This allows for the refocusing of the quadrupolar anisotropy to always occur at $t_2 = 0$ even for long t_1 -delays. Therefore, Fourier transformations in both dimensions yield 2D spectra for which the different sites are spread out along the F_2 -axis without the need for a shearing. The theoretical evidence can be found in Brown et al.¹⁸

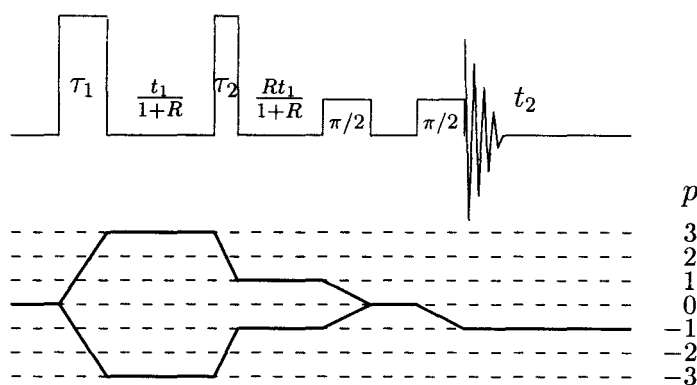


Figure 2.14: Pulse sequence for the split- t_1 3QMAS experiment

Apart from reducing hypothetical line distortions that may arise from the shearing process, this method which is referred to as the split- t_1 method, increases the overall sensitivity of the MQMAS experiment (compared to a shifted-echo experiment). Indeed, since the echo does not move forward in t_2 -domain, the length of the acquisition period, and thus the introduction of

noise, can be set to a minimum. Furthermore, the optimization of the S/N ratio during processing is simplified in comparison to simple shifted-echo methods as weighting functions can be t_1 -independent. Other implementations have been proposed by the same authors (amplitude-modulated z -filtered split- t_1) and further details may be found in the references previously cited.

Rotor Synchronization

The study of triple-quantum excitations upon other anisotropic interactions (especially CSA) reveals that the effects are magnified by a factor of 3 and result in an increase of the number of spinning sidebands in the F_1 dimension. Though, no additional spinning sidebands arise in the MAS dimension F_2 .

Although several authors analyzed spinning sidebands and extracted important information about the nature and size of the interactions,²³⁻²⁵ the presence of spinning sidebands is generally bothersome for two reasons. First of all, it causes the spreading of the signal intensity of the centerbands over spinning sidebands and thus decreases the S/N ratio. Secondly, it increases the risk of overlapping between the bands of different origins. Consequently, the centerband lineshape is distorted and multiple acquisition of 2D datasets may be necessary at different spinning speeds to avoid a misinterpretation of the results (see 3QMAS spectra of sillimanite in Massiot²⁶). In this case, the acquisition time may be substantially increased.

Massiot proposed a method of rotor-synchronization which offered as main advantage the reduction of the experimental time by a factor of about 5.²⁶ The principle is to set the spectral window SW_1 of the second dimension equal to the spinning speed so that sidebands are folded back onto the centerband. Of course, the speed must be high enough to include all the sites on the spectrum. Our standard 4mm probe allows for rotor speeds up to

15 kHz which revealed to be the minimum for rotor-synchronized 3QMAS spectra of zeolite samples, on a 400 MHz spectrometer. The other advantage of this technique is that the rotor-synchronized spectrum can be seen as an approximation of the infinite-spinning-rate acquisition with a gain of sensitivity for the centerbands. Our quantification based on simulations was therefore rendered much easier since no spinning sidebands had to be taken into account in the calculation.

Experimentally, the increment Δt_1 is deduced from Eq. 2.24 and values are typically in the order of $70\mu sec$.

$$\Delta t_1 = \frac{2\pi}{\omega_r} \quad (2.24)$$

where ω_r stands for the rotor spinning speed.

We have just given the main contributions that led to a significant improvement of the MQMAS experiment. We had to make a selection amongst the numerous articles that were published, keeping in mind that our goal was to get the best MQMAS spectrum possible (pure absorption, optimized S/N ratio, etc.) in aim of a subsequent quantification.

Other modifications of the MQMAS sequence would have deserved a special attention.²⁷⁻²⁹ The original aspects of these works are mainly found in the number of pulses that are used in the sequences and the phase cycles that follow. Yet, we made no mention of the experimental conditions that should go with these sequences and only took notice that the excitation and conversion processes were more effective with strong rf fields, whatever the pulse sequence that we have presented so far. The next section will be devoted to the optimization of the experimental parameters that should always precede the acquisition of the 2D MQMAS spectrum itself.

2.2.2 Determination of Experimental Parameters

We will limit our explanations to the method that we finally used for acquiring 3QMAS spectra. Indeed, we found the amplitude-modulated MQMAS experiment, in association with an additional z -filter pulse, to be the best compromise between quality of the spectrum and sensitivity. Moreover, its implementation as well as the determination of its optimum parameters prove to be much easier than for most of the techniques previously cited.

phase cycle considerations

Let us recall that the two first pulses must be as powerful as possible to excite with a good efficiency multiple-quantum transitions whereas the third pulse is a selective 90° pulse that prevents other transitions (multiple-quantum and satellite) from transferring into the observable quantum level, when possible (see Fig. 2.12). Echo and antiecho pathways are selected simultaneously using the method of States and they are retrieved during processing. This keeps the number of phases applied to either the first pulse or the second pulse, to a minimum of $N_1 = 6$ for 3Q excitation ($N_1 = 2p$ for $p=5,7,9$ quantum excitations, see rule 3 on page 73). The z -filter pulse needs also to be phase cycled to avoid contributions from non-desired pathways. We have performed a 3QMAS experiment on a sample of aluminophosphate $\text{AlPO}_4 - 14$, using a 6-phase cycle ($N_1 = 6$) for triple-quantum selection but without cycling the z -filter pulse ($N_2 = 1$) (Fig. 2.16-b). The spectrum should be compared to the one (Fig. 2.16-a) we obtained with the same sample and under the same experimental conditions except that a 4-phase cycle was applied to the last pulse ($N_2 = 4$). This result clearly demonstrates that a selective 90° pulse can not single handedly get rid of parasitic signals. In this case, the use of a cycling seems essential.

Figs. 2.15 exhibit the different pathways that may contribute to the acquisition signal when the number N_2 of phases is respectively 1, 2 and 4 for a spin 5/2. For the sake of simplifying the figures, we did not consider jumps Δp greater than five. When N_2 was set to the minimum ($N_2 = 1$), none of the coherence order pathways are removed by phase cycling. Therefore, even if pulse lengths are set for a triple-quantum excitation, other coherences are present on the spectrum. As N_2 is increased, some pathways totally disappear, reducing the risk of distorted lineshapes. Theoretically, the number of phases should be chosen such that it fulfills the Eq. 2.25 to make sure that only the central transition is transferred.

$$N_2 > 2I \quad (2.25)$$

For spins 3/2, $N_2 = 4$ ensures that only the desired pathways (solid lines) are selected. For spins 5/2, even if a minimum of 6 phases is theoretically required, we obtained identical 2D spectra for 2 and 4 phases (not shown). This tends to prove that when each pulse is correctly optimized, the number N_2 can be reduced, especially if the z -filter time is long enough (1 or 2 rotor cycles). As far as our sequence is concerned, we opted for a 24 phase cycle with $N_1 = 6$ and $N_2 = 4$ as given in table 2.4.

Pulse Length Optimization

The previous section emphasized the fact that pulse length optimization is much more critical than the choice of the phase cycle. Therefore, care should be taken at this stage of the experiment if one wants to obtain a nice MQMAS spectrum. To optimize the pulse lengths, one can adopt either a theoretical

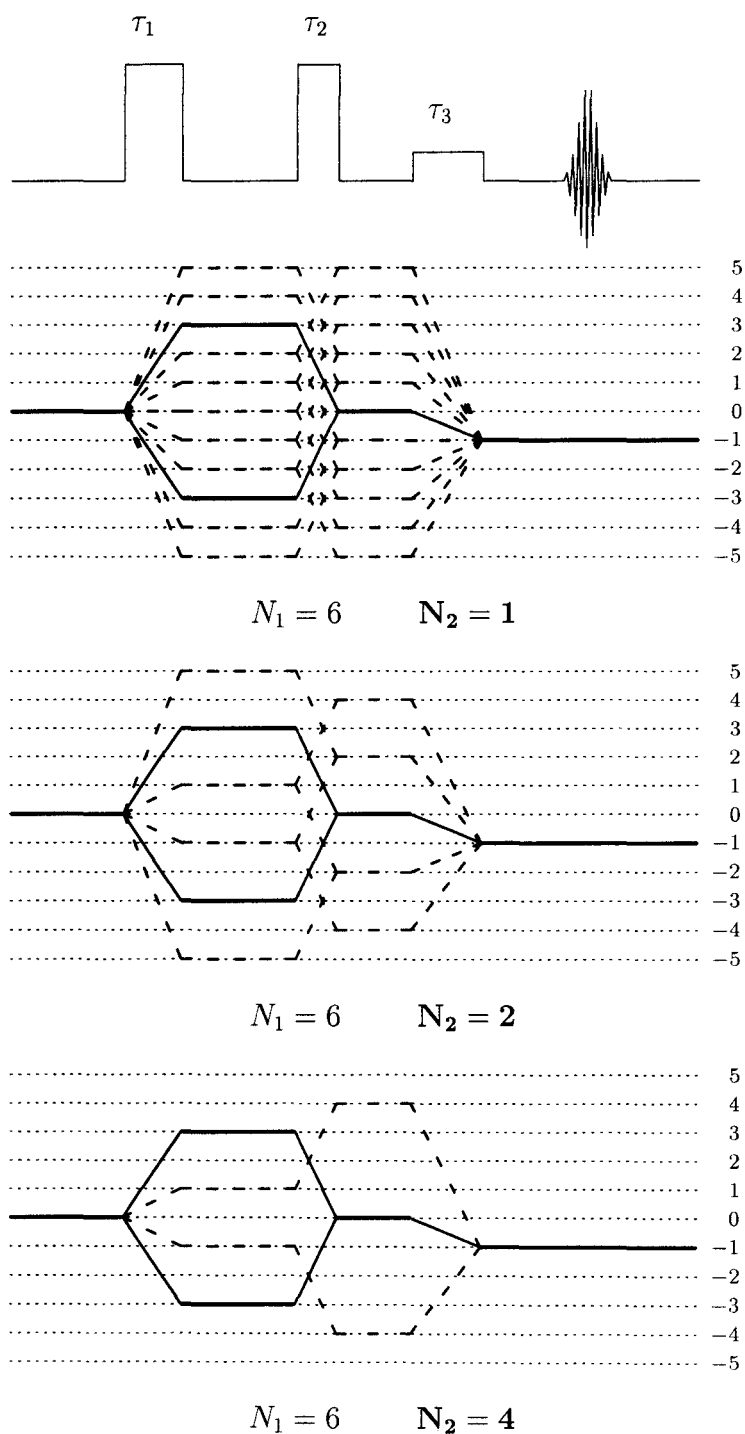


Figure 2.15: Selected pathways in a z -filter sequence as a function of the number N_2 of phases applied to the third pulse, for a spin $5/2$. N_1 : number of phases for the first or second hard pulse. N_2 number of phases for the third pulse (selective 90°).

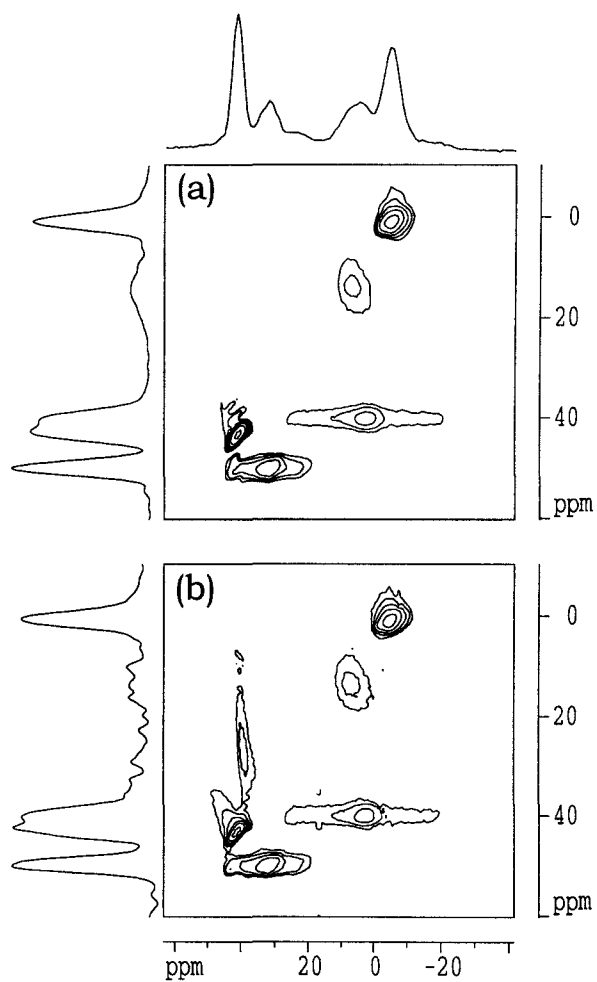


Figure 2.16: ^{27}Al 3QMAS spectra of $\text{AlPO}_4 - 14$ acquired with $N_2 = 4$ (a) and $N_2 = 1$ (b).

ψ_1	0					
ψ_2	0	60	120	180	240	300
ϕ_3	0					
	90					
	180					
	270					
ψ^{rec}	0	240	120	0	240	120
	90	330	210	90	330	210
	180	60	300	180	60	300
	270	150	30	270	150	30

Table 2.4: Phase cycle for the excitation of triple-quantum coherences (echo and anti-echo) in a three-pulse z -filter sequence. Phases may need to be shifted to set receiver phases to a multiple of 90° .

or an experimental approach. They both lead to fairly good 2D datasets. Both of these approaches will now be reviewed.

Some authors have calculated the optimum experimental conditions for MQMAS limiting their investigations to the original two-pulse sequence.^{15, 30} Later, Amoureux et al. fully described the MQMAS technique, showing the advantages of z -filter sequence especially for higher-order multiple-quantum excitations.³¹ They explained that the triple-quantum excitation pulse is identical for both two- and three-pulse sequences (c.a., 240° for $3/2$, 180° for $5/2$) whereas the conversion pulse is slightly different. Table 2.5 gives the optimal θ_1 and θ_2 flip angles for a triple-quantum excitation of spins $3/2$ and $5/2$ using our three-pulse sequence. Flip angles are directly functions of the rf amplitude ω_{rf} and pulse lengths τ_1 and τ_2 . The theoretical efficiencies of excitation and conversion processes are also included in the table. As mentioned by several authors, the conversion (3Q to 0Q) is an inefficient process that limits the sensitivity of the MQMAS experiment.

I	pulse	θ	Eff
3/2	1	240	1.5
	2	80	0.3
5/2	1	180	1.5
	2	55	0.3

Table 2.5: Optimum flip-angles and corresponding relative efficiencies (Eff) for $\omega_Q/\omega_{rf} = 1.25$. Eff=1 corresponds to the central transition signal observed with a perfectly selective 90° pulse.

The optimization of the third pulse requires special attention as it was previously said that it should be a selective 90° pulse. The power of the

third pulse must be low in order to selectively transfer the signal from $0Q$ states to the observable $-1Q$. Indeed, a strong power may transfer other coherences that are not fully averaged out by phase cycling as well as single-quantum transitions different from the central one. On the other hand, if the rf amplitude is not big enough, the excitation may be uneven and lead to distortions. Therefore, we consider that the rf field should be equal to the spectral area to assure at least a good transfer. For instance, for ^{27}Al nuclei, the sites are spread over a range of about 100 ppm which suggests the use of a rf power bigger than 10 kHz.

Even if these theoretical flip angles yield fairly good 2D acquisitions, we think that the optimization of pulse lengths should always be checked experimentally. Indeed, the estimation of the rf power is sometimes imprecise rendering the theoretical setting inaccurate. The experimental optimization enables us to avoid making any assumption on this parameter. Moreover, the calculation of the optimized pulse lengths is performed using square rf pulses whereas real pulses are strongly affected by the inhomogeneity of the rf field and by rising and falling times which are all the more important that the rf power is high.

First, the maximum rf power which is about 150 kHz for most standard 4mm probes, must be used for the excitation and the conversion pulses. As far as our experiments were concerned, they were performed with a probe specially developed by Bruker for the MQMAS technique. We could obtain rf fields of up to 350 kHz that yield much higher sensitivity. At this frequency, the hard pulses are not rectangular pulses anymore as they must be very short (around $0.3\mu\text{sec}$ for τ_2) for an optimized transfer. Moreover, we noticed that an arcing effect occurred for an $\omega_{rf} > 300$ kHz which would have resulted in an inhomogeneous MQMAS excitation. Therefore, for most experiments, we

opted for a slightly weaker rf field ($250 \text{ kHz} < \omega_{rf} < 300 \text{ kHz}$).

Second, our experimental optimization takes advantage of the fact that the signal is cosine-amplitude modulated in t_1 , for the z -filter MQMAS experiment. The consequence of this is that the first row of the 2D dataset, for which the evolution time t_1 is null, is equivalent to the 1D MAS spectrum since there is no signal dephasing resulting from the $3Q$ -evolution. Therefore, the determination of the optimal parameters can be performed using the phase cycle of the 2D multiple-quantum MAS experiment, but without incrementing the time t_1 .

A rough estimate of the rf power may be useful to determine the approximate values of τ_1 and τ_2 from the theoretical calculation (Table 2.5). Indeed, such set of values can be a good starting point for the experimental optimization. Finally, each parameter (τ_1 , τ_2 and τ_3) can be independently incremented while the others are fixed and the optimum value coincides with the one that leads to the maximum of amplitude for the first row signal.

Figs. 2.17 shows the result of such experimental optimization for τ_1 and τ_2 using the z -filter sequence and two rf amplitudes (for τ_2 only). A few observations should be made from these figures. The most important point is undoubtedly that the optimum values for any rf field are easily deduced from the curves. Then, we notice that the first top corresponds to the maximum of efficiency such that pulses are kept as short as possible. Finally, we have the experimental evidence that high rf power yields better S/N ratio.

Optimization of time delays

Using the z -filter pulse sequence, the optimization of the pulse lengths is not as critical as in the two-pulse sequence. However, a bad setting would result in a poor S/N ratio, yielding much longer experimental durations.

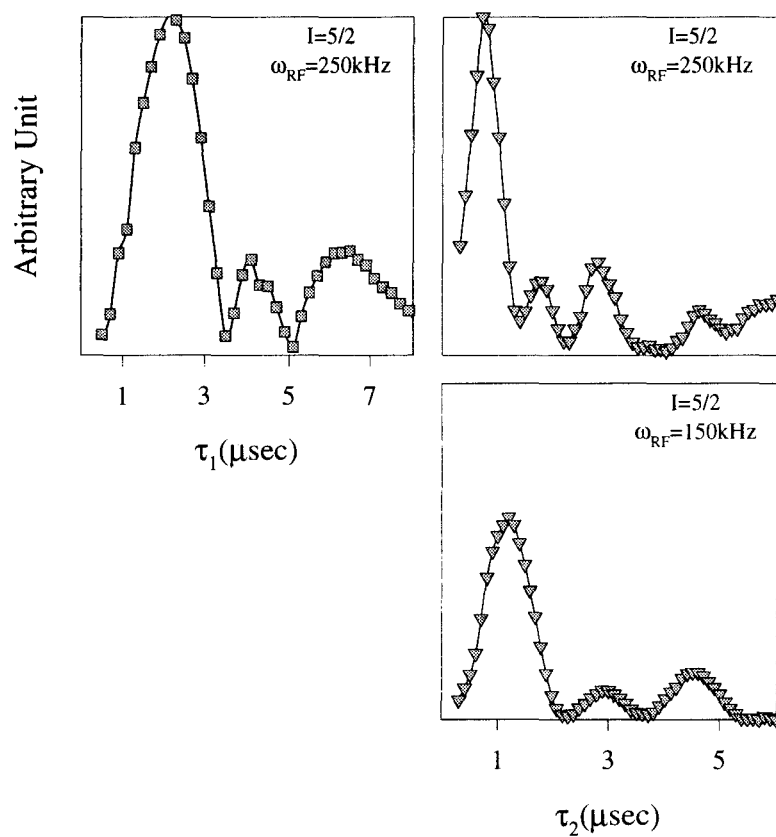


Figure 2.17: Experimental optimization of the pulse lengths τ_1 and τ_2 using the z -filter sequence. The curves were obtained by integration of the tetrahedral ^{27}Al resonance in a zeolite Y sample. The optimization of the second pulse τ_2 was performed at two rf power to show the influence of this parameter.

Other parameters, e.g. pulse delays that are present in the z -filter sequence, should also be taken into in the optimization procedure.

First, the delay between two acquisitions should be chosen such that the spins are brought back to the equilibrium. In single-pulse experiments, we generally check the relaxation delay that spread over a wide range of time depending on the nucleus. In the case of the multiple-quantum MAS experiment, we observed that for certain nuclei, the relaxation time was longer than in the single-pulse MAS experiment. A too short delay would not only further decrease the S/N ratio but the intensity for such sites would be underestimated. To gain good results for our quantification procedure, we needed to reduce to a minimum the experimental constraints (especially relaxation). Consequently, we have always checked this delay using the same procedure than for the pulse length optimization. This sometimes led us to use relaxation times that were 10 times longer than in the MAS experiment, significantly increasing the experimental duration but multiplying the S/N ratio by a factor of about 4, for the same number of scans.

In contrast to the delay t_1 which depends on the type of experiment that one wants to perform (rotor-synchronization or not) rather than on a specific optimization, the time between the second and third pulses must be carefully chosen. Indeed, even though the second pulse is supposed to transfer the magnetization along the static field, some transverse magnetization may still be present leading to parasitic signals. Therefore, the delay should be long enough to ensure that this transverse magnetization disappears through relaxation. We think that a few hundred of μsec is sufficient to prevent other coherence orders from appearing on the spectrum. Some authors³² have recommended the use of a multiple of $2\pi/\omega_r$ in order to keep a good phase for the sidebands along F_1 when t_1 -rotor synchronization is not used.

In this section, we have dealt with several aspects of how to optimize MQMAS experiments. The most important steps to take into account have been presented with an emphasis on those that we used in the experimental section (Chapter 4). Furthermore, a procedure for the experimental optimization of MQMAS was given for the z -filter MQMAS sequence. It is obvious from the few 3QMAS spectra that have been shown so far, that this technique provides an incomparable facility to know the number of crystallographically non-equivalent sites present in a sample. The ease with which spectra are obtained put MQMAS far beyond other high-resolution second-order averaging techniques (DOR, DAS). The next section has been written with the aim to demonstrate that MQMAS technique is far more than another high-resolution experiment.

2.3 Further on with MQMAS

Chapter 1 explained that the Larmor frequency, and thus the position of a lineshape on the spectrum, is linked to the magnitude of the static magnetic field. Hence, the use of frequency units makes the comparison of spectra difficult when they are acquired at different fields. Consequently, it is better to manipulate 1D and 2D spectra in normalized units (ppm). We will therefore explain how MQMAS spectra should be scaled especially after a shearing transformation. If the determination of the number of sites is the main purpose of MQMAS, further information (quadrupolar parameters) can be deduced from a 2D spectrum on condition that the second dimension is properly scaled. The quantification of MQMAS spectra is also based on a correct scaling.

Several authors have already taken advantage of the incomparable versabil-

ity of NMR to introduce new techniques that use the potential of MQMAS for high-resolution. As we have contributed to these developments, we will give an overview of what has been achieved so far as well as an insight into the future of MQMAS. All these new pulse sequences can be divided in two parts: a multiple-quantum excitation leading to a high-resolved dimension and another spin manipulation (CP, REDOR, etc.) that provides an additional information.

2.3.1 Scaling spectra

before shearing

It has been shown that the projection of a 2D p -quantum MAS spectrum before shearing onto the vertical axis reflect the evolution of the p -Q coherence orders. Consequently, the shift ω_1 on the second dimension, of the centre of gravity of a line is magnified in comparison with the shift ω_2 on the MAS dimension. ω_2 and ω_1 are functions of the actual chemical shift of the site δ_{CS} and of a quadrupolar induced shift $\omega_{QIS}(p)$ that differs on both dimensions (Eqs. 2.26 and 2.27).

$$\omega_2 = \omega_0 \delta_{CS} + \omega^{QIS}(-1) \quad (2.26)$$

$$\omega_1 = -p\omega_0 \delta_{CS} + \omega^{QIS}(p) \quad (2.27)$$

$\omega^{QIS}(-1)$ and $\omega^{QIS}(p)$ are given in Eq. 2.28 which is deduced from Eq. 2.11 after substituting p to m .

$$\omega^{QIS}(p) = \frac{3p}{10} \frac{1}{\omega_0} C_Q^2 \left(1 + \frac{\eta^2}{3} \right) \frac{[4I(I+1) - 3p^2]}{[4I(2I-1)]^2} \quad (2.28)$$

As we said earlier, it is common to introduce the Larmor frequency in order to remove the static field dependency. In single-pulse experiments as well as in the MAS dimension of MQMAS experiments, the shift δ expressed in ppm is simply

$$\delta_2(ppm) = \frac{\omega_2}{\omega_0}. \quad (2.29)$$

In such a case, the shift $\delta_2(ppm)$ is composed of two terms: the actual chemical shift δ_{CS} and the quadrupolar induced shift $\delta_{QIS}(-1)$. The latter is in inverse proportion to ω_0^2 favouring the use of strong static fields to decrease the difference between the position of the center of gravity of the band and the actual chemical shift δ_{CS} . Unlike δ_{QIS} however, δ_{CS} should be independent of the experimental features (magnitude of the static field, single- or multiple-quantum excitations, etc.) as it allows the sites to be classified regardless of the strength of their quadrupolar interactions.

Considering Eq. 2.27, it comes out that the virtual Larmor frequency along the MQ dimension, must also be magnified by a factor of $-p$ such that the shifts δ_1 and δ_2 remain the sum of the same isotropic chemical shift δ_{CS} and a quadrupolar induced shift δ_{QIS} that differs on both dimensions. Shifts are given in ppm, in Eqs. 2.30 and 2.31 for MAS and MQMAS dimensions, respectively.

$$\delta_2 = \delta_{CS} - \frac{3}{10}C_Q^2 \left(1 + \frac{\eta^2}{3}\right) \frac{[4I(I+1) - 3]}{[4I(2I-1)\omega_0]^2} \cdot 10^6 \quad (2.30)$$

$$\delta_1 = \delta_{CS} - \frac{3}{10}C_Q^2 \left(1 + \frac{\eta^2}{3}\right) \frac{[4I(I+1) - 3p^2]}{[4I(2I-1)\omega_0]^2} \cdot 10^6 \quad (2.31)$$

after shearing

Ernst et al.¹² explicitly give the effect of the shearing upon the scaling of 2D spectra. They write (pp. 337-339) that the shearing transformation shifts the peaks that henceforth appear at frequency ω_{iso} following Eq. 2.32 (after shearing, the vertical axis will now be referred to as the isotropic axis).

$$\omega_{iso} = \frac{1}{1 + |R|}(\omega_1 + |R|\omega_2) \quad (2.32)$$

By replacing ω_1 and ω_2 in the previous equation by their respective mathematical expression (Eqs. 2.26, 2.27), we find that the isotropic frequency in the sheared dimension can be written

$$\omega_{iso} = \left(\frac{|R| - p}{|R| + 1} \right) \omega_0 \left\{ \delta_{CS} + \frac{3}{17} C_Q^2 \left(1 + \frac{\eta^2}{3} \right) \frac{[4I(I+1) - 3p^2]}{[4I(2I-1)\omega_0]^2} \right\}. \quad (2.33)$$

Again this time, a virtual Larmor frequency $(|R| - p)\omega_0/(|R| + 1)$ should be defined to scale the isotropic axis. In such a case, the shift δ_{iso} takes the following form, when expressed in ppm:

$$\delta_{iso} = \delta_{CS} + \frac{3}{17} C_Q^2 \left(1 + \frac{\eta^2}{3} \right) \frac{[4I(I+1) - 3p^2]}{[4I(2I-1)\omega_0]^2} \cdot 10^6. \quad (2.34)$$

The use of normalized scales in association with the definition of new Larmor frequencies is grandly justified if we compare the previous equations giving the chemical shifts in ppm onto the three axes. Let us consider the case of a site for which the quadrupolar interaction is null ($C_Q = 0$). The quadrupolar induced shift terms should be removed from the equations so that only the isotropic chemical shift δ_{CS} remains. Therefore, a projection of the peak onto any of the three axes ($\delta_2, \delta_1, \delta_{iso}$) would allow to determine

directly this value. However, the quadrupolar interaction is never negligible and an additional calculation is necessary to deduce quadrupolar parameters from MQMAS spectra. The next section is devoted to this purpose and should help understand 2D spectra.

Whereas the previous scaling has been adopted as a standard by most researchers, it reveals inaccurate when spinning-sidebands along the second dimension are examined. We remind that if the spectral window is large in the MQMAS dimension, many sidebands arise partly due to the fact that most interactions are magnified by a factor of p . According to the rules that we imposed for the scaling and before any shearing transformation is applied, spinning sidebands are separated by ω_r along ω_1 and ω_2 . But, after shearing, Eq. 2.32 leads to a frequency spacing in Hertz of $\omega_r^{iso} = \omega_r/(|R|+1)$ between spinning sidebands along the isotropic dimension. In order to keep a sideband spacing of ω_r after shearing, the scaling of the isotropic axis should follow the Eq. 2.35.

$$\omega_{iso} = (\omega_1 + |R|\omega_2) \quad (2.35)$$

Nevertheless, this alternative convention does not alter relations when expressed in ppm if the virtual Larmor frequency along δ_{iso} is $(|R| - p)\omega_0$. Only expressions given previously in Hertz along the isotropic axis must be multiplied by a factor $(1 + |R|)$.

2.3.2 Determination of Quadrupolar Parameters

The previous scaling remains unnecessary if the use of the MQMAS experiment was only motivated by the determination of the number of nonequivalent sites. Indeed, the isotropic projection of the 2D MQMAS spectrum should

help understand the often ambiguous 1D MAS spectrum. But, the scaling of the isotropic dimension of an MQMAS spectrum gives access to additional information such as the quadrupolar parameters (C_Q) or the actual chemical shift (δ_{CS}) that reflect the local environment of the nucleus.

According to Eqs. 2.30 and 2.34, we find that the shifts on both dimensions differ by their quadrupolar induced shifts δ_{QIS} and δ_{QIS}^{iso} on δ_2 and δ_{iso} axes, respectively. In fact, both quadrupolar induced shifts are proportional following Eq. 2.36.

$$\delta_{QIS}^{iso}(I, C_Q, \eta) = -\frac{10}{17}\delta_{QIS}(I, C_Q, \eta) \quad (2.36)$$

Therefore, a QIS axis can be added on the 2D spectrum to scale the magnitude of the quadrupolar interaction. The slope of the QIS axis is simply equal to the coefficient $-10/17$ which correlates the quadrupolar induced shifts on both dimensions. The interesting information that follows Eq. 2.36 is that the coefficient is independent on the spin number I as well as the coherence order p such that there is a single definition of the QIS axis for all kinds of MQMAS experiments.³¹ A CS axis should also be defined in order to determine the actual chemical shift of a site. The slope of the CS axis is deduced from the comparison of Eqs. 2.30 and 2.34 and is equal to 1. As shown in Fig. 2.18-a, the CS axis can be scaled to obtain approximate values for the actual chemical shifts of the different sites by a projection parallel to the QIS axis, of the center of gravity of each band. Of course, the QIS axis may also be scaled but we will see that the magnitude of the quadrupolar interaction is better determined providing a subsequent calculation.

The experimental determination of the real chemical shifts is illustrated on Fig. 2.18 where the CS and QIS axes have been drawn. This 3QMAS spectrum was obtained with an aluminophosphate $AlPO_4 - 14$. We observe

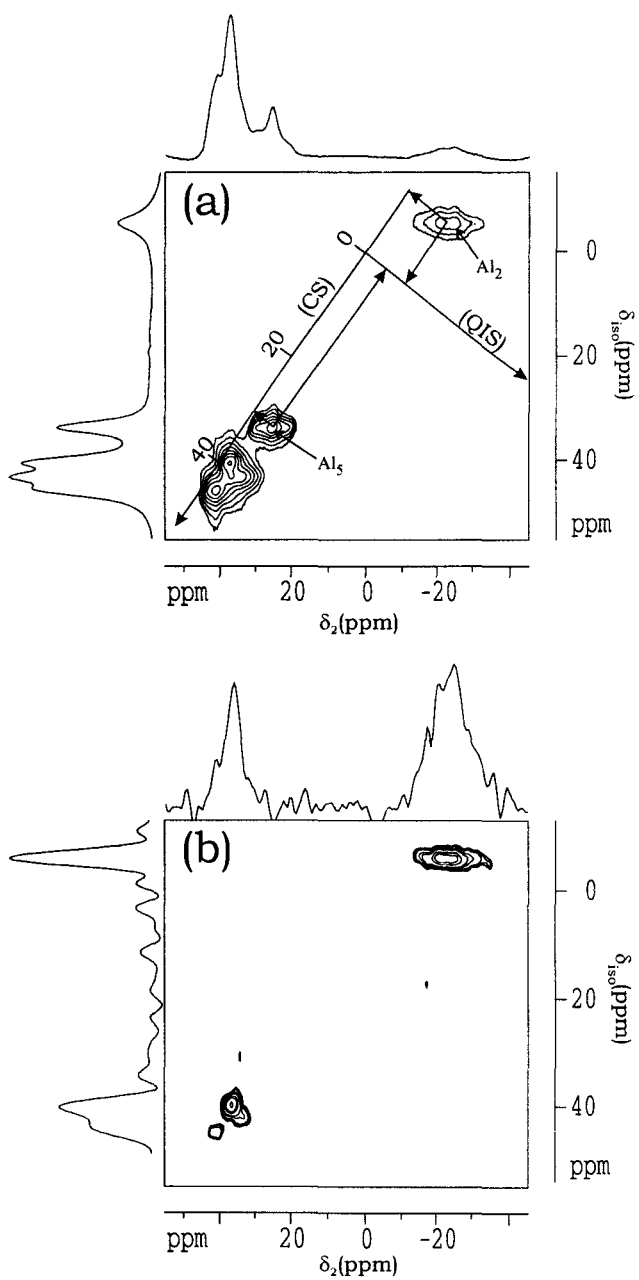


Figure 2.18: Sheared 3QMAS (a) and CP 3QMAS (b) spectra of $\text{AlPO}_4 - 11$.

on the QIS axis that site Al_2 experiences a stronger quadrupolar interaction than site Al_5 whereas chemical shifts δ_{CS} are found around -10 ppm and 30 ppm for Al_2 and Al_5 , respectively.

Making use of the definitions of δ_2 and δ_{iso} (Eqs. 2.37), one can obtain mathematical expressions for δ_{CS} and δ_{QIS} (Eqs. 2.38). Thus, the projection of the center of gravity of a line onto the sheared MQMAS and MAS axes leads to δ_{CS} and δ_{QIS} , hence avoiding the addition of the CS and QIS axes.

$$\begin{cases} \delta_2 = \delta_{CS} + \delta_{QIS} \\ \delta_{iso} = \delta_{CS} - \frac{10}{17}\delta_{QIS} \end{cases} \quad (2.37)$$

$$\begin{cases} \delta_{CS} = \frac{17\delta_{iso} + 10\delta_2}{27} \\ \delta_{QIS} = \frac{17}{27}(\delta_2 - \delta_{iso}) \end{cases} \quad (2.38)$$

We have seen that δ_{QIS} was a function of the spin number I , as well as the quadrupolar parameters C_Q and η_Q (Eq. 2.30). Therefore, the calculation of these two parameters is impossible from the single determination of δ_{QIS} . Indeed, a more detailed analysis of the lineshape is necessary to reach such information. Nevertheless, the quadrupolar parameters can be grouped into a single expression denoted P_Q (sometimes denoted SOQE, Second-Order Quadrupolar Effects) which also describes the magnitude of the quadrupolar interaction. This new parameter will be written

$$P_Q = C_Q \sqrt{1 + \frac{\eta^2}{3}} \quad (2.39)$$

The quadrupolar induced shift can be rewritten

$$\delta_{QIS} = -\frac{3}{10} \cdot \frac{P_Q^2}{\omega_0^2} \cdot \frac{1}{K} \cdot 10^6 \quad (2.40)$$

where

$$K = \frac{[4I(2I - 1)]^2}{4I(I + 1) - 3}$$

Table 2.6 summarizes the values of K for different spin numbers I . The P_Q parameter can finally be calculated from the graphic determination of δ_{iso} and δ_2 using Eq. 2.41, which is completely independent of p .

$$P_Q = \frac{\omega_0}{9000} \cdot \sqrt{170 \cdot K \cdot (\delta_{iso} - \delta_2)} \quad (2.41)$$

I	3/2	5/2	7/2	9/2
K	12	50	588/5	216

Table 2.6: K values as a function of the spin number I .

The determination of P_Q for each site is with no doubt the first step towards the understanding of the local surrounding of the nucleus. Using MQMAS experiments, the calculation of this parameter is straightforward and requires the acquisition of a single 2D spectrum whereas previous high-resolution methods such as DOR required the acquisition of several spectra at different static fields in order to change the magnitude of the quadrupolar induced shifts. This constitutes a major drawback of the DOR experiment upon the MQMAS experiment, in addition to the technical challenge of the double rotation that was discussed in Chapter 1.

2.3.3 Combination With Other Spin Manipulations

The first year that followed the discovery of MQMAS, most researchers' aim was to increase the efficiency of the multiple-quantum coherence excitation

as well as to obtain pure-phase 2D spectra. Then, they imagined how the technical simplicity of the experiment could be associated with the versatility of NMR to propose new methods in order to gain an additional structural information. An important group of NMR techniques uses spin manipulations to retrieve the dipolar information that is eliminated by the magic-angle rotation. Therefore, for the last two years, we focused on the possible association of multiple-quantum excitations with cross-polarization (CP) and rotational echo double resonance (REDOR) spin manipulations.

Cross-Polarized 3QMAS Experiments

The cross-polarization (CP) has been first investigated by Hartmann et al.³³ and further studied by Vega³⁴ under magic-angle spinning. The basic CP sequence includes a delay (contact time) during which the magnetization is transferred from an NMR sensitive spin I (high γ) to a less sensitive spin S . It was initially employed to increase the sensitivity of the NMR excitation of carbon through a cross-polarization with protons. By comparing MAS and CP-MAS spectra, one can also get some information on the environment of the non-abundant nucleus. Pruski et al.,³⁵ and Fernandez et al.³⁶ have made the most of the latter feature to add a CP sequence to the initial MQMAS sequence. The schematic diagrams of the pulse sequences and the coherence transfer pathways that were used by Fernandez are shown in Fig. 2.19. The main difference between MQMAS and CP-MQMAS experiments is in the preparation period: in the first step of the experiment, magnetic spin polarization is transferred from ^1H nuclei to the single-quantum coherence of the ^{27}Al nuclei using a CP pulse sequence. Then, the classical z -filter MQMAS sequence is added before acquisition in a two-dimensional mode. Note that the authors opted for a separation of the CP and the MQMAS se-

quences instead of the excitation of the triple-quantum coherences via cross-polarization. Thus, an additional z -filter pulse precedes the triple-quantum coherence excitation.

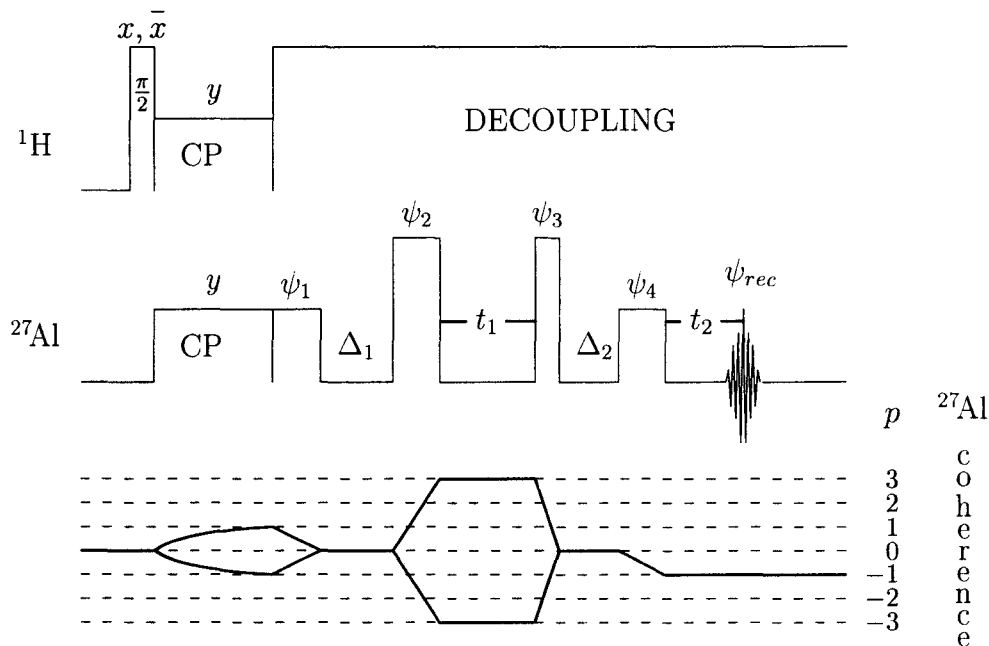


Figure 2.19: Pulse sequence used in the CP 3QMAS experiment

In order to illustrate the capability of the CP-MQMAS sequence to achieve a complete discrimination between hydrated and non-hydrated ^{27}Al sites, we present the ^{27}Al 3QMAS (Fig. 2.18-a) and ^{27}Al CP 3QMAS (Fig. 2.18-b) spectra of a fully hydrated $\text{AlPO}_4 - 11$ aluminophosphate. We have reproduced the two isotropic projections in Fig. 2.20 for a better understanding of the results. Clearly, this technique provides a more direct evidence of the interaction of various aluminium sites with water. It is obvious that the Al_2 resonance exhibits the strongest CP intensity while the Al_5 resonance is absent. These observations are consistent with the previous ^{27}Al DOR NMR

and X-ray diffraction data of Peeters et al.³⁷ and the CP DOR results of Wu et al., which also suggested that Al_2 and Al_5 sites are the most and the least susceptible to hydration, respectively. Furthermore, the CP-MQMAS technique shows that among the remaining tetrahedral sites, Al_4 interacts with water more strongly than Al_1 and Al_3 . These results are in agreement with the crystallographical structure of the aluminophosphate as explained in Fernandez et al.'s paper.³⁶

Even though the CP-MQMAS technique suffers from a lack of efficiency, the authors proved with this first experiment, that it was possible to use the high-resolution of MQMAS in combination with another spin manipulation to reach additional structural information. Nevertheless, the strong quantitative uncertainties that go with a CP transfer between spin 1/2 and quadrupolar nuclei limit the experiment to providing only a qualitative result. Therefore, Fernandez et al. have introduced a new MQ-REDOR experiment that gives new insights into the measure of connectivities between quadrupolar and spin-1/2 nuclei.

Multiple-Quantum REDOR NMR

The REDOR technique³⁸ has been implemented to reintroduce the dipolar interaction that is averaged out by the fast magic angle spinning. The conventional experiment is composed of an echo sequence for the observed nucleus S while a series of π -pulses spaced by an integer number of half-rotor periods, is applied to the other studied nucleus I . The number of π -pulses is regularly incremented in a set of experiments in order to increase the dephasing due to the dipolar interaction. The dephasing resulting from the application of the π -pulses is proportional to the dipolar interaction such that the intensity of the resonance is reduced. The comparison of the spectra obtained

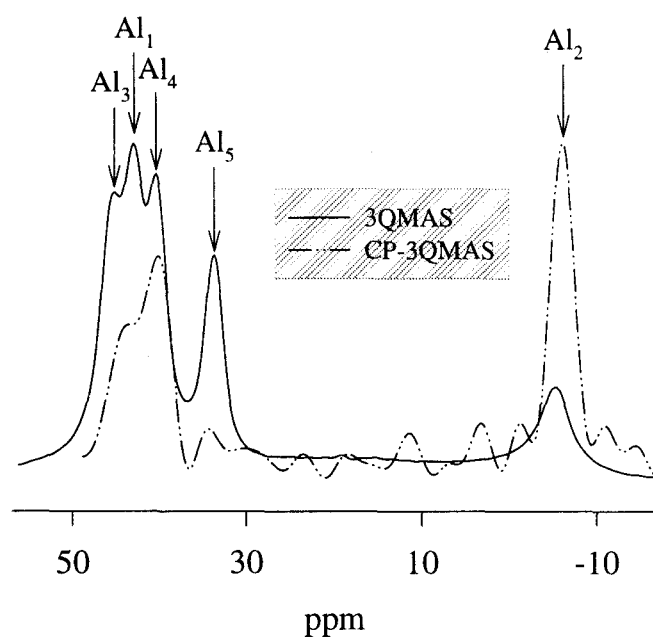


Figure 2.20: 3QMAS and CP-3QMAS isotropic projections obtained with the AlPO_4-11 aluminophosphate.

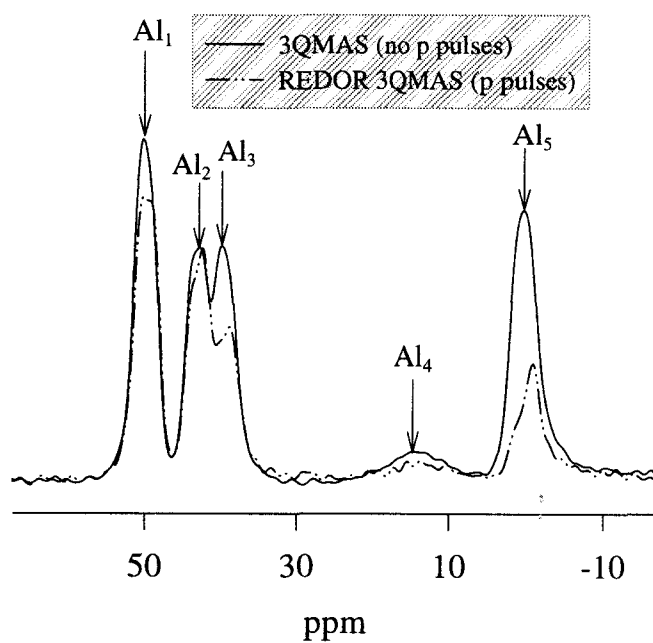


Figure 2.21: 3QMAS and 3Q-REDOR isotropic projections obtained with the $\text{AlPO}_4 - 14$ aluminophosphate.

with and without the dephasing pulses allows for a qualitative analysis of the connectivities.

Fernandez et al.³⁹ have recently added a REDOR sequence to the z -filter sequence in order to take advantage of the high-resolution provided by the latter. They described an MQ-REDOR experiment of which the diagram is given in Fig. 2.22. The first part of the experiment consists in exciting triple-quantum coherences using two strong rf pulses. Then, according to adequate phase cycling, the z -filter pulse transfers the magnetization of spins S into single-quantum transitions during which the dephasing π -pulses are applied to the spin- $1/2$ I . REDOR curves can be measured for various ^{27}Al species by comparing intensities on 2D spectra acquired with and without π -pulses on I and for different values of n , the number of rotor periods. Additional experimental features such as rf powers, phase cycles, etc. can be found in the paper previously cited.

The ^{27}Al MQ-REDOR experiment is demonstrated on a sample of aluminophosphate $\text{AlPO}_4 - 14$ which encloses five nonequivalent ^{27}Al sites, one of them resulting from the presence of an impurity.⁴⁰ As for the $\text{AlPO}_4 - \text{CHA}$ aluminophosphate that was used in Fernandez' experiment, water molecules were present in the sample, suggesting the study of ^1H - ^{27}Al spin pairs. Two 2D spectra (not shown) were recording using the sequence of Fig. 2.22 with a number of rotor periods equal to 6. One experiment was performed with the maximum of power available on ^1H spins while the π -pulses were removed to acquire a second spectrum used as a reference. The isotropic projections of sheared 3QMAS and 3Q-REDOR spectra are shown in Fig. 2.21. The advantage of the MQ-REDOR technique is that it provides direct evidence

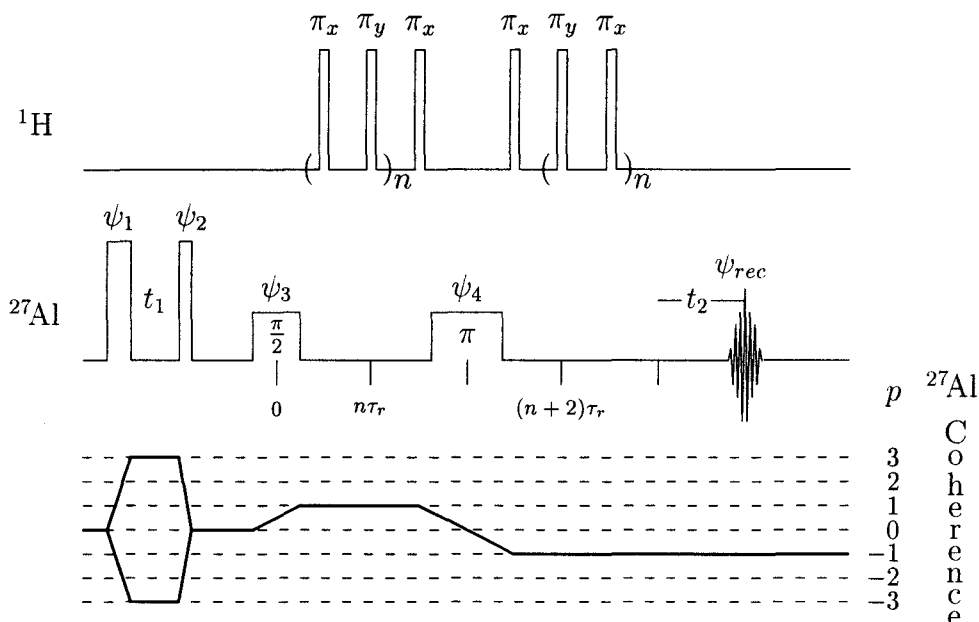


Figure 2.22: Pulse sequence used in the 3Q-REDOR experiment

of the proximity of ^1H and ^{27}Al . The projections were scaled in reference to species Al_2 for which the REDOR effect is minimum. We clearly see that the REDOR dephasing is more important for Al_5 species suggesting that water molecules preferably interact with octahedral sites. Other tetrahedral species can also be classified as far as their predisposition to hydration is concerned. Fernandez et al. have gone further in their analysis by MQ-REDOR technique as they measured complete REDOR curves for three ^{27}Al sites in $\text{AlPO}_4 - \text{CHA}$ and they compared the results with calculated curves to estimate dipolar couplings and distances $^{27}\text{Al}-^1\text{H}$.

The aim of the present section was to show the flexibility of the MQMAS experiment that is evident in the CP MQMAS and MQ-REDOR implementations. Experimental information will be better found in the various articles given in the bibliography. With the achievement of a high-resolved dimen-

sion, some researchers have also involved other spin manipulations such as heteronuclear correlation experiments.⁴¹ No doubt that the future of new experiments in solid-state NMR of quadrupolar nuclei is now strongly linked to the MQMAS technique.

2.4 Conclusion

This chapter has shown that NMR is a powerful technique in the sense that one can “play” on both the spatial and spin parts of the Hamiltonian in order to remove and/or reintroduce the contribution of certain interactions. For example, Chapter one showed that second-order quadrupolar broadenings can not be averaged out by the only action of sample reorientations. Therefore, the MQMAS experiment combines the magic angle spinning feature with the excitation of multiple-quantum transitions. We have shown that one can obtain an isotropic projection, i.e. with no quadrupolar broadening, using a two-dimensional acquisition mode. Among the different MQMAS pulse sequences that have been proposed for the last three years, the z -filter approach is, in our opinion, the best way to get a pure absorption spectrum with an optimised S/N ratio. The experimental procedure (optimisation, acquisition and processing) was also fully described.

Then, we focussed on the information that is provided by an MQMAS spectrum. In addition to the determination of the number of non-equivalent sites, important parameters characterising the local environment of the nucleus, can be easily calculated. Finally, the flexibility of this new experiment makes it possible to develop new experiments involving the MQMAS sequence and other spin manipulations.

Nevertheless, no mention was made of a possible quantification of these

2D MQMAS spectra even though it is very important in numerous applications. Indeed, chemists are often interested in obtaining an estimation of the relative population of the sites. Therefore, the next chapter will deal with the problem of quantification in NMR, especially in MQMAS experiments.

2.5 L'expérience MQMAS (résumé)

2.5.1 Bases Théoriques du MQMAS

Développement des termes de spins

Dans le chapitre précédent, nous nous sommes limités au développement des termes spatiaux de l'Hamiltonien quadrupolaire. Il apparaît que le moyennage spatial de l'interaction au second ordre requiert une double rotation qui reste aujourd'hui encore, difficile techniquement. A ce moment là, les commutateurs $[T_{2,-m}, T_{2,m}]$ faisant intervenir les opérateurs de spins $T_{2,-m}$, étaient volontairement laissés de côté et nous avons préféré les regrouper dans les termes ξ_L . Par conséquent, il nous faut maintenant écrire ces composantes explicitement afin de montrer l'efficacité du MQMAS à éliminer les élargissements quadrupolaires.

En utilisant le même formalisme qu'au premier chapitre, le commutateur de spin $[T_{2,-m}, T_{2,m}]$ peut être réduit en une somme de tenseurs sphériques irréductibles $T_{L,0}$ ($0 \leq L \leq 4$). En fonction du signe des coefficients de Clebsch-Gordan, certaines composantes disparaissent de sorte que seuls les termes de rang 1 et de rang 3 subsistent (cf. Eqs. 2.2). La fréquence quadrupolaire $\omega_Q^{(2)}(m)$ pour un niveau d'énergie m est proportionnelle aux coefficients $C_L^I(m)$ donnés par les équations 2.6. Enfin, avec l'aide des matrices de Wigner, nous pouvons écrire la fréquence quadrupolaire au second ordre pour chaque cristallite, lorsque l'échantillon est soumis à une rotation autour d'un axe faisant un angle θ avec \mathbf{B}_0 ,

$$\omega_Q^{(2)}(m) = \frac{\omega_Q^2}{36\omega_0} \left[A_0 C_0^I(m) + A_2(\alpha, \beta) C_2^I(m) P_2(\cos \theta) + A_4(\alpha, \beta) C_4^I(m) P_4(\cos \theta) \right]. \quad (2.42)$$

Les termes dépendant de l'orientation des crystallites sont regroupés dans les $A_L(\alpha, \beta)$ (cf. Eqs. 2.9) alors que $P_2(\cos \theta)$ et $P_4(\cos \theta)$ sont les polynômes de Legendre d'ordre 2 et 4, définis dans le premier chapitre. Nous retrouvons bien sûr les 3 parties qui découlent du calcul au second ordre de l'Hamiltonien quadrupolaire. Le 1er terme est indépendant des angles α et β et donne lieu à un déplacement induit ω_{QIS} qui dépend de la transition $(m, -m)$ que l'on considère (Eq. 2.43).

$$\omega_{m,-m}^{QIS} = -\frac{2m}{30} \frac{\omega_Q^2}{\omega_0} \left(1 + \frac{\eta^2}{3}\right) [I(I+1) - 3m^2] \quad (2.43)$$

Dans l'expérience MQMAS, nous exciterons des transitions symétriques telles que les transitions triple-quanta ($m = 3/2$) alors que nous observerons toujours les transitions à simple-quanta ($m = -1/2$). Les différents déplacements induits seront utiles pour déterminer les paramètres quadrupolaires, δ_{CS} et P_Q (cf. 2.5.3).

La technique MQMAS fait appel aux expériences à 2 dimensions qui sont très courantes en RMN des liquides mais encore rares à l'état solide (DAS, HETCOR, ...). De façon concise, une expérience 2D est composée de deux périodes d'évolution des spins, et de pulses (minimum de 2) qui vont exciter certaines transitions et finalement transférer (mixing period, cf. Fig. 2.2) le signal dans la cohérence $p = -1$ pour l'observation. L'expérience MQMAS consiste donc à faire évoluer les cohérences 3Q ($p = \pm 3$) pendant un temps t_1 en appliquant un champ rf le plus important possible. Après cette période d'évolution, un deuxième pulse permet l'acquisition d'un signal d'écho au sommet duquel toute l'anisotropie quadrupolaire est annulée. En effet, la corrélation des évolutions pendant t_1 et t_2 des cohérences triple-quanta et simple-quanta, permet d'éliminer le troisième terme de l'équation 2.42. Si l'expérience se fait en plus à l'angle magique $\theta_M = 54.7^\circ$, alors le deuxième

terme de cette même équation est tout simplement éliminé. Afin d'obtenir un spectre 2D, en fréquence, il faut acquérir un signal d'écho en incrémentant régulièrement le temps t_1 d'évolution des cohérences triple-quanta. Après une double transformée de Fourier, nous obtenons un spectre sur lequel la position des différents sites dépend de leur déplacement chimique δ_{CS} et de leur constante quadrupolaire C_Q . Comme l'évolution du signal d'écho dépend du rapport $R(I, p) = -C_4^I(p)/C_4^I(-1)$, les bandes de résonance des sites cristallographiques s'étendent le long d'un axe de même pente $R(I, p)$ propre à chaque spin et à chaque expérience multi-quanta. Par conséquent, il est souhaitable d'effectuer un "shearing" du spectre afin que les bandes de résonances soient parallèles à l'axe horizontal. Ainsi, une projection du spectre 2D sur l'axe vertical δ_{iso} donne un spectre isotrope, débarrassé des élargissements quadrupolaire.

Acquisition

L'acquisition d'un spectre à 2 dimensions, suit des règles bien précises qui s'appliquent aussi bien en RMN des liquides qu'à l'état solide. La section 2.1.3 traite des différents éléments essentiels à l'obtention d'un spectre 2D parfaitement phasé (spectre d'absorption pure). Dans ce résumé, nous ne donnerons que les étapes les plus importantes qui permettent cette acquisition.

Nous avons vu que l'expérience à 2 dimensions comprenait au moins 2 pulses pour former, dans le domaine d'acquisition t_2 , un signal d'écho. Néanmoins, pour les faibles valeurs de t_1 , l'écho est tronqué et la transformée de Fourier du seul signal d'écho donne un spectre 2D impossible à phaser et comportant des parties dispersives. Par conséquent, le signal d'antiécho doit aussi être enregistré afin d'obtenir un spectre d'absorption pure. Les

signaux d'écho et d'antiécho sont obtenus en sélectionnant simultanément ou séquentiellement les 2 chemins de cohérence symétriques $p = \pm 3$ pendant la période t_1 (pour une expérience 3QMAS). La figure 2.6 représente les chemins de cohérence conduisant aux signaux d'écho et d'antiécho, pour un spin $I = 3/2$. Il est important de préciser que pour un spin $I = 5/2$, l'écho correspond à la cohérence $p = +3$. Ces conditions dépendent du signe de $R(I, p)$ et de règle générale, le signal d'écho est obtenu grâce au chemin $(0 \rightarrow +p \rightarrow -1)$ sauf lorsque $p = 2I$. En sélectionnant séquentiellement l'écho et l'antiécho, nous observons une évolution des signaux présentées sur la figure 2.7.

La sélection des différents chemins de cohérence se fait généralement en jouant sur la phase des différents pulses ainsi que la phase du récepteur. Les règles de sélection sont données page 73. Il est intéressant de s'attarder sur la règle 3 qui stipule que selon le nombre de phases N_i appliquées au pulse, les signaux provenant d'autres chemins de cohérence peuvent s'ajouter au chemin de cohérence choisi. Cela veut dire que pour une expérience à 3-quanta, un choix de $N_i = 6$ phases différentes pour l'un des deux pulses afin de sélectionner simultanément l'écho et l'antiécho.

Par ailleurs, l'acquisition des composantes réelle et imaginaire est indispensable pour pouvoir phaser le spectre 2D dans la deuxième dimension. Cependant, le déphasage entre parties réelle et imaginaire n'est pas égal à 90° comme pour l'observation des transitions simple quanta. Ainsi, pour obtenir la partie imaginaire dans une expérience à 3-quanta, il nous faut enregistrer un deuxième set de données en utilisant la même séquence de pulse mais avec une phase de 30° ($\pi/2p$ avec $p = 3$) appliquée au 1er pulse. Les phases des pulses sont données dans les tables 2.2 et 2.3.

Processing

La manipulation des données enregistrées est fonction de la méthode d'acquisition qui a été choisie. En ce qui nous concerne, nous avons opté pour une acquisition simultanée des signaux d'écho et d'antiécho de sorte que pour chaque incrément t_1 , nous obtenons 2 parties $S_X(t_1, t_2)$ (partie réelle) et $S_Y(t_1, t_2)$ (partie imaginaire) qui sont une combinaison linéaire de l'écho et de l'antiécho. Les équations 2.44 permettent de calculer les signaux d'écho $S_E(t_1, t_2)$ et d'antiécho $S_A(t_1, t_2)$ à partir de $S_X(t_1, t_2)$ et $S_Y(t_1, t_2)$.

$$\begin{aligned} S_E(t_1, t_2) &= S_X(t_1, t_2) - iS_Y(t_1, t_2) \\ S_A(t_1, t_2) &= S_X(t_1, t_2) + iS_Y(t_1, t_2) \end{aligned} \quad (2.44)$$

Nous avons aussi vu l'intérêt du shearing pour obtenir un spectre isotrope par projection sur l'axe vertical. Cette transformation peut se faire après une double transformée de Fourier de $S_E(t_1, t_2)$ et $S_A(t_1, t_2)$. Cependant, nous avons préféré manipuler les données après la première transformée de Fourier en t_2 en multipliant $S_E(t_1, t_2)$ et $S_A(t_1, t_2)$ par une exponentielle dépendant de $\phi(t_1, \omega_2) = R(I, p) \omega_2 t_1$.

$$\begin{aligned} S'_E(t_{iso}, \omega_2) &= e^{i\phi(t_1, \omega_2)} S_E(t_1, \omega_2) \\ S'_A(t_{iso}, \omega_2) &= e^{-i\phi(t_1, \omega_2)} S_A(t_1, \omega_2) \end{aligned} \quad (2.45)$$

Enfin, le spectre 2D d'absorption pure est obtenu par transformé de Fourier en t_{iso} de $S'_E(t_{iso}, \omega_2)$ et $S'_A(t_{iso}, \omega_2)$ et en additionnant les 2 signaux (Eq. 2.46).

$$S(\omega_{iso}, \omega_2) = S'_E(\omega_{iso}, \omega_2) + S'_A(-\omega_{iso}, \omega_2) \quad (2.46)$$

Les étapes du processing sont résumés sur la figure 2.8.

2.5.2 Optimisation de la Séquence z -filtering MQMAS

Séquence z -filtering MQMAS

La séquence de pulses qui a été présentée jusqu'à maintenant, comprend 2 pulses, l'un pour exciter les cohérences 3-quanta et l'autre pour transférer la magnétisation vers les transitions observables. Les chemins de cohérence ($0 \rightarrow +3 \rightarrow -1$) et ($0 \rightarrow -3 \rightarrow -1$) sont sélectionnés simultanément par cyclage de phase. Cependant, il est facile de s'apercevoir que ces deux chemins ne sont pas parfaitement symétriques et ne vont donc pas contribuer au signal d'acquisition avec la même intensité (cf. 2.10). De plus, l'optimisation d'une telle séquence est difficile et le résultat est souvent médiocre (parties dispersives sur le spectre final).

Amoureux et al.¹⁹ ont donc proposé d'ajouter un troisième pulse à la séquence précédente afin de rendre parfaitement symétrique l'évolution des cohérences $+3Q$ et $-3Q$. La séquence z -filter est présentée à la figure 2.12. Le deuxième pulse (maximum de puissance) transfère la magnétisation le long du champ statique (OQ) au lieu de directement acquérir le signal ($-1Q$). Même si l'efficacité de la séquence z -filter est un peu inférieur à celle d'une séquence à 2 pulses, la qualité du spectre final est nettement améliorée puisque les parties dispersives disparaissent complètement. En plus, la détermination des paramètres expérimentaux (longueurs des pulses, temps de relaxation, ...) en est grandement simplifiée (cf. 2.2.2).

D'autres séquences de pulses sont développées dans la section 2.2.1 et présentent toutes certains avantages. Il est préférable de se reporter aux articles traitant de ces nombreuses améliorations.

Synchronisation du rotor en t_1

Lors de la publication des premiers spectres 2D MQMAS, il est apparu que le nombre de bandes de rotation était bien souvent plus grand le long de l'axe isotrope que le long de l'axe anisotrope (MAS). Certains spectres présentaient tellement de bandes de rotation, d'intensité importante, qu'il devenait difficile de les différencier de la bande principale. En effet, l'intensité de la résonance principale diminue d'autant plus qu'il y a de bandes de rotation. De plus, la multiplication de résonances (principales ou dues à la rotation) augmente le risque de recouvrement des raies et complique l'analyse du spectre.

Massiot a récemment proposé une méthode de synchronisation du rotor en t_1 qui permet de complètement éliminer les bandes de rotation dans la dimension isotrope. Le principal avantage de la synchronisation est que le temps d'expérience est réduit à peu près d'un facteur 5. Le principe est tout simplement de fixer la fenêtre spectrale dans la seconde dimension égale à la vitesse de rotation du rotor ($\Delta t_1 = 2\pi/\omega_r$). Il est essentiel que la vitesse de rotation du rotor soit la plus grande possible afin de contenir tous les sites cristallographiques dans la fenêtre spectrale en ω_1 . Dans ce cas, les bandes de rotation se replient sur la résonance principale ce qui augmente aussi son rapport S/N.

En ce qui concerne les spectres présentés dans cette thèse, nous les avons obtenu avec la synchronisation du rotor. Cette méthode a aussi grandement simplifié la quantification des spectres puisqu'il n'était pas nécessaire de prendre en compte les bandes de rotation dans le calcul numérique.

Détermination des paramètres expérimentaux

L'optimisation des paramètres expérimentaux est essentielle pour obtenir un spectre MQMAS sans partie dispersive et avec le meilleur rapport S/N.

Nous rappelons que nous avons opté pour une séquence à 3 pulse, avec un z -filter pour symétriser les chemins de cohérence. Les paramètres suivants sont les plus importants à optimiser.

Cyclage de phase Dans notre expérience MQMAS, le cyclage de phase doit être choisi de façon à ne pas conserver des chemins de cohérence supplémentaires qui amèneraient des signaux parasites sur le spectre final. Il doit aussi rester le plus court possible afin de ne pas augmenter inutilement le temps de l'expérience. La sélection des cohérences $3Q$ se fait en appliquant 6 phases au second pulse. Le troisième pulse, quant à lui doit éviter de transférer des cohérences parasites qui seraient dues à un mauvais ajustement des longueurs des pulses. Dans la section 2.2.2, nous avons étudié les différents chemins de cohérence parasites qui peuvent apparaître à l'acquisition pour différents cyclages du dernier pulse ($N_2 = 1, 2, 4$) (cf. Fig. 2.15). Expérimentalement, nous observons (cf. 2.16) un spectre distordu lorsque $N_2 = 1$ alors que pour $N_2 \geq 2$ le spectre est "propre". Pour nos expériences, nous avons choisi $N_2 = 4$ pour assurer une bonne sélection des chemins de cohérence.

Longueur des pulses L'optimisation des longueurs de pulse nous est apparue bien plus cruciale que le choix du cyclage de phase. Les longueurs de pulse, notamment celui de création des cohérences $0Q \rightarrow 3Q$ et celui de conversion $3Q \rightarrow 0Q$, dépendent fortement du champ rf disponible. Par conséquent, nous avons décidé de toujours optimiser expérimentalement ce paramètre. Pour cela, nous utilisons la séquence de pulse z -filter mais en ne faisant que l'acquisition de la première rangée (spectre 1D) pour laquelle le temps d'évolution des cohérences $3Q$ est nul ($t_1 = 0$). Puis, la longueur de chaque pulse est indépendamment incrémentée afin de déterminer la valeur qui donnera le max-

imum de signal sur le spectre. Expérimentalement, nous retrouvons les valeurs théoriques (Table 2.5) calculées grâce au programme PULSAR (cf. chapitre 3 pour plus d'information sur PULSAR). Les courbes d'optimisation pour τ_1 et τ_2 sont présentées à la figure 2.17.

Temps de relaxation Le temps nécessaire pour que la magnétisation retrouve sa position d'équilibre le long de \mathbf{B}_0 après une séquence d'impulsion doit être déterminé précisément pour différentes raisons : rapport S/N, quantification, temps d'expérience, etc. Nous avons remarqué que le temps de relaxation des spins était parfois bien plus grand dans l'expérience MQMAS que dans les expériences à une impulsion (1D MAS). Par conséquent, ce paramètre a toujours été vérifié après l'optimisation des longueurs de pulse afin de ne pas fausser la quantification des spectres.

2.5.3 Avantages du MQMAS

Nous venons de voir que l'interaction quadrupolaire au second ordre pouvait être complètement éliminée par excitation des cohérences à multi-quanta et acquisition d'un spectre à 2 dimensions. La dimension isotrope du spectre MQMAS permet de séparer les différents sites cristallographiques. Dans cette partie, nous avons aussi démontré qu'un spectre MQMAS fournit d'autres informations sur l'environnement des noyaux. En effet, non seulement les paramètres quadrupolaires (P_Q et δ_{CS}) sont déterminés directement par projection sur le spectre 2D, mais la flexibilité de cette nouvelle technique rend possible des combinaisons du MQMAS avec d'autres manipulations de spins (CP, REDOR).

Détermination des paramètres δ_{CS} et P_Q

La comparaison des spectres RMN obtenus à différents champs statiques n'est possible que si l'on définit la position d'une résonance en *parties par million* (ppm). Il en est de même pour les expériences à 2 dimensions. Le "scaling" des spectres MQMAS est discuté dans la section 2.3.1, avant et après shearing.

L'étude de l'interaction quadrupolaire au second ordre a montré que la position du centre de gravité d'une résonance était la somme d'un déplacement chimique δ_{CS} et d'un déplacement quadrupolaire induit δ_{QIS} . Si le déplacement chimique est le même dans les 2 dimensions du spectre MQMAS, les déplacements quadrupolaires induits ne sont pas égaux mais proportionnels (Eq. 2.47).

$$\delta_{QIS}^{iso}(I, C_Q, \eta_Q) = -\frac{10}{17}\delta_{QIS}(I, C_Q, \eta_Q) \quad (2.47)$$

Ces relations nous amènent à définir 2 axes sur le spectre MQMAS : les axes CS et QIS de pentes respectives, 1 et $-10/17$. A condition d'étalonner les axes CS et QIS, nous pouvons donc, par projection du centre de gravité d'une résonance sur un des axes, parallèlement à l'autre, déterminer approximativement les valeurs de δ_{CS} et $P_Q = C_Q\sqrt{1 + \eta_Q^2/3}$. De plus, comme le coefficient reliant les déplacements quadrupolaires induits sur les axes anisotrope δ_2 et isotrope δ_{iso} est indépendant du nombre de spin I et de la cohérence excitée p , cette définition des axes CS et QIS reste vraie quelque soit le noyau étudié et l'expérience MQMAS exécutée.

Nous insistons sur le fait qu'il est impossible de séparer les contributions de la constante quadrupolaire C_Q et du paramètre d'assymétrie η_Q d'après la seule position des raies de résonances sur les spectres MQMAS. En ef-

fet, la détermination du paramètre η_Q requiert l'analyse par simulation de l'enveloppe du spectre MAS. Ceci explique l'introduction d'une nouvelle constante P_Q , qui globalement décrit les *effets quadrupolaires au second ordre*. La valeur de P_Q peut aussi être obtenue par projection sur les axes δ_2 et δ_{iso} ce qui évite de devoir étalonner l'axe QIS (cf. Eq. 2.41).

La détermination du paramètre P_Q est un premier pas vers l'analyse de l'environnement local du noyau. L'acquisition d'un seul spectre 2D MQMAS permet de connaître cette valeur alors qu'il fallait plusieurs expériences DOR à différents champs statiques pour obtenir la même information. Ceci constitue sans aucun doute un avantage certain du MQMAS sur les méthodes de double rotation.

Combinaison avec d'autres manipulations de spins (CP et REDOR)

Même si la plupart des chercheurs se sont d'abord penchés sur le problème de l'efficacité du MQMAS et sur les possibles améliorations des spectres (rapport S/N, dispersion, etc.), certains d'entre eux se sont vite rendu compte que cette méthode était suffisamment flexible pour être associée à d'autres manipulations de spins. Le but de telles combinaisons est de tirer profit de la haute résolution fourni par le MQMAS.

Notre groupe à Lille, en collaboration avec le Prof. M. Pruski à Ames, USA, a développé les 2 techniques CP-MQMAS et MQ-REDOR pour les noyaux quadrupolaires. Le principe, communs à ces 2 nouvelles méthodes, est d'ajouter la séquence z -filter MQMAS avant (REDOR) ou après (CP) une autre manipulation de spin. Les figures 2.19 et 2.22 sont respectivement les séquences de pulses utilisées dans nos expériences de CP-3QMAS et 3Q-REDOR. Nous présentons aussi, dans la section 2.3.3, les résultats obtenus avec 2 échantillons aluminophosphates ($\text{AlPO}_4 - 11$ et $\text{AlPO}_4 - 14$). Le but

était de mettre en évidence les noyaux ^{27}Al qui sont à proximité des protons ^1H . Les projections isotropes des spectres MQMAS "classiques" et des nouvelles expériences sont comparées sur les figures 2.20 et 2.21. Les effets sont très importants et sont en accord avec la structure des matériaux.

La méthode MQ-REDOR est très prometteuse comme en témoigne les premiers articles qui la décrivent. En effet, en réintroduisant le couplage dipolaire, il est maintenant possible d'obtenir les distances entre noyaux. Fernandez et al. ont associé un calcul théorique afin de déterminer les distances $^{27}\text{Al}-^1\text{H}$ dans l'aluminophosphate $\text{AlPO}_4 - \text{CHA}$.

Nous avons présenté dans ce chapitre, la technique MQMAS en insistant sur l'acquisition et le processing d'un spectre. Les quelques exemples qui sont fournis attestent de la puissance de cette technique, comparée aux expériences de double rotation (DOR et DAS). Cependant, il n'a pas encore été fait mention de la quantification des spectres 2D MQMAS. Par conséquent, le chapitre suivant concerne les problèmes de quantification des spectres en RMN et la méthode que nous avons développée pour corriger les intensités relatives des différents sites.

Bibliography

1. DUER M. AND STOURTON C. *J. of Magn. Reson.* 124 (1997), pp. 189–199.
2. FRYDMAN L. AND HARWOOD J. S. *J. Am. Chem. Soc.* 117 (1995), pp. 5367–5368.
3. SAMOSON A. *Chem. Phys. Lett.* 119 (1985), pp. 29–32.
4. JAKOBSEN H., SKIBSTED J., BILDSOE H. AND NIELSEN N. *J. of Magn. Reson.* 85 (1989), pp. 173–180.
5. DUER M. AND STOURTON M. Pacific Grove, CA. In *35th ENC, Poster WP222*, 1994.
6. NIELSEN N., BILDSOE H. AND JAKOBSEN H. *Chem. Phys. Lett.* 191 (1992), pp. 205–212.
7. AMOUREUX J.-P. *Solid-State NMR* (1993), pp. 83–88.
8. HAHN E. *Phys. Rev.* 80 (1950), p. 580.
9. FERNANDEZ C. AND AMOUREUX J.-P. *Chem. Phys. Lett.* 242 (1995), pp. 449–454.

10. MASSIOT D., TOUZO B., TRUMEAU D., COUTURES J., VIRLET J., FLORIAN P. AND GRANDINETTI P. *Solid-State NMR* 6 (1996), pp. 73–83.
11. WU G., ROVNYAK D., SUN B. AND G.GRIFFIN R. *Chem. Phys. Lett.* 249 (1996), pp. 210–217.
12. ERNST R., BODENHAUSEN G. AND WOKAUN A. *Principles of Nuclear Magnetic Resonance in One and Two Dimensions*. Oxford University Press, New York, 1987.
13. STATES D., HABERKORN R. AND RUBEN D. *J. of Magn. Reson.* 48 (1982), pp. 286–292.
14. BODENHAUSEN G. *Prog. Nucl. Magn. Reson. Spectrosc.* 14 (1981), p. 137.
15. AMOUREUX J.-P., FERNANDEZ C. AND FRYDMAN L. *Chem. Phys. Lett.* 259 (1996), pp. 347–355.
16. SORENSEN O., RANCE M. AND ERNST R. *J. of Magn. Reson.* 56 (1984), pp. 527–534.
17. MUELLER K., WOOTEN E. AND PINES A. *J. of Magn. Reson.* 92 (1991), pp. 620–627.
18. BROWN S., HEYES S. AND WIMPERIS S. *J. of Magn. Reson.* 119 (1996), pp. 280–284.
19. AMOUREUX J.-P., FERNANDEZ C. AND STEUERNAGEL S. *J. of Magn. Reson.* 123 (1996), pp. 116–118.

20. GRANDINETTI P., BALTISBERGER J., LLOR A., LEE Y., WERNER U., EASTMAN M. AND PINES A. *J. of Magn. Reson.* 103 (1993), pp. 72–81.
21. BROWN S. AND WIMPERIS S. *J. of Magn. Reson.* 124 (1997), pp. 279–285.
22. BROWN S. AND WIMPERIS S. *J. of Magn. Reson.* 128 (1997), pp. 42–61.
23. AMOUREUX J.-P., PRUSKI M., LANG D. AND FERNANDEZ C. *J. of Magn. Reson.* 131 (1998), pp. 170–175.
24. MARINELLI L. AND FRYDMAN L. *Chem. Phys. Lett.* (1998), In Press.
25. DUER M. *Chem. Phys. Lett.* 277 (1997), pp. 167–174.
26. MASSIOT D. *J. of Magn. Reson.* 122 (1996), pp. 240–244.
27. HANAYA M. AND HARRIS R. *Solid-State NMR* 122 (1996), pp. 240–244.
28. VOSEGAARD T., LARSEN F., JAKOBSEN H., ELLIS P. AND NIELSEN N. *J. Am. Chem. Soc.* 119 (1997), pp. 9055–9056.
29. MARINELLI L., MEDEK A. AND FRYDMAN L. *Solid-State NMR* (1998), p. In Press.
30. MEDEK A., HARWOOD J. S. AND FRYDMAN L. *J. Am. Chem. Soc.* 117 (1995), pp. 12779–12787.
31. AMOUREUX J.-P. AND FERNANDEZ C. *Solid-State NMR* 10 (1998), pp. 211–223.
32. CHARPENTIER T. *Résonance Magnétique Nucléaire Haute-Résolution sur les Noyaux Quadrupolaires dans les Solides*. PhD thesis, Service de Physique Condensé, Université de Paris XI, Orsay, 1998.

33. HARTMANN S. AND HAHN E. *Phys. Rev.* 100 (1958), p. 865.
34. VEGA S. *Phys. Rev.* 23 (1981), p. 3152.
35. PRUSKI M., LANG D., FERNANDEZ C. AND AMOUREUX J.-P. *Solid-State NMR* 7 (1997), p. 327.
36. FERNANDEZ C., DELEVOYE L., AMOUREUX J.-P., LANG D. AND PRUSKI M. *J. Am. Chem. Soc.* 119 (1997), pp. 6858–6862.
37. PEETERS M., HAAN J. D., DE VEN L. V. AND HOOFF J. V. *J. Phys. Chem.* 97 (1993), p. 5363.
38. GUILLION T. AND SCHAEFER J. *J. of Magn. Reson.* 81 (1989), p. 196.
39. FERNANDEZ C., LANG D., AMOUREUX J.-P. AND PRUSKI M. *J. Am. Chem. Soc.* 120 (1998), pp. 2672–2673.
40. FERNANDEZ C., AMOUREUX J.-P., CHEZEAU J., DELMOTTE L. AND KESSLER H. *Microporous Materials* 6 (1996), pp. 331–340.
41. WANG S., PAUL S. D. AND BULL L. *J. of Magn. Reson.* 125 (1997), pp. 364–368.

Chapter 3

Quantification of MQMAS spectra

3.1 Problem of Quantitative NMR

3.1.1 Quantification of MAS spectra

Solid state NMR is an incomparable technique useful to probe the local environment in single crystals as well as in powder samples. Nevertheless, the separation of crystallographically non-equivalent sites does not provide much information unless it is followed of a quantification of the spectra. Even though the quantification of spectra is rather straightforward for nuclei with a spin $I = 1/2$, the extraction of quantitative information has always been a major topic of discussion in solid-state NMR of quadrupolar nuclei.¹ This problem is still sometimes present, even for the common 1D MAS experiment. Thus, some care must be taken during the acquisition of the spectra and additional tools, such as a program of simulation, are essential to obtain quantitative results.

In the first chapter, we have shown that the multiple possible orientations of crystallites yield an anisotropic broadening of the resonance. This also means that the crystallites experience different quadrupolar effects depending on the orientation of their PASs with respect to the static magnetic field. Consequently, the pulse conditions (rf power and pulse lengths) must be chosen in order to try to identically excite all crystallites regardless of their orientation. In the case of a rf power which is strong (“hard” pulse) compared to the quadrupolar interaction, the evolution of the spin system is principally the result of the rf field. Such excitation is said to be nonselective. However, quadrupolar effects can rarely be neglected as they are often in the range of a few MHz (compared to rf fields of a few hundred of kHz). Thus, most of the time, a nonselective excitation becomes impossible for substance with a non-cubic symmetry. In fact, the amplitude of the exciting pulse is often much smaller than the strength of the quadrupolar interaction such that the excitation becomes selective ($\mathcal{H}_Q \gg \mathcal{H}_{rf}$). As a consequence, pulses will populate certain transitions, giving the central transition preference to the detriment of the satellite transitions in powder samples.

The behavior of the crystallites can be predicted using computational methods.² A representation of the intensity of the central transition observed in static single crystals, is obtained versus the pulse length τ_1 of the exciting pulse (Fig. 3.1). In such a computation, the second-order interaction is numerically introduced. Furthermore, it is seen that the intensity of the central transition is strongly dependent on the quadrupolar interaction $\bar{\omega}_Q$. It must be recalled that $\bar{\omega}_Q$ depends on the quadrupole frequency ω_Q and on the crystallite orientation (α, β) with respect to \mathbf{B}_0 (Eq. 1.35). Therefore, in powder samples (crystallites have many different orientations), pulse lengths must be chosen to be within the linear part (short pulses) of the curves for

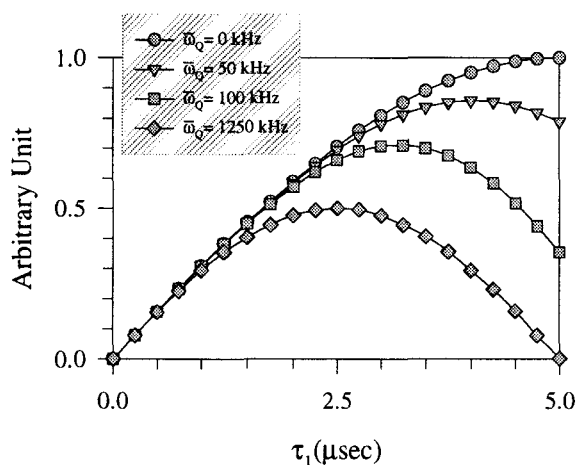


Figure 3.1: Amplitude of the central transition for spin $3/2$ for a single crystallite, as a function of the pulse length τ_1 , for a rf field of $\nu_{rf} = 50$ kHz, taking into account the second-order quadrupolar interaction ($\nu_0 = 100$ MHz). The calculation was performed in static conditions (cf. Eqs. 1.34 and 1.35).

which the intensities are independent of the quadrupolar interaction $\bar{\omega}_Q$ (cf. Fig. 3.2). This region is inverse proportional to the rf field suggesting that a better selective excitation, identical for all crystallites is reached at low rf power. On the other hand, a too low rf field may not be sufficient to irradiate the whole central transition on a powder sample, suggesting that the choice of the rf power should be the result of a compromise. It has been demonstrated that the optimal rf value is approximately the central transition linewidth divided by $I + 1/2$.²

The conclusion of the previous paragraph is that quantitative MAS spectra can be obtained if both rf power and pulse lengths are judiciously chosen. Still, a straightforward quantification of the spectra might be uncertain as lineshapes are various, parameter-dependent and not predicted by commer-

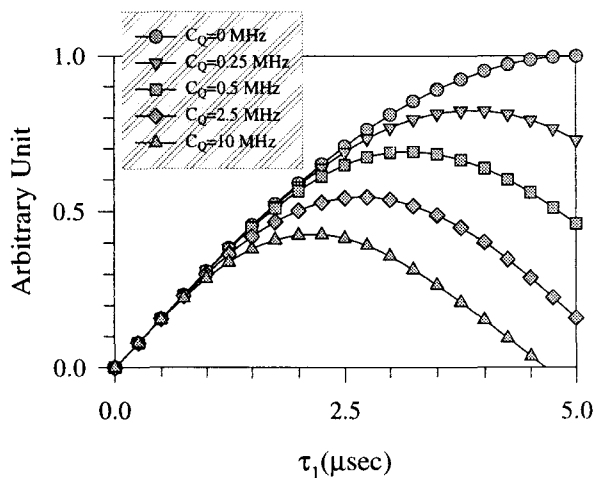


Figure 3.2: Amplitude of the central transition for spin 3/2 for a powder as a function of the pulse length τ_1 , for a rf field of $\nu_{rf} = 50$ kHz, taking into account the second-order quadrupolar interaction ($\nu_0 = 100$ MHz).

cial fitting packages when several different interactions are present in the sample under observation. Thus, a specific fitting program (QUASAR) has been developed by Profs. Amoureux and Fernandez to fit static and MAS powder spectra using a least-square method. QUASAR has already proven its reliability and capability to solve structural problems.^{3, 4} The main characteristics of the program are that it is able to combine the effects of J couplings, dipolar, CSA and quadrupolar interactions with different PAS orientations, in a single fit, taking into account all relevant parameters such as the spinning speed ω_r , the asymmetry parameters η_Q and η_σ , the quadrupolar constants C_Q , the chemical shift parameters, δ_{CS} and $\Delta\sigma$, the dipolar constants, the J couplings as well as the relative proportion of up to five non-equivalent sites, simultaneously. However, the problem remains in that the fitting of MAS spectra with no a priori knowledge of certain parameters strongly increases

the inaccuracy of the result. Indeed, QUASAR needs a first set of parameters in order to initiate the calculation.

Considering the MAS projection of $\text{AlPO}_4 - 11$, shown in Fig. 2.18, it is obvious that the ^{27}Al tetrahedral region ($\approx 40\text{ppm}$) is strongly subject to overlapping rendering the determination of the number of sites ambiguous. Thus, a subsequent fitting of the spectrum is likely to yield inaccurate results as too many parameters are uncertain. This example puts forth the limits of the MAS technique alone in the characterization of crystallographically non-equivalent sites in powder samples.

3.1.2 Using MQMAS and MAS Spectra

The main advantage of MQMAS upon the classical MAS experiment is that an additional high-resolved dimension removes the ambiguity of the number of sites. Thus, the MQMAS technique could completely replace the 1D MAS experiment if one can get a precise quantification of the 2D spectrum. Unfortunately, it has been proven⁵⁻⁷ that the excitation of the multiple-quantum coherences was not uniform for the different sites, rendering a straightforward quantification impossible. Indeed, unlike MAS for which a correct experimental parameter setting (short selective pulse) yields a quantitative spectrum, long excitation pulses are necessary to get an efficient multiple-quantum excitation, increasing at the same time the dependency on the crystallite orientation. The efficiency of the multiple-quantum excitation can be monitored as a function of the quadrupolar constant C_Q (or P_Q). This dependency can be very important as shown in Figs. 3.3 which result from a numerical calculation using the program PULSAR.⁸ The characteristics of this package, developed by Prof. Amoureux, will be explained in section 3.3.1. A 2 MHz difference in the P_Q parameter corresponds to a relative intensity reduced

by a factor of about two (region [1-3 MHz] for $\nu_{rf} = 50$ kHz). We can also notice that the region where the efficiency of the multiple-quantum excitation reaches a maximum, gets sharper and sharper as the rf field decreases, confirming that the strongest rf field available should be used. Consequently, MQMAS and MAS experiments are rendered complementary to obtain enhanced resolution and quantitative results, respectively.

Let us describe the logical procedure that we should follow to analyse MQMAS and MAS spectra. Of course, the first and straightforward information that is deduced from the 2D dataset is the number of non-equivalent sites enclosed in the sample. In addition to that, we have seen in Chapter 2 that approximate values of P_Q and δ_{CS} could be determined by projections onto CS, δ_2 and δ_{iso} axes. These parameters may sometimes be sufficient to initiate lineshape-pattern fitting of the MAS spectrum. However, one should take more advantage of the 2D spectrum by extracting for each site, the slice for t_1 -rotor-synchronized experiment or the summation along δ_{iso} of all slices (centerband and spinning sidebands). Then, each slice must be fitted separately (using a program such as QUASAR) in order to get a set of precise values for δ_{CS} , C_Q and η_Q (instead of P_Q) for each site. These values can then be used as a starting point for the fit of the MAS spectrum. At this point, the relative proportion of the different sites constitutes the only unknown parameter. This method reveals to be very precise with well-crystallised samples, as a preliminary analysis of the MQMAS lineshapes and it has the capacity to considerably reduce the uncertainty of the MAS simulation.

As an example, we refer to the quantification of the ^{27}Al sites in the aluminophosphate $\text{AlPO}_4 - 11$. An overlapping of the resonances makes the tetrahedral region featureless (cf. Fig. 2.18). For the $\text{AlPO}_4 - 11$, it is obvious that the MQMAS spectrum provides additional valuable infor-

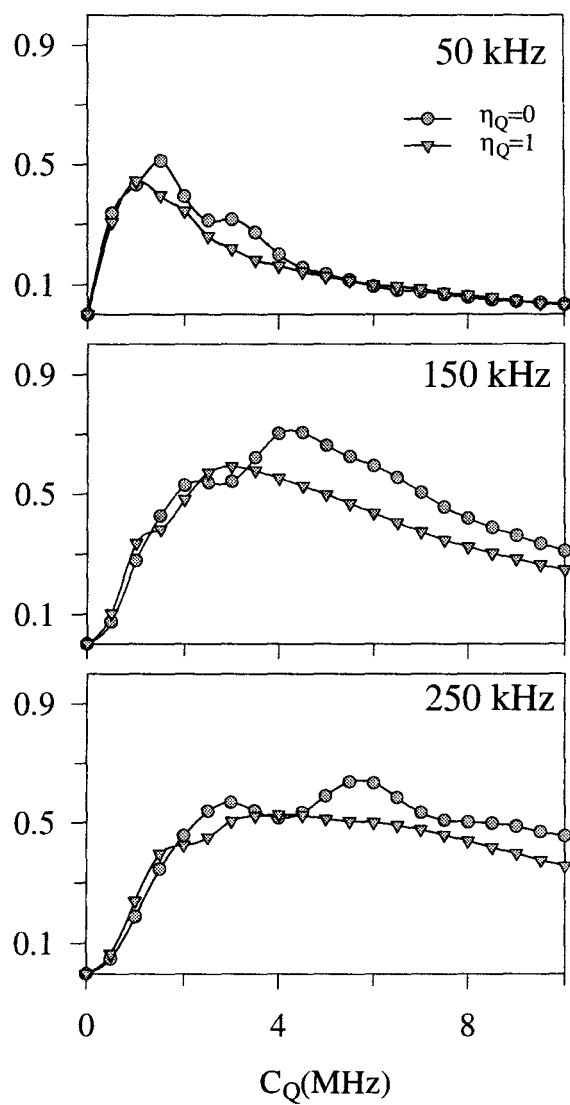


Figure 3.3: Efficiency of the 3QMAS z -filter experiment versus the quadrupolar constant C_Q for three rf fields.

mation emphasizing the complementarity of MAS and MQMAS techniques. Indeed, five different ^{27}Al sites are clearly separated on the 2D dataset, four of which are located in the tetrahedral region. Moreover, since aluminophosphates are generally well crystallised samples, lineshape patterns are typical of quadrupolar nuclei and can be separately analysed from the 2D dataset. Fig. 3.4 shows the centerslice of each site in $\text{AlPO}_4 - 11$. From the fit of each slice, we obtained the parameters presented in Table 3.1. These values were used for the simulation of the MAS spectrum in order to get an estimation of the relative concentration of the different sites. We found that the five non-equivalent sites were in the expected ratio of 1:1:1:1:1, within an accuracy of 5%. We will see later that in the case of amorphous or vitreous samples, broad resonances are observed even on the isotropic projection, rendering difficult the determination of the η_Q values from a fit of the centerslice (cf. section 3.1.4).

^{27}Al site	Al_1	Al_2	Al_3	Al_4	Al_5
%	1	1	1	1	1
δ_{CS} (ppm)	43.9	-9.0	47.6	43.5	35.8
C_Q (MHz)	2.9	4.0	2.0	2.1	3.0
η_Q	0.37	0.64	0.71	0.60	0.81

Table 3.1: Parameters obtained by fitting the slices deduced from the 3QMAS of $\text{AlPO}_4 - 11$.

3.1.3 Using Isotropic MQMAS projection

Even though the relative intensities of the resonances on the MQMAS spectrum do not reflect the real population of the different sites (see the isotropic

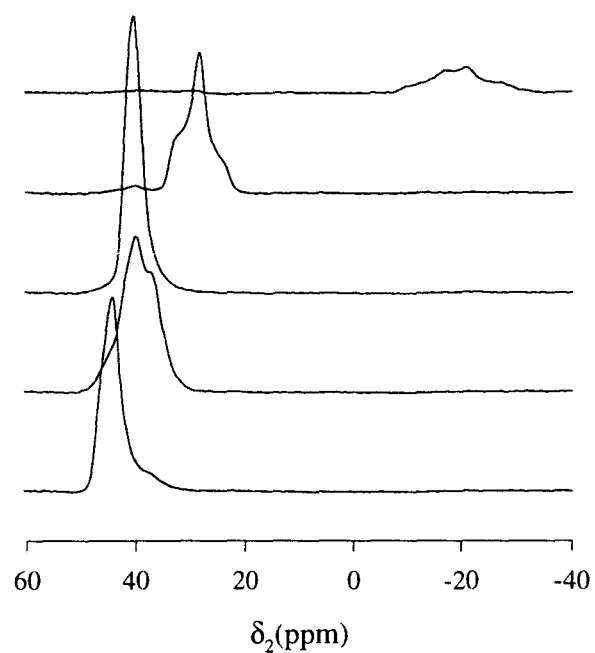


Figure 3.4: Individual 1D MAS lineshapes for the 5 sites in AlPO₄ - 11, obtained by extraction of each centerslice from the 2D 3QMAS spectrum shown in Fig. 2.18.

projection for $\text{AlPO}_4 - 11$), a quantitative information can still be obtained in specific cases. Indeed, we have shown in the previous section that the efficiency of the multiple-quantum excitation could be calculated versus the quadrupolar constant (see curves in Figs.3.3). Consequently, the intensities obtained by a fit of the isotropic spectrum (using gaussian and lorentzian functions) can be corrected if each site is located on the curve, by using their P_Q quadrupolar constant previously deduced.

We have applied this method for $\text{AlPO}_4 - 11$. Approximate values of P_Q were obtained by adequate projections on the 2D spectrum. Then, we have fitted the isotropic projection using mainly gaussian functions. Finally, using the curve for a rf field of 250 kHz, we calculated and corrected the intensities obtained by the previous fit. Again, the five non-equivalent sites were in the expected ratio of 1 : 1 : 1 : 1 : 1 within an accuracy of 7%.

3.1.4 Distribution of Nucleus Surroundings

The three methods that have just been presented, enable the quantification of non-equivalent sites and give a quantitative information with a relatively high precision. They are based on NMR results obtained using MAS and/or MQMAS experiments. However, it must be noted that we have illustrated the different methods of quantification using aluminophosphates which are generally well-organised samples. In fact, those structures exhibit typical quadrupolar MAS lineshape patterns such that the presence of various singularities makes the determination of quadrupolar parameters, especially η_Q , easier. On the other hand, the previous methods lead to quantitative results which become all the more uncertain as the crystallinity ratio is low. Indeed, many samples that are of great interest for chemists, industrials, etc., are not perfectly crystallised in the sense that a crystallographic site is not

represented by an unique set of quadrupolar parameters (δ_{CS} , C_Q and η_Q). Thus, we are now going to see how this special feature sometimes affects both MAS and MQMAS spectra.

First, let us consider a perfectly crystallised sample which gives a nice quadrupolar pattern, represented by a unique set of parameters δ_{CS} , C_Q and η_Q . Slight changes of the bond lengths and/or bond angles from one site to another, directly influence these three values which will now be distributed over a certain range. The consequence is that the lineshape of the total 1D MAS spectrum is composed of an infinite number of individual spectra for which the set of parameters slightly differs. In the case of a distribution of chemical shift, each band corresponds to a different δ_{CS} whereas other parameters, especially C_Q and η_Q , are constant. Therefore, all individual spectra have a different position of the center of gravity and contribute with their own intensity to the final MAS spectrum even if their linewidths are identical (see MAS projection on Fig. 3.5). The horizontal projection in Fig. 3.6 is a schematic representation of the influence of a distribution of quadrupolar constant on the MAS spectrum. The variation of quadrupolar constants makes it so that each resonance is shifted by a different δ_{QIS} and has a different broadening. Hence, the sum of these numerous bands gives the final MAS spectrum (solid line) from which the envelope is clearly smoothed. This explains why MAS spectra of non-crystalline or amorphous samples loose their singularities which are so characteristic of quadrupolar nuclei. Of course, a computing analysis of the lineshape using QUASAR is doomed to failure as such a program can not easily take into account the different distributions.

If we now consider a 2D MQMAS spectrum, we realise that the lineshape representing a crystallographic site is broadened in both dimensions.

In fact, it is composed of an infinite number of narrow bands differing by one of the parameters (C_Q or δ_{CS}) and shifted in both dimensions. For a distribution of chemical shifts, the bands keep the same pattern, defined by C_Q and η_Q , but they move along a line which is parallel to the CS axis (see the schematic representation in Fig. 3.5). On the other hand, if the distribution is of quadrupolar constants, the bands are of various widths (depending on C_Q) and are spread out along the QIS axis (cf. Fig. 3.6). Experimentally, we often observe a distribution of chemical shifts and quadrupolar constants together such that each slice which composes the 2D lineshape is itself featureless, preventing its detailed analysis. Like the MAS spectrum, the isotropic projection of the MQMAS spectrum is broadened by the distributions. One can notice that this broadening is irregular, rendering the isotropic bands assymmetric, especially for a pure distribution of quadrupolar constant (cf. Fig. 3.6). Moreover, the assymetry of the isotropic dimension can sometimes lead to a false analysis if one interprets the shoulder as an additional site. Therefore, the fitting of this projection using gaussian and lorentzian functions is much more difficult suggesting that a quantification of the populations using the curves in Fig. 3.3 should be avoided.

Various NMR methods have been presented to quantify the relative proportions of different sites in powder samples. They usually give correct results when the structure is highly crystallised. The problem of quantitative information mainly arises when the crystallinity of the sample is poor which is often the case in zeolite samples, for example. 2D lineshapes, isotropic projection as well as the MAS spectrum are broadened preventing the use of any of the previous cited methods. Nevertheless, an MQMAS spectrum undoubtedly provides an additional information that must be judiciously manipulated in order to have access to the quantification. In the next section,

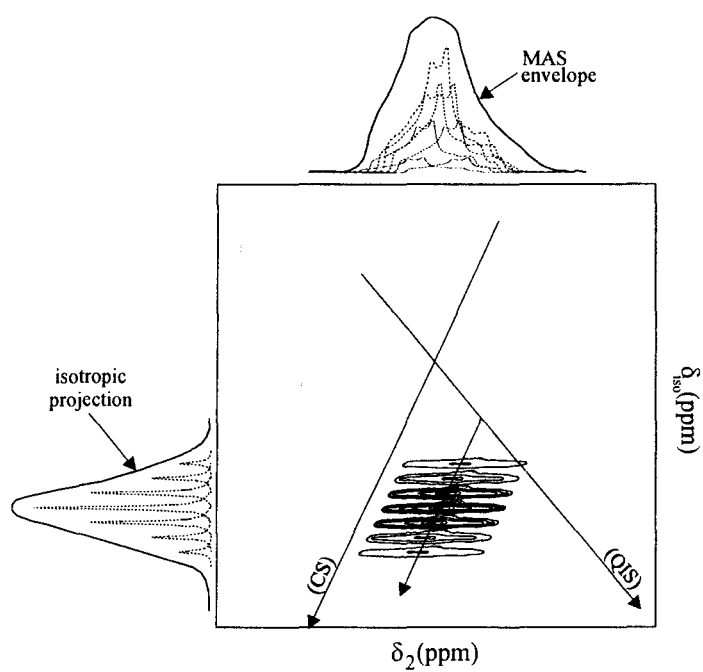


Figure 3.5: Schematic representation of a gaussian distribution of isotropic chemical shift δ_{CS} .

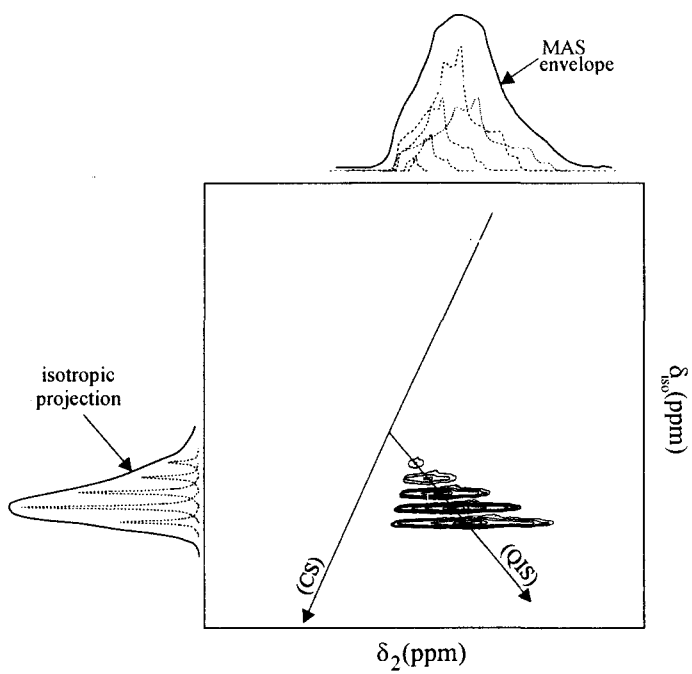


Figure 3.6: Schematic representation of a gaussian distribution of quadrupolar constant C_Q .

we describe a calculation based on a regularization method, which leads to the quantification of the MQMAS spectra in badly-crystallised or amorphous systems.

3.2 Basics of Regularization Method

3.2.1 General

The method that we have developed has been initiated by the calculations that Zwanziger introduced for the quantification of two-dimensional DAS spectra.⁹ We basically applied the theoretical basics of Zwanziger's work to the specific case of the MQMAS experiment. For the sake of clarity, we will try to keep as much as possible the notation that he used.

Previously, we showed that the broadened lineshape in an NMR spectrum of disordered materials (MAS or MQMAS) could be seen as a sum of an infinite number of bands, each one defined by a unique set of chemical shift, quadrupolar constant and asymmetry parameter. Therefore, the intensity of the experimental lineshape $I(\omega)$ is described by the following integral.

$$I(\omega) = \int I_0(\omega; \mathbf{R}) \Pi(\mathbf{R}) d\mathbf{R} \quad (3.1)$$

The function $I(\omega)$ stands for the experimental NMR lineshape broadened by a distribution of parameters $R_\alpha, R_\beta, \dots = \mathbf{R}$. $I_0(\omega; \mathbf{R})$ represents the calculated NMR lineshape for a given set of parameters R_α, R_β . The density of probability of a site to have parameter R_α in the range $R_\alpha + dR_\alpha$, R_β in the range $R_\beta + dR_\beta$, etc., will be denoted $\Pi(\mathbf{R})$. The latter function is also the mathematical form of the distribution that we will later calculate using the regularization method. In order to simplify our study, we will

consider that samples are only subject to a distribution of chemical shift δ_{CS} and second-order quadrupolar parameter P_Q , thus reducing the number of integrated parameters to 2. In fact, the variations of the asymmetry parameter are included through those of P_Q . The limits of integration extend over the physical range of each parameter, i.e., $\delta_{CS} = [-\infty; +\infty]$ and $P_Q = [0; +\infty]$.

Considering the 1D MAS experiment, the previous equation would simply be rewritten as

$$I(\delta_2) = \int_{-\infty}^{+\infty} d\delta_{CS} \int_0^{+\infty} I_0(\delta_2; \delta_{CS}, P_Q) \Pi(\delta_{CS}, P_Q) dP_Q. \quad (3.2)$$

Eq. 3.2 shows that it is difficult to obtain an approximate of the distribution of P_Q and δ_{CS} using a single 1D MAS spectrum. Indeed, the effects of the distributions are not clearly separated but rather added up to give this featureless MAS lineshape.

On the other hand, the CS and QIS axes have been introduced in chapter 2 to help with the interpretation of the 2D MQMAS spectrum. Thus, it is possible to separate both chemical shift and quadrupolar constant distributions taking advantage of the additional dimension on the MQMAS spectra. For each slice at an isotropic location δ_{iso} , we write the equation

$$I(\delta_2, \delta_{iso}) = \int_{-\infty}^{+\infty} d\delta_{CS} \int_0^{+\infty} I_0(\delta_2, \delta_{iso}; \delta_{CS}, P_Q) \Pi(\delta_{CS}, P_Q) dP_Q. \quad (3.3)$$

in which the δ_{iso} -dependency is highlighted. Eqs. 3.4 and 2.34 allow δ_{iso} to be substituted by δ_{CS} in Eq. 3.3.

$$\delta_{iso} = \delta_{CS} - \frac{10}{17} \delta_{QIS}(P_Q) \quad (3.4)$$

Moreover, this constraint (Eq. 3.4) allows Eq. 3.3 to be reduced to a set of 1D integral equations by introducing the Dirac function Δ . Indeed, for each δ_{iso} verifying Eq. 3.4, Eq. 3.3 is written such that the experimental intensity becomes

$$I(\delta_2, \delta_{iso}) = \int_{-\infty}^{+\infty} d\delta_{CS} \int_0^{+\infty} I_0(\delta_2; \delta_{CS}, P_Q) \Delta[\delta_{iso} - (\delta_{CS} - 10\delta_{QIS}/17)] \cdot \Pi(\delta_{CS}, P_Q) dP_Q . \quad (3.5)$$

Finally, after removing the Dirac function, we obtain the following equation, which is in a form that can easily be handled numerically using the formalism of Fredholm equations.

$$I(\delta_2, \delta_{iso}) = \int_0^{+\infty} I_0(\delta_2; \delta_{CS}(P_Q), P_Q) \Pi(\delta_{CS}(P_Q), P_Q) dP_Q \quad (3.6)$$

3.2.2 Numerical Approach

Eq. 3.6 has the form of *Fredholm equations of the first kind* which are fully described in the Numerical Recipes.¹⁰ For each value of δ_{iso} , the function of distribution $\Pi(\delta_{CS}, P_Q)$, also called the *kernel* can be evaluated versus the quadrupolar constant P_Q . By using the relation described in Eq. 3.4, we obtain a particular curve on the two-dimensional representation of P_Q versus δ_{CS} . Then, for different values of δ_{iso} , weighted by the corresponding experimental amplitude, we can retrieve the complete 2D distribution $\Pi(\delta_{CS}, P_Q)$ by the union of the different curves. Yet, this Fredholm equation has still to be transformed into a form that can be further handled numerically, i.e., the integral must be replaced by a discrete sum over a range of P_Q values. Since a limited set of P_Q^i s must be chosen to limit the computational time, one

could approximately determine the most probable range of this parameter, using the 2D dataset, and finally decide that the function will be evaluated at N equally spaced values of P_Q^i s. In such a case, weighting coefficients W_i in Eq. 3.7 are equal whatever the P_Q^i considered.

$$I(\delta_2, \delta_{iso}) \approx \sum_{i=1}^N W_i I_0(\delta_2; \delta_{CS}^i, P_Q^i) \Pi(\delta_{CS}^i, P_Q^i) \quad (3.7)$$

However, both the weighting coefficients and the location of the abscissas P_Q^i at which the function is to be evaluated, can be better determined using a quadrature scheme. As Zwanziger did, we found that the Gaussian quadrature, especially the *Gauss-Legendre* one, was the most adapted to our integration formula (cf. pp.144-146 in Numerical Recipes¹⁰). Thus, using the `gauleg` subroutine and giving the lower and upper limits of integration for the quadrupolar parameter P_Q , we obtain a set of N values P_Q^i , typically $N = 32$, and their corresponding weights W_i .

For a given δ_{iso} , the approximation in Eq. 3.7 is consequently carried out for N values of P_Q and for M values of δ_2 . This leads to a system of M linear equations with N unknowns. The same equation can thus be written in a convenient matrix form

$$\mathbf{K} \cdot \mathbf{\Pi} = \mathbf{I}. \quad (3.8)$$

For the sake of clarity, Eq. 3.8 is also given in its developed form.

$$\begin{aligned}
& \begin{pmatrix} W_1 I_0(\delta_2^1; \delta_{CS}^1, P_Q^1) & W_2 I_0(\delta_2^1; \delta_{CS}^2, P_Q^2) & \cdots & W_N I_0(\delta_2^1; \delta_{CS}^N, P_Q^N) \\ W_1 I_0(\delta_2^2; \delta_{CS}^1, P_Q^1) & W_2 I_0(\delta_2^2; \delta_{CS}^2, P_Q^2) & \cdots & W_N I_0(\delta_2^2; \delta_{CS}^N, P_Q^N) \\ \vdots & \vdots & \ddots & \vdots \\ W_1 I_0(\delta_2^M; \delta_{CS}^1, P_Q^1) & W_2 I_0(\delta_2^M; \delta_{CS}^2, P_Q^2) & \cdots & W_N I_0(\delta_2^M; \delta_{CS}^N, P_Q^N) \end{pmatrix} \\
& \times \begin{pmatrix} \Pi(\delta_{CS}^1, P_Q^1) \\ \Pi(\delta_{CS}^2, P_Q^2) \\ \vdots \\ \Pi(\delta_{CS}^N, P_Q^N) \end{pmatrix} = \begin{pmatrix} I(\delta_2^1, \delta_{iso}) \\ I(\delta_2^2, \delta_{iso}) \\ \vdots \\ I(\delta_2^M, \delta_{iso}) \end{pmatrix}
\end{aligned} \tag{3.9}$$

with

$$\delta_{iso} = \delta_{CS}^i - \frac{10}{17} \delta_{QIS}^i \tag{3.10}$$

There are two ways of solving Eq. 3.9. The straightforward and easiest method would be to guess a distribution Π that would be used to weight the ideal NMR response \mathbf{I}_0 . The result would then be compared with the experimental data. The deviations between experimental and ideal calculated data could help improve the “guessed” distribution. Finally, by subsequent iterations, one may optimize the agreement. Even though this method is mathematically simple, it requires some initial guess for the distribution. The alternative and more complicated strategy is obviously to get the distribution without any assumption on its form. This method is the one that we chose even if it involves the inversion of the Fredholm equation which is not simple mathematically.

The different elements which compose the last equation should be considered in details. Both Π and \mathbf{I} are column matrices with N and M elements,

respectively, while the kernel \mathbf{K} is represented by a rectangular matrix of dimension $M \times N$. In our case, the number of points M at which the powder spectrum $I(\delta_2^j)$ is to be evaluated, is much bigger than the P_Q^i values such that the matrix \mathbf{K} is said *singular*, i.e., it has many more rows than columns. This also means that a degeneracy occurs due to the fact that we find ourselves with more linear equations than unknowns. Consequently, without any special care, the inversion of Eq. 3.9 would give a wildly oscillating, instead of a smooth, positive and bounded solution Π . A first approach to this problem is found in the *Singular Value Decomposition* (SVD). The main characteristic of the method is to decompose the kernel \mathbf{K} in such a way that the resulting matrices do not diverge to infinite by the effect of the inversion.

SVD is based on a theorem of linear algebra: An $M \times N$ matrix, whose number of rows M is greater than or equal to its number of columns N , can be written as a product of an $M \times N$ column-orthogonal matrix \mathbf{U} , an $N \times N$ diagonal matrix \mathbf{W} and the transpose of an $N \times N$ orthogonal matrix \mathbf{V} . The next equation gives a schematic decomposition of the kernel \mathbf{K} .

$$\begin{pmatrix} \mathbf{K} \end{pmatrix} = \begin{pmatrix} \mathbf{U} \end{pmatrix} \cdot \begin{pmatrix} w_1 & & \\ & \dots & \\ & & w_N \end{pmatrix} \cdot \begin{pmatrix} \mathbf{V}^T \end{pmatrix} \quad (3.11)$$

The matrices \mathbf{U} and \mathbf{V} are orthogonal in the sense that $\mathbf{U}^T \cdot \mathbf{U} = \mathbf{V}^T \cdot \mathbf{V} = \mathbf{1}$.

At this moment, the inversion of Eq. 3.8 can be carried out in order to determine the vector $\Pi(\delta_{CS}^i, P_Q^i)$ representing the distribution. Obviously, the orthogonal property of matrices \mathbf{U} and \mathbf{V} , as well as the diagonal characteristics of \mathbf{W} , make it much easier to calculate the solution Π which is deduced from Eq. 3.12.

$$\begin{pmatrix} \Pi \end{pmatrix} = \begin{pmatrix} \mathbf{V} \end{pmatrix} \cdot \begin{pmatrix} \text{diag}(1/w_i) \end{pmatrix} \cdot \begin{pmatrix} \mathbf{U}^T \end{pmatrix} \cdot \begin{pmatrix} \mathbf{I} \end{pmatrix} \quad (3.12)$$

Two algorithms (`svdcmp` and `svdksb`) are proposed in the Numerical Recipes to solve Eq. 3.8. The role of the subroutine `svdcmp` is to construct the three matrices resulting from the decomposition of the input \mathbf{K} matrix whereas `svdksb` takes \mathbf{U} , \mathbf{V} and \mathbf{W} as an input and computes the solution Π according to Eq. 3.12. This procedure is supposed to solve the problem of degeneracy and should give a bounded and non-oscillating vector Π .

Even though the previous method is generally sufficient to overcome the degeneracy resulting from the presence of an overdetermined set of linear equations, we found the regularisation method (cf. Chapter 18 in Numerical Recipes) to be better adapted to the numerical solution of Fredholm equations. Nevertheless, we will later see that the previous SVD can in fact be combined with the regularization method to solve the inverse problem.

3.2.3 Linear Regularization Method

Our main purpose is still to solve the equation $\mathbf{K} \cdot \Pi = \mathbf{I}$ or, in other terms, to minimise the residual κ given by Eq. 3.13.

$$\kappa = (\mathbf{K} \cdot \Pi - \mathbf{I})^2 \quad (3.13)$$

When κ is minimized, the agreement between the model \mathbf{K} and the experimental data \mathbf{I} is very good. On the other hand, the solution becomes simultaneously extremely unstable and oscillating. In the regularization method, we do not minimize the residual κ but the sum of κ with an additional term ϱ , the regularizing operator, that works as a constraint (Eq. 3.14). The role of ϱ is to smooth and stabilize the desired solution Π to the slight detriment of the agreement between model and data. In Eq. 3.14, λ is a constant that gives more or less weight to the constraint ϱ . The choice of λ is crucial as it corresponds to a compromise between getting a correct solution and getting a system that is non-oscillating. Indeed, if λ is too small, the solution is widely oscillating whereas a big λ gives more importance to the “smoothing” term ϱ , which introduces an artificial broadening of the distribution surroundings. In fact, λ can easily be optimized to be set to a value of 5% which is almost independent of the experimental data.

$$\text{minimize :} \quad \chi = \kappa + \lambda\varrho \quad (3.14)$$

The choice of the smoothing term ϱ is also of great importance. The first or higher derivatives of the function $\Pi(\delta_{CS}, P_Q)$ with respect to δ_{CS} and P_Q are generally chosen to provide the smoothing effect. As far as we are concerned, we found the first derivative to be the best choice as it

corresponds to our *a priori* belief that the solution $\Pi(\delta_{CS}, P_Q)$ is continuous and non-oscillating. Thus, the regularizing function can be written as

$$\varrho \propto \sum_{i=1}^{N-1} [\Pi(\delta_{CS}^i, P_Q^i) - \Pi(\delta_{CS}^{i+1}, P_Q^{i+1})]^2. \quad (3.15)$$

ϱ can be rewritten in a matrix form as

$$\varrho = \Pi \cdot (\mathbf{L}^T \cdot \mathbf{L}) \cdot \Pi = \Pi \cdot \mathbf{H} \cdot \Pi. \quad (3.16)$$

where \mathbf{L} is the $(N - 1) \times N$ first difference matrix

$$\mathbf{L} = \begin{pmatrix} -1 & 1 & 0 & 0 & 0 & 0 & 0 & \cdots & 0 \\ 0 & -1 & 1 & 0 & 0 & 0 & 0 & \cdots & 0 \\ \vdots & & & \ddots & & & & & \vdots \\ 0 & \cdots & 0 & 0 & 0 & 0 & -1 & 1 & 0 \\ 0 & \cdots & 0 & 0 & 0 & 0 & 0 & -1 & 1 \end{pmatrix} \quad (3.17)$$

and therefore \mathbf{H} is the $N \times N$ matrix

$$\mathbf{H} = \mathbf{L}^T \cdot \mathbf{L} = \begin{pmatrix} 1 & -1 & 0 & 0 & 0 & 0 & 0 & \cdots & 0 \\ -1 & 2 & -1 & 0 & 0 & 0 & 0 & \cdots & 0 \\ 0 & -1 & 2 & -1 & 0 & 0 & 0 & \cdots & 0 \\ \vdots & & & \ddots & & & & & \vdots \\ 0 & \cdots & 0 & 0 & 0 & -1 & 2 & -1 & 0 \\ 0 & \cdots & 0 & 0 & 0 & 0 & -1 & 2 & -1 \\ 0 & \cdots & 0 & 0 & 0 & 0 & 0 & -1 & 1 \end{pmatrix}. \quad (3.18)$$

The main purpose now consists in minimising the sum χ given in Eq. 3.19.

$$\chi = (\mathbf{K} \cdot \Pi - \mathbf{I})^2 + \lambda(\Pi \cdot \mathbf{H} \cdot \Pi) \quad (3.19)$$

Solving our problem requires some additional mathematical manipulations in order to reduce the previous equation to a linear set of *normal equations* such that the unknown vector Π is isolated. Eq. 3.19 can be rewritten in a developed form as

$$\chi = \sum_{j=1}^M \left(\sum_{i=1}^N K_{ji} \Pi_i - I_j \right)^2 + \lambda \sum_{k=1}^N \sum_{l=1}^N \Pi_k H_{kl} \Pi_l. \quad (3.20)$$

where indexes i, j, k, l stand for row and column numbers in the different matrices previously defined.

The minimization of χ requires the derivative of Eq. 3.20 with respect to the parameters $\Pi_i = \Pi(\delta_{CS}^i, P_Q^i)$ ($i = 1, \dots, N$) to be annuled. Such calculation yields Eq. 3.21.

$$\sum_{i=1}^N \frac{\partial \chi}{\partial \Pi_i} = 2 \sum_{j=1}^M \left[\sum_{i=1}^N K_{ji} \Pi_i - I_j \right] K_{jn} + 2\lambda \sum_{i=1}^N H_{ni} \Pi_i = 0 \quad (3.21)$$

with $n = 1, \dots, N$.

By interchanging the order of the summation, we can write Eq. 3.21 as

$$\sum_{i=1}^N \left[\left(\sum_{j=1}^M K_{ji} K_{jn} \right) + \lambda H_{ni} \right] \Pi_i = \sum_{j=1}^M K_{jn} I_j. \quad (3.22)$$

Such transformations are explained in § 15.4 of the Numerical Recipes. Eq. 3.22 becomes much more friendly and convenient when written in a vector notation as

$$(\mathbf{K}^T \cdot \mathbf{K} + \lambda \mathbf{H}) \cdot \Pi = \mathbf{K}^T \cdot \mathbf{I}. \quad (3.23)$$

Let us now consider each term in this equation. The sum into brackets is equivalent to a single $N \times N$ matrix \mathcal{A} while the product $\mathbf{K}^T \cdot \mathbf{I}$ gives an N component vector \mathcal{B} . Consequently, Eq. 3.23 is rewritten in a very simple form as

$$\mathcal{A} \cdot \Pi = \mathcal{B}. \quad (3.24)$$

First, it is worth noticing the resemblance with Eq. 3.8 except that Eq. 3.24 only involves *square matrices* whereas we previously had to deal with *singular matrices* that required a special Singular Value Decomposition. Here, the regularization got rid of this problem to provide a stable system of N equations for N unknowns. Different approaches are possible to solve the last equation, amongst them the *LU* decomposition, which is presented in § 2.3 of the Numerical Recipes. However, we used the SVD procedure as it can be applied to problems involving both singular and square matrices. Moreover, it appeared that SVD yielded more stable solutions than the *LU* decomposition.

3.3 Quantification using Regularisation Method

3.3.1 Description of REGULAR

In the previous section, the mathematical foundations of the regularization method have been exposed with a particular focus on the MQMAS case. We obtained Eq. 3.24, which resolved the problem of degeneracy as \mathcal{A} is now a

square matrix. The main matrices have also been given. Let us recall that the vector \mathbf{I} corresponds to one row of the experimental 2D spectrum, the matrix \mathbf{H} is chosen to be the first derivative as expressed in Eq. 3.18, λ is a constant and Π the function of distribution that we want to calculate. Yet, the elements of the matrix \mathbf{K} (Eq. 3.9) have still to be clearly defined. Thus, as \mathbf{K} contains the simulated part through the matrix elements $I_0(\delta_2^i; P_Q^j)$, we need a program able to predict both the shape and the intensity of the resonance which depend on several parameters, especially the quadrupolar strength P_Q . The next two sections will be dedicated to the presentation and description of the program PULSAR that we used. We will also broach the problem of initiating the regularisation.

PULSAR

In order to get a function of distribution Π with corrected relative intensities of the different sites, we must be able to simulate powder lineshapes taking into account most relevant experimental parameters that are introduced in the pulse sequence, as well as the parameters which concern the nucleus itself. PULSAR has been built by Prof. Amoureux.⁸ Its primary function is to predict the NMR response resulting from any pulse sequence applied on quadrupolar and spin-1/2 nuclei in powder samples. Since PULSAR is based on the complete calculation of the density matrix, we will now shortly introduce this concept.

The use of the density matrix makes it much easier to follow the evolution of the spin system during and after one or several pulse excitations. The evolution of the density matrix $\rho(t) = |\Psi(t)\rangle\langle\Psi(t)|$ where $\Psi(t)$ is the state vector deduced from the Schrödinger's equation, is monitored by the Liouville-Von Neumann's equation

$$\frac{d\rho(t)}{dt} = -\frac{i}{\hbar} [\mathbf{H}(t), \rho], \quad (3.25)$$

where $H(t)$ is the total Hamiltonian matrix which describes the spin system at time t . The solution $\rho(t) = \mathbf{U}(t) \rho(0) \mathbf{U}^{-1}(t)$ of such differential equation is calculated recursively using its initial value $\rho(0)$ at $t = 0$. $\mathbf{U}(t)$ is commonly called the propagator matrix. For an isolated nucleus with a spin number I , the density matrix is composed of $(2I + 1)^2$ ρ_{nm} elements (complex numbers) which correspond to $(n - m)$ -quantum level coherences which were introduced in previous chapters. Fig. 3.7 shows both the density matrix for spin 5/2 and the correspondence between energy levels m, n and coherence orders p .

Referring to PULSAR, Prof. Amoureux considered separately periods where rf pulses are applied and periods of free precession present within the pulse sequence. During the excitation, the Average Hamiltonian Theory is used for the reasons given in Chapter 1. This means that the pulse is truncated into short delays $\Delta\tau$ during which the Hamiltonian is considered time-independent (cf. Fig. 3.8). Under the effect of a rf field during a delay $\Delta\tau$, the Hamiltonian matrix is no longer diagonal in the Zeeman basis. In our case, the truncation also called the “leap-frog” method grandly simplifies the diagonalisation of the matrix \mathbf{H} which is necessary to keep the secular part of the Hamiltonian. Successive iterations lead to the determination of all the elements in the density matrix at time τ .

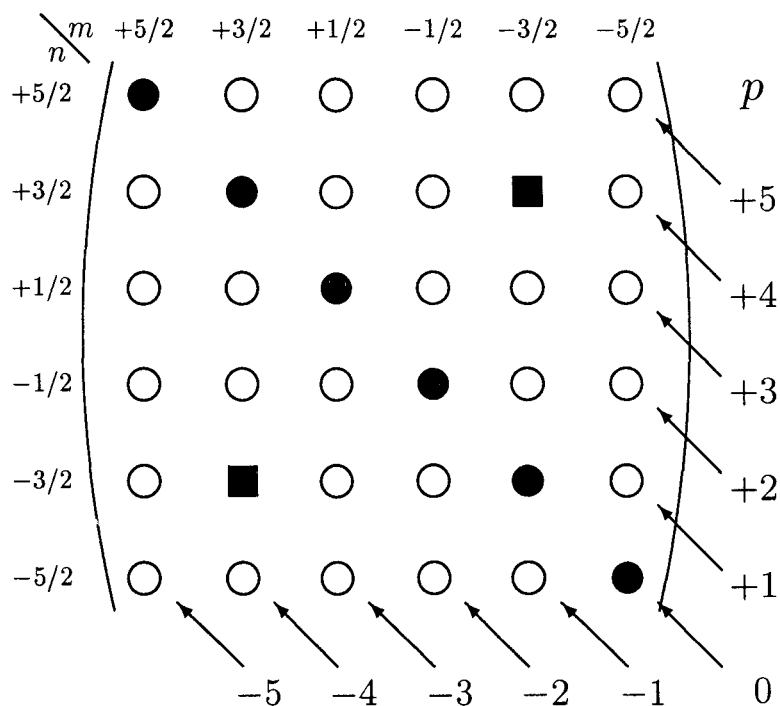


Figure 3.7: Density matrix for a spin $I = 5/2$. Diagonal elements (plain dots) correspond to the Zeeman transitions. Plain squares represent the symmetrical triple-quantum coherences ($\pm 3/2 \longleftrightarrow \mp 3/2$) which are excited in the MQMAS experiment.

At the end of a pulse excitation and during a delay t that separates 2 pulses, the Hamiltonian is represented by a diagonal matrix. Therefore, the amplitude of each coherence (calculated from the real and imaginary parts of ρ_{nm}) in the density matrix is unchanged after t . However, the phase of a coherence ρ_{nm} changes with a frequency proportional to the gap between the two Zeeman energy levels n and m . It must be noted that PULSAR does not take into account relaxation phenomena due to molecular motions or flip-flop terms.

Applying this procedure as many times as there are pulses and delays in

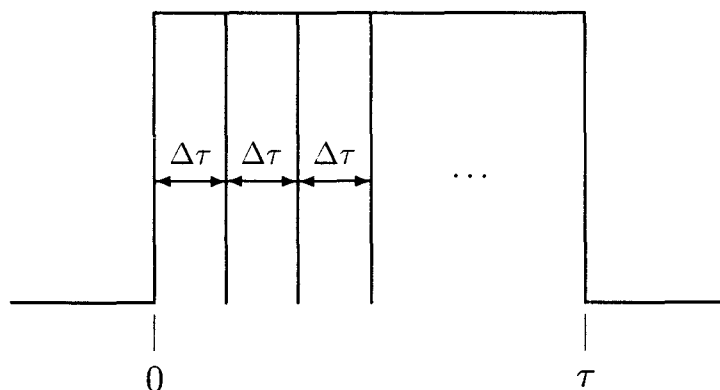


Figure 3.8: So-called “leap-frog” method: the Hamiltonian is considered to be independent during each short delay $\Delta\tau$.

the sequence, we obtain, just prior acquisition, a completely defined density matrix. Then, two approaches are possible for the calculation of the acquired signal: the calculation can either be performed in time or in frequency domain. In the time domain, each point of the FID must be calculated. Such an approach requires as many spatial powder averagings as points in the FID. The powder spectrum is obtained after a Fourier transform of the FID. On the other hand, the second approach (in frequency domain) takes full advantage of the information provided by the density matrix. Indeed, for a crystallite the intensity of the resonances (central and satellite ones) is just given by the modulus of the off-diagonal matrix elements (plain dots in Fig. 3.9). The frequency at which the resonance will appear is furthermore given by the gap between successive Zeeman energy levels (arrows in Fig. 3.9). Finally, a powder averaging is performed in the frequency domain to give the lineshape pattern. The FID is also obtained by an inverse Fourier transform of the spectrum. Of course, the second method is the one used in PULSAR as it is much less time consuming.

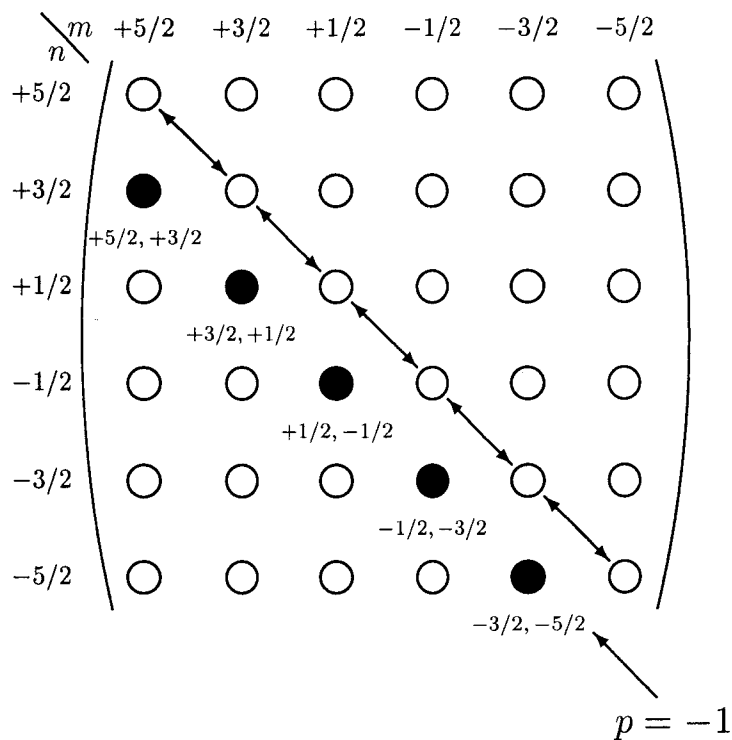


Figure 3.9: Representation of the density matrix for a spin $I = 5/2$. Off-diagonal complex elements (plain dots) correspond to the acquired signal (single-quantum transition). Real and imaginary values yield the intensity of the central and satellite transitions for one crystallite orientation. The difference calculated between Zeeman energy levels (diagonal elements) provides the position of each resonance.

Let us now enumerate the different features of PULSAR.² First, calculations for static samples and rotating samples about one (MAS, VAS, MQMAS) or two axes (DOR, DAS) can be achieved taking into account all interactions (inhomogeneous dipolar, J scalar coupling, CSA and first- and second-order quadrupolar interactions) during both delays and pulses. Only “flip-flop” dipolar terms and relaxation phenomena are neglected. Any multiple-pulse sequence involving one or several nuclei can be simulated rendering the program attractive for the development of double and triple resonance experiments (CP-MAS, REDOR, etc.)

Choice of Parameters in REGULAR

It is crucial to properly select several parameters if a realistic and stable solution is to be determined. First, the experimental dataset that will be used later on to create the vector \mathbf{I} , must be read through a graphic interface. This way, the spectral windows can be adjusted manually so that the portion of the spectrum to be quantified can be selected (the tetrahedral region only, for example). Sometimes, the spectral window in δ_2 must be reduced as it is often taken too wide compared to the region where the resonances appear. Furthermore, one must make sure that the size of the chosen sub-dataset is sufficient compared to the size of the desired solution. In concret terms, we found that for an experimental dataset of 256×128 , the number N of P_Q values should not exceed 48. Indeed, when we increased N we observed a deterioration of the stability in the solution and consequently, we obtained a deterioration of the quality of the solution. Therefore, a medium resolution ($N = 32$ or 48) was preferred in order to preserve the stability. Note that it is important not to have intense signals close to the limits of the selected

sub-dataset. This would result in strong oscillations of the solution.

The second step concerns the simulation of a set of 1D spectra for N different values of P_Q , taking into account the most relevant experimental parameters used in PULSAR. As explained in the previous section, the values of P_Q as well as the weighting coefficients are calculated using a quadrature scheme (subroutine `gauleg`). Nevertheless, one should take advantage of the fact that an average P_Q value can be directly read from the 2D spectra for each site. This averaged value will be useful to select a proper range for this parameter. Fig. 3.10 shows the 1D spectra that were calculated by PULSAR for different P_Q values given by `gauleg`. For the sake of clarity, we only presented 10 of the spectra instead of 32 or 48. It must be pointed out that since PULSAR predicted the intensity of the lineshape for each P_Q value, we could expect the relative proportion of the different sites to be corrected after inversion of the experimental dataset.

For the regularisation, we only considered the distribution of the chemical shift and the quadrupolar constant, deliberately ignoring the asymmetry parameter η_Q . In fact, we replaced the quadrupolar constant C_Q by the second-order quadrupolar effect P_Q , which contains both C_Q - and η_Q -dependencies. Nevertheless, this approximation was unlikely to alter considerably the quantification. Indeed, Figs. 3.3 show that the difference in efficiency of the 3QMAS experiment for $\eta_Q = 0$ and $\eta_Q = 1$ does not exceed 15%, whatever the rf field. Consequently, it can be considered that a simulation of the 1D spectra using PULSAR, taking an average value for η_Q , will minimize the error. In our studies, the distribution was such that the quadrupolar pattern could not reveal a particular value of η_Q . Therefore, we used an average value of $\eta_Q = 0.6$ and we estimated the error of the quantification to be inferior to 10%.

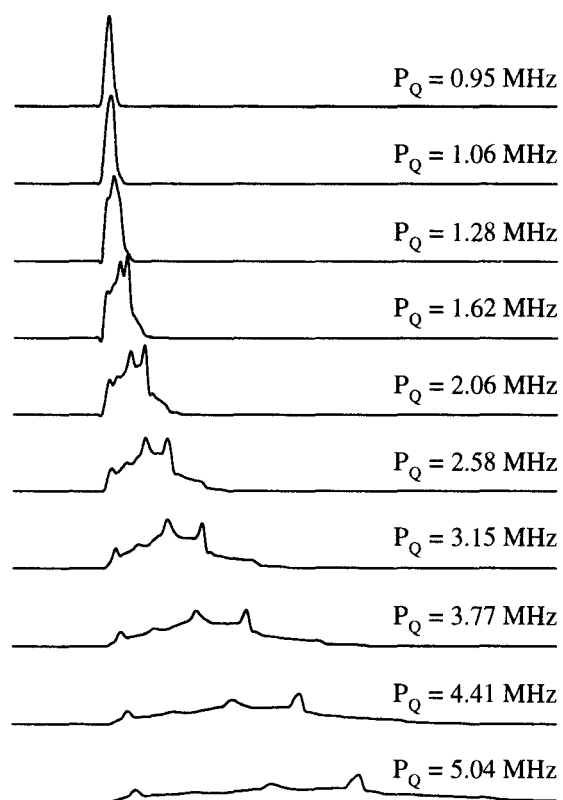


Figure 3.10: 1D spectra generated by PULSAR, using the 3QMAS z -filter pulse sequence, and its particular experimental specifications. The spinning speed was taken equal to 15 kHz for the calculation.

Finally, PULSAR needs experimental parameters for the simulation. They are summarised in Table 3.2. The values are given for the ^{27}Al MQMAS experiments that we have performed in our studies.

spin number	5/2
p -quantum	± 3
rf power	≈ 250 kHz
pulse lengths (1st and 2nd pulses)	$\tau_1 = 2.2\mu\text{sec}$ $\tau_2 = 0.65\mu\text{sec}$
Larmor frequency ω_0	104.26 MHz
Rotor speed ω_r	14.925 kHz

Table 3.2: Most relevant experimental parameters that are introduced in the PULSAR calculation.

3.3.2 Application to the Quantification of ^{27}Al and ^{17}O MQMAS spectra

Quantification of ^{27}Al sites in $\text{AlPO}_4 - 11$

The aim of this application on the $\text{AlPO}_4 - 11$ was initially to verify the accuracy of the calculation using REGULAR. Therefore, we chose an aluminophosphate sample, for which the distribution of the ^{27}Al environment is not very strong. Moreover, the relative proportion of the five ^{27}Al sites was well known, following the results published by previous studies and those obtained with the methods of quantification presented in section 3.1. The figure 3.11 is the canonical representation obtained by inversion of the 2D ^{27}Al 3QMAS spectrum of $\text{AlPO}_4 - 11$.

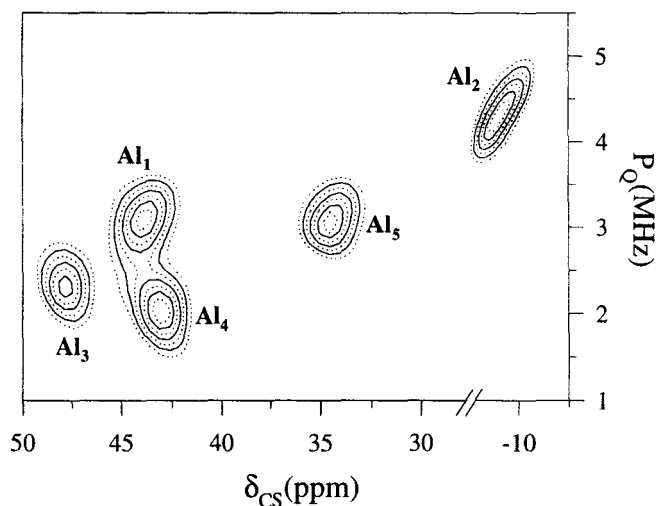


Figure 3.11: Calculated quantification of the ^{27}Al 3QMAS spectrum of $\text{AlPO}_4 - 11$ using the program REGULAR.

First, we notice that the five sites are retrieved. They appear at the position P_Q and δ_{CS} , which corresponds to the values we previously determined by projection onto the δ_2, δ_{iso} axes of the 2D 3QMAS spectrum. The fact that the quadrupolar parameters P_Q and the chemical shifts δ_{CS} experienced by the different sites, are spread over a wide range of values renders a satisfying representation. Indeed, the spots on Fig. 3.11 barely overlap. The main purpose of the inversion of the MQMAS spectrum using the regularisation is still to obtain an accurate quantification of the crystallographically non-equivalent sites. For the aluminophosphate $\text{AlPO}_4 - 11$, REGULAR determines that the 5 sites are indeed in the same ratio of 1:1:1:1:1 within an precision of 5%. In fact, the intensity of the site Al_3 is slightly underestimated compared to the four other sites which are in the same proportion. Finally, we observed that the spots on the canonical representation have a minimum width on both dimensions even when applied to well-crystallised

samples like the $\text{AlPO}_4 - 11$. So far, we have not been able to go under 0.5 MHz and 2 ppm for the widths of the spots on the P_Q and δ_{CS} axes, respectively. This is due to the mathematical inversion which introduces a broadening. Nevertheless, as the crystallinity rate goes down, this effect is lost in the broadening resulting from the distribution of surroundings.

Quantification of ^{17}O sites in zeolite ZSM - 5

Later, we applied the regularisation method to the determination of the relative proportions of the different ^{17}O sites in a zeolite ZSM - 5. The quantitative results using REGULAR, are complementary to the work that was published in collaboration with the group in Leipzig (Prof. D. Freude).¹¹ The ^{17}O 3QMAS spectrum of the zeolite has been acquired on a very high magnetic field of 17.6 T (Bruker DMX 750) at a Larmor frequency of 101.7 MHz. The sample was spun at 17.5 kHz. The rf field of the two hard pulses (z -filter sequence) was set to 100 kHz using a ^{17}O water sample and pulse lengths were experimentally adjusted for maximum signal to $3.4\mu\text{s}$ and $1.2\mu\text{s}$ for the first and second pulse, respectively. The z -filter pulse (third pulse) was a selective 90° pulse of length equal to $50\mu\text{s}$.

The ^{17}O MAS spectrum of ZSM - 5 (Fig 3.12) exhibits a featureless wide resonance ($\approx 30\text{ppm}$) that does not provide much information on the ^{17}O environments. This broad line may be due to either a strong distribution (C_Q and/or δ_{CS}) of the ^{17}O environment or to the presence of several ^{17}O sites, the resonance of which would strongly overlap. On the other hand, the 3QMAS spectrum shown in Fig. 3.13, completely removes such an ambiguity as it clearly separates two ^{17}O sites, which were attributed to Si - O - Si and Si - O - Al environments (cf. Amoureux et al.¹¹). Moreover, we observe that not only are the two resonances barely distributed along the CS and QIS

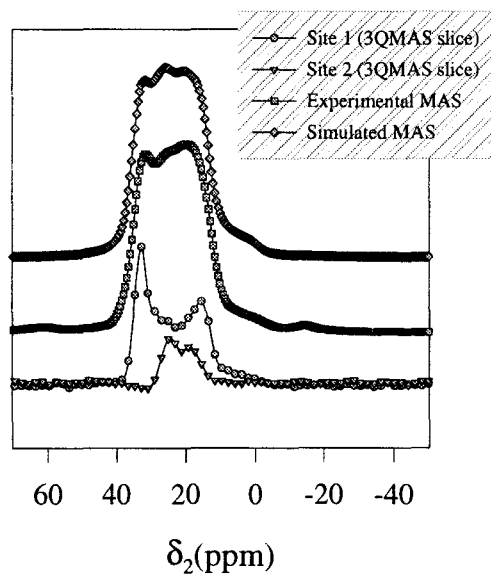


Figure 3.12: ^{17}O 3QMAS slices (bottom), experimental ^{17}O MAS spectrum (middle) and simulated ^{17}O MAS spectrum using QUASAR (top) of the zeolite ZSM – 5.

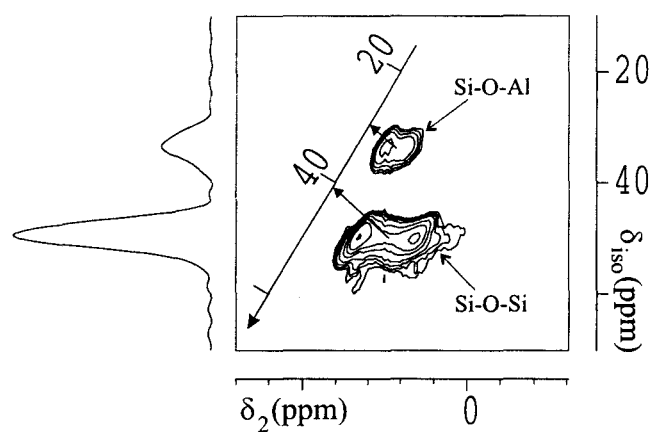


Figure 3.13: 2D ^{17}O 3QMAS spectrum and its isotropic projection for the zeolite ZSM – 5.

axes but also that the lineshapes exhibit singularities, which are typical of quadrupolar nuclei. Therefore, a separate simulation of each site is possible in order to deduce both quadrupolar and chemical shift parameters. It is pointed out that the asymmetry parameter η_Q can be determined with high precision. This simulation provides a set of parameters for each environment, as summarised in Table 3.3. These values have been used to evaluate the relative proportion of the two sites by fitting of the MAS spectrum. We found that the Si – O – Si and Si – O – Al sites were in a ratio of 80/20. 3QMAS slices as well as the MAS simulated spectrum are compared to the experimental MAS spectrum in Fig. 3.12.

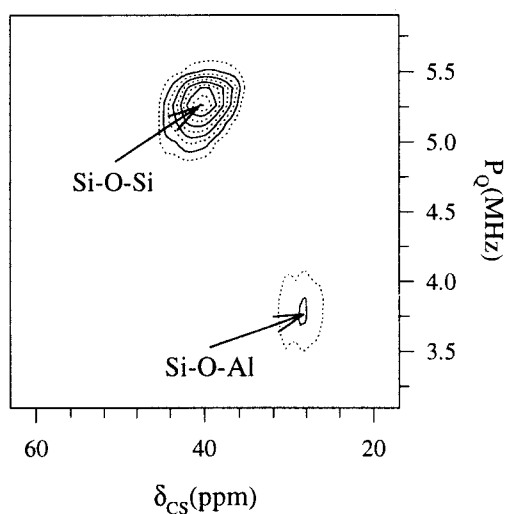


Figure 3.14: Canonical representation of the distribution resulting from the inversion of the ^{17}O 3QMAS spectrum (Fig. 3.13). Quantitative results are compared with those obtained by the QUASAR simulation (MAS and 3QMAS slices) in Table 3.3.

The inversion of the 3QMAS spectrum is presented in Fig. 3.14. All experimental parameters have been introduced in the calculation of the 1D spectra

site		Si – O – Si	Si – O – Al
QUASAR	conc.	80%	20%
	δ_{CS}	40 ppm	30 ppm
	C_Q	5.3 MHz	3.5 MHz
	η_Q	0.12	0.29
	P_Q	5.31 MHz	3.6 MHz
REGULAR	conc.	82%	18%
	δ_{CS}	40 ppm	29 ppm
	C_Q	—	—
	η_Q	—	—
	P_Q	5.25 MHz	3.75 MHz

Table 3.3: Comparison of quantitative results obtained with QUASAR (3QMAS slices and MAS simulations) and with REGULAR (inversion of 2D 3QMAS spectrum).

(PULSAR). Since the two sites possess a similar asymmetry parameter (0.12 and 0.29), we fixed this constant to a mean value of 0.2. As previously explained, the choice of η_Q is not critical and other values have been tried, giving a quantitative result, within 10% of accuracy. Table 3.3 also presents the δ_{CS} , P_Q parameters as well as the relative proportion of Si – O – Si and Si – O – Al sites which were deduced from Fig. 3.14. Quantitative results are in good agreement with the QUASAR simulation of the MAS spectrum.

3.4 Conclusion

Even though the MQMAS experiment is a real improvement in solid state NMR due to its efficiency in separating the non-equivalent sites, one must admit that the extraction of a quantitative result is not straightforward. Of course, the resolution provided by the MQMAS spectrum can be complementary to the quantitative MAS spectrum. However, such procedure becomes imprecise when the samples are not well-crystallised, because of the strong broadening that follows the distribution of quadrupolar constant and/or chemical shift.

The method of quantification that we described in this chapter is based on the calculation of the NMR response, using the software PULSAR. The final program, called REGULAR, takes full advantage of the information included in the 2D MQMAS spectrum to quantify the distribution of nucleus surroundings in badly-crystallised or amorphous samples. We obtain a 2D dataset giving the quadrupolar constant versus the chemical shift, in which each site is represented with its correct relative intensity.

So far, we have verified that this new program is able to quantify with accuracy ^{27}Al and ^{17}O nuclei in an aluminophosphate and a zeolite, respec-

tively. Therefore, the last chapter will give the possible applications of both the MQMAS experiment and its quantification to solve different structural problems.

3.5 Quantification des spectres MQMAS (résumé)

3.5.1 Quantification en RMN

Les 2 chapitres précédents nous prouvent que le problème de l'élargissement des bandes de résonance en RMN des noyaux quadrupolaires n'est pas insurmontable. Le MQMAS est aujourd'hui la technique de choix pour obtenir une haute résolution et différencier les sites cristallographiquement différents. Néanmoins, pour que la RMN soit un outil d'investigation complet, il faudrait pouvoir déduire une information sur la population relative des sites présents sur le spectre. Cette section présente les quelques méthodes disponibles pour quantifier les spectres en RMN. Enfin, nous donnerons les limites de ces méthodes lorsque les échantillons étudiés sont sujet à une forte distribution d'environnement.

Spectre MAS

La quantification des spectres MAS obtenus sur des noyaux quadrupolaires n'est pas simple puisqu'elle n'est possible que si l'acquisition a été effectuée selon certains critères. De plus, l'utilisation d'un programme de simulation (QUASAR) capable de prédire l'allure d'une résonance à partir des paramètres quadrupolaires est indispensable.

Nous avons vu dans le premier chapitre que l'élargissement anisotrope d'une résonance était dû aux multiples orientations possibles des cristallites. En fait, pour un site donné, chaque cristallite possède une force quadrupolaire qui dépend de l'orientation de son PAS par rapport au champ statique. Par conséquent, les conditions d'excitation (longueur de pulse, champ rf) doivent

être judicieusement choisies pour ne pas favoriser certaines orientations du PAS par rapport à d'autres. Ainsi, en utilisant un fort champ rf ("hard pulse"), l'excitation est non sélective et tous les cristallites sont excités uniformément, rendant possible la quantification du spectre. Cependant, comme l'amplitude de l'interaction quadrupolaire est bien souvent grande par rapport au champ rf disponible, les conditions d'excitation sont sélectives, favorisant certaines transitions (transition centrale) au détriment d'autres transitions (satellites).

Lorsque l'on observe l'intensité de la transition centrale en fonction de la durée d'impulsion τ_1 , pour plusieurs valeurs de l'interaction quadrupolaire (cf. Fig. 3.2), nous remarquons que la partie commune aux différentes courbes correspond aux faibles valeurs de τ_1 ($< 1\mu\text{sec}$). Par conséquent, le choix du champ rf et de la longueur de l'impulsion est le résultat d'un compromis : le champ rf doit être le plus faible possible afin d'être le plus sélectif possible mais une valeur trop faible pourrait se révéler insuffisante pour exciter entièrement la transition centrale. Il a ainsi été démontré que la valeur optimale du champ rf est à peu près égale à la largeur de la transition centrale divisée par $I + 1/2$.²

Une fois le spectre MAS obtenu, il faut pouvoir simuler les bandes de résonance provenant des différents sites en utilisant un programme qui tiendra compte des nombreux paramètres qui influent directement sur l'allure du spectre. En ce qui nous concerne, nous utilisons QUASAR qui est capable d'extraire les paramètres représentatifs des 4 interactions les plus importantes (couplage J, couplage dipolaire, CSA et quadrupolaire) par "fitting" du spectre MAS. Cependant, QUASAR étant basé sur une méthode des moindres carrés, l'incertitude sur un très grand nombre de paramètres réduit considérablement les chances d'obtenir une solution unique. De plus, les recouvrements des résonances compliquent le spectre. L'analyse avec QUASAR

devient alors difficile puisque l'on ne connaît même pas le nombre exact de sites, paramètre qui est essentiel pour initier la simulation.

Grâce au MQMAS et au MAS

Le principal avantage du MQMAS par rapport au MAS est qu'il permet de déterminer facilement le nombre de sites cristallographiques. Néanmoins, le spectre MQMAS n'est pas quantitatif. Les courbes 3.3 sont le résultat du calcul de l'efficacité de l'expérience MQMAS en fonction de la constante quadrupolaire C_Q et pour 3 champs rf. Même si ces courbes confirment le fait que l'utilisation d'un champ rf le plus élevé possible fournit un meilleur rapport S/N, elles montrent surtout que l'intensité d'une résonance sur un spectre MQMAS varie considérablement en fonction de son environnement. La méthode de quantification qui apparaît donc est de déterminer le nombre de sites grâce au spectre MQMAS et d'introduire cette information dans QUASAR pour fitter le spectre MAS.

Cependant, l'analyse du spectre MQMAS permet de réduire encore plus le nombre de paramètres à faire varier dans la simulation du spectre MAS. D'abord, nous avons vu dans le chapitre 2 que les valeurs de P_Q et δ_{CS} pouvaient être calculées par simple projection sur les axes CS, δ_2 et δ_{iso} . Il est même possible parfois d'extraire la bande centrale de chaque site sur le spectre MQMAS et de la simuler avec QUASAR afin d'obtenir des valeurs précises pour les 3 paramètres suivants δ_{CS} , C_Q et η_Q . Finalement, dans ce cas très favorable, tous les paramètres qui définissent l'allure d'une résonance sont connus et servent de point de départ à la simulation du spectre MAS, de sorte qu'il ne reste plus qu'à faire varier la proportion relative des différents sites.

Projection isotrope MQMAS

La dernière méthode de quantification des spectres RMN consiste à essayer de corriger les intensités relatives déduites de la projection isotrope sur le spectre MQMAS. En effet, grâce aux programmes de calcul qui ont été développés dans notre laboratoire, notamment PULSAR,⁸ il est possible de prédire la réponse d'un cristallite à une excitation donnée. Par exemple, les courbes 3.3 ont été calculé par PULSAR. Elles permettent de corriger les intensités relatives déduites du fit de la projection isotrope, à condition de connaître la constante quadrupolaire C_Q (ou approximativement le P_Q) de chaque site et par conséquent la position du site sur la courbe calculée pour le champ rf expérimental. Cette valeur de P_Q est donc extraite du spectre MQMAS par simple projection sur les axes (cf. 2.3.2).

Dans la partie en anglais, traitant des problèmes de quantification en RMN, (cf. section 3.1) vous trouverez le résultat obtenu sur l' $\text{AlPO}_4 - 11$ pour chaque méthode précédemment citée. Pour un tel échantillon bien cristallisé, la proportion relative des 5 sites ^{27}Al est obtenue avec une bonne précision (< 10%).

Problèmes liés à la distribution d'environnement

Nous allons expliquer dans cette section pourquoi les 3 méthodes précédentes donnent des résultats moyens, parfois complètement erronés, lorsque l'échantillon étudié est amorphe ou présente une distribution d'environnement.

De façon générale, une distribution d'environnement a pour effet d'élargir les résonances, que ce soit sur le spectre MAS ou sur le spectre MQMAS.¹² En effet, une légère variation de l'environnement pour un site donné va conduire à une légère variation des paramètres quadrupolaires (C_Q et δ_{CS}) définissant ce site. Ainsi, un site cristallin n'est plus représenté par un bande de résonance

dont l'enveloppe dépend d'une seule valeur de C_Q et la position du centre de gravité d'une seule valeur de δ_{CS} . Le spectre MAS (tout comme le spectre MQMAS) est alors composé d'un nombre infini de spectre MAS dont les paramètres C_Q et δ_{CS} varient légèrement les uns par rapport aux autres. L'allure du spectre MQMAS lors d'une distribution de déplacement chimique δ_{CS} est représentée schématiquement sur la figure 3.5. Nous observons un élargissement des projections MAS et isotropes, rendant difficile leur simulation. La figure 3.6 représente une distribution gaussienne de constante quadrupolaire C_Q . Nous remarquons l'allure dissymétrique de la projection isotrope qui rend encore plus incertaine la quantification par fitting de ce spectre (troisième méthode). Enfin, les méthodes précédentes sont toutes basées sur l'hypothèse que chaque résonance est relié à une seule valeur de C_Q et/ou δ_{CS} ce qui n'est pas le cas lorsqu'il y a une distribution d'environnement. Il n'est donc pas réaliste de vouloir déterminer une information quantitative précise à partir des projections MAS ou MQMAS. La section suivante présente le calcul de quantification que nous avons développé et qui permet de déduire du spectre 2D la proportion relative des sites cristallographiques.

3.5.2 Méthode de Régularisation

Nous venons de voir que l'intensité d'une résonance sur un spectre MQMAS, pour un échantillon désordonné, pouvait être considérée comme la somme d'un nombre infini de résonances dont l'un des paramètres C_Q ou δ_{CS} (ou les deux) varie légèrement. Mathématiquement, l'intensité d'une résonance $I(\omega)$ s'écrit comme l'intégrale sur ces deux paramètres d'une fonction $I_0(\omega; \mathbf{R})$ multipliée par la fonction de distribution $\Pi(\mathbf{R})$ (Eq. 3.26).

$$I(\omega) = \int I_0(\omega; \mathbf{R}) \Pi(\mathbf{R}) d\mathbf{R} \quad (3.26)$$

\mathbf{R} représente les paramètres de distribution les plus significatifs (C_Q et δ_{CS} dans notre cas). $I_0(\omega; \mathbf{R})$ est le spectre calculé pour une certaine valeur de C_Q et δ_{CS} . Enfin, $\Pi(\mathbf{R})$ est la fonction de distribution que nous voulons calculer et qui permettra de représenter les intensités corrigées des sites sur un diagramme P_Q en fonction de δ_{CS} .

Après de légères manipulations (cf. paragraphe 3.2.1) et en tenant compte des spécificités de l'expérience MQMAS (axes δ_2 , δ_{iso} , δ_{QIS} , etc.), l'intensité d'une résonance sur le spectre expérimental, peut s'écrire, pour chaque valeur δ_{iso} ,

$$I(\delta_2, \delta_{iso}) = \int_0^{+\infty} I_0(\delta_2; \delta_{CS}(P_Q), P_Q) \Pi(\delta_{CS}(P_Q), P_Q) dP_Q. \quad (3.27)$$

L'équation précédente est de la forme des équations de Fredholm telles qu'elles sont définies dans le Numerical Recipes.¹⁰ Le calcul de la fonction de distribution se fait en 2 étapes : pour une valeur de δ_{iso} , le *noyau* $\Pi(\mathbf{R})$ est évalué pour un nombre N de valeurs de P_Q ($N \approx 32$ ou 48). Cela correspond à une courbe de niveau sur la représentation 2D de la fonction de distribution. En répétant le calcul pour plusieurs valeurs de δ_{iso} , donc de δ_{CS} , nous obtenons les courbes de niveaux qui, une fois reliées donneront la représentation 2D de la fonction $\Pi(\mathbf{R})$. Le calcul numérique de $\Pi(\mathbf{R})$ nécessite le remplacement de l'intégrale par une somme discrète sur les N valeurs de P_Q (Eq. 3.28).

$$I(\delta_2, \delta_{iso}) \approx \sum_{i=1}^N W_i I_0(\delta_2; \delta_{CS}^i, P_Q^i) \Pi(\delta_{CS}^i, P_Q^i) \quad (3.28)$$

Les coefficients W_i permettent de donner plus de poids à certaines valeurs de P_Q . Dans notre cas, nous avons considéré que la distribution était gaussienne et les coefficients ont été calculés grâce à l'algorithme `gauleg` basé sur la quadrature de Gauss-Legendre. La dernière équation s'écrit alors sous forme matricielle $\mathbf{K} \cdot \Pi = \mathbf{I}$ (cf. Eq. 3.9).

Il existe 2 méthodes pour calculer la fonction $\Pi(\mathbf{R})$. La première consiste à choisir une fonction $\Pi(\mathbf{R})$ et de calculer le spectre 2D MQMAS. La comparaison des spectres calculés et expérimentaux permet alors de savoir si l'hypothèse faite au départ sur la fonction est correcte. Par itération successive, nous pouvons espérer améliorer l'accord entre l'expérience et la simulation. La deuxième méthode que nous avons utilisée, consiste à inverser le spectre pour obtenir la fonction de distribution, sans faire d'hypothèse de départ sur sa forme.

L'inversion d'une telle équation n'est pas simple mathématiquement. En effet, la matrice \mathbf{K} , de dimension $M \times N$ est une matrice singulière ($M \gg N$). Ainsi, l'inversion d'un tel système d'équations, sans précaution, a de grande chance de fournir une solution instable. Nous avons donc opté pour une méthode de régularisation. Généralement, l'accord entre l'expérience \mathbf{I} et le modèle \mathbf{K} se fait en minimisant le reste $\kappa = \mathbf{K} \cdot \Pi - \mathbf{I}$. Dans la régularisation, nous ne minimisons pas κ mais la somme $\chi = \kappa + \lambda \rho$. Le rôle du terme supplémentaire ρ est de lisser et stabiliser la solution $\Pi(\mathbf{R})$ déduite de l'inversion. Nous avons choisi de prendre ρ égale à la dérivée première de $\Pi(\mathbf{R})$ par rapport aux paramètres de distribution C_Q et δ_{CS} (la matrice \mathbf{H} de dimension $N \times N$ (cf. Eq. 3.18) décrit la dérivée première). λ est un coefficient qui doit être ajusté "à la main" et qui permet de plus ou moins lisser la fonction. Il est bien entendu que le lissage se fait au détriment de l'accord entre le modèle et l'expérience de sorte qu'un compromis doit être trouvé pour λ .

Le reste χ à minimiser s'écrit alors,

$$\chi = (\mathbf{K} \cdot \Pi - \mathbf{I})^2 + \lambda(\Pi \cdot \mathbf{H} \cdot \Pi), \quad (3.29)$$

et les différentes matrices qui composent cette équation sont données explicitement dans la partie en anglais.

Finalement, la minimisation revient à annuler la dérivée de χ par rapport aux paramètres $\Pi_i = \Pi(\delta_{CS}^i, P_Q^i)$ ($i = 1, \dots, N$) (cf. page 160). Après quelques transformations, nous ramenons le problème au système matricielle

$$\mathcal{A} \cdot \Pi = \mathcal{B}, \quad (3.30)$$

qui a l'avantage de ne contenir que des matrices carrés puisque \mathcal{A} et \mathcal{B} sont toutes deux de dimension $N \times N$. Les définitions de \mathcal{A} et \mathcal{B} sont déduites de l'équation 3.23. Le calcul de la fonction Π par inversion de l'équation 3.30 est réalisé simplement en utilisant l'une des 2 décompositions proposées dans le Numerical Recipes (décomposition LU ou SVD). Nous avons essayé les 2 algorithmes pour en déduire que la méthode SVD donnait une solution plus stable.

3.5.3 Régularisation appliquée aux spectres MQMAS

La plupart des éléments qui composent l'équation 3.23 ont été précédemment défini. Cependant, il reste encore à calculer les éléments $I_0(\delta_2^i; P_Q^i)$ de la matrice \mathbf{K} . Pour cela, nous avons besoin d'un programme de simulation capable de prédire l'allure et l'intensité d'une bande de résonance en fonction des paramètres expérimentaux et des paramètres du noyau. Nous présenterons dans un premier temps les caractéristiques du programme PULSAR,

développé par le Prof. Amoureux. Puis, les paramètres essentiels permettant d'initier le calcul de quantification des spectres MQMAS seront brièvement passés en revue.

PULSAR

La simulation des spectres 1D $I_0(\delta_2^i; P_Q^i)$ est une partie très importante de la quantification. En effet, comme l'intensité des résonances dépend de l'environnement du noyau, de la séquence d'impulsions utilisée, de nombreux paramètres doivent être introduits dans le calcul pour espérer obtenir un résultat précis. Le programme PULSAR, basé sur le calcul complet de la matrice densité, remplit ces conditions. La réponse d'un spin (noyaux 1/2 ou quadrupolaire) dans un échantillon de poudre, tournant autour d'un ou deux axes (VAS, MAS, MQMAS, DOR, DAS) peut être simulée en tenant compte de toutes les interactions (couplage scalaire J, inhomogénéité dipolaire, CSA, et interaction quadrupolaire aux 1er et 2nd ordres) pendant les pulses et les délais. Toutes les séquences de pulses faisant intervenir un ou plusieurs noyaux peuvent être simulées ce qui rend le programme particulièrement attrayant pour le développement des expériences de double et de triple résonance (CP-MAS, REDOR).

L'opérateur d'évolution de la matrice densité $\rho(t)$ est déduit de l'équation différentielle Eq. 3.25 de façon récursive à partir de sa valeur initiale. Dans la section 3.3.1, nous donnons les correspondances entre les cohérences à simple et à multiple quanta et les éléments de la matrice densité (cf. Fig. 3.7). Pour le calcul de l'opérateur densité dans PULSAR, Prof. Amoureux a considéré séparément les périodes pendant lesquelles les pulses sont appliqués et les périodes de précession libre présentes dans la séquence de pulses. Ainsi, pendant les excitations radio-fréquence, la théorie de l'Hamiltonien moyen est

utilisée : les pulses sont tronqués en petits incréments $\Delta\tau$ pendant lesquels l'Hamiltonien est considéré indépendant du temps. Le problème revient alors à diagonaliser l'Hamiltonien après chaque $\Delta\tau$ afin de ne garder que sa partie séculaire. Par incrément successif, nous déterminons les éléments de la matrice densité à la fin de chaque pulse. Pendant les délais, les cohérences subissent un déphasage dont la vitesse correspond à l'écart entre les niveaux d'énergie Zeeman. Les autres phénomènes, tels que la relaxation et la diffusion de spin réversible (termes de flip-flop) ne sont pas pris en compte par PULSAR. Cette procédure s'applique autant de fois qu'il y a de pulses et de délais dans la séquence.

Enfin, l'acquisition se fait dans le domaine fréquentiel en utilisant toute l'information que contient la matrice densité : la fréquence de résonance d'une cristallite correspond à l'écart entre les niveaux d'énergie Zeeman alors que son amplitude est donnée par le module des éléments complexes à simple quanta ($p = -1$ sur la figure 3.9). Enfin, une moyenne de poudre, effectuée dans le domaine fréquentiel, nous fournit le spectre simulé.

Principaux paramètres de REGULAR

Il est évident que la quantification par inversion des spectres MQMAS n'est pas simple et direct. Certaines précautions sont nécessaires lors du choix des paramètres initiaux.

Dans le programme que nous avons développé (REGULAR), une interface graphique permet de sélectionner manuellement sur le spectre MQMAS, une fenêtre spectrale. Pour chaque valeur de δ_{iso} , nous créons alors un vector \mathbf{I} . Nous avons remarqué que le nombre de points expérimentaux devait être suffisamment grand par rapport au nombre N de valeurs de P_Q . En effet, une valeur de N trop importante (> 48) rend la solution instable. De plus,

la présence de résonances intenses en bordure de fenêtre spectrale conduit, suite à l'inversion, aussi à une solution oscillante.

La deuxième étape consiste à simuler les spectres 1D à l'aide de PULSAR pour les N valeurs de P_Q fournies par la quadrature de Gauss-Legendre. En calculant approximativement la force de l'interaction quadrupolaire (P_Q) par projection sur le spectre MQMAS (cf. Chapitre 2), il est possible de définir un domaine de valeurs de P_Q afin de ne pas calculer des spectres 1D inutiles pour l'inversion. La figure 3.10 montre quelques-uns des spectres simulés par PULSAR. Enfin, les paramètres expérimentaux dont PULSAR se sert sont résumés dans la table 3.2.

Dans la section 3.3.2, nous présentons deux exemples de quantification de sites ^{27}Al et ^{17}O à partir des spectres 3QMAS d'échantillons microporeux.

Dans un premier temps, nous avons étudié l'échantillon d' $\text{AlPO}_4 - 11$ puisque la proportion relative des différents sites nous était connue et permettait donc de vérifier l'exactitude de nos calculs. L'inversion par régularisation conduit à la représentation canonique (cf. Fig. 3.11) de la fonction de distribution $\Pi(\delta_{CS}, P_Q)$. Les 5 sites ^{27}Al de l' $\text{AlPO}_4 - 11$ y apparaissent à la position attendue correspondante aux valeurs approximatives de P_Q et δ_{CS} calculées par projection sur le spectre 2D. L'information la plus intéressante est néanmoins que la proportion relative des sites est dans le rapport 1 : 1 : 1 : 1 : 1 avec une précision inférieure à 5% dans ce cas là.

Nous avons aussi appliqué la méthode de quantification par inversion du spectre 3QMAS à l'étude des sites ^{17}O dans une zéolite ZSM - 5. Le spectre MAS (Fig. 3.12) ne permet pas de différencier les différents environnements cristallographiques à cause du recouvrement des résonances. Par contre, le spectre 3QMAS montre sans aucun doute possible, qu'il existe 2 sites ^{17}O attribuées aux environnements Si - O - Si et Si - O - Al.[REF] Dans un pre-

mier temps, la quantification a été faite à partir des informations provenant des spectres MAS et MQMAS. Nous avons simulé séparément chacune des tranches du spectre 3QMAS afin de déterminer les paramètres quadrupolaires (C_Q, η_Q) et le déplacement chimique δ_{CS} . Ces valeurs ont ensuite été introduites dans la simulation du spectre MAS. La concentration relative des 2 sites ^{17}O était alors le seul paramètre à faire varier et QUASAR a trouvé un rapport de 80/20 pour respectivement les sites Si – O – Si et Si – O – Al. Les différents spectres expérimentaux sont présentés aux figures 3.12 et 3.13 ainsi que la simulation obtenue avec QUASAR.

L'inversion du spectre 3QMAS est représentée sous forme canonique par la figure 3.14. Tous les paramètres expérimentaux, citée dans la section 3.3.2 ont servi à simuler les spectres individuels avec PULSAR. Comme les 2 sites ont un paramètre d'asymétrie très proche (0.12 et 0.29), nous avons choisi une valeur moyenne de 0.2. Le tableau 3.3 permet de comparer les résultats obtenus avec les méthodes (QUASAR et REGULAR). Comme pour l' $\text{AlPO}_4 - 11$, les proportions relatives des 2 sites sont très proches puisque l'incertitude est inférieur à 5%.

Ce chapitre présente une nouvelle méthode de quantification des spectres MQMAS. Par inversion du spectre 2D, nous obtenons une représentation canonique (P_Q versus δ_{CS}) sur laquelle les intensités des différents sites sont corrigées en fonction des paramètres expérimentaux et propres au noyau. Le dernier chapitre concerne les applications du MQMAS et de la quantification à l'étude structurale de matériaux microporeux.



Bibliography

1. FREUDE D. AND HAASE J. *Quadrupole Effects in Solid-State Nuclear Magnetic Resonance*. Springer-Verlag, 1993.
2. DUMAZY Y. *Les Echos Quadrupolaires: Optimization et Applications à la Caractérisation de Composés à base de Sodium, de Cuivre et de Nobium*. PhD thesis, Sciences des Matériaux, Université de Lille I, 1997.
3. FERNANDEZ C., BODART P. AND AMOUREUX J.-P. *Solid-State NMR* 3 (1994), pp. 79–91.
4. FERNANDEZ C., AMOUREUX J.-P., BODART P. AND MAIJANEN A. *J. of Magn. Reson. A113* (1995), pp. 205–209.
5. AMOUREUX J.-P., FERNANDEZ C. AND FRYDMAN L. *Chem. Phys. Lett.* 259 (1996), pp. 347–355.
6. MASSIOT D., TOUZO B., TRUMEAU D., COUTURES J., VIRLET J., FLORIAN P. AND GRANDINETTI P. *Solid-State NMR* 6 (1996), pp. 73–83.
7. FERNANDEZ C., AMOUREUX J.-P., CHEZEAU J., DELMOTTE L. AND KESSLER H. *Microporous Materials* 6 (1996), pp. 331–340.

8. AMOUREUX J.-P., FERNANDEZ C. AND DUMAZY Y. *J. Chim. Phys.* 2 (1995), p. 1939.
9. ZWANZIGER J. *Solid-State NMR* 3 (1994), pp. 219–229.
10. PRESS W., TEUKOLSKY S., VETTERLING W. AND FLANNERY B. *Numerical Recipes in Fortran: The art of Scientific Computing*. Cambridge University Press, UK, 1992.
11. AMOUREUX J.-P., BAUER F., ERNST H., FERNANDEZ C., FREUDE D., MICHEL D. AND PINGEL U. *Chem. Phys. Lett.* 285 (1998), p. 10.
12. BODART P. *J. of Magn. Reson.* (1998), In Press.

Chapitre 4

Quelques Applications du MQMAS

4.1 Etude structurale d'amphiboles

Triple-quantum ^{27}Al and ^{23}Na MAS NMR study of amphiboles

publié dans *J. Chem. Soc., Faraday Trans.*

Les résultats qui ont été publiés dans cet article, constituent une partie du travail que j'ai effectué lors de mes séjours dans l'équipe du Dr. Klinowski, au département de chimie de l'université de Cambridge, UK.

La structure des amphiboles, composées d'octaèdres et de tétraèdres est représentée à la figure 1 de l'article. Notre étude est axée sur l'environnement des sites ^{27}Al présents dans les tétraèdres. Dans le cas de l'Edenite, le spectre MQMAS a révélé la présence de deux environnements tétraédriques différents, qui ont été attribués aux sites Q^3 et Q^2 , dans un rapport de concentration de 9 pour 1 (cf. Fig. 3). Les constantes quadrupolaires, P_Q , calculées à partir du spectre, sont plus grandes que dans les zéolithes, qui elles ne sont composées que des sites Q^4 . L'absence de molécules d'eau dans les

amphiboles contribue aussi à l'augmentation du P_Q . Bien que les données cristallographiques (longueurs et angles de liaisons avec les premiers voisins) montrent sans ambiguïté que l'environnement du site Q^3 est plus symétrique que celui du site Q^2 , les valeurs de P_Q ($P_Q(Q^3) > P_Q(Q^2)$) laissent penser le contraire. Cependant, les amphiboles étant des matériaux compacts, l'influence des seconds et troisièmes voisins n'est pas à négliger et explique ce résultat.

En ce qui concerne la Pargasite, l'expérience MQMAS n'a pas pu mettre en évidence la présence des deux sites tétraédriques (cf. Fig. 4) alors que l'étude par RMN du ^{29}Si (MAS) avait montré indirectement la présence d' ^{27}Al dans les tétraèdres Q^2 . Néanmoins, la forme de la résonance est asymétrique dans la dimension isotrope. Il est donc fort probable que les sites Q^3 et Q^2 aient des valeurs similaires de déplacements chimiques et de constantes quadrupolaires conduisant à un recouvrement des résonances même dans la dimension isotrope.

Dans une deuxième étude, l'expérience MQMAS a confirmé la présence des deux cations M(4) et A dans un rapport 2 :1 (cf. Fig. 6-a). Les constantes déduites du spectre 2D ont permis de simuler le spectre MAS avec le programme QUASAR. Le site M(4) est facilement identifié comme celui subissant la plus forte interaction quadrupolaire, due à un environnement composé d'une part des octaèdres et d'autre part des chaînes de tétraèdres. Par contre, l'environnement du site A est bien plus symétrique. Le spectre MQMAS à 200°C (cf. Fig 6-b) montre clairement que la transition de phase affecte principalement le site A. La mobilité des cations ^{23}Na dans la cavité A expliquerait alors la faible intensité de la résonance sur le spectre MQMAS.

Triple-quantum ^{27}Al and ^{23}Na MAS NMR study of amphiboles

Laurent Delevoye,^{a,c} Shuangxi Liu,^a Mark D. Welch,^b Christian Fernandez,^c Jean-Paul Amoureux^c and Jacek Klinowski^{a*†}

^a Department of Chemistry, University of Cambridge, Lensfield Road, Cambridge, UK CB2 1EW

^b Department of Mineralogy, The Natural History Museum, Cromwell Road, London, UK SW7 5BD

^c Laboratoire de Dynamique et Structure des Matériaux Moléculaires, CNRS URA 801, Université des Sciences et Technologies de Lille, F-59830 Villeneuve d'Ascq, France

DAY

Triple-quantum magic-angle spinning (MAS) enhances the resolution of ^{27}Al and ^{23}Na NMR spectra of amphiboles, although the structural complexity of these compact materials can limit the efficiency of the method in comparison with its performance with molecular sieves. Two aluminium environments are resolved in fluor-edenite, unequivocally demonstrating the presence of some long-range Si—Al disorder. ^{23}Na multi-quantum (MQ)-MAS of hydro-sodian-magnesiocummingtonite (HSMC) at two temperatures demonstrates that a phase transition affects mainly site A. MQ-MAS allows the direct determination of the number of distinct sites with their quadrupolar parameters and isotropic chemical shifts. The technique is very useful for the simulation of MAS spectra.

Amphiboles, hydrous double-chain silicates related to micas, exert a major influence upon the H_2O budgets and the residence and behaviour of protons in the Earth's crust and upper mantle. They are, therefore, of considerable interest to earth scientists in unravelling the sources of deep waters for partial melting, magma production and, ultimately, surface volcanism. The stability and behaviour of amphiboles are affected by cation order/disorder and structural phase transitions. Configurational entropy associated with the former can affect the thermal stability of an amphibole by hundreds of degrees.¹ We focus upon the characterization of Al—Si ordering on tetrahedral sites and the study of a displacive phase transition involving a mobile 'excess' proton in amphiboles, both relevant to upper-mantle processes.

The amphibole structure (Fig. 1) consists of a strongly bonded unit comprising a ribbon of octahedrally coordinated cations sandwiched between two double-chains of tetrahedral sites, giving the characteristic 'I-beam' or 'double-anvil' feature. I-beam units are interconnected by seven- to eight-coordinate cations [the M(4) sites] on the flanks of the I-beams to create a chequer-board motif. Groups of four I-beams surround a large channel site which can be empty or occupied by Na^+ or K^+ . The chemistry of the flanking M(4) sites and channel sites largely defines the three major types of amphibole: $\text{Mg}^{2+}/\text{Fe}^{2+}$ = orthorhombic, $\text{Ca}^{2+}/\text{Na}^+\text{Ca}^{2+}$ = calcic/calcic-sodic and Na^+ , Li^+ = alkali amphiboles.

The 'Q' notation is often adopted for the description of building units in silicates.² In this notation, Q stands for a tetrahedral atom bonded to four oxygen atoms forming a tetrahedron. The superscript n indicates the connectivity, *i.e.* the number of other Q units attached to the unit in question and the central T-atom is written in bold. Q^4 stands for three-dimensionally cross-linked $\text{T}(\text{OT})_4$ units, Q^3 for $\text{T}(\text{OT})_3$ units and Q^2 for $\text{T}(\text{OT})_2$ units. The double-chain comprises two types of tetrahedral sites, T(1) and T(2), corresponding to Q^3 and Q^2 sites. These sites may be filled by Si or a mixture of Al and Si up to 25% Al. X-Ray diffraction provides indirect evidence (average bond lengths) for very strong ordering of Al at T(1) relative to T(2).^{3,4} However, a recent ^{29}Si MAS NMR study of amphiboles synthesized at high temperatures (900–

1100 °C) indicates that there is significant disordering (up to 45% long-range disorder) of Al over T(1) and T(2) sites.⁵

NMR can provide information about two aspects of Si—Al ordering on tetrahedral sites in amphiboles: (i) short-range ordering due to local next-nearest neighbour (NNN) Si—Al clusters; and (ii) long-range ordering of Si and Al between T(1) and T(2) sites. As the Loewenstein rule is obeyed in amphiboles,⁶ all ^{141}Al have Si NNNs. Hence, in the ^{27}Al MQ-MAS experiment we are simply looking at $\text{Al}(\text{Si}_2)$ and $\text{Al}(\text{Si}_3)$ NNN groupings, *i.e.* long-range ordering. In this case, ^{27}Al MQ-MAS is complementary to ^{29}Si MAS NMR in that it allows long-range effects to be treated separately from short-range effects. The extent of long-range order can, in principle, be quantified directly by ^{27}Al MQ-MAS and then used with ^{29}Si MAS NMR results (which contain information on long- and short-range order) to obtain a complete picture of the Si—Al ordering. ^{27}Al MQ-MAS and ^{29}Si MAS NMR are thus a powerful combination.

The two very different Q^3 and Q^2 tetrahedral sites of the amphibole structure provide an opportunity to apply ^{27}Al MQ-MAS and obtain a direct measurement of tetrahedral-site populations, and hence determine the long-range ordering behaviour. Similarly, ^{23}Na MQ-MAS can be used to establish which of the two Na sites, the channel site (A) or the M(4) site, in the amphibole structure influences the displacive phase transition involving proton mobilisation.

We have studied amphiboles which are geologically important synthetic analogues of upper mantle minerals with sufficiently well constrained compositions to be suitable for ^{27}Al MQ-MAS NMR. We have examined three samples: (a) two pargasites, both with a formula $\text{NaCa}_2\text{Mg}_4\text{Al}(\text{Si}_6\text{Al}_2)\text{O}_{22}(\text{OH})_2$, synthesized at 1 kbar and 930 and 1080 °C; (b) fluor-edenite, $\text{NaCa}_2\text{Mg}_5(\text{Si}_7\text{Al})\text{O}_{22}\text{F}_2$, synthesized at 2 kbar and 1040 °C. These compositions, which except for their tetrahedral chemistries are very similar, allow us to see if the tetrahedral Al : Si ratio also affects long-range ordering of Al and Si over T(1) and T(2), in addition to the temperature effects. For the ^{23}Na MQ-MAS study, the amphibole is hydro-sodian-magnesiocummingtonite, $\text{Na}(\text{Na}_2)\text{Mg}_5\text{Si}_8\text{O}_{22}(\text{OH})_2(\text{OH})$ (HSMC), in which there are two Na at M(4) and one in the channel site. The excess proton is believed to be bonded to the two O(4) oxygens associated

† E-mail: jk18@cam.ac.uk

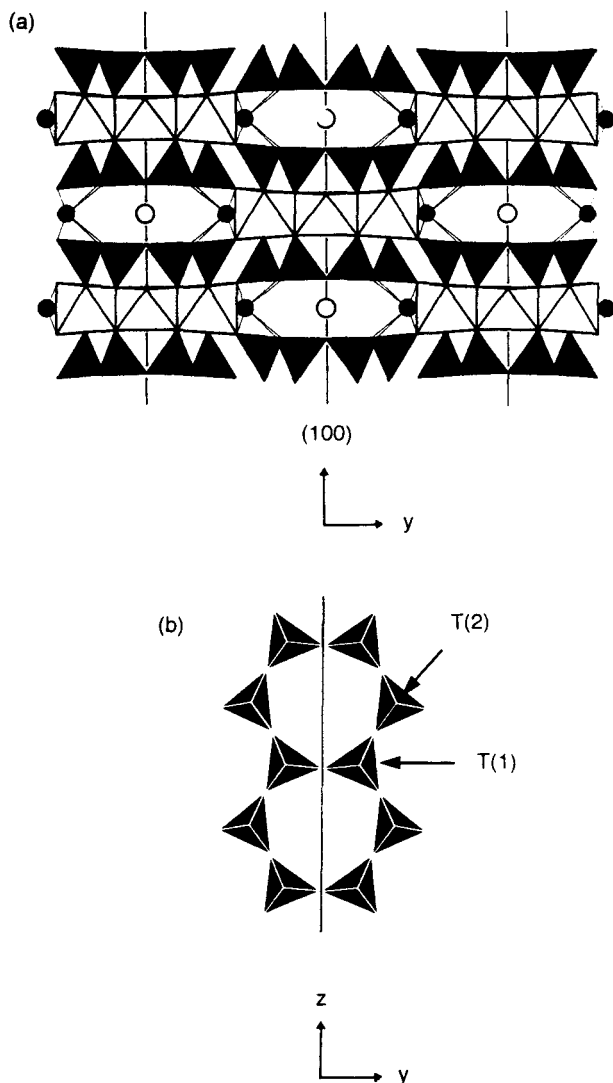


Fig. 1 The amphibole structure. (a) A view down the z axis parallel to the direction of the double chains (black tetrahedra) showing the characteristic I-beam units in which the ribbons of octahedral sites (white polyhedra) are sandwiched between a pair of double chains. The M(4) sites flanking the I-beams are shown as black circles. The channel cations (A-sites) are shown as white circles. The (100) mirror plane bisects the double chain, the octahedral ribbon and the A-site cation. (b) (100) view of the tetrahedral double chain distinguishing the T(1) (Q^3) and T(2) (Q^2) sites.

with the eight-fold M(4) site. For details of the phase transition in this amphibole see ref. 7 and the ^{29}Si and ^{23}Na MAS NMR study.⁸

The anisotropic part of the quadrupolar interaction is given by

$$\nu_p = \frac{C_Q^2}{\nu_0} [A_2(I, p)B_2(\eta, \alpha, \beta)P_2(\theta) + A_4(I, p)B_4(\eta, \alpha, \beta)P_4(\theta)] \quad (1)$$

where p is the order of the multi-quantum coherence, α and β are the Euler angles corresponding to the orientation of each crystallite in the powder with respect to the rotor axis, I is the spin quantum number, θ is the angle of the spinner axis with respect to the strong static magnetic field and ν_0 is the Larmor frequency of the nucleus and C_Q and η are the quadrupolar constant and asymmetry parameter, respectively. The orientation-dependent terms B_2 and B_4 are responsible for the broadening.⁹ P_2 and P_4 are the second- and fourth-order Leg-

endre polynomials:

$$P_2(\theta) = \frac{3 \cos^2 \theta - 1}{2};$$

$$P_4(\theta) = \frac{35 \cos^4 \theta - 30 \cos^2 \theta + 3}{8}$$

While MAS cancels out the polynomial P_2 , and so eliminates the first term in eqn. (1), P_4 remains. As a result, the last term in eqn. (1) leads to a broadening of the spectral lines. In double rotation (DOR)^{10,11} and dynamic-angle spinning (DAS)^{12,13} the sample is spun at two angles simultaneously or sequentially. Unfortunately, both methods suffer from drawbacks. In DAS the minimum time required for changing the angle of the spinner axis is usually longer than the relaxation time of the nucleus.

Under MAS at a sufficiently high spinning speed, CSA, dipolar and the second term P_2 in eqn. (1) are removed. For a powdered sample, the frequency of a p -quantum transition in a crystallite is therefore

$$\nu = -p\nu_{\text{CS}} + \nu_Q(I, p) + A_4(I, p)B_4(\eta, \alpha, \beta)P_4(\theta_{54.74}) \quad (2)$$

The isotropic chemical shift ν_{CS} and the quadrupole-induced shift ν_Q do not broaden the lines but specify the position of their centre of gravity. It is the third term in eqn. (2) which is responsible for the broadening of the lines.

It was recently demonstrated¹⁴⁻¹⁶ that the use of the MQ transitions p eliminates the last term in eqn. (2). If p -quantum transitions are excited and the signal evolves during time t_1 , a second pulse converts the signal to a (-1) -quantum transition, the only transition observable by NMR. An echo occurs at

$$t_2 = -\frac{A_4(I, p)}{A_4(I, -1)} t_1 \quad (3)$$

When condition (3) is satisfied, the quadrupolar interaction in eqn. (2) is averaged out. The use of the pulse sequence enables a two-dimensional representation of the spectra. Thus a regular increment of t_1 , the evolution time, provides a second dimension ('the p -quantum dimension'), free of quadrupolar interactions. Consequently, the position of each line in both dimensions is the sum of the isotropic chemical and quadrupole-induced shifts. The lines are aligned along the anisotropic axis, the slope of which corresponds to the ratio $A_4(I, p)/A_4(I, -1)$.

The two-dimensional spectra can be processed further. The most interesting operation is the shearing transformation which aligns the anisotropic axis and the different lines with the F_2 axis. Thus, a vertical projection of the spectrum onto the F_1 axis provides a one-dimensional spectrum in which each site is represented by a narrow line (a few ppm), free of any quadrupolar broadening.

Although the principle of MQ-MAS is simple, the optimal conditions, especially pulse lengths, are difficult to establish. The method has been refined in order to facilitate the acquisition of MQ-MAS spectra.¹⁷⁻²⁰ MQ-MAS is being used increasingly for the study of quadrupolar nuclei (^{27}Al , ^{85}Rb , ^{23}Na , ^{11}B and ^{93}Nb).

Experimental

MAS and MQ-MAS NMR spectra were recorded using a Chemagnetics CMX-400 spectrometer operating at 104.2 MHz for ^{27}Al and 105.8 MHz for ^{23}Na and a commercial MAS probehead with zirconia rotors 4 mm in diameter driven by nitrogen gas. The maximum available radiofrequency field strength of ca. 125 kHz was used in all experiments in order to increase the efficiency of MQ excitation. A short pulse of 0.35 μs was used for the MAS experiments with a recycle delay of 0.5 s. The pulse sequence for MQ-MAS experiments was com-

posed of three pulses: the third (Z-filtering) pulse is used to equalize the two coherence pathways.²¹ The three pulses have been experimentally optimized and their respective durations were 4.7, 1.3 and 8 μ s for ²⁷Al ($I = 5/2$) and 5.4, 2.0 and 8 μ s for ²³Na ($I = 3/2$). The spectrum of edenite was acquired with 48 scans per increment and a recycle delay of 25 s. 160 increments were necessary in t_1 to avoid the truncation of the signal. For the other spectra, rotor synchronization was used in order to eliminate spinning sidebands²² and the interval between the two first pulses was regularly incremented by 90.992 μ s (corresponding to MAS rate of 10.99 kHz). Under these conditions, 50 increments in t_1 were sufficient. The MQ-MAS spectrum of pargasite required 192 scans per increment with 12 s pulse delay. ²³Na MQ-MAS spectra at room temperature and at 200 °C were accumulated with 192 scans per increment and 5 s pulse delay. ²⁷Al and ²³Na line positions are given in ppm from external Al(H₂O)₆³⁺ and 1 M aqueous solution of NaCl, respectively.

Results and Discussion

Al—Si long-range ordering in edenite and pargasite

The structures of edenite and pargasite are very similar. ²⁷Al MAS NMR resolves two six-coordinate sites in pargasite (Fig. 2). However, although the lineshapes in the four-coordinate region in the spectra of both minerals, particularly edenite, are clearly asymmetric, the two four-coordinate Al environments are not well resolved.

The ²⁷Al MQ-MAS spectrum of edenite (Fig. 3) shows lines from two crystallographically distinct aluminium sites, Q² and Q³. However, as the position along the F_2 axis of spinning sidebands on each side of the central lines does not enable us to assign them to the individual sites, we have used an isotropic projection of the spectrum taking into account the spinning rate (top of Fig. 3). The efficiency of MQ excitation for a given site is not the same for all crystallites. The sidebands correspond to the Q³ site only, showing that the quadrupolar interactions for sites Q³ and Q² are very different. The quadrupolar parameters and the isotropic chemical shifts have been calculated directly from the spectrum (Table 1). The presence of spinning sidebands only for the Q³ sites is probably due to the stronger quadrupolar interaction on these sites in comparison with the Q² sites. The origin of the spinning sidebands in the F_1 dimension of the MQ-MAS spectra has been examined in detail.²³ The MQ-MAS spectrum and its iso-

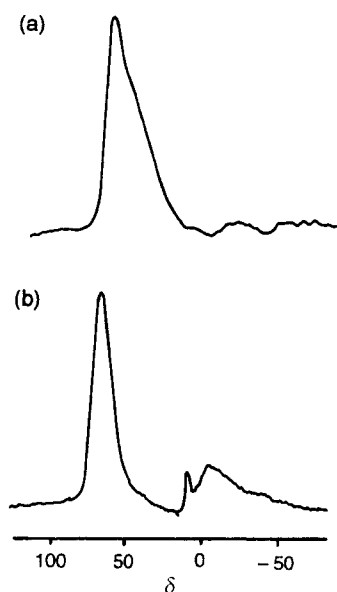


Fig. 2 ²⁷Al MAS NMR spectra of (a) edenite and (b) pargasite

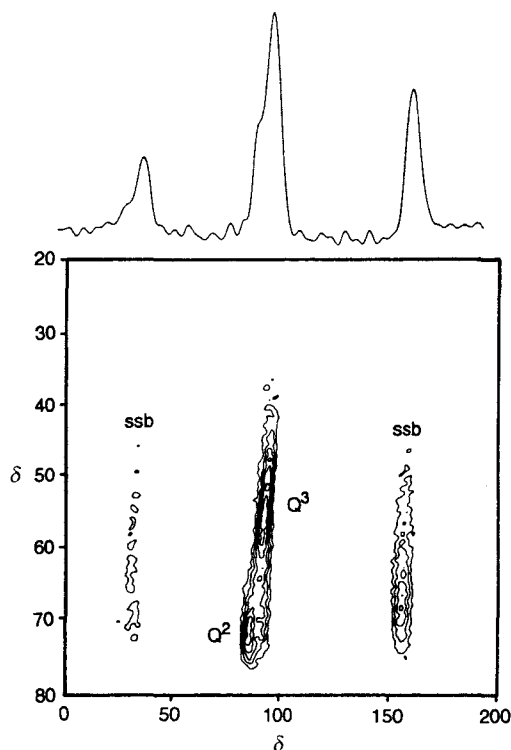


Fig. 3 ²⁷Al MQ-MAS NMR spectrum of edenite and its isotropic projection. ssb denotes spinning sidebands.

tropic projection show that the populations of the two sites are not the same, in agreement with X-ray diffraction studies [mean T(1)—O and T(2)—O bond lengths] which clearly show that aluminium is preferentially located on the Q³ sites. Note that, even if quantitative analysis of MQ-MAS spectra would underestimate the population of sites subjected to strong quadrupolar interactions, in our case this would mainly affect the intensity of the line from the Q³ site. The values of the second-order quadrupolar effect defined as

$$S_Q = C_Q \left(1 + \frac{\eta^2}{3} \right)^{1/2}$$

indicate that the environment of the Q³ site is more asymmetric than that of the Q² site, while the crystallographic data for bond lengths and angles^{3,24} indicate that the environment of the Q³ site is more symmetric with respect to the first-nearest neighbours. However, in compact silicates longer-distance environment (second- and third-nearest neighbours) must be taken into account to explain this result.

Fig. 4 shows that ²⁷Al MQ-MAS does not resolve the two tetrahedral environments in pargasite, although indirect evidence from ²⁹Si MAS NMR on the same sample shows unequivocally that there is significant Al at T(2).⁵ While the lineshape is asymmetric, the isotropic projection (not shown) does not have a shoulder which could be attributed to the Q² site. However, the intensity of the line along the F_2 axis is significantly lower in the spectrum of the pargasite than in the MAS and MQ-MAS spectra of edenite. The calculated value of S_Q (Table 1) reveals that the Q³ site in pargasite does not

Table 1 Second-order quadrupolar effect S_Q , and the isotropic chemical shift, δ_{CS} , calculated from the MQ-MAS spectra

mineral	site	S_Q /MHz	δ_{CS}
edenite	Q ²	3.0	76
	Q ³	5.9	77
pargasite	Q ³	4.0	77

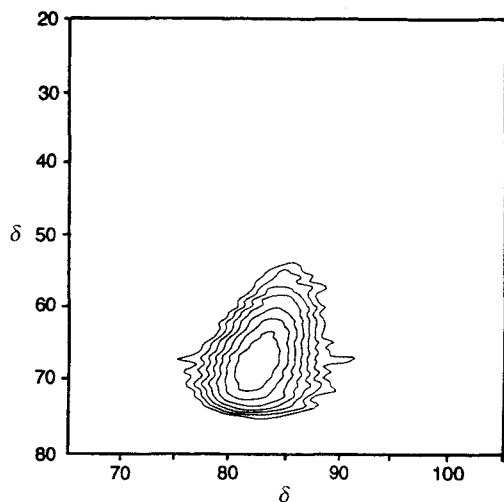


Fig. 4 ^{27}Al MQ-MAS NMR spectrum of pargasite

experience the same quadrupolar interaction as in edenite. Therefore, the isotropic chemical shifts and the quadrupolar constants for sites Q^2 and Q^3 in pargasite are very similar. It follows that the different lineshapes in the MAS spectra of edenite and pargasite (Fig. 2) are not caused by the different populations of aluminium sites, but by different quadrupole interactions on the Q^3 site. This is a consequence of a different environment of the Q^3 site which reduces the strength of the quadrupolar interaction (and greatly complicates NMR measurements). The six-coordinate region of the MQ-MAS spectrum of pargasite does not provide more information than the MAS spectrum, but does confirm the presence of two different sites.

MQ-MAS enables different crystallographic sites to be separated according to their isotropic chemical shifts and quadrupolar parameters. Studies of aluminosilicate and aluminophosphate molecular sieves have demonstrated that the technique is useful for the separation of different aluminium environments. However, tetrahedral sites in these materials are all Q^4 and the structure is composed of channels and cavities, which limits the strength of the quadrupolar interactions. Moreover, molecular sieves readily adsorb water. As a result, the quadrupolar constants for such materials are in the 1–5 MHz range. Amphiboles are more complex compact materials which do not contain water, the presence of which often decreases the quadrupolar interaction. In the extreme case of two sites with large quadrupolar constants and similar isotropic chemical shifts, MQ-MAS is able to distinguish both environments in edenite, even though the resolution of MQ-MAS spectra suffers when these values become very close. Thus, despite the failure to reveal clearly the two tetrahedral sites in pargasite, the experiment provides much more structural information than the conventional MAS spectra. A simulation of the latter spectra using QUASAR, a home-made program, did not provide a conclusive result, mainly because of the overlap of the two resonances which obscures the specific lineshapes of quadrupolar nuclei. We conclude that quantitative information on the tetrahedral sites in edenite cannot be obtained by MAS alone. However, such information can be obtained by using MQ-MAS in tandem with spectral simulation, which allows the isotropic chemical shift to be mapped *versus* the S_Q . The simulation takes into account parameters such as the strength of the radiofrequency field, pulse length *etc.* in order to correct for different efficiency of three-quantum excitation in different crystallites. The calculation will be fully explained in another article and it is not in the scope of this paper to develop its theoretical parts. As a result, a quantitative analysis of the spectra is possible, if not

straightforward. The simulation leads to a $Q^2 : Q^3$ population ratio of 1 : 9, and confirms the quadrupolar parameters and the isotropic chemical shifts in Table 1.

Monitoring phase transition in HSMC by ^{23}Na MQ-MAS

HSMC contains sodium located in two distinct sites, M(4) and A, in the 2 : 1 population ratio. The ^{23}Na MAS spectrum of HSMC [Fig. 5(a)] is a typical quadrupolar pattern. Simulation of this spectrum requires the use of at least two species and leads to the parameters given in Table 2. However, the calculation cannot be accurate unless the exact number of sites is known. The isotropic dimension of MQ-MAS spectra makes this possible. The two ^{23}Na sites in HSMC are clearly resolved in Fig. 6(a). The third resonance corresponds to a NaCl impurity and has a small quadrupolar interaction, which leads to an overestimation of its intensity. Quadrupolar parameters deduced from spectrum must be compared with the parameters obtained by simulation. We can easily identify the site with the largest quadrupolar interaction as M(4). Looking at the structure of amphiboles, the environment of M(4) is influenced by the octahedral sites on one side and by the double chains on the other side. On the other hand, the A site is in a large cavity, symmetric with respect to the mirror (020) plane. Moreover, even though the intensities of the lines must be considered carefully, their comparison on the isotropic projection removes the ambiguity.

Since the MAS spectrum exhibits a major change at ca. 180 °C, indicating a phase transition, we have repeated the experiment at 200 °C. Even at such high temperature, the ^{23}Na nuclei remain in the sites M(4) and A, respectively, in the

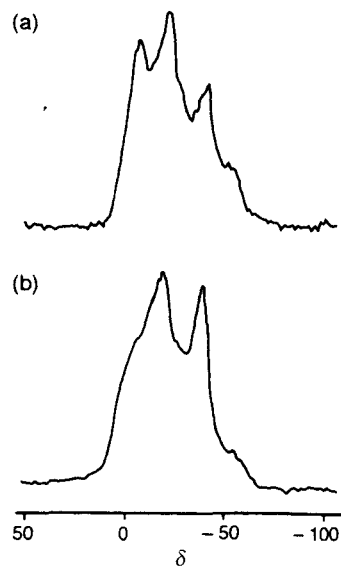


Fig. 5 ^{23}Na MAS NMR spectra of HSMC (a) at room temperature and (b) at 200 °C

Table 2 Quadrupolar parameters obtained by iterative fitting of the MAS spectra of HSMC at room temperature (rt) and at 200 °C using the QUASAR program

site	temperature / °C	population	δ_{CS}	C_Q/MHz	η
M(4)	rt	2	9.3	3.9	0.49
A	rt	1	5.5	2.9	0.26
M(4)	200	2	7.7	3.8	0.46
A	200	1	12.3	3.2	0.7

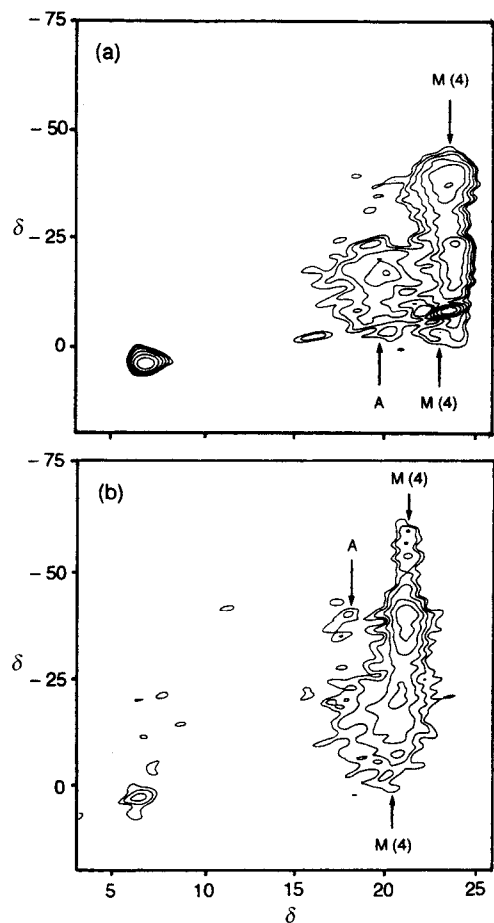


Fig. 6 ^{23}Na MQ-MAS NMR spectra of HSMC (a) at room temperature and (b) 200°C

same population ratio. The difference observed in the MAS spectra is, therefore, caused by the changed environment of each species. The MQ-MAS spectrum is shown in Fig. 6(b). While the lineshape of the resonance from site M(4) is basically the same at 200°C , species A is now barely detectable. This result is in agreement with the parameters deduced from the simulation of the MAS spectra (Table 2). Only the parameters of the A cation change significantly between the two temperatures. This means that site M(4) does not change much during the phase transition, whereas the environment of the A site is different. It has been shown that the efficiency of MQ-MAS depends on both the quadrupolar constant and the asymmetry parameter.¹⁷ This could explain the low intensity of the resonance for site A. Nevertheless, selective efficiency cannot fully account for this decrease in intensity since the quadrupolar interactions and the asymmetry parameters for the two sites are similar. Neither can it explain the differences in the MAS spectra. Na can occupy several possible sub-sites within the large A-cavity,^{6,25,26} which constitute local potential minima. The multinuclear (^1H , ^{23}Na and ^{29}Si) study of the monoclinic-triclinic phase transition in HSMC⁸ showed that the excess proton is in some way 'mobile'

during the phase transition and that its motion couples to Na motion in the A-site. Their ^{23}Na MAS NMR spectra show clear changes in the behaviour of the A-site peak, while the Na at M(4) changes little throughout the phase transition. The absence of the A-site peak in the 200°C MQ-MAS spectrum may therefore reflect Na motion (positional disordering) in the A-site cavity.

We conclude that triple-quantum MAS complements MAS in the study of amphiboles. Two tetrahedral aluminium sites are clearly resolved in edenite, although the method fails when dealing with sites with similar quadrupolar parameters. Long-range Si-Al disorder exists in fluor-edenite. MQ-MAS also enables the separation of two sodium sites in amphiboles. These results are a first step towards the simulation of MAS spectra.

References

- 1 C. M. Graham, W. V. Maresch, M. D. Welch and A. R. Pawley, *Eur. J. Mineral.*, 1989, **1**, 535.
- 2 G. Engelhardt and D. Michel, *High-Resolution Solid-State NMR of Silicates and Zeolites*, Wiley, Chichester, 1987.
- 3 R. Oberti, N. Sardone, F. C. Hawthorne, M. Raudsepp and A. C. Turnock, *Can. Mineral.*, 1995, **33**, 25.
- 4 R. Oberti, L. Ungaretti, E. Canillo, F. C. Hawthorne and I. Memmi, *Eur. J. Mineral.*, 1995, **7**, 1049.
- 5 M. D. Welch, S. Liu and J. Klinowski, *Am. Mineral.*, submitted.
- 6 F. C. Hawthorne, *Can. Mineral.*, 1983, **21**, 173.
- 7 W. V. Maresch, G. Mische, M. Czank, H. Fuess and W. Schreyer, *Eur. J. Mineral.*, 1991, **3**, 899.
- 8 S. X. Liu, M. D. Welch, J. Klinowski and W. V. Maresch, *Eur. J. Mineral.*, 1996, **8**, 223.
- 9 J. P. Amoureux, *Solid State NMR*, 1993, **2**, 83.
- 10 A. Llor and J. Viret, *Chem. Phys. Lett.*, 1988, **152**, 248.
- 11 A. Samoson, E. Lippmaa and A. Pines, *Mol. Phys.*, 1988, **65**, 1013.
- 12 K. T. Mueller, E. W. Wooten and A. Pines, *J. Magn. Reson.*, 1991, **92**, 620.
- 13 K. T. Mueller, B. Q. Sun, G. C. Chingas, J. W. Zwanziger, T. Terao and A. Pines, *J. Magn. Reson.*, 1990, **86**, 470.
- 14 A. Medek, J. S. Harwood and L. Frydman, *J. Am. Chem. Soc.*, 1995, **117**, 12779.
- 15 L. Frydman and J. S. Harwood, *J. Am. Chem. Soc.*, 1995, **117**, 5367.
- 16 L. Frydman, *ACS Abs.*, 1996, **212**, 45-IEC.
- 17 C. Fernandez, J. P. Amoureux, J. M. Chézeau, L. Delmotte and H. Kessler, *Microporous Mater.*, 1996, **6**, 331.
- 18 C. Fernandez, L. Delevoeye and J. P. Amoureux, *ACS Abs.*, 1996, **212**, 74-IEC.
- 19 C. Fernandez, J. P. Amoureux, L. Delmotte and H. Kessler, *Microporous Mater.*, 1996, **6**, 125.
- 20 C. Fernandez and J. P. Amoureux, *Solid State NMR*, 1996, **5**, 315.
- 21 J. P. Amoureux, C. Fernandez and S. Steuernagel, *J. Magn. Reson. A*, 1996, **123**, 116.
- 22 D. Massiot, *J. Magn. Reson. A*, 1996, **122**, 240.
- 23 J. P. Amoureux and C. Fernandez, *J. Chem. Phys.*, submitted.
- 24 K. F. Boschmann, P. C. Burns, F. C. Hawthorne, M. Raudsepp and A. C. Turnock, *Can. Mineral.*, 1994, **32**, 21.
- 25 M. Cameron, S. Sueno, J. J. Papike and C. T. Prewitt, *Am. Mineral.*, 1983, **68**, 924.
- 26 F. C. Hawthorne and H. D. Grundy, *Nature Phys. Sci.*, 1972, **235**, 72.

Paper 7/01848G; Received 17th March, 1997

4.2 Caractérisation des sites ^{27}Al dans une levyne

2D multiple-quantum ^{27}Al NMR and ^{29}Si NMR characterization of levyne

submitted in *Colloids and Surfaces*

Les résultats présentés dans cette article ont été obtenus dans notre laboratoire à Lille, à partir d'échantillons provenant du laboratoire du Prof. B'Nagy à Namur, Belgique.

Le but de ce travail était d'étudier l'effet d'une calcination sur la distribution des atomes d' ^{27}Al dans la levyne. La structure de cette zéolithe est composée de deux sites tétraédriques 36T_1 et 18T_2 cristallographiquement distincts. La RMN du silicium (^{29}Si MAS NMR) ne fournit pas d'informations quantitatives sur les sites ^{27}Al . Par contre, les expériences MQMAS que nous avons effectuées sur les deux échantillons de levyne ("as-made" et calciné) ainsi que la quantification des spectres (REGULAR) nous permettent de statuer sur le caractère aléatoire ou non de la distribution des sites ^{27}Al . En comparant les résultats obtenus par RMN MQMAS de l' ^{27}Al avant et après calcination, nous avons aussi démontré que le processus chimique affectait de façon préférentielle le site T_1 .

Pour l'échantillon avant calcination ("as-made"), l'expérience MQMAS met en évidence les deux sites Al_1 et Al_2 (cf. Fig. 3). La quantification du spectre 2D avec REGULAR (cf. Fig. 4) confirme la proportion relative 2 :1 pour respectivement les sites Al_1 et Al_2 . Ceci est donc la preuve que la distribution des atomes d' ^{27}Al sur les sites tétraédriques T_1 et T_2 est complètement aléatoire. Pour la levyne calcinée, un troisième site tétraédrique Al_3 apparaît sur le spectre MQMAS (cf. Fig. 5), en plus de l' ^{27}Al octaédrique déjà apparent sur le spectre MAS (cf. Fig. 1-B). Ce site supplémentaire possède un

effet quadripolaire au second ordre P_Q plus important que les autres sites tétraédriques Al_1 et Al_2 et pourrait être le résultat d'une déformation du tétraèdre. L'analyse quantitative des deux échantillons de levyne est résumée dans la Table II. La population relative des sites Al_2 reste constante pendant le processus de calcination, tendant à prouver que le troisième site aluminium et le site octaédrique proviennent d'un changement de l'environnement des sites Al_1 . De plus, les sites Al_1 et Al_3 ne diffèrent que par leur valeur de P_Q et ont pratiquement le même déplacement chimique δ_{CS} .

2D multiple quantum ^{27}Al NMR and ^{29}Si NMR characterization of levyne

P. Lentz, J. B. Nagy*

*Laboratoire de Résonance Magnétique Nucléaire
Facultés Universitaires Notre-Dame de la Paix, B-5000 Namur, Belgium*

L. Delevoye, Y. Dumazy, C. Fernandez, J.-P. Amoureux

*Laboratoire de Dynamique et Structure des Matériaux Moléculaires, CNRS URA801
Université des Sciences et Technologies de Lille, F-59655 Villeneuve d'Ascq Cedex, France*

C. V. Tuoto, A. Nastro

*Department of Chemical Engineering and Materials
University of Calabria, Arcavacata di Rende, I-87030 Rende (CS), Italy*

Combined 1D and 2D multiple-quantum ^{27}Al NMR results together with ^{29}Si NMR data provide interesting information on the siting of Al in levyne zeolite. It is clearly shown that the distribution of Al is random in the structure, as the relative intensity of the two tetrahedral species is equal to 2. This corresponds to the ratio of T_1 over T_2 , which are crystallographically different tetrahedral sites. The dealumination which occurs during calcination appears to be specific. Only the tetrahedral Al atoms on sites T_1 are transformed into deformed tetrahedral species and extraframework octahedral species, while the Al atoms on sites T_2 remain unchanged.

INTRODUCTION

Until recently, characterization of zeolites by high resolution solid state nuclear magnetic resonance (NMR) was restricted to magic angle spinning (MAS) experiments. Nevertheless, in the study of quadrupolar nuclei, line broadening arising from second-order quadrupolar effect was sufficient to prevent the chemist from getting further useful information about the number of sites and distribution of the quadrupolar nucleus in the zeolite lattice.

In the nineties, new techniques have been settled and perfected to lower or void the importance of this second-order quadrupolar effect: double rotation [1,2] (DOR) and dynamic angle spinning [3] (DAS) turn out to be very useful, even though they rely on technologically sophisticated hardware and are restricted in their application. The bidimensional multi-quantum MAS (MQMAS) method, first proposed by Frydman and Harwood [4], requires no more than a widespread MAS probehead. It therefore appears as the method of choice since it can provide, in addition to the impressively resolved spectrum, further information on the quadrupolar interaction: the ^{27}Al isotropic shift, quadrupolar coupling constant C_Q and the asymmetry parameter η_Q .

Natural levyne-type zeolites have the general composition $\text{Ca}_3(\text{Al}_{18}\text{Si}_{36}\text{O}_{108})50\text{H}_2\text{O}$. The unit cell has a trigonal symmetry and all 54 T atoms (Si or Al) are in tetrahedral sites [5]. They are characterized by a bidimensional lattice made of a sequence of single six-membered rings, and by rather small size pores ($4.8\text{\AA} \times 3.6\text{\AA}$). Despite their first synthesis in 1969 [6] and their use in industrial catalysis for the transformation of methanol to

low molecular weight olefins [7], not much is yet known about the aluminum sites in the structure. ^{29}Si MAS NMR revealed the presence of two crystallographically non-equivalent sites, T_1 and T_2 but no information on the distribution of the aluminum could be obtained from ^{29}Si and ^{27}Al MAS NMR spectra [8,9].

In this paper, we report the study of the ^{27}Al nucleus in two levyne samples using two-dimensional triple-quantum (3QMAS) NMR.

EXPERIMENTAL

The global composition of the initial gel was $4\text{Na}_2\text{O} - 2\text{K}_2\text{O} - 6\text{MeQI} - \text{Al}_2\text{O}_3 - 30\text{SiO}_2 - 500\text{H}_2\text{O}$ where MeQ=methylquinuclidinium ion. The reaction gel was prepared by mixing 30% NaOH aqueous solution (pellets EPR, Carlo Erba), MeQI, $\text{Al}(\text{OH})_3$ (dry gel, Pfaltz and Bauer), distilled water and SiO_2 (fumed silica, Serva). MeQI was prepared by mixing quinuclidine (1-azabicyclo-[2,2,2]octane, Aldrich) and iodomethane. The reaction mixture was heated at 150°C under autogeneous pressure in static conditions for programmed times, using modified Morey type autoclaves (8cm^3) [10]. The calcination of the sample was carried out in air, heating the sample from 30°C to 700°C at a rate of $10^\circ\text{C}/\text{minute}$ under a $15\text{ ml}/\text{minute}$ air flow.

The 1D NMR spectra were recorded either on a Bruker MSL-400 or a Bruker CXP-200 spectrometer. For ^{29}Si (39.7 MHz), a $6.0\ \mu\text{s}$ ($\theta = \pi/2$) pulse was used with a repetition time of 6.0 s. For ^{27}Al (104.3 MHz), a $1.0\ \mu\text{s}$ ($\theta = \pi/12$) was used with a repetition time of 0.2 s.

The 3QMAS experiments at 9.4 T were performed on a Bruker ASX-400 using a recently developed 4 mm MQMAS probehead (Bruker) spinning at 15 kHz, with a radiofrequency field ν_{rf} estimated at ca. 280 kHz. The pulse sequence was composed of three pulses corresponding to the Z-filter MQMAS method [11], which yields pure absorption spectra. The pulse lengths were experimentally adjusted to 1.75 μ s, 0.6 μ s (ν_{rf} = 280 kHz) and 8 μ s (ν_{rf} = 10 kHz), respectively. The recycle delay was the same as for 1D 27 Al MAS experiments. The delay t_1 between the first and second pulse was regularly incremented by 67 μ s, according to the method of rotor synchronisation [12]. This allows to remove spinning sidebands which generally appear along the isotropic axis, and to reduce significantly the acquisition time. 576 and 2304 scans per increment were used for the as-made and calcined levyne samples, respectively.

QUANTITATIVE ANALYSIS OF MQMAS SPECTRA

The MQMAS method has been previously described [4,13–15]. We may recall that in addition to the total elimination of the second-order quadrupolar interactions, this technique yields a separation of the different species by both their isotropic chemical shift δ_{CS} and their second-order quadrupolar interaction $P_Q = C_Q \cdot (1 + \eta^2/3)^{1/2}$. Nevertheless, it remains difficult to deduce a quantitative information from the MQMAS spectra as the efficiency for the excitation of multiple quantum transitions strongly depends on the quadrupolar coupling constant of each species [15]. Indeed, it is shown that the intensity detected in MQMAS, for sites experiencing very weak and very strong quadrupolar interactions is likely to be underestimated whereas for sites with similar quadrupolar parameters, the direct comparison of the isotropic projection may give a good approximation of their relative population. However, using PULSAR [16], a home-made simulation software which calculates the response of a nucleus to a series of pulses, taking into account both the quadrupolar parameter and the experimental radio-frequency field, one can predict the actual spectral intensity for each site. Thus, a method to quantify the experimental MQMAS spectra is to compare the experiment with these theoretical calculations. This is easy to perform when each site is well characterized by a pure quadrupolar lineshape and thus a unique set of parameters (P_Q , δ_{CS}). But in the case of a distribution of parameters, such a comparison becomes extremely difficult and inaccurate, and it is advantageous to use the method recently developed by Zwanziger [17] for the analysis of DAS spectra. A detailed description of the inverse theory and regularization methods used for this analysis and their effective application to MQMAS is outside the scope of this paper. It will be pub-

lished elsewhere. This method has already been applied with success to provide a precise knowledge of the relative population of five sites in a well-crystallized $\text{AlPO}_4 - 11$ aluminophosphate [18].

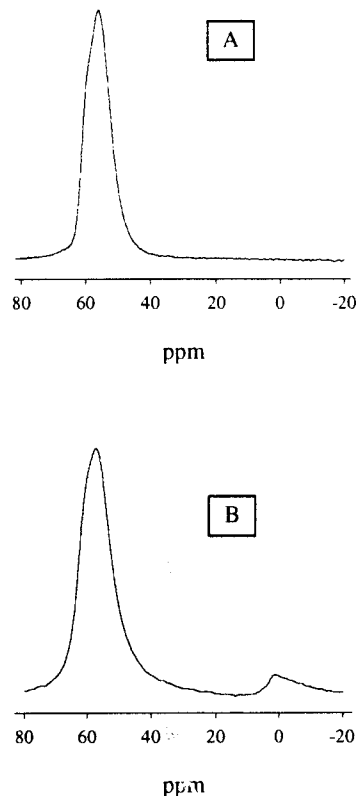


FIG. 1. MAS 27 Al NMR spectra of the as-made levyne sample (A) and of the calcined sample at 700°C (B).

RESULTS AND DISCUSSION

The Si/Al ratio of the as-synthesized sample is close to 15, the ratio of the initial gel. This equality means that the incorporation of the aluminum into the levyne structure is quite effective [8,10]. Indeed, the 27 Al MAS NMR spectrum of the as-made sample clearly shows that only one NMR line at 53.8 ppm is detected, which is characteristic of tetrahedral coordination (Figure 1-A). During the calcination at 700°C, some of the framework tetrahedral aluminum leaves the structure and this extraframework aluminum becomes octahedral at ca. 0 ppm (Figure 1-B).

Previous 13 C NMR measurements of the occluded MeQ^+ ions have shown that they are incorporated intact in the levyne channels [8]. However, the thermal analysis of the precursor samples still containing the MeQ^+ ions has demonstrated that two different MeQ^+ ions were present in the channels [10]. The ones which are decomposed at lower temperature (460 °C) neutralize some of

the SiO^- defect groups (2.7/u.c.) while the ones decomposed at higher temperature (590°C) neutralize the negative charges linked to the presence of the tetrahedral aluminum in the structure, the $(\text{SiOAl})^-$ groups (3.4/u.c.).

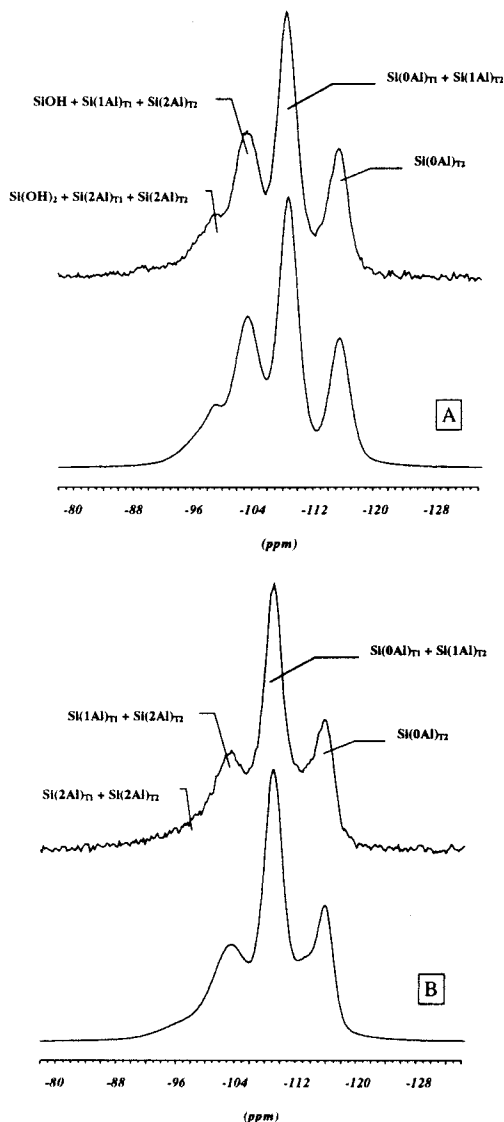


FIG. 2. MAS ^{29}Si NMR spectra of the as-made levyne sample (A) and of the calcined sample at 700°C (B).

The high resolution solid-state ^{29}Si NMR spectra of the as-made and calcined levyne samples are shown in Figure 2. As the levyne structure contains two crystallographically different tetrahedral sites, 36 T_1 and 18 T_2 sites [5], care has to be taken in interpreting the NMR spectra. The relative intensities of the various lines of both the as-made and the calcined samples are reported in Table I. The NMR line at -115 ppm is assigned to Si(OAl) configuration of the T_2 sites [8,9]. The other NMR lines are tentatively assigned as follows. The -108 ppm line could stem from Si(1Al) configuration on T_2

sites and Si(OAl) configuration of T_1 sites. The -103 ppm line could correspond to the sum of $\text{Si(2Al)}_{\text{T}_2}$ and $\text{Si(1Al)}_{\text{T}_1}$ configurations. Finally, the -97 ppm line could stem from the sum of $\text{Si(3Al)}_{\text{T}_2}$ and $\text{Si(2Al)}_{\text{T}_1}$ configurations [8]. However, this hypothesis cannot lead to a quantitative interpretation of the NMR spectra.

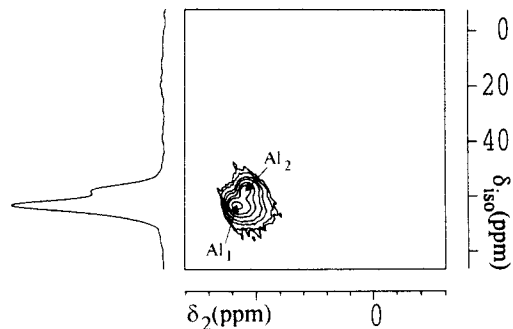


FIG. 3. ^{27}Al 3Q-MAS NMR spectrum of the as-made levyne sample.

The discrepancy very probably stems from the presence of a high amount of defect groups $\equiv \text{SiOM}$ ($\text{M}=\text{Na}$, K , H and/or MeQ). It can be seen from Figure 2 that the intensity of the -103 ppm line decreases during calcination and that the intensity of the -97 ppm line is drastically reduced. It is rather well known that the former could include the $\equiv \text{SiOM}$ defect groups, while the latter includes either $=\text{Si(OM)}_2$ or $=\text{Si(OAl)}\equiv(\text{OM})$ defect groups [19]. The relative intensities of the NMR lines can certainly not be compared directly because the number of NMR lines is different in the as-made and calcined samples.

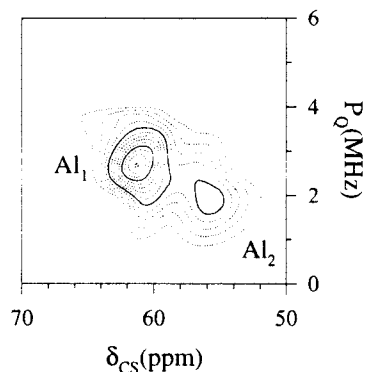


FIG. 4. Result of the inversion for the as-made levyne sample.

The presence of two crystallographically different sites raises interesting questions concerning the siting of aluminum on the T_1 and T_2 sites. Is the aluminum distribution random or specific [20,21]? Is the dealumination random or specific? The high resolution ^{27}Al NMR spectra gives valuable information and helps in answering

the above-stated questions. The ^{27}Al MAS NMR spectra (Figure 1) already suggests the presence of two different tetrahedral aluminum atoms in the structure; but in order to better characterize the levyne samples, 2D multiple-quantum ^{27}Al NMR experiments have been carried out. Indeed, it has already been shown that the use of three-quantum transitions greatly increases the resolution. The 3QMAS ^{27}Al NMR spectra of the as-made and calcined samples are shown in Figures 3 and 5, respectively. The 3QMAS NMR spectrum of the as-made sample clearly shows two different species at $\delta = 62$ ppm (Al_1) and $\delta = 56$ ppm (Al_2) (Figure 3 and Table II). Moreover, the relative intensities of the two lines are respectively 2:1, suggesting that the aluminum distribution is random in the structure. Indeed, this ratio corresponds to the ratio of the crystallographically different tetrahedral sites in the levyne structure, $T_1/T_2=2$. The attribution of the two different tetrahedral aluminum species is hence obvious. The 62 ppm line (Al_1) characterizes the tetrahedral atoms on sites T_1 , while the 56 ppm line (Al_2) stems from the tetrahedral Al atoms on sites T_2 . The determined quadrupolar coupling constants P_Q being similar (1.9 MHz and 2.7 MHz respectively), the relative intensities on the isotropic projection are regarded as correct. This assumption is confirmed by the computation of the 3QMAS spectrum (Figure 4), which gives an accurate result for the relative populations (Table II).

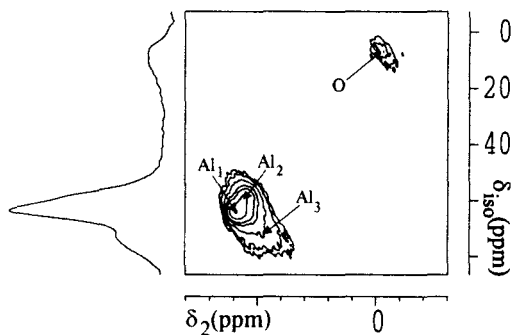


FIG. 5. ^{27}Al 3Q-MAS NMR spectrum of the calcined sample at 700°C .

During calcination, a small amount of extraframework octahedral aluminum species (O site) appears around 4 ppm (Figure 6). In addition, a new tetrahedral species (Al_3) is also detected at $\delta = 64$ ppm (Figure 5), which could be due to deformed tetrahedral aluminum atoms. The P_Q of the Al_3 species is much larger than for the other two tetrahedral sites and is equal to 4.8 MHz.

The quantitative analysis of the 3QMAS spectrum (Figure 6) yields a better understanding of the dealumination process. Table II reports all the data for the three tetrahedral species at 57, 62 and 64 ppm, respectively, and the octahedral species at around 4 ppm. As the relative population of Al_2 remains constant throughout calcina-

tion, it seems clear that the third tetrahedral species Al_3 and the octahedral species which appear during calcination are generated from the Al_1 species. Moreover, Al_1 and Al_3 species have close isotropic chemical shifts and only differ in their P_Q . This is every indication that the Al_1 atoms, which occupy the T_1 site in the structure, undergo a distortion to yield the Al_3 species. Hence, one can conclude that the tetrahedral Al atoms on sites T_1 at 62 ppm (Al_1) are partially transformed into deformed tetrahedral species at 64 ppm (Al_3). On the other hand, the 4% octahedral species formed during calcination seem to stem also from Al_1 species. These results strongly suggest that the dealumination occurring during calcination is highly specific, involving only the crystallographic tetrahedral T_1 sites. A more systematic work on the dealumination will be carried out in order to check the specific dealumination from the T_1 sites. This represents a very interesting result and its importance could be checked in catalytic reactions. Specific dealumination could also be suggested from the framework of offretite using the changes in the ^{27}Al MAS NMR and the ^{29}Si MAS NMR spectra during dealumination.

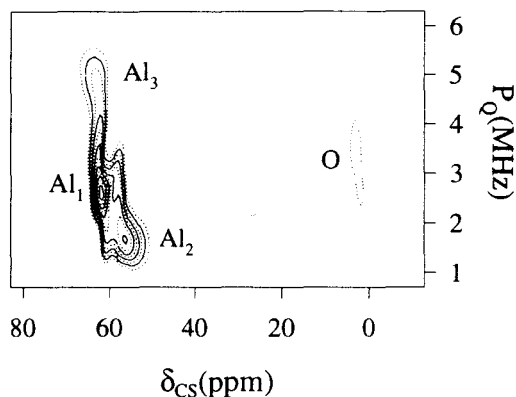


FIG. 6. Result of the inversion for the calcined sample at 700°C .

CONCLUSION

We have shown that the ^{27}Al NMR studies of levyne type zeolites can be improved using the 3QMAS NMR experiment. The technique appears to be complementary to ^{29}Si MAS NMR experiments as it totally removes the ambiguity on the distribution of Al on the crystallographically different sites. Quantitative analysis of the MQMAS spectra has been performed using an appropriate method of spectral inversion and has allowed the determination of the relative populations of the different species. It is concluded that the distribution of Al is random in the as-made sample. The dealumination yielding octahedral aluminum species seems to affect only the Al_1 species, which occupy the T_1 sites. In addition, some of the original tetrahedral Al atoms on site T_1 are

transformed into deformed tetrahedral species and to extraframework octahedral species.

ACKNOWLEDGEMENTS

P.L. is grateful to F.R.I.A. for providing financial support. L.D, Y.D, C.F. and J.-P.A. are grateful to Bruker for technical help. Finally, the authors wish to thank Mr Guy Daelen for his skillful help in taking the ^{29}Si MAS NMR spectra.

TABLE I. ^{29}Si MAS NMR data of the as-made and calcined levyne samples at 700°C.

Sample	$\delta(\text{ppm})$	I(%)	$\delta(\text{ppm})$	I(%)	$\delta(\text{ppm})$	I(%)	$\delta(\text{ppm})$	I(%)
As-made	-98.4	11	-103.1	25	-108.3	43	-114.9	21
Calcined	-96.1	6	-102.8	27	-109.0	46	-115.6	21

TABLE II. ^{27}Al 3QMAS NMR data of the as-made and calcined levyne samples at 700°C.

Sample	Tetrahedral region						Octahedral region					
	Al_1			Al_2			Al_3			0		
	δ_{CS} (ppm)	P_Q (MHz)	I (%)									
As-made	62	2.7	69	56	1.9	31	—	—	—	—	—	—
Calcined	62	2.6	53	57	1.8	31	64	4.8	12	4	3.5	4

* To whom correspondence should be addressed

- [1] A. Samoson, E. Lipmaa and A. Pines, *Mol. Phys.* **65**, 1013 (1988).
- [2] A. Llor and J. Virlet, *Chem. Phys. Letters* **152**, 258 (1988).
- [3] B.F. Chmelka, K.T. Mueller, A. Pines, J. Stebbins, Y. Wu and J.W. Zwanziger, *Nature* **42**, 339 (1989).
- [4] L. Frydman and J.S. Harwood, *J. Am. Chem. Soc.* **117**, 5367 (1995).
- [5] W.M. Meier, D.H. Olson, *Atlas of Zeolites Structure Types*, Butterworth-Heinemann, 114 (1992).
- [6] G.T. Kerr, US Patent 3 459 676, (1969).
- [7] Z. Tvaruzkova, M. Tupa, P. Jiru, A. Nastro, G. Giordano, F. Trifirò, *Catalysis Letters* **2**, 369 (1989).
- [8] C.V. Tuoto, J.B. Nagy and A. Nastro, *Stud. Surf. Sci. Catal.* **105A**, 213 (1996).
- [9] P. Cautlet, J. Patarin, A.C. Faust in *Proc. III Convegno Nazionale Scienza e Tecnologia delle Zeoliti*, R. Aiello, ed., Cetraro, Italy, 28-29 Sett. 1995, p55.
- [10] C.V. Tuoto, J.B. Nagy and A. Nastro, *Stud. Surf. Sci. Catal.* **97**, 551 (1995).
- [11] J.-P. Amoureux, C. Fernandez, S. Steuernagel, *J. Magn. Reson.* **A123**, 116 (1996).
- [12] D. Massiot, *J. Magn. Reson.* **A122**, 240 (1996).
- [13] C. Fernandez, J.-P. Amoureux, *Chem. Phys. Letters* **242**, 449 (1995).
- [14] C. Fernandez, J.-P. Amoureux, J.-M. Chezeau, L. Delmotte, H. Kessler **6**, 331 (1996).
- [15] J.-P. Amoureux, C. Fernandez, L. Frydman, *Chem. Phys. Letters* **259**, 347 (1996).
- [16] J.-P. Amoureux, C. Fernandez, Y. Dumazy, *J. Chim. Phys.* **2**, 1939 (1995).
- [17] J.W. Zwanziger, *Solid State NMR* **3**, 219 (1994).
- [18] C. Fernandez, L. Delevoye, J.-P. Amoureux, D.P. Lang, M. Pruski, **119**, 6858 (1997).
- [19] G. Engelhardt and D. Michel *High Resolution Solid-State NMR of Silicates and Zeolites*, Wiley, Chichester, 1987.
- [20] P. Bodart, J.B. Nagy, G. Debras, Z. Gabelica, and P.A. Jacobs, *J. Phys. Chem.* **90**, 5183 (1986).
- [21] F. Raatz, J.C. Roussel, R. Cantiani, G. Ferre and J.B. Nagy, *Stud. Surf. Sci. Catal.* **37**, 301 (1988)

4.3 Caractérisation des cations dans l'ETS-10

Anisotropic Chemical Shielding, M-Site Ordering, and Characterization of Extraframework Cations in ETS-10 Studied through MAS/MQ-MAS NMR and Molecular Modeling Techniques

published in *J. Am. Chem. Soc.*

L'ETS-10 est un matériau de la famille des titanosilicates microporeux dont la structure de base est essentiellement composée de tétraèdres SiO_4 et d'octaèdres TiO_6 . Les figures 4.1 et 4.2 sont des représentations structurales de l'ETS-10, dans deux directions perpendiculaires.

Cet article écrit en collaboration avec nos collègues de Pune, India, est le résultat d'expériences réalisées à Lille et en Inde. Pour ce qui est du travail que j'ai effectuée avec le Prof. Ganapathy, lors de sa visite dans notre laboratoire, il concerne l'application de la technique MQMAS à l'étude des sites cationiques ^{23}Na dans l'ETS-10 (purement silicium) et dans l'ETAS-10 (aluminium substitué : $\text{Si}/\text{Al} = 62, 42, 22$).

Dans l'ETS-10, les atomes de titane (Ti) forment des chaînes dans deux directions perpendiculaires (cf. Figs. 4.1 et 4.2). Dans l'ETS-10 et dans l'ETAS-10, le rôle des cations ^{23}Na est de contrebalancer les charges négatives apportées par les atomes de titane. Une étude préalable (REAP-DOR et Biosym) ¹ avait permis de déterminer les positions des atomes de ^{23}Na dans l'ETS-10. L'expérience MQMAS devait alors confirmer les résultats précédemment obtenus.

La figure 10 de l'article montre que la technique MAS est incapable de séparer les différents sites. Nous remarquons simplement un élargissement des

¹S. GANAPATHY AND S. VEGA, *J. Am. Chem. Soc.* 120 (1998), pp. 1078–1079

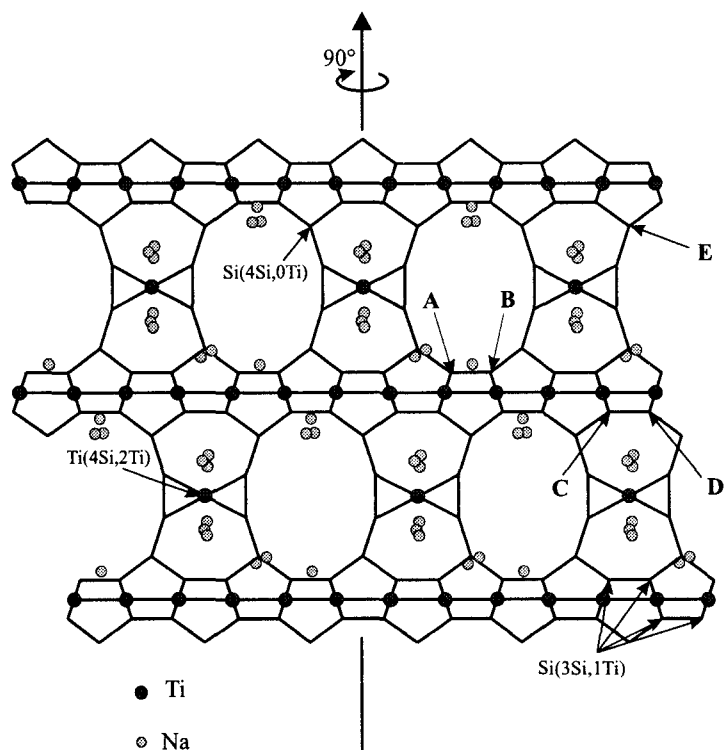


FIG. 4.1: Représentation schématique de la structure de l'ETS-10. Les atomes de titane forment des chaînes dans deux directions perpendiculaires. Une simulation moléculaire (Biosym) a permis de déterminer les positions des atomes de sodium en minimisant l'énergie totale de la structure. Les résultats obtenus sont en accord avec le calcul des distances inter-atomiques $^{29}\text{Si}^{23}\text{Na}$ déduite d'une expérience REAPDOR.

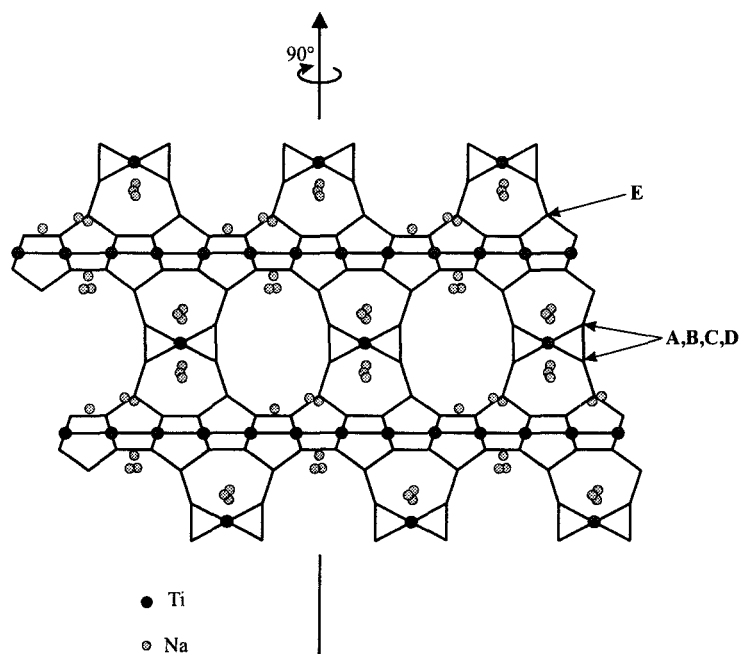


FIG. 4.2: Autre représentation de la structure de l'ETS-10 obtenue par rotation de la figure 4.1, d'un angle de 90° autour de l'axe vertical. Les chaînes de titane qui étaient dans le plan sur la figure précédente, sont maintenant perpendiculaires à ce même plan, et vice-versa. Cette figure montre que les atomes de ^{23}Na , qui paraissaient appartenir aux larges pores (12-membered rings) sur la figure 4.1, sont en fait logés dans les plus petits pores (7-membered rings).

résonances lorsque le rapport Si/Al diminue. Par contre, le spectre MQMAS (cf. Fig. 11 de l'article) montre la présence dans la structure de l'ETS-10, de 3 environnements différents pour le sodium. L'un des atomes de sodium (III) possède une constante quadrupolaire plus importante que les deux autres atomes (I) et (II). D'ailleurs, ces 2 derniers environnements ne diffèrent que légèrement par leur déplacement chimique δ_{CS} . La figure 12 représente les projections isotropes des spectres MQMAS obtenus à partir des échantillons de ETS-10 et ETAS-10 (3 valeurs de rapport Si/Al). Nous observons un élargissement et un recouvrement des résonances, surtout dans la région des sites (I) et (II). La distortion de la résonance le long de l'axe CS (sites I et II) suggère l'existence d'une distribution de déplacement chimique δ_{CS} .

L'étude de la structure de l'ETS-10 met en évidence la présence de 3 sites titanium nonéquivalents dont 2 ont un environnement similaire. L'expérience MQMAS faite sur le sodium confirme donc la présence de ^{23}Na aux côtés des atomes de titanium puisque 2 des sites ^{23}Na ont pratiquement les mêmes constantes quadrupolaires et déplacements chimiques. Ce résultat est une autre preuve que les atomes de sodium ont pour rôle de compenser les charges négatives des atomes de titanium. Nous remarquons aussi que même si 2 atomes de ^{23}Na sont nécessaires pour contrebalancer la charge apportée par 1 atome de titanium, nous n'obtenons que 3 résonances sur le spectre MQMAS et non 6 signaux correspondant à 6 environnements différents pour le sodium. Ceci est probablement dû à la position symétrique par rapport au titanium, des 2 atomes de sodium (cf. la position des atomes ^{23}Na par rapport aux titaniums sur les Figs. 4.1 et 4.2).

Enfin, nous avons quantifié les proportions relatives des différents sites ^{23}Na en appliquant le calcul REGULAR au spectre 3QMAS de l'ETS-10. Comme les sites titanium sont dans un rapport de 1 :1 :1, pour les 3 envi-

ronnements possibles, nous devrions retrouver le même rapport pour les sites ^{23}Na , tout au moins une valeur de 2 :1 pour respectivement les sites (I,II) et (III). Sur la projection isotrope, l'intensité de la résonance correspondant au site (III) est probablement sous-estimée et le fit de cette projection ne conduit à la concentration de 2 pour 1 par rapport à la résonance des sites (I,II). En effet, nous avons vu que l'expérience MQMAS était très sensible à la force de l'interaction quadripolaire. L'intensité de la résonance, correspondant au site (III), fortement quadripolaire, doit être corrigée. Le résultat de la quantification des sites ^{23}Na dans l'ETS-10, est représenté par la figure 13 de l'article. La proportion relative 2 :1 des sites (I,II) et (III) a été déterminée précisément avec REGULAR. Nous pouvons remarquer que le calcul n'a pas su différencier les sites (I) et (II) qui était d'ailleurs à peine discernable sur le spectre 2D.

Anisotropic Chemical Shielding, M-Site Ordering, and Characterization of Extraframework Cations in ETS-10 Studied through MAS/MQ-MAS NMR and Molecular Modeling Techniques

S. Ganapathy,^{*,†} T. K. Das,[†] R. Vetrivel,[†] S. S. Ray,[†] T. Sen,[†] S. Sivasanker,^{*,†} L. Delevoye,[‡] C. Fernandez,[‡] and J. P. Amoureux[‡]

Contribution from the National Chemical Laboratory, Pune - 411 008, India, and Laboratoire de Dynamique et Structure des Matériaux Moléculaires, CNRS URA 801, Université des Sciences et Technologies de Lille, F-59655 Villeneuve D'ASCQ Cedex, France

Received August 5, 1997

Abstract: The local structural characteristics of Si and Ti sites in ETS-10 as derived from a combination of high-resolution magic angle spinning (MAS) NMR spectroscopic and molecular modeling studies are reported. Pure and highly crystalline ETS-10 and aluminum-substituted ETS-10 (ETAS-10), devoid of impurity ETS-4 phase, were synthesized and fully studied by MAS and multiple-quantum magic angle spinning (MQ-MAS) NMR. More accurate assignments of the experimentally observed ²⁹Si resonances to the crystallographically nonequivalent Si sites are made, and a correlation with T-site geometry is established. ²⁹Si slow MAS NMR is shown to be a very general and powerful methodology to unequivocally establish heteroatom substitution in the zeolite lattice, and this was used to probe the local symmetry and chemical shielding at different Si sites in ETS-10 and ETAS-10. ²⁹Si and ²⁷Al MAS NMR spectral analysis of ETAS-10 is used to confirm that the aluminum substitution occurs only in Si[4Si,0Ti] silicon sites. This, in turn, was used to generate cluster models for computer graphics techniques. The electronic structure of such cluster models and the calculated aluminum substitution energy values pinpoint the topographical location of aluminum in ETAS-10. The acidity of ETAS-10 is predicted on the basis of the quantum chemical cluster model calculations. The first application of MQ-MAS NMR to study cation environments in molecular sieves is also reported and is used in the present study to investigate the local structural characteristics of sodium cations in ETS-10 and ETAS-10.

Introduction

An industrially significant discovery is the titanosilicate (TS-1) with MFI framework structure,¹ which is constructed of linked SiO₄ tetrahedra and TiO₄ tetrahedra. Though it is widely accepted that Ti is in a distorted tetrahedral coordination, there are differences of opinion regarding the extent of distortion. It has been pointed out by On Trong et al.² that the distortion is so high that the Ti ions cannot be considered anymore as part of the framework. However, Bellusi and Fattore³ argued that the distortion is minimal and hence titanium can be assumed to be in the framework. The dispute has not been solved because the concentration of the titanium is too low (Si/Ti = 30) to be characterized by any bulk analytical techniques and the coordination around Ti is so labile that it depends on the experimental conditions.

ETS-10 is a prominent member of a microporous titanosilicate family whose basic structural characteristics comprise corner-sharing SiO₄ tetrahedra and TiO₆ octahedra linked through bridging oxygens. Although it has been just recently discovered, there have been a large number of studies⁴⁻⁴⁰ due to its

interesting structural features. The pore system of ETS-10 has a stacking disorder,^{17,18,24} comprising two ordered polymorphs,

- (6) Kuznicki, S. M. U.S. Patent 4,853,202, 1989.
- (7) Kuznicki, S. M.; Thrush, K. A. Eur. Pat. 0405978A1, 1990.
- (8) Kuznicki, S. M. U.S. Patent 5,011,591, 1991.
- (9) Kuznicki, S. M.; Thrush, K. A. U.S. Patent 4,994,191, 1991.
- (10) Sommerfeld, D. A.; Ellis, W. R., Jr.; Eyring, E. M.; Kuznicki, S. M.; Thrush, K. A. *J. Phys. Chem.* **1992**, *96*, 9975-9978.
- (11) Kuznicki, S. M.; Thrush, K. A.; Allen, F. M.; Levine, S. M.; Hamil, M. M.; Hayhurst, D. T.; Mansour, M. *Synth. Microporous Mater.* **1992**, *1*, 427-453.
- (12) Kuznicki, S. M.; Thrush, K. A. U.S. Patent 5,208,006, 1993.
- (13) Garfinkel, H. M.; Kuznicki, S. M.; Thrush, K. A. WO Pat. 9300152, 1993; EP Pat. 544892, 1993.
- (14) Bozhilov, K. N.; Valtchev, V. *Mater. Res. Bull.* **1993**, *28*, 1209-1214.
- (15) Review article: Looming Ban on Production of CFCs, Halons Spurs Switch to Substitutes. *Chem. Eng. News* **1993** (Nov. 15), 12-18.
- (16) Kuznicki, S. M.; Dang, D.; Hayhurst, D. T.; Thrush, K. A. U.S. Patent 5,346,535, 1994.
- (17) Anderson, M. W.; Terasaki, O.; Ohsuna, T.; Philippou, A.; Mackay, S. P.; Ferreira, A.; Rocha, J.; Lidin, S. *Nature* **1994**, *367*, 347-351.
- (18) Ohuna, T.; Terasaki, O.; Watanabe, D.; Anderson, M. W.; Lidin, S. *Stud. Surf. Sci. Catal.* **1994**, *84*, 413-420.
- (19) Das, T. K.; Chandwadkar, A. J.; Sivasanker, S. *Mater. Res. Bull.* **1994**, *17*, 1143-1153.
- (20) Deeba, M.; Keweshan, C. F.; Koermer, G. S.; Kuznicki, S. M.; Madon, R. S. *Catalysis of Organic Reactions*; Kosak, J. R., Johnson, T. A., Eds.; Marcel Dekker Inc.: New York, 1994; pp 383-396.
- (21) Valtchev, V. *J. Chem. Soc., Chem. Commun.* **1994**, 261-262.
- (22) Valtchev, V.; Mintova, S. *Zeolites* **1994**, *14*, 697-700.
- (23) Blosser, P. W.; Kuznicki, S. M. U.S. Patent 5,453,263, 1995.
- (24) Anderson, M. W.; Terasaki, O.; Ohsuna, T.; Malley, P. J. O.; Philippou, A.; Mackay, S. P.; Ferreira, A.; Rocha, J.; Lidin, S. *Philos. Mag. B* **1995**, *71*, 813-841.
- (25) Das, T. K.; Chandwadkar, A. J.; Budhkar, A. P.; Belhekar, A. A.; Sivasanker, S. *Microporous Mater.* **1995**, *4*, 195-203.

* Corresponding authors. E-mail: siva@ems.ncl.res.in. or ganpat@ems.ncl.res.in. Fax: +91-212-334761/330233.

[†] National Chemical Laboratory.

[‡] Université des Sciences et Technologies de Lille.

(1) Taramasso, M.; Perego, G.; Notari, B. U.S. Patent 4,410,501, 1983.
(2) On Trong, D.; Bittar, A.; Sayari, A.; Kaliaguine, S.; Bonneviot, L. *Catal. Lett.* **1992**, *16*, 85.

(3) Bellussi, G.; Fattore, V. *Stud. Surf. Sci. Catal.* **1991**, *69*, 79-92.

(4) Kuznicki, S. M. Indian Pat. 171379, 1988.

(5) Kuznicki, S. M. Indian Pat. 171483, 1988.

termed A and B.^{17,24} It is titanium-rich (Si/Ti = 5) and is also the first microporous material wherein the location and coordination of metal atom, namely titanium, has been established from crystallographic and related techniques.^{17,24} For a better utilization of newer materials (such as ETS-10) for molecular sieving and catalytic applications, it is essential to devise efficient and simple synthesis procedures and understand the structural features such as T-site ordering, as well as evaluate its electronic properties and acidity characteristics. Our paper focuses on the above aspects of ETS-10 through magic angle spinning (MAS) NMR, multiple-quantum magic angle spinning (MQ-MAS) NMR, and molecular modeling studies.

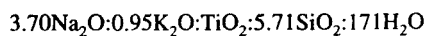
From the MAS NMR point of view, contrary to aluminosilicates,⁴¹ the titanosilicate framework does not lead to dipolar broadening of the silicon lines since titanium can be considered to be magnetically dilute (⁴⁷Ti, ⁴⁹Ti; $n = 7.28, 5.51\%$). Thus, the ²⁹Si MAS NMR spectra can be obtained at high magnetic fields (ca. 7 T) with increased resolution even for a very low value of Si/Ti, and additionally, they are readily amenable for a slow MAS spectral analysis to characterize the anisotropic chemical shielding and local symmetry at the various silicon sites. As shown in this paper, this approach is very general and therefore is useful in resolving disputes regarding heteroatom substitutions in the frameworks of microporous materials. Further, the recently discovered⁴² MQ-MAS NMR techniques offer new opportunities to probe the sodium cation environment through ²³Na 3Q MAS and the aluminum substitution through ²⁷Al 3Q and 5Q MAS NMR.

We reported recently an efficient synthesis procedure for getting crystalline ETS-10 devoid of ETS-4 impurity.³¹ We now report the structural and electronic characteristics of ETS-10 derived from high-resolution MAS NMR spectroscopy and molecular modeling techniques. ETS-10 is known to exist in two polymorphic forms A and B as reported by Anderson et al.^{17,24} All our simulations, modeling, and the interpretation of the MAS NMR results are based on the crystal structure of polymorph B. The 80 silicon atoms in the unit cell of ETS-10 fall either into 11 types of Si sites in polymorph B or into 20 types of Si sites in the case of polymorph A. Thus our interpretation of results for polymorph B is applicable to

polymorph A also, since the correspondence of the Si sites between the two polymorphs is known.^{17,24} The as-synthesized ETS-10 is highly crystalline and has exceptional phase purity as observed from an enhanced signal multiplicity in ²⁹Si MAS experiments. Details of T-site ordering, cation site characterization, the framework substitution, and the favorable location of aluminum substitutions and acidity of ETS-10 are reported here.

Experimental Section

Synthesis. Different methods of preparation of ETS-10 have been reported in the literature based on the titanium compounds used as the source of titanium. We recently reported a method for rapidly synthesizing ETS-10 in a highly crystalline and pure form.³¹ The hydrothermal synthesis of ETS-10 using TiCl₄ was carried out with a gel of the following molar composition:



In a typical synthesis, a solution of 9.3 g of NaOH in 40 g of distilled water was added to a vigorously stirred solution of 52.5 g of sodium silicate (28.6% SiO₂, 8.82% Na₂O, 62.58% H₂O) and 40 g of distilled water. This was followed by the dropwise addition of 32.75 g of a TiCl₄ solution (25.42 wt % TiCl₄, 25.92 wt % HCl, 48.60 wt % H₂O) to this mixture (colorless gel) with rapid stirring. KF·2H₂O (7.8 g) was next added to the above gel (pH = 11.2 ± 0.1) and the mixture stirred well. The mixture was then transferred to a stirred stainless steel autoclave (Parr Instruments, U.S.) and the crystallization carried out at 473 K with a stirrer speed of 300 rpm for 16 h. After crystallization, the products were filtered and washed with deionized water until the pH of the filtrate was 10.7–10.8. It was dried at 373 K for 8–10 h. In earlier procedures, where TiCl₃ was the source of titanium,^{17,19,24–27,33–35} ETS-4 or ETS-10 needed to be used as seed. Further, the crystallization time was long (many days) and the product invariably contained ETS-4 impurity.

ETS-10 was synthesized using the same starting materials as ETS-10 except that a certain amount of sodium aluminate was added to the gel to get the desired Si/Al ratio in the product, the synthesis conditions being the same as above. Three samples with Si/Al ratios 62, 42, and 22 were synthesized.

MAS/MQ-MAS NMR Spectroscopy. MAS NMR spectra were recorded on a Bruker MSL-300 Fourier transform (FT) NMR spectrometer at ambient probe temperature (298 K). ²⁹Si NMR spectra were recorded at 59.621 MHz, while ²⁷Al NMR spectra were recorded at 78.206 MHz. The spinning speed was controlled to within ±5 Hz using a Bruker pneumatic speed controller. The magnetic field was carefully shimmed on the ¹H resonance sample of spinning TMS, which was subsequently used as external reference for ²⁹Si. The magic angle was precisely set using KBr and maximizing the rotational echo intensities of the satellite transitions of ⁷⁹Br. Free induction decays were accumulated in a 18-kHz spectral window using a 45° flip angle, 3-μs pulse, and 4-s relaxation delay. Typically, 8000–12 000 transients were accumulated before they were remotely processed on a SiliconGraphics Indigo2 workstation using the Bruker UXP software package.⁴³

MQ-MAS NMR experiments were performed on a Bruker ASX-400 FT-NMR spectrometer equipped with a specially made MAS probehead capable of high-speed spinning (up to 15 kHz) and radio frequency field (rf) generation (up to 350 kHz). A three-pulse sequence, which incorporates a zero-quantum filter, was used. This pulse scheme ensures optimum selection of the mirror echo and anti-echo coherence transfer pathways to give pure absorption mode line shapes in the final two-dimensional (2D) SQ-MQ correlation plot. The first pulse was individually optimized for the 3Q (²³Na and ²⁷Al) experiments to obtain the best efficiency for the multiple-quantum (±3Q) coherence creation. In a similar way, the second pulse, which transfers these two symmetrical coherences into ZQ coherence, was also optimized. The further conversion to (−1Q) single-quantum coherence of the observed

(26) Rocha, J.; Lin, Z.; Ferreira, A.; Anderson, M. W. *J. Chem. Soc., Chem. Commun.* **1995**, 867–868.

(27) Anderson, M. W.; Philippou, A.; Lin, Z.; Ferreira, A.; Rocha, J. *Angew. Chem., Int. Ed. Engl.* **1995**, *34*, 1003–1005.

(28) Davis, R. J.; Liu, Z.; Tabora, J. E.; Wieland, W. S. *Catal. Lett.* **1995**, *34*, 101–113.

(29) Carli, R.; Bianchi, C. L.; Ragaini, V. *Catal. Lett.* **1995**, *33*, 49–55.

(30) Robert, R.; Rajmohanan, P. R.; Hegde, S. G.; Chandwadkar, A. J.; Ratnasamy, P. J. *Catal.* **1995**, *155*, 345–352.

(31) Das, T. K.; Chandwadkar, A. J.; Sivasanker, S. *J. Chem. Soc., Chem. Commun.* **1996**, 1105–1106.

(32) Sankar, G.; Bell, R. G.; Thomas, J. M.; Anderson, M. W.; Wright, P. A.; Rocha, J. *J. Phys. Chem.* **1996**, *100*, 449–452.

(33) Anderson, M. W.; Rocha, J.; Lin, Z.; Philippou, A.; Orion, I.; Ferreira, A. *Microporous Mater.* **1996**, *6*, 195–204.

(34) Das, T. K.; Chandwadkar, A. J.; Budhkar, A. P.; Sivasanker, S. *Microporous Mater.* **1996**, *5*, 401–410.

(35) Das, T. K.; Chandwadkar, A. J.; Sivasanker, S. *J. Mol. Catal.* **1996**, *107*, 199–205.

(36) Grillo, M. E.; Carrazza, J. *J. Phys. Chem.* **1996**, *100*, 12261–12264.

(37) Mihailova, B.; Valchev, V.; Mintova, S.; Konstantinov, L. *Zeolites* **1996**, *16*, 22–24.

(38) Yang, X.; Truitt, R. E. *J. Phys. Chem.* **1996**, *100*, 3713–3718.

(39) Liu, X.; Thomas, J. M. *J. Chem. Soc., Chem. Commun.* **1996**, 1435–1436.

(40) De Luca, P.; Nastro, A. *Stud. Surf. Sci. Catal.* **1996**, *105*, 221–228.

(41) Engelhardt, G.; Michel, D. *High-Resolution Solid State NMR of Silicates and Zeolites*; John Wiley & Sons: New York, 1987.

(42) Frydman, L.; Harwood, J. S. *J. Am. Chem. Soc.* **1995**, *117*, 5367–5368.

(43) *UXNMR, Acquisition and Processing of NMR Data*; Bruker: Karlsruhe, Germany, 1991.

($-1/2$, $+1/2$) central transition was achieved using a soft 90° pulse of duration $9 \mu\text{s}$. The phase cycling was designed to select only the desired pathway $(0) - (\pm 3) - (0) - (-1)$. Rotor synchronization ($\nu_r = 14.925 \text{ kHz}$) along t_1 was used to eliminate intense sidebands appearing along the MQ dimension. Typical accumulation involved $2048 (t_2) \times 128 (t_1)$ values for ^{23}Na and ^{27}Al 3Q experiments. For each t_1 step, the number of scans was typically 240 and 2400 for 3Q MAS on ^{23}Na and ^{27}Al , respectively. A 2D Fourier transform with respect to t_1 and t_2 leads to pure absorption mode 2D spectra.

Computer Simulations of Slow MAS Spectra. The computer simulations of slow MAS spectra were carried out using the time domain rotational echo analysis of Maricq and Waugh.⁴⁴ For the simulations, the experimentally identified silicon resonances in distinct environments were considered together with their site occupancies.

The overall time domain response of the observed ^{29}Si magnetization is adequately described by summing the chemical shielding experienced by silicon nuclei located at distinct crystallographic positions. However, for the slow MAS experiments, the spectral resolution is sufficient to distinguish only three distinctly different silicon environments (Si_I , Si_{II} , and Si_{III}) in the case of ETS-10 and four (above three and the silicon environment with an aluminum neighbor) in the case of ETAS-10. Further distinction within each of these based on crystallographic nonequivalence could not be made from slow MAS spectra due to instrumental and signal-to-noise considerations. However, this is found to be sufficient for the complete sideband analysis to be made for these silicon environments and these form the basis for our further discussion.

We consider that only the anisotropic chemical shielding interaction contributes to the sideband intensities. This allows us to write, for free induction decay of a spinning solid,

$$G(t) = \sum_i \exp(i\omega_0 \delta t) \sum_{\alpha, \beta, \gamma} \exp\{i\omega_0 \delta \int_0^t \xi(t') dt'\} \quad (1)$$

where

$$\xi(t') = C_1 \cos \omega_r t' + S_1 \sin \omega_r t' + C_2 \cos 2\omega_r t' + S_2 + \sin 2\omega_r t'$$

$$\delta = \sigma_{33} - \sigma_{11}$$

$$\bar{\sigma} = 1/3 \text{Tr}(\sigma)$$

$$\eta = \frac{\sigma_{11} + \sigma_{33} - 2\sigma_{22}}{\sigma_{33} - \sigma_{11}}$$

The detailed definition of the modulation coefficients C_1 , S_1 , C_2 , and S_2 may be found in ref 44. σ_{11} , σ_{22} , and σ_{33} are the principal elements of the chemical shielding tensor defined in the principal axis system and the summation "i" is over I-, II-, III-type silicons. The sideband intensities are governed by the anisotropy (δ) and asymmetry (η) of the chemical shielding, and these are determined from the analysis of the slow MAS spectra. It may be noted that the conventional assignment of chemical shielding tensors, namely $\sigma_{11} \leq \sigma_{22} \leq \sigma_{33}$, has been used and the asymmetry parameter η has a value between -1 and $+1$, the extreme values corresponding to axially symmetric tensors. Here, the Euler angles (α , β , and γ) define the orientation of the chemical shielding tensor of the i th silicon species in the MAS rotor frame which in turn is oriented at an angle $\cos^{-1}(1/\sqrt{3})$ with respect to the main magnetic field.

A powder averaging was done in the three-dimensional Cartesian space defined by the Euler angles (α , β , and γ), and using eq 1, the rotational echo was calculated by evaluating the integral over one rotor period ($0 - 2\pi/\omega_r$) for a series of equally spaced time intervals with the spacing chosen to give an adequate spectral width. The rotational echo was replicated over a 230-ms period to give the resultant free induction decay. This was subsequently convoluted with an exponential line broadening function before Fourier transformation to give the slow MAS spectra. The simulations were carried out on a personal computer using a program written in Fortran.

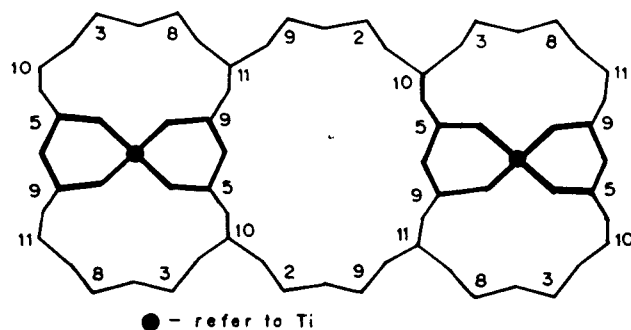


Figure 1. Computer graphics view of ETS-10 framework projected down the c axis showing the framework of Si and Ti atoms. The oxygens, lying approximately in the middle of the M atoms (where M = Si or Ti), are not labeled. For the numbering and connectivity of the M sites, please refer to Table 1. Atoms 1, 4, 6, and 7 occur in alternate layers below 10, 2, 5, and 5, respectively.

Table 1. Geometric Data of the Polymorph B of ETS-10 Structure

site (M)	M-O distance ^a (Å)	M-O-M angle ^b (deg)	connectivity ^c
Ti ₁	1.887	145.990	Si ₅ , Si ₅ , Si ₉ , Si ₉ , Ti ₃ , Ti ₃
Ti ₂	1.887	144.687	Si ₃ , Si ₃ , Si ₇ , Si ₇ , Ti ₃ , Ti ₃
Ti ₃	1.883	145.340	Si ₈ , Si ₆ , Ti ₁ , Si ₄ , Ti ₂ , Si ₂
Si ₁	1.575	149.700	Si ₄ , Si ₄ , Si ₇ , Si ₇
Si ₂	1.577	142.820	Si ₆ , Si ₉ , Si ₁₀ , Ti ₃
Si ₃	1.577	142.652	Si ₇ , Si ₈ , Si ₁₀ , Ti ₂
Si ₄	1.577	144.352	Si ₅ , Si ₈ , Si ₁ , Ti ₃
Si ₅	1.577	143.447	Si ₄ , Si ₉ , Si ₁₀ , Ti ₁
Si ₆	1.580	143.147	Si ₂ , Si ₁₀ , Si ₇ , Ti ₃
Si ₇	1.580	142.507	Si ₃ , Si ₁ , Si ₆ , Ti ₂
Si ₈	1.577	145.140	Si ₃ , Si ₄ , Si ₁₁ , Ti ₃
Si ₉	1.577	143.762	Si ₂ , Si ₅ , Si ₁₁ , Ti ₁
Si ₁₀	1.577	150.772	Si ₂ , Si ₃ , Si ₅ , Si ₆
Si ₁₁	1.580	152.190	Si ₈ , Si ₈ , Si ₉ , Si ₉

^a The M-O distances are the average of six Ti-O distances for TiO₆ octahedra and the average of four Si-O distances for SiO₄ tetrahedra.

^b The M-O-M angles are the average of six Ti-O-M (where M = Ti or Si) angles for the TiO₆ octahedra and the average of four Si-O-M (where M = Ti or Si) angles for SiO₄ tetrahedra. ^c Neighboring M sites connected through bridging oxygen.

Molecular Modeling. The computer graphics (CG) visualization of ETS-10, the cluster model generation, and the semiempirical quantum chemical calculations were performed on a SiliconGraphics Indigo2 workstation using the Insight II software package⁴⁵ supplied by Biosym Technologies Inc. (U.S.). The ETS-10 lattice was modeled from the crystal structure reported by Anderson et al.^{17,24} for the polymorph B. The unit cell of ETS-10 has a stoichiometry of $[\text{M}_{96}\text{O}_{208}]^{32-}$ (where M = Si or Ti), or precisely $[(\text{SiO}_2)_{80}(\text{TiO}_3)_{16}]^{32-}$ where the Si/Ti ratio is 5.

A CG view of the ETS-10 framework showing the various Si and Ti sites is given in Figure 1. There are 11 distinct Si sites and three distinct Ti sites in the crystal structure of ETS-10 (polymorph B). All of the Ti sites are octahedrally coordinated, where two oxygen atoms are bridging to adjacent Ti sites and the remaining four oxygen atoms are bridging to Si sites. All of the Si sites are tetrahedrally coordinated, and there are basically two types of silicons; there are silicons [Si(4Si)], where all the four oxygen atoms are bridging to adjacent Si sites, and silicons [Si(3Si,1Ti)], where three oxygen atoms are bridging to adjacent Si sites and the remaining oxygen atom bridging to adjacent Ti sites. The average M-O distances and M-O-M angles (where M = Si or Ti), calculated from the reported crystal structure, are given in Table 1. Semiempirical quantum chemical calculations using standard MNDO procedure were carried out on cluster models representing the Si sites in ETS-10 to understand the electronic structure, preferred locations for Al substitution, and resulting acidity.

(45) *Insight II user Guide*, Version 2.3.5; Biosym Technologies: San Diego, CA, 1994.

(44) Maricq, M. M.; Waugh, J. S. *J. Chem. Phys.* **1979**, *70*, 3300-3316.

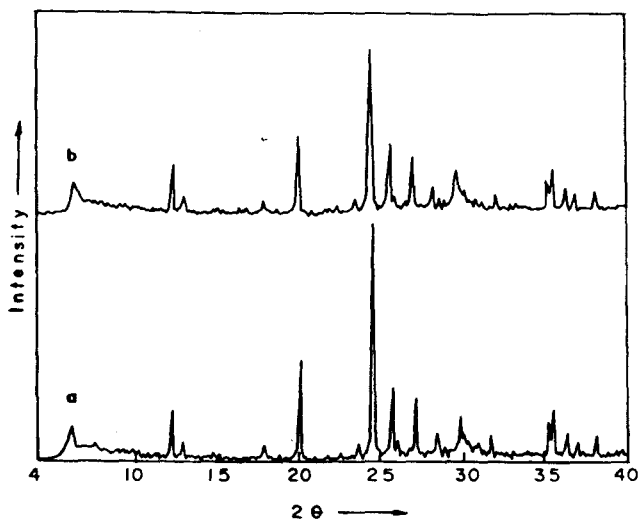


Figure 2. X-ray diffraction patterns obtained on (a) ETS-10 and (b) ETAS-10 synthesized as outlined in the text. The narrow reflections are readily indexed to the known structure of the highly crystalline ETS-10 phase, while the small broad feature is attributable to a possible stacking disorder in the structure.

Results and Discussion

The identification of the crystalline phase of the material and its exceptional phase purity were verified by XRD (Rigaku, Model D-max III). The diffraction pattern, shown in Figure 2 (as-synthesized), exhibits both broad and sharp reflections, as noted by Anderson et al.,^{24,33} indicating that the material is highly crystalline exhibiting disorder. The XRD patterns in the range $2\theta = 4\text{--}40^\circ$ could be indexed to the ETS-10 structure,^{17,25,33–35,39} and the absence of impurity peaks shows that a highly crystalline ETS-10 and ETAS-10, devoid of the ETS-4 phase, has been synthesized. The diminished intensity of the peaks in the low- 2θ region is attributable to occluded water.

²⁹Si MAS NMR Spectra of ETS-10. The ²⁹Si MAS NMR spectrum of ETS-10, referenced to tetramethylsilane, is shown in Figure 3a (here, a resolution enhancement using a suitable window function was carried out by apodizing the time domain NMR data with the UXNMR software package to enhance the spectral resolution). There is a noticeable absence of signal in the region around 90.0 ppm which confirms the absence of ETS-4 impurity and also the absence of silicon environment corresponding to [SiOH, Si(OH)₂] or the defect sites. Thus, the NMR results show that the synthesized material exhibits exceptional phase purity with the absence of defect sites.

The spectrum in Figure 3a shows three types of distinct silicon environments. The resonances (δ) due to the titanium-rich [Q⁴-(3Si,1Ti)] (−94 to −95 ppm; −96 to −97 ppm) and silicious [Q⁴(4Si,0Ti); −103 to −104 ppm] environments are readily identified and marked as I, II, and III, respectively, for further discussion. The observed spectrum could be deconvoluted into seven resonances as shown in Figure 3b, whose chemical shifts and peak areas can be measured accurately for quantitative analysis. The results are given in Table 2.

The approximate ratio of the intensity of the signals of I, II, and III sites is 4:4:2, which is in correspondence with the earlier reports.^{17,24} In ETS-10, among the 11 crystallographically distinct Si sites, Si₁, Si₁₀, and Si₁₁ are of the type III, namely Si(4Si,0Ti). Si₁ and Si₁₁ have half-occupancy compared to the full occupancy of Si₁₀. Each of the two signals of equal intensity of type III Si sites can be assigned to Si₁ + Si₁₁ and Si₁₀ or vice versa. This distinction within type III Si sites was not reported earlier probably due to poor spectral resolution.^{17,24}

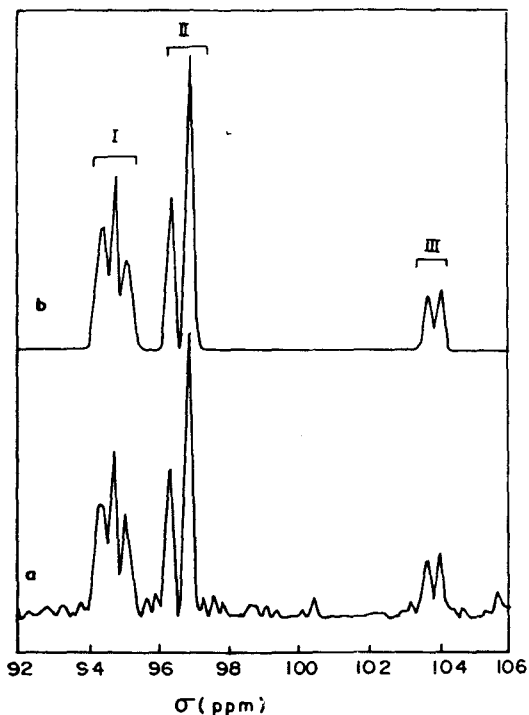


Figure 3. (a) Resolution-enhanced ²⁹Si MAS NMR spectrum of ETS-10 showing the distinct resonances corresponding to Si(4Si,0Ti) and two types of Si(3Si,1Ti) environments. (b) Simulation of spectrum (a) using a Gaussian function.

However, we could clearly distinguish two silicon resonances at −103.6 and −103.9 ppm (Figure 3a) with almost 1:1 intensity. The exact assignment of these resonances to the silicon sites could not be made because of the large deviation in M–O–M angles (see later).

The signals due to type I and II Si sites have been classified into four distinct types, namely A, B, C, and D, by Anderson et al.^{17,24} This classification was based on their location in a 12-ring or 7-ring. However, an inspection of the structure shows that all Si sites have locations common to 12- and 7-rings. From the CG analysis of the topography of these silicon sites, we observe that there are two types of silicons, with respect to their coordination to titanium; Si₂, Si₄, Si₆, and Si₈ are coordinated to Ti₃, whereas Si₃, Si₅, Si₇, and Si₉ silicons are coordinated to either Ti₁ or Ti₂. Two distinct sodium ions, which balance the two negative charges on titanium, with different quadrupole tensors have been reported.²⁴ This points to possible occurrence of two different types of exchangeable cations corresponding to (Ti₁ or Ti₂) and (Ti₃) and suggests that type I and II [Si(3Si,1Ti)] sites could be classified on the basis of the titanium coordinated to it. However, our NMR results on ETAS-10 and molecular modeling rule out this possibility. This is discussed below.

²⁷Al and ²⁹Si MAS NMR of ETAS-10. The ²⁷Al MAS NMR spectrum of ETAS-10, synthesized in a typical Si/Al ratio of 42, is shown in Figure 4a. Tetrahedral framework incorporation of Al is borne out in Figure 4a by a very intense resonance at = 57.3 ppm. The presence of a weak signal at the octahedral Al position (~0 ppm) is more clearly visible in the ²⁷Al MQ-MAS study and is attributable to occluded aluminum oxide in the pores.

The ²⁹Si MAS NMR spectrum of ETAS-10 (Si/Al = 42) is shown in Figure 4b. While type I, II, and III environments noticed in ETS-10 are seen to be retained in ETAS-10, additional resonances at −90.2 and −92.0 ppm appear. The loss of

Table 2. ^{29}Si Peak Positions and Relative Intensities of ETS-10 and ETAS-10

sample	property	type I	type II	type III	additional peaks ^a	
					A	B
ETS-10	peak positions ^b	-94.1, -94.5, -94.7	-96.1, -96.6	-103.6, -103.9		
	relative intensity ^c	3.9 (1.7:1.3:0.9)	4.1 (1.8:2.3)	2.0 (1:1)		
ETAS-10; Si/Al = 42	peak positions	-93.9	-96.0	-103.5	-90.2	-92.0
	relative intensity	3.0	3.6	1.4	1.7	0.3

^a Due to Si[2Si,1Ti,1Al] corresponding to Al substitution at Si (see text). ^b Peak positions (δ) are given in ppm with reference to TMS. ^c Values in parentheses denote integrated intensities of peaks resolved in each type.

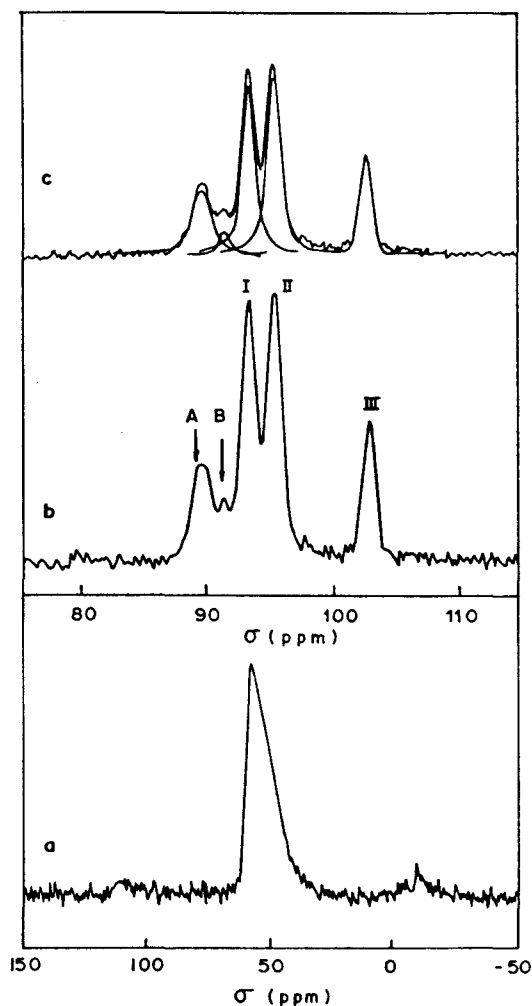


Figure 4. (a) ^{27}Al MAS NMR spectrum of ETAS-10 (Si/Al = 42). (b) ^{29}Si MAS NMR spectrum of ETAS-10 (Si/Al = 42). (c) Deconvoluted ^{29}Si MAS NMR spectrum of ETAS-10 (Si/Al = 42).

resolution due to peak broadening of the silicon resonances is observed in Figure 4b, compared to that in Figure 3, due to the incorporation of Al in the framework. The increased broadening is attributable to second nearest neighbor effects through the dipolar interactions between the spin- $1/2$ ^{29}Si nucleus and the spin- $5/2$ ^{27}Al nucleus, not eliminated in MAS experiments due to nonvanishing electric field gradients at the aluminum sites.⁴⁶ This is especially aggravated at our 7.1-T field of operation. Deconvolution assuming a Gaussian-type peak function were performed with UXNMR software package. The deconvoluted spectrum was simulated, and the chemical shift values as well as the peak areas of these signals were calculated for quantitative analysis (Table 2).

It is known that Al substitution in various zeolite structures gives rise to a deshielding of ~ 4.00 ppm for each Si substituted

by Al.⁴¹ This would imply that the new resonances in ETAS-10 samples arise from lattice substitution corresponding to an environment where Si coordinates to a titanium and aluminum. That this occurs in the neighborhood of type I and II sites would imply a preferential substitution of Al at the siliceous Si[4Si,0Ti] environments and hence an Al-Ti avoidance,^{27,33} as clearly indicated in our studies. Among the two new peaks, the resonance at -90.2 ppm is more intense and arises from a preferential substitution of Al at the completely siliceous site which is adjacent to site I. We rule out the possibility that this peak is due to ETS-4 impurity as we find that the peak intensity increases with increasing Al substitution and, further, the XRD data shows an absence of the impurity of ETS-4 phase. Similarly, the less intense peak at -92.0 ppm is due to Al substitution adjacent to site II. Quantum chemical calculations pinpoint the topographical location of the preferred silicon site for Al substitution and allow us to make further T-site assignments, of I and II in ETS-10.

^{29}Si Slow MAS NMR and Disruption of Local Symmetry. A striking feature of the ^{29}Si MAS spectrum of ETS-10 is the revelation of an intense and characteristic sideband pattern when the sample was spun at much slower speeds, namely ~ 385 and 700 Hz. Typical spectra at these two spinning speeds are presented in Figure 5, parts a and b, respectively. This is in contrast to the spectrum taken at moderate spinning speeds (2.5–3.5 kHz, Figure 3) where the presence of spinning sidebands can be hardly noticed. The sideband pattern of signals of silicons of type I and II are quite similar, whereas type III is nearly sideband free, showing that the anisotropic chemical shielding at the siliceous and titanium-rich environments are markedly different.

The sideband intensities for the resonance at -103.9 ppm fall off very rapidly; a near-isotropy for the chemical shielding is readily discerned for the set of two resonances which were identified as $\text{Si}_1 + \text{Si}_{11}$ and Si_{10} . Our observations of very near isotropic nature of chemical shielding therefore reaffirm the earlier contention^{17,24} that the set of resonances occurring in the -103.6 to -103.9 ppm range arises purely from siliceous environments devoid of any Si-O-Ti linkage, as only a central silicon connected tetrahedrally to four other lattice silicons can present a nearly perfect T_d symmetry for the chemical shielding. These are further supported from computer simulations of the slow MAS spectra shown in Figure 5c,d. A silicon in an isolated perfect tetrahedral environment of four more silicons has a T_d symmetry, and the chemical shielding tensor is spherically symmetric; the shielding anisotropy therefore vanishes by definition. The observation of the near-isotropy for chemical shielding reinforces our view that, while the tetrahedral arrangement of the siliceous environment is preserved, the slight distortions in the T-site geometry cause the tensor to slightly deviate from being isotropic, thus causing a slight anisotropy, albeit small, to be introduced. This is precisely the reason an empirical correlation of the T-site geometrical parameter, such as, for example, the T-O-T angle, with ^{29}Si chemical shifts

(46) Naito, A.; Ganapathy, S.; McDowell, C. A. *J. Magn. Reson.* **1982**, *48*, 367–381.

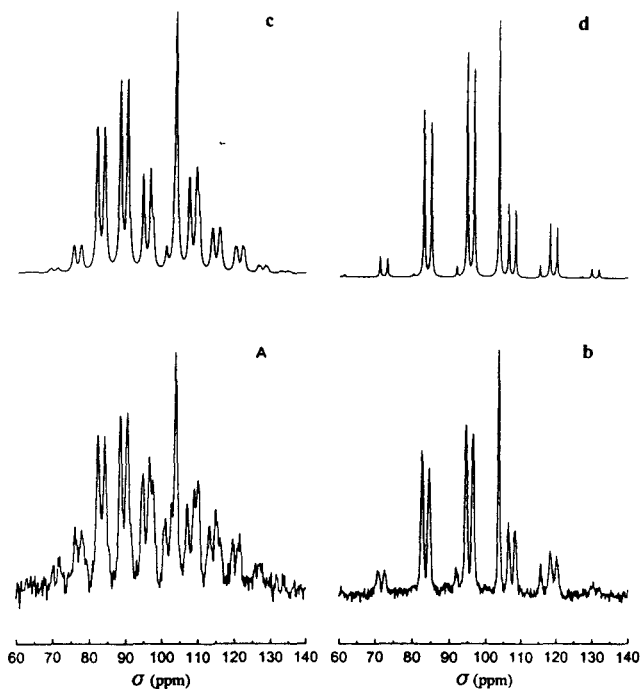


Figure 5. ^{29}Si slow MAS NMR experimental spectra of ETS-10, when the sample was spun at (a) 385 Hz and (b) 700 Hz. The corresponding computer-simulated spectra c and d are also shown above the experimental spectra. The additional splitting in sideband profile in spectrum a, especially for the type I and II resonances, is due to somewhat inferior spinner stability (± 25 Hz) and is partly accounted for in the simulation. An exponential line broadening of 60 Hz was used in the simulations.

have been found.⁴⁷ In other words, the anisotropic shielding at each distinct Si site in the siliceous environment varies in a manner that is purely dictated by the extent of deviation from an ideal tetrahedral symmetry and has a direct bearing on the shielding tensor. This, in turn, causes the isotropic shift to change as well, thus giving rise to multiplicity of silicon resonances in the MAS spectra of highly siliceous zeolites.^{48,49} Thus, the precise correspondence between structure and electronic shielding emerges as a consequence of bond geometry distortions in an ordered zeolite framework obeying a particular space group symmetry.

The intense spinning sidebands for the silicon resonances at ~ -94.5 and -96.5 ppm lend themselves for an immediate analysis. Computer simulations of the slow MAS spectra (Figure 5c,d; see also Table 3) show that the silicon environment is characterized by an anisotropic chemical shielding tensor with the principal elements σ_{11} and σ_{22} being equal in magnitude and σ_{33} distinct. The chemical shielding at I and II is therefore axially symmetric, and unmistakably, there is a transformation from a near- T_d symmetry to C_{3v} symmetry. A Si environment which has three silicons and one titanium as bridged neighbors would make this symmetry transformation possible. Our observations therefore conclusively show that Si[3Si,1Ti] type silicons occur in ETS-10 and further confirm earlier assignment of the silicon signals at -94.6 and -96.6 ppm to these type of silicons. On the basis of symmetry considerations, the 3-fold rotational axis of symmetry will be along the Si-Ti vector. An inspection of the X-ray-determined structure of ETS-10 shows the presence of a chain of $-\text{Ti}-\text{O}-\text{Ti}-$ which connects all of

Table 3. Anisotropic ^{29}Si Chemical Shielding Parameters^a for ETS-10 and ETAS-10

sample	type	σ_{11}^b	σ_{22}^b	σ_{33}^b	$\bar{\sigma}^b$	δ^b	η^b
ETS-10 ^c	I	79.8	79.8	124.5	94.7	44.7	1.0
	II	81.8	81.8	126.5	96.7	44.7	1.0
	III	94.0	108.1	109.0	103.7	15.0	-0.9
ETAS-10 ^d	I	79.5	79.5	125.0	94.7	45.5	1.0
	II	81.5	81.5	127.0	96.7	45.5	1.0
	III	94.0	108.2	109.0	103.4	15.0	-0.9
	A, B	75.5	76.5	121.0	90.8	45.5	1.0

^a Values in ppm with respect to TMS. Positive values (in σ scale) denote increasing shielding. I, II, III, and (A, B) refer to the silicon environments as discussed in the text. ^b For definition see text. ^c From 700-Hz slow MAS computer simulations. ^d From 645-Hz slow MAS computer simulation.

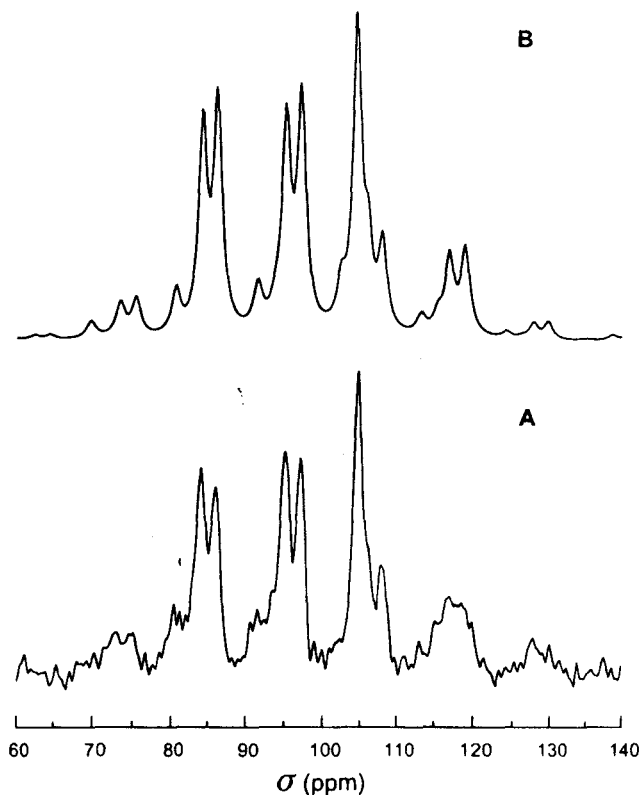


Figure 6. ^{29}Si slow MAS spectrum (A) of ETAS-10 (Si/Al = 62) when the sample was spun at 645 Hz. (B) corresponding computer-simulated spectrum. An exponential line broadening of 260 Hz was used in the simulations.

the titanium octahedra. From the connectivity between SiO_4 tetrahedra and TiO_6 octahedra, the orientation of the unique C_{3v} axis of the chemical shielding tensor of Si[3Si,1Ti] is perpendicular to the long $-\text{Ti}-\text{O}-\text{Ti}-$ chains.

The analysis of the slow MAS spectra of ETAS-10 (Si/Al = 42) was carried out as before, and these results are also collected in Table 3. The corresponding spectral simulations are shown in Figure 6. For this simulation, four distinct Si environments shown in Figure 4b were considered (I, II, III, and A). The peak B is not resolved under low spinning because of increased broadening. Three of them correspond to Si sites belonging to types I, II, and III, as in the parent ETS-10 structure, while the fourth one, belongs to Si[2Si,1Ti,1Al]. Despite the small differences in the simulated intensities obtained, the spectra could be simulated using the anisotropy and asymmetry parameters found for ETS-10. The chemical shielding tensors for Si sites of types I, II, and III are completely preserved in the ETAS-10 structure, thus ensuring identical or near-identical

(47) Ramdas, S.; Klinowski, J. *Nature* **1984**, *308*, 521-523.

(48) Radeaglia, R.; Engelhardt, G. *Chem. Phys. Lett.* **1985**, *114*, 28-30.

(49) Fyfe, C. A.; Grondy, H.; Feng, Y.; Kokotailo, T. *J. Am. Chem. Soc.* **1990**, *112*, 8812-8820.

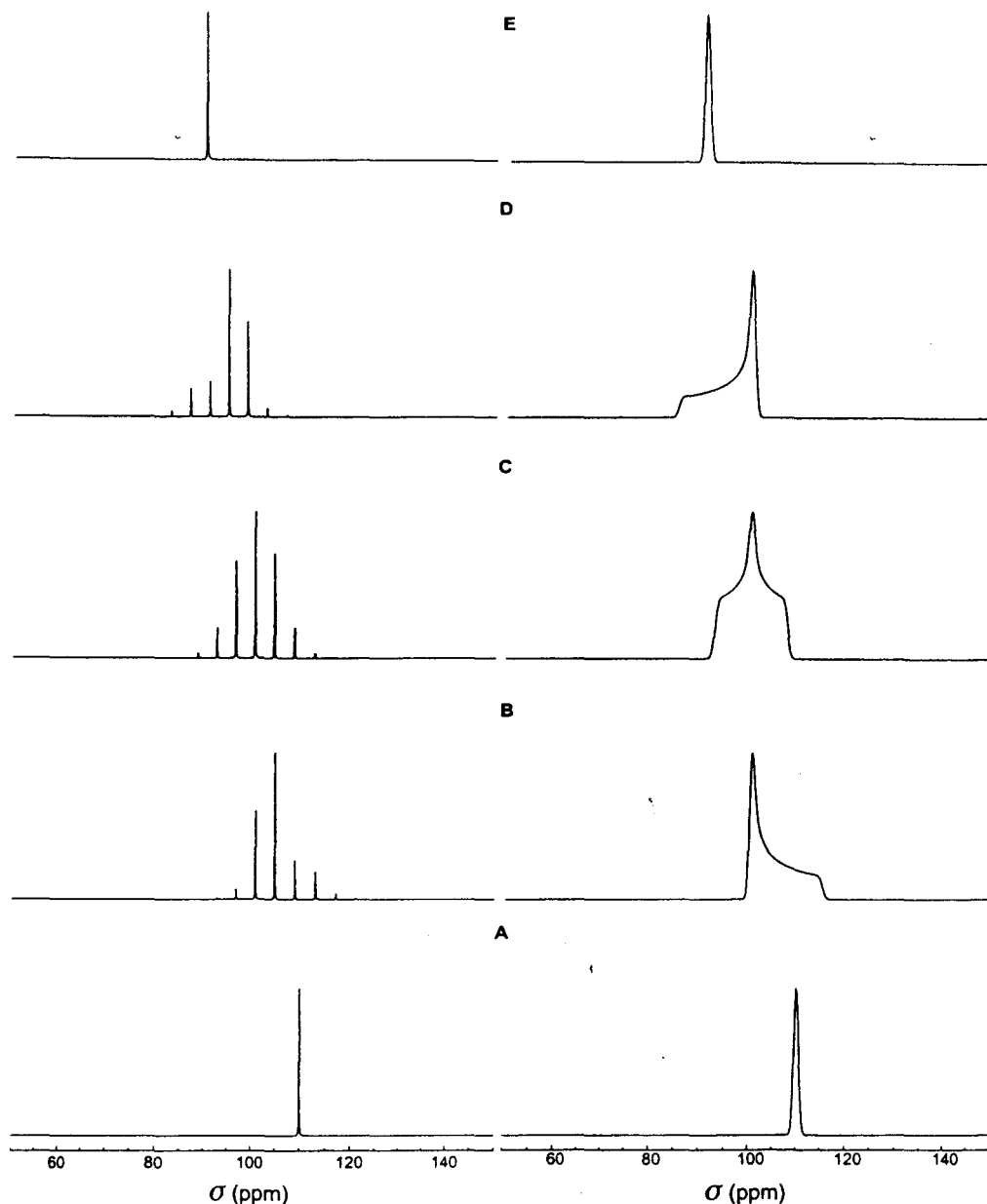


Figure 7. Computer simulations of ^{29}Si slow MAS spectra at a representative spinning speed of 400 Hz to show the correspondence between the change in local symmetry due to heteroatom (M) substitution and the ^{29}Si chemical shielding (A) Si(4Si,0M); (B) Si(3Si,1M); (C) Si(2Si,2M); (D) Si(1Si,3M); (E) Si(0Si,4M). The Gaussian broadened static spectra are also shown side by side. Spectral simulations were carried out using $\delta = 15$ ppm (B, C, and D). A downfield isotropic shift of 5 ppm for every M substitution has been considered in the simulations.

T-site geometries for these sites in the structures of Al-substituted materials. The additional sideband pattern noticed for the Si[2Si,1Ti,1Al] environment also fits to an axial tensor. It is probable that Al substitutes the Si site isomorphously without disturbing the T_d coordination of the T site. However, the geometry varies in such a way that the heteroatom substitution causes the net isotropic shift to change by as much as 5 ppm, and yet, this environment possesses a overall C_{3v} symmetry for the electronic shielding, considering the presence of one neighboring Ti site.

Our approach has general utility in resolving disputes in all zeolite lattices where heteroatoms are isomorphously substituted in place of Si. The stepwise substitution by a heteroatom (M) would transform the local symmetry in the order T_d (0M) \rightarrow C_{3v} (1M) \rightarrow C_{2v} (2M) \rightarrow C_{3v} (3M) \rightarrow T_d (4M) as the extent of substitution increases. As an aid to this generalization of the slow MAS approach for isomorphous heteroatom substitutions, we show in Figure 7 the computer simulated slow MAS and

static ^{29}Si spectra for generic representations of lattice substitution by none [Q⁴(4Si,0M)](A), one [Q⁴(3Si,1M)](B), two [Q⁴(2Si,2M)](C), three [Q⁴(1Si,3M)](D), and four [Q⁴(0Si,4M)](E) heteroatoms (M), and these serve to indicate that indeed the change in local symmetry has a great influence on the ^{29}Si chemical shielding which can be conveniently monitored at high superconducting magnetic fields.

Molecular Modeling Studies. MNDO (modified neglect of differential overlap) calculations were performed to compute the energies of substitution of a single aluminum atom in place of silicon in the ETS-10 framework leading to ETAS-10. The preferred site of aluminum substitution and its consequences on the acidic properties of ETAS-10 are also studied. The geometry of a typical cluster model representing the crystallographic site Si₁₀ is shown in Figure 8. Similar cluster models are derived for the other sites in ETS-10 from the reported crystal structure of polymorph B. A cluster containing one tetrahedral group, namely Si(OH)₄ (denoted as monomer), is

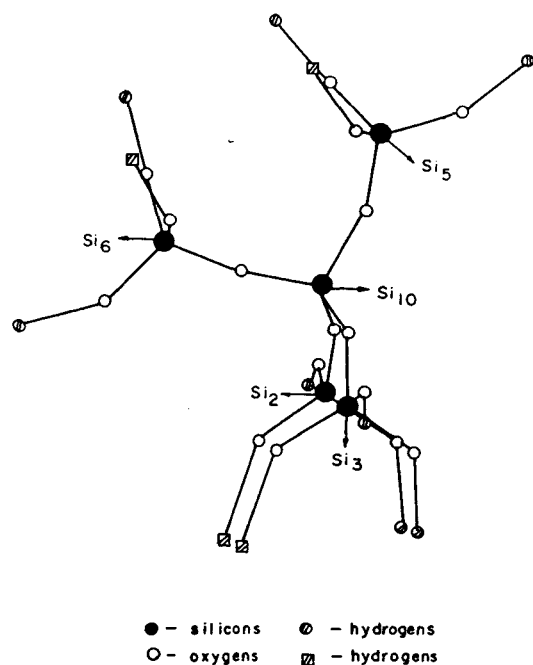
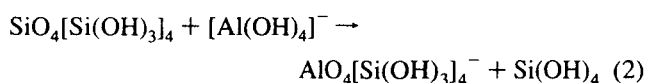


Figure 8. Computer graphics picture of the cluster model chosen to study the electronic property of Si_{10} site. Hydrogens marked as squares represent neighboring Ti sites, while hydrogens marked as circles represent neighboring Si sites.

considered for studying the electronic properties. The terminal oxygen atoms of SiO_4 group are bonded to hydrogen atoms to maintain the electrical neutrality of the cluster. The positions of these terminal hydrogen atoms are located at the nearest-neighbor M-site (where M = Si or Ti) locations.

A larger pentamer cluster model was generated to study the aluminum substitution process. The pentamer cluster model $\{\text{SiO}_4[\text{Si}(\text{OH})_3]_4\}$ represents a SiO_4 group which shares the corners with four adjacent SiO_4 groups through bridging oxygen atoms. Such pentameric cluster models were generated for the Si sites of type III, namely Si_1 , Si_{10} , and Si_{11} , since our MAS NMR studies conclusively showed that these are the sites where Al substitution occurs. The process of substitution of aluminum in ETS-10 lattice is considered as follows:



The substitution energy (SE) of aluminum for silicon in the above process is calculated from their total energies (TE) according to the equation

$$\text{SE} = \text{TE}_{\text{products}} - \text{TE}_{\text{reactants}} \quad (3)$$

The acidity is studied by compensating the negative charge in the $\text{AlO}_4[\text{Si}(\text{OH})_3]_4^-$ cluster by adding a hydrogen to the bridging oxygen between Al and Si. Although there are four possible bridging oxygens, the hydrogen is attached to the bridging oxygen which is facing the large 12-member ring of the ETS-10 lattice. The binding energy of the proton (BE_H) is calculated by considering the following process:



and the following relation:

$$\text{BE}_\text{H} = \text{TE}(\text{AlO}_4\text{H}[\text{Si}(\text{OH})_3]_4) - \text{TE}(\text{AlO}_4[\text{Si}(\text{OH})_3]_4^-) \quad (5)$$

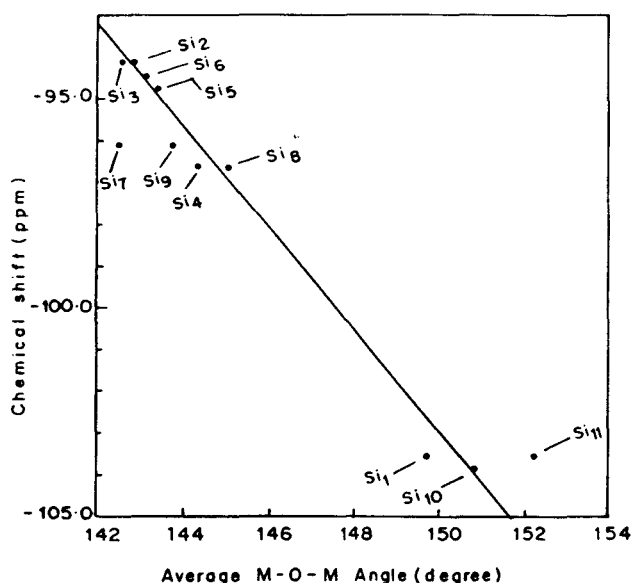


Figure 9. Assignment of crystallographically nonequivalent Si sites based on their chemical shift correlation with the M-O-M angles derived from X-ray structure of ETS-10.

Table 4. Energetics Derived from Quantum Chemical Calculations for Various Cluster Models Representing the Sites Si_1 , Si_{10} , and Si_{11}

cluster site	cluster model	total energy (eV)	relative aluminum substitution energy (eV)	relative proton binding energy (eV)
1	$\text{Si}(\text{OH})_4$	-3816.80		
10	$\text{Si}(\text{OH})_4$	-3815.22		
11	$\text{Si}(\text{OH})_4$	-3813.56		
1	$[\text{Al}(\text{OH})_4]^-$	-3562.40		
10	$[\text{Al}(\text{OH})_4]^-$	-3560.86		
11	$[\text{Al}(\text{OH})_4]^-$	-3559.23		
1	$\text{SiO}_4[\text{Si}(\text{OH})_3]_4$	-5724.73		
10	$\text{SiO}_4[\text{Si}(\text{OH})_3]_4$	-5724.45		
11	$\text{SiO}_4[\text{Si}(\text{OH})_3]_4$	-5724.20		
1	$\text{AlO}_4[\text{Si}(\text{OH})_3]_4^-$	-5682.55	-0.15	-0.31
10	$\text{AlO}_4[\text{Si}(\text{OH})_3]_4^-$	-5682.85	-0.69	0.00
11	$\text{AlO}_4[\text{Si}(\text{OH})_3]_4^-$	-5681.94	0.00	-0.69

The cluster site, the cluster model and total energy of the clusters are given in Table 4. The substitution energy evaluated according to eq 3 for process 2 at the three possible sites are also given in Table 4. The substitution energy of aluminum at the Si_{10} site is the most favorable and hence preferential substitution at Si_{10} is expected. When Si_{10} is substituted by aluminum, the silicons adjacent to Si_{10} , which are Si_2 , Si_3 , Si_5 , and Si_6 , are expected to undergo a downfield shift by 4 ppm, as is indeed observed. With this, the resonances of type II silicons could be assigned to Si_4 , Si_7 , Si_8 , and Si_9 .

In earlier reports,⁴⁷⁻⁴⁹ it has been shown that there is a linear correlation between the NMR chemical shifts and the Si-site geometry, namely the average Si-O-Si angle. We derived the Si-O-Si angle for all the 11 sites from the structural report and then plotted against the experimental chemical shift. However, when more than one peak could not be deconvoluted, the average Si-O-Si angles were considered. Our assignment is further testified from the plot of chemical shift versus M-O-M angle as shown in Figure 9, which shows almost a linear variation.

The slight deviations noticed in T-site correlation are thought to arise from the influence of other geometrical parameters such as M-O distances, O-M-O angles, and O-M-O-M dihedral angles. It may also be noted that the signals for the eight silicons

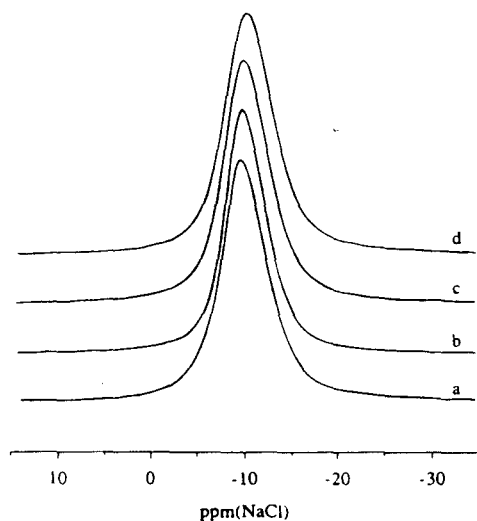


Figure 10. 105.8-MHz ^{23}Na MAS spectra of ETS-10 (a) and ETAS-10, Si/Al = 62 (b), 42 (c), and 22 (d).

of type I and type II lie in rather restricted chemical shift range -94.1 to -96.6 ppm. Further enhancement in chemical shift dispersion may become noticeable at very high magnetic fields.

The cations compensating the anionic framework charge due to aluminum substitution can be protons and they impart Bronsted acidity. The binding strength of protons to the oxygen atoms bridging silicon and aluminum is an indication of acid strength. We have evaluated the acidity of protons bonded to different oxygen sites, by calculating the proton binding energy according to eq 5. It is observed that the site where most facile substitution of aluminum occurs, namely Si_{10} , creates the stronger acidity. As predicted by the proton binding energy, the proton is weakly bound, when Al substitutes Si_{10} (Table 4).

^{23}Na and ^{27}Al MQ-MAS NMR. Recently, a new 2D MQ-MAS experiment on quadrupolar nuclei was proposed by Frydman and Harwood⁴² and further developed by Fernandez and Amoureux.^{50,51} Since this method completely averages out anisotropic interactions, such as dipolar and chemical shieldings, as well as second-order quadrupolar broadening, it gives new access for studying half-integer quadrupolar nuclei, such as the sodium cations and the aluminum sites in molecular sieves. In this experiment, an isotropic spectrum of the quadrupolar nucleus can be obtained from 2D correlation of 3Q (or 5Q in ^{27}Al) and 1Q transitions. Separation of contributions from quadrupole interactions and chemical shieldings is readily achieved, and one can get valuable information about the distribution of CS of nonequivalent sites and further of the electric field gradients at these sites. Our application of this method to ETS-10 and ETAS-10 is also the first attempt to characterize the cation environment in molecular sieves by MQ-MAS NMR.

In ETS-10 and ETAS-10, sodium cations partly counterbalance the negative framework charge due to octahedrally coordinated titanium. Simple ^{23}Na MAS spectra of ETS-10 and ETAS-10, shown in Figure 10, are featureless, and no information can be discerned about the cation environments. All spectra display single asymmetric lines devoid of quadrupolar features. Although the second-order quadrupole broadening of the observed $(-1/2, +1/2)$ central transition is less severe at the high-field (9.4-T) operation, no clue about the cation site distribution

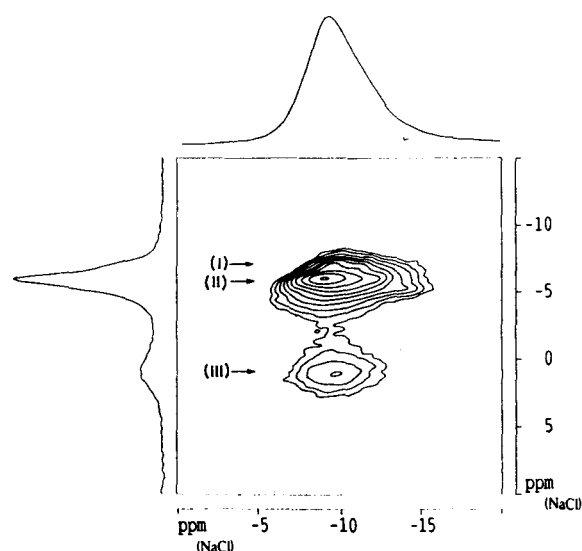


Figure 11. 105.8-MHz ^{23}Na 3Q MAS spectrum showing the resolution of cation sites in ETS-10. The labels (I), (II) and (III) correspond to the different sodium environments as discussed in the text.

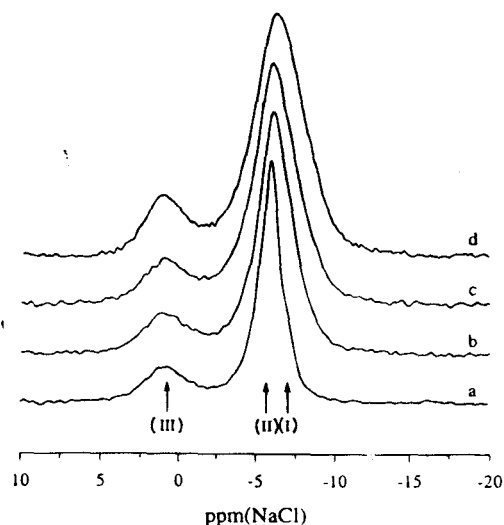


Figure 12. Isotropic projection of ^{23}Na 3Q MAS spectra of ETS-10 (a) and ETAS-10, Si/Al = 62 (b), 42 (c), and 22 (d). These spectra were obtained by a projection of the sheared 2D data sets as mentioned in the text.

is available from those spectra. In ETAS-10 samples, there is an increasing broadening with increasing aluminum substitution (Figure 10,b-d).

3Q-MAS correlation experiments were performed on ETS-10 and ETAS-10 using a three-pulse sequence as discussed in the Experimental Section. The result is shown in Figure 11 as a 2D contour plot for the 3Q-MAS experiment conducted on ETS-10. A shear transformation during 2D Fourier transform has been used to align the anisotropic (A) direction parallel to the δ_2 horizontal axis, so that a projection parallel to this axis gives rise to the isotropic (δ_{iso}) dimension and yields a high-resolution spectrum of sodium without second-order quadrupole broadening. The isotropic spectra so obtained on ETS-10 and ETAS-10 are compared in Figure 12. Several important aspects of MQ-MAS results are discussed below.

We recognize distinct sodium environments from the results presented in Figures 11 and 12. A careful inspection of the isotropic spectrum (Figures 11 and 12a) reveals three non-equivalent sodium sites in the structure of ETS-10. One of these sites is well-resolved, whereas two other sites have considerable

(50) Fernandez, C.; Amoureux, J. P. *Chem. Phys. Lett.* **1995**, *242*, 449-454.

(51) Fernandez, C.; Amoureux, J. P. *Solid State Nucl. Magn. Reson.* **1996**, *5*, 315.

3Q spectral overlap. The three sites are marked (I), (II), and (III) in the figure. A recourse to ETS-10 structure shows that the asymmetric unit contains three crystallographically non-equivalent titaniums, of which Ti_1 and Ti_2 are similar due to the silicon and titanium connectivities to their immediate neighbors, while site Ti_3 is distinct (see also connectivity Table 1). This is also noticed in the ^{29}Si MAS NMR spectrum, as discussed earlier. The charge-balancing role of the sodium cations at these distinct titanium sites is clearly borne out from our 3Q-MAS studies. Although for complete charge balancing we require two sodiums for each nonequivalent titanium, the observation of only three sodium sites from 3Q-MAS experiments suggests that sodium cations probably occupy symmetry-related positions so that the two sodiums on each titanium become pairwise equivalent. Indeed, such a picture emerges from cation modeling of sodium positions in ETS-10.⁵² It is noticed that sodium ions coordinate to titanium atoms in such a way that they are located on either side of titanium and form a chain of sodium atoms that run almost parallel with Ti—O—Ti chains, the sodiums residing in the small pores built from 7-member rings. It is essentially sodium-rich, and the presence of potassium ions at low concentration is not likely to alter our conclusions about sodium environments derived from MQ-MAS NMR studies.

The expected 2:1 relative intensity of site (I, II) to site (III) is not readily apparent in the isotropic spectra of Figures 11 and 12. It is realized that sites (I, II) and (III) experience quadrupolar interaction of different magnitude. In the MQ-MAS experiment, sites with different quadrupolar interactions are not excited to the same extent for the generation of multiple-quantum coherences with the same efficiency. In particular, site (III), which experiences a much stronger quadrupolar interaction, develops weaker coherence compared to that for (I, II). However, by the knowledge of the rf field, especially of the multiple-quantum creation and conversion pulses, and also by the first estimate of C_q of each line, it is possible to stimulate the pulse response of the sites to a given experimental condition. The numerical method which involves the computation of the density matrix evolution under the rf power and spinning speed used in the experiment is fully described in ref 53. The result of this calculation is shown in Figure 13. The relative intensity found by this method is in remarkably good agreement with the expected 2:1 sodium site population.

The sodium sites are further characterized by C_q and δ_{CS} , which are the quadrupole interaction and isotropic chemical shift parameters, respectively. After shearing, the chemical shift axis is located with a slope of 1, while the QIS direction has a slope of $-10/17$. It is readily seen from Figure 11 that the two contours associated with (III) and (I, II) are displaced with respect to both of these axes so that they are characterized by different sets of quadrupolar and chemical shift parameters. An analysis of the 2D data gives an estimate of C_q and δ_{CS} , which are 0.9 MHz, -7 ppm and 1.65 MHz, -2.5 ppm for sites (I, II) and (III), respectively.

We show in Figure 12b–d the ^{23}Na 3Q MAS isotropic projection spectra for ETAS-10 with increasing aluminum substitution. These spectra are devoid of the second-order broadening and reveal distinct sodium sites whose peak maxima occur at the sum of the isotropic chemical shift and the quadrupole triple-quantum-induced shift.⁵⁴ When compared with the result obtained on ETS-10 (Figure 12a), it is clear that

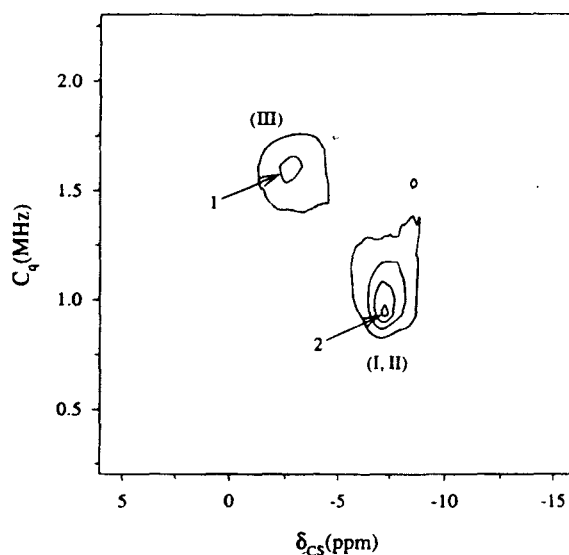


Figure 13. Quantification of the experimentally determined sodium sites (I, II) and (III) in ETS-10. This is obtained by a computer simulation of the actual response on the experimentally observed 2D data matrix to give the indicated population numbers as well as the quadrupole (C_q) and chemical shift (δ_{CS}) parameters.

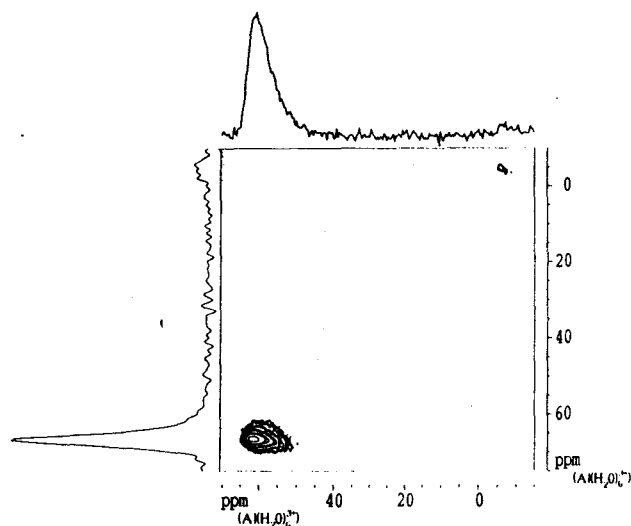


Figure 14. 104.3-MHz ^{27}Al 3Q MAS spectrum of ETAS-10 (Si/Al = 22). The intense contour is due to tetrahedral framework aluminum. The sodium environments are intact in the aluminum-substituted materials, except for the additional broadening. This broadening is seen to increase with increasing aluminum content, and the distinction of (I) and (II) type environments is quickly lost. It may also be noted that the site (III) position is unchanged. The ^{29}Si MAS NMR results discussed earlier show that the framework structure of the aluminum-substituted material conforms to parent ETS-10 structure. In addition, the present 3Q MAS observations in ETAS-10 show that the cation environment is unchanged as well. Taken together, our studies lend credence to the view that the overall structure of ETAS-10 is the same as that of ETS-10 and that the heteroatom substitution occurs isomorphically. We believe that the observed broadening arises mainly from a distribution of isotropic chemical shifts and is only slightly due to a distribution caused by quadrupolar effects, since the 2D contour plots show distorted patterns with ridges that extend along the diagonal of slope 1.

In an effort to characterize the tetrahedrally substituted aluminum sites by MQ-MAS NMR, we have performed the 3Q MAS experiments for the $I = 5/2$ aluminum nuclei in ETAS-10 with different Si/Al. The triple-quantum–single-quantum cor-

(52) Yang, X.; Blosser, P. W. *Zeolites* **1996**, *17*, 237–243.

(53) Zwanziger, J. W. *Solid State Nucl. Magn. Reson.* **1994**, *3*, 219.

(54) Medek, A.; Harwood, J. S.; Frydman, L. *J. Am. Chem. Soc.* **1995**, *117*, 12779–12787.

relation is shown as a 2D contour plot in Figure 14 for Si/Al = 22. Despite the low Al loading, presence of octahedral aluminum is clearly visible in the 2D plot. Similar spectral features were noticed in other samples with increasing Si/Al. A feature of the 3Q MAS result is that the isotropic projection spectrum gives a much sharper resonance for the tetrahedral site at 65 ppm along the isotropic dimension, suggesting that a highly crystalline material has been synthesized. Within the resolution afforded by 3Q MAS, we however do not get any clue about the presence of nonequivalent tetrahedral aluminum sites. It is probable that the aluminum substitution occurs preferentially at the silicious environments, in the manner that molecular modeling studies show.

Conclusions

In this paper, we have presented a detailed analysis of the MAS NMR of highly pure ETS-10 and ETAS-10 molecular sieves which were synthesized without the use of any ETS-4 seeds. The ^{29}Si MAS NMR spectra at 7.1-T field display superior resolution and allow individual T sites to be recognized. A combination of NMR and molecular modeling is shown to

be a very powerful approach for the exact location of Al substitution and the Bronsted acidic sites and the assignment of different tetrahedral silicon sites. The strategy involves isomorphic substitution of silicon by Al in ETS-10 lattice and Al substitution energy calculations by quantum chemical methods. We have also addressed the question of heteroatom lattice substitution in molecular sieves by slow MAS NMR. We show that this approach is very effective in establishing isomorphic substitution in molecular sieves through changes in chemical shielding tensor brought by transformation of local symmetry. This has been demonstrated in ETS-10 and ETAS-10. The power of the MQ-MAS NMR technique to determine the cationic sites occupied by sodium in ETS-10 and ETAS-10 is demonstrated.

Supporting Information Available: Tables of Si–O and Ti–O distances and Si–O–Si and Si–O–Ti angles in ETS-10 (2 pages, print/PDF). See any current masthead page for ordering information and Web access instructions.

JA972714O

Conclusion

General considerations on the MQMAS experiment

The recently developed MQMAS experiment allows all anisotropic interactions that occur in solid-state NMR to be averaged out, this includes first- and second-order quadrupolar interactions. A development of the quadrupolar Hamiltonian was necessary to explain the foundations of the method presently used. Moreover, the procedure for acquiring and processing an MQMAS spectrum in a two dimensional way required special care. For the last three years, the improvements that we made to the MQMAS experiment were directed towards the aim of getting (1) a pure absorption 2D spectrum and (2) a higher efficiency of the multiple-quantum excitation.

Amongst the different variations of the MQMAS experiment which have arised, we put the emphasis on the need of including a z -filter in the sequence. Meanwhile, numerical calculations and experimental optimisations converged to provide the optimal conditions of the multiple-quantum excitation. These enhancements of the Frydman's original MQMAS experiment made it possible to acquire high-resolved spectra of quadrupolar nuclei, the quality of which was satisfactory for a subsequent quantification.

Today, we have gotten to the point where the basic MQMAS sequence can be efficiently used as a routine and should not need further improvement. Nevertheless, a better efficiency of the multiple-quantum transfers is still

possible if additional developments of the equipment (stronger rf field, higher spinning speed) are undertaken.

Quantification by inversion

In a subsequent step, we have shown that the excitation of the multiple-quantum coherences is uneven such that a straightforward quantification of the 2D spectrum is almost impossible. The methods using MAS and MQMAS spectra failed to provide an accurate quantitative result, especially when the materials are badly-crystallised. Therefore, the main part of the present work was to precisely determine the relative concentration of each site by inversion of the MQMAS spectrum. The calculation that was introduced leads to a canonical representation of the different sites taking advantage of the fact that the position of a band on the 2D dataset is fully determined by the P_Q and δ_{CS} parameters. If a correction of the intensities using a powerful simulation program, is included during the inversion, we obtain a canonical representation for which the relative proportion of the unequivalent sites is close to what it is in reality.

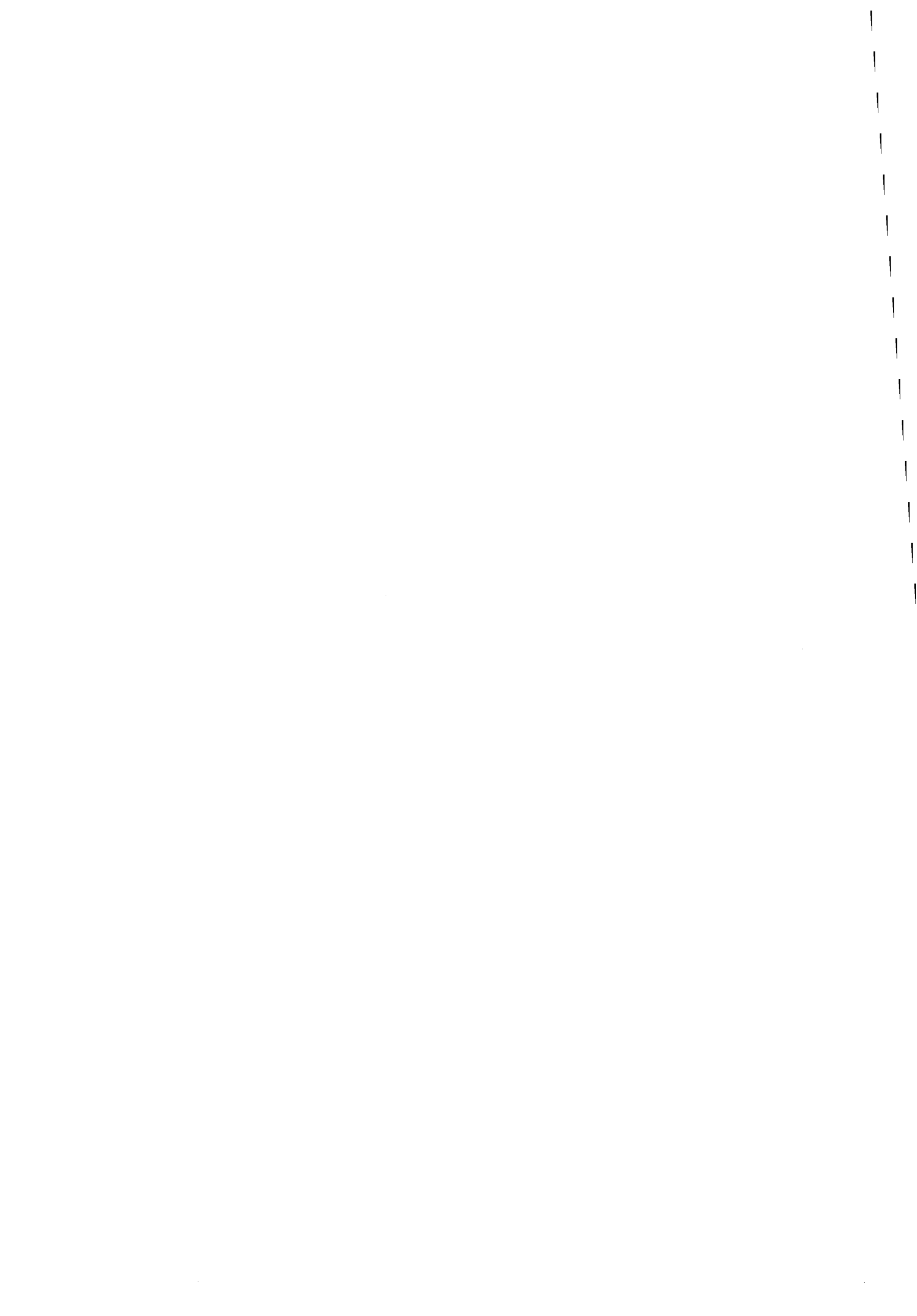
Our method of inversion provided a precise determination (within 10% accuracy) of the proportion of ^{27}Al , ^{17}O and ^{23}Na sites in several microporous materials. This quantification, combined with the capability of the MQMAS experiment to separate crystallographically non equivalent sites, has revealed to be an unequalled technique for investigating the present materials. Indeed, ^{29}Si MAS experiments as well as previous X-Ray diffraction studies had failed to give such precise information.

We also observed that there was a minimum width for the spots appearing on the canonical representation, even for very well-crystallised samples. However, this broadening resulting from the inversion is less critical when it is

applied to badly-crystallised or amorphous samples for which this calculation is designed.

Future of MQMAS-based experiments

The MQMAS technique has revealed its full potential to the NMR community. Thanks to its ease of use, numerous chemical studies now integrate this experiment as a routine. Indeed, an MQMAS spectrum can be acquired without any technological sophisticated equipment, unlike DOR and DAS experiments. The other great advantage of the MQMAS is also that the basic sequence is pretty flexible and additional spin manipulations can easily be added before, after or during the multiple-quantum evolution. After finding a way to get rid of all the anisotropic broadenings, we can imagine further spin manipulations which will independently reintroduce each interaction for a subsequent and separate analysis. The CP-MQMAS and MQ-REDOR sequences presented here are preliminary to a new class of experiments in solid-state NMR of quadrupolar nuclei. Today, the preference is given to the MQ-REDOR sequences as it allows the inter-nuclear distances to be determined through the reintroduction of the dipolar interaction. No doubt that other spin and spatial manipulations will be associated in the future to provide complementary structural information on powder samples.



Appendix

Flow Chart of REGULAR

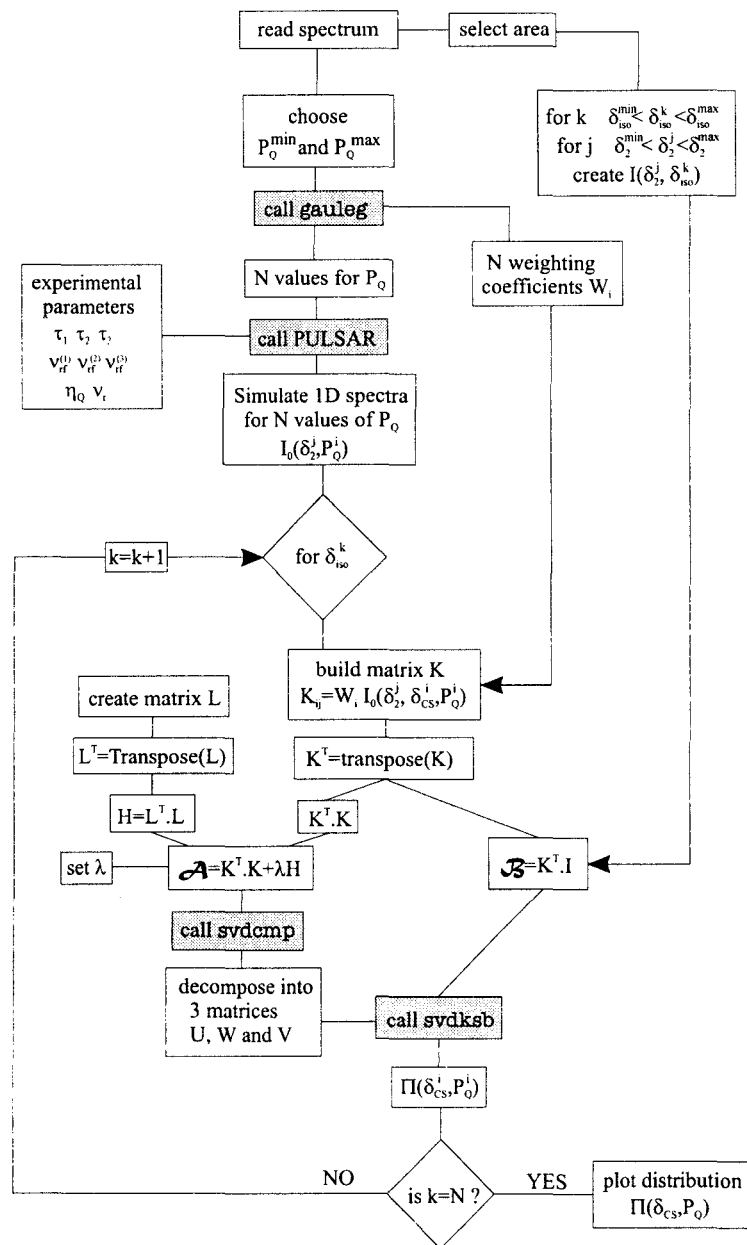


FIG. 4.3: Main steps in REGULAR.

Subroutine gauleg

```

!=====
subroutine gauleg(x1,x2,x,w,n)
!=====
integer n
real x1,x2,x(n),w(n)
double precision eps
parameter (eps=3.d-14)
! Given the lower and upper limits of integration x1 and x2,
! and given n, this routine returns arrays x(1:n) and w(1:n)
! of length n, containing the abscissas and weights of the
! Gaussian Legendre n-point quadrature formula.
integer i,j,m
double precision p1,p2,p3,pp,xl,xm,z,z1
m=(n+1)/2
xm=0.5d0*(x2+x1)
xl=0.5d0*(x2-x1)
do i=1,m
  z=cos(3.141592654d0*(i-.25d0)/(n+.5d0))
  1 continue
  p1=1.0d0
  p2=0.0d0
  do j=1,n
    p3=p2
    p2=p1
    p1=((2.d0*j-1.d0)*z*p2-(j-1.d0)*p3)/j
  end do
  pp=n*(z*p1-p2)/(z*z-1.d0)
  z1=z
  z=z1-p1/pp
  if (abs(z-z1).gt.EPS) goto 1
  x(i)=xm-xl*z
  x(n+1-i)=xm+xl*z
  w(i)=2.d0*xl/((1.d0-z*z)*pp*pp)
  w(n+1-i)=w(i)
end do
return
end

```

Subroutine svdcmp

```

!=====
subroutine svdcmp(a,m,n,mp,np,w,v)
!=====
integer m,mp,n,np,NMAX
real a(mp,np),v(np,np),w(np)
parameter (NMAX=500)
! Given a matrix a(1:m,1:n), with physical dimensions mp by np,
! this routine computes its singular value decomposition,
! A=U.W.VT. The matrix U replaces a on output. The diagonal
! matrix of singular values W is output as a vector w(1:n).
! The matrix V (not the transpose VT) is output as v(1:n,1:n).
integer i,its,j,jj,k,l,nm
real anorm,c,f,g,h,s,scale,x,y,z,rv1(NMAX),pythag

g=0.0
scale=0.0
anorm=0.0
do i=1,n
  l=i+1
  rv1(i)=scale*g
  g=0.0
  s=0.0
  scale=0.0
  if (i.le.m) then
    do k=i,m
scale=scale+abs(a(k,i))
    end do
    if (scale.ne.0.0) then
do k=i,m
  a(k,i)=a(k,i)/scale
  s=s+a(k,i)*a(k,i)
end do
f=a(i,i)
g=-sign(sqrt(s),f)
h=f*g-s
a(i,i)=f-g
do j=1,n
  s=0.0
  do k=i,m
    s=s+a(k,i)*a(k,j)
  end do
  f=s/h

```

```
do k=i,m
  a(k,j)=a(k,j)+f*a(k,i)
end do
end do
do k=i,m
  a(k,i)=scale*a(k,i)
end do
  end if
end if
w(i)=scale*g
g=0.0
s=0.0
scale=0.0
if ((i.le.m).and.(i.ne.n)) then
  do k=1,n
scale=scale+abs(a(i,k))
  end do
  if (scale.ne.0.0) then
do k=1,n
  a(i,k)=a(i,k)/scale
  s=s+a(i,k)*a(i,k)
end do
f=a(i,1)
g=-sign(sqrt(s),f)
h=f*g-s
a(i,1)=f-g
do k=1,n
  rv1(k)=a(i,k)/h
end do
do j=1,m
  s=0.0
  do k=1,n
    s=s+a(j,k)*a(i,k)
  end do
  do k=1,n
    a(j,k)=a(j,k)+s*rv1(k)
  end do
end do
do k=1,n
  a(i,k)=scale*a(i,k)
end do
  end if
end if
anorm=max(anorm,(abs(w(i))+abs(rv1(i))))
end do
```

```
do i=n,1,-1
  if (i.lt.n) then
    if (g.ne.0.0) then
      do j=1,n
        v(j,i)=(a(i,j)/a(i,1))/g
      end do
      do j=1,n
        s=0.0
        do k=1,n
          s=s+a(i,k)*v(k,j)
        end do
        do k=1,n
          v(k,j)=v(k,j)+s*v(k,i)
        end do
      end do
    end if
    do j=1,n
      v(i,j)=0.0
      v(j,i)=0.0
    end do
    end if
    v(i,i)=1.0
    g=rv1(i)
    l=i
  end do
do i=min(m,n),1,-1
  l=i+1
  g=w(i)
  do j=1,n
    a(i,j)=0.0
  end do
  if (g.ne.0.0) then
    g=1.0/g
    do j=1,n
      s=0.0
      do k=1,m
        s=s+a(k,i)*a(k,j)
      end do
      f=(s/a(i,i))*g
      do k=i,m
        a(k,j)=a(k,j)+f*a(k,i)
      end do
    end do
  end if
  do j=i,m
```

```
a(j,i)=a(j,i)*g
  end do
  else
    do j=i,m
a(j,i)=0.0
    end do
  end if
  a(i,i)=a(i,i)+1.0
end do
do k=n,1,-1
  do its=1,30
    do l=k,1,-1
nm=l-1
if (abs((abs(rv1(l))+anorm)-anorm).lt.1.E-15) goto 2
if (abs((abs(w(nm))+anorm)-anorm).lt.1.E-15) goto 1
      end do
      1      c=0.0
      s=1.0
      do i=1,k
f=s*rv1(i)
rv1(i)=c*rv1(i)
if ((abs(abs(f)+anorm)-anorm).lt.1.E-15) goto 2
g=w(i)
h=pythag(f,g)
w(i)=h
h=1.0/h
c=(g*h)
s=-(f*h)
do j=1,m
  y=a(j,nm)
  z=a(j,i)
  a(j,nm)=(y*c)+(z*s)
  a(j,i)=- (y*s)+(z*c)
end do
      end do
      2      z=w(k)
      if (l.eq.k) then
if (z.lt.0.0) then
  w(k)=-z
  do j=1,n
    v(j,k)=-v(j,k)
  end do
end if
goto 3
      end if
```

```

    if (its.eq.30) write(*,*) 'no convergence in svdcmp'
    x=w(1)
    nm=k-1
    y=w(nm)
    g=rv1(nm)
    h=rv1(k)
    f=((y-z)*(y+z)+(g-h)*(g+h))/(2.0*h*y)
    g=pythag(f,1.0)
    f=((x-z)*(x+z)+h*((y/(f+sign(g,f)))-h))/x
    c=1.0
    s=1.0
    do j=1,nm
    i=j+1
    g=rv1(i)
    y=w(i)
    h=s*g
    g=c*g
    z=pythag(f,h)
    rv1(j)=z
    c=f/z
    s=h/z
    f=(x*c)+(g*s)
    g=-(x*s)+(g*c)
    h=y*s
    y=y*c
    do jj=1,n
        x=v(jj,j)
        z=v(jj,i)
        v(jj,j)=(x*c)+(z*s)
        v(jj,i)=-(x*s)+(z*c)
    end do
    z=pythag(f,h)
    w(j)=z
    if(z.ne.0.0) then
        z=1.0/z
        c=f*z
        s=h*z
    end if
    f=(c*g)+(s*y)
    x=-(s*g)+(c*y)
    do jj=1,m
        y=a(jj,j)
        z=a(jj,i)
        a(jj,j)=(y*c)+(z*s)
        a(jj,i)=-(y*s)+(z*c)
    end do

```

```

end do
  end do
  rv1(1)=0.0
  rv1(k)=f
  w(k)=x
end do
  3 continue
end do
return
end

```

Subroutine svdksb

```

!=====
subroutine svdksb(u,w,v,m,n,mp,np,b,x)
!=====
integer m,mp,n,np,NMAX
real b(mp),u(mp,np),v(np,np),w(np),x(np)
parameter (NMAX=500)
! Solves A.X=B for a vector X, where A is specified by the
! arrays u, w, v as returned by the svdcmp. m and n are the
! logical dimensions of a, and will be equal for square
! matrices. mp and np are the physical dimensions of a. b(1:m)
! is the input right-hand side. x(1:n) is the output solution
! vector. No input quantities are destroyed, so the routine
! may be called sequentially with different b's.
integer i,j,jj
real s,tmp(NMAX)
do j=1,n
  s=0.
  if (w(j).ne.0.) then
    do i=1,m
      s=s+u(i,j)*b(i)
    end do
    s=s/w(j)
  end if
  tmp(j)=s
end do
do j=1,n
  s=0.
  do jj=1,n

```



```
        s=s+v(j,jj)*tmp(jj)
    end do
    x(j)=s
end do
return
end
```